

University of Alberta

**Overflow on the Mackenzie Delta Sea Ice Surface
and the Hydraulics of Strudel Flows**

by

Maxime Bélanger

A thesis submitted to the Faculty of Graduate Studies and Research
in partial fulfillment of the requirements for the degree of

**Master of Science
in
Water Resources Engineering**

Department of Civil and Environmental Engineering

© Maxime Bélanger
Fall 2010
Edmonton, Alberta

Permission is hereby granted to the University of Alberta Libraries to reproduce single copies of this thesis and to lend or sell such copies for private, scholarly or scientific research purposes only. Where the thesis is converted to, or otherwise made available in digital form, the University of Alberta will advise potential users of the thesis of these terms.

The author reserves all other publication and other rights in association with the copyright in the thesis and, except as herein before provided, neither the thesis nor any substantial portion thereof may be printed or otherwise reproduced in any material form whatsoever without the author's prior written permission.

Examining Committee

Dr. Faye Hicks, Civil and Environmental Engineering

Dr. Mark Loewen, Civil and Environmental Engineering

Dr. Martin Sharp, Earth and Atmospheric Sciences

Abstract

The main objective of this study was to describe the overflow of freshwater onto the sea ice surface in the Mackenzie Delta and to investigate the hydraulic behaviour of the upwelling and strudel events. This study was performed from the analysis of data collected during field investigations, from satellite images and from experimental laboratory studies. A forecasting method using the water level in the Mackenzie River was formulated to predict the overflow initiation about five days before its occurrence. The physical modelling of a strudel flow through a circular hole established a relation between the overflow depth and the discharge coefficient. Velocity measurements of the free-surface vortex using an Acoustic Doppler Velocimeter found that velocities at the vortex's core were influenced by its vorticity. Finally, predictions of maximum strudel scour, which are of great importance for the determination of burial depth of pipelines, were predicted from published impinging jet experiments.

Acknowledgments

I would like to thank the following individuals and groups for their help and support in making the completion of this thesis a success. First, thanks to my thesis supervisors, Dr. Faye Hicks and Dr. Mark Loewen for their continuous support throughout my studies and for their help and advice with the technical writing and the data analysis. A great amount of recognition goes to Steve Solomon of NRCan for introducing the strudel topic to me and for sharing his knowledge and his expertise during the field work in the Mackenzie Delta which occurred in spring 2008 and 2009. Steve also made the field work arrangements and greatly helped with the data collection and the data analysis. Personal acknowledgments are given to the University of Alberta water resources engineering technologists, Perry Fedun and Chris Krath for constructing the laboratory apparatus and providing continuous support regarding the laboratory experiments. Additional thanks are given to the water resources professors and support staff of the water resources department at the University of Alberta which help and support was useful and well appreciated. I would also like to thank my fellow classmates, my friends, my parents, my sister, my brother-in-law, and my girlfriend who supported me throughout these years.

I would like to acknowledge the Geological Survey of Canada (Atlantic) group of NRCan for supplying measuring instruments, equipment and for providing travel and accommodation arrangements during the field work in the Mackenzie Delta in spring 2008 and 2009. Free data provided by Environment Canada (Water Survey of Canada, National Climate Data and Information Archive), Fisheries and Oceans Canada and National Resources of Canada (Atlas of Canada, Geological Survey of Canada (Atlantic)), and free satellite images provided by USGS, ESA and GINA were very useful as I could not have fulfilled the majority of my research objectives without their availability. This research was funded by the Government of Canada International Polar Year (IPY) program, the Natural Sciences and Engineering Research Council of Canada (NSERC), National Resources of Canada (NRCan), and by the University of Alberta through scholarships. These financial supports are greatly acknowledged.

Table of Contents

1.0	Introduction.....	1
2.0	Ice Overflow, Upwellings, Strudel Drains and Strudel Scours in the Mackenzie Outer Delta	7
2.1	Overview	7
2.2	Literature Review	7
2.2.1	Ice Overflow Descriptions and Observations.....	7
2.2.2	Strudel Drains Definitions and Observations.....	9
2.2.3	Strudel Scour Descriptions and Observations	10
2.2.4	Strudel Scour Measurements and Statistics	12
2.2.5	Risk Assessment to Man-Made Structures	13
2.2.6	Interannual Variability of the Overflow and Strudel Events.....	15
2.3	Study Area – The Mackenzie Delta	16
2.4	Data Collection and Methodology	17
2.4.1	General	17
2.4.2	Satellite Images.....	19
2.4.3	Land-Water Feature Map	21
2.4.4	Overflow Delineation.....	25
2.4.5	Floating Channel Ice Delineation	26
2.4.6	Bottomfast Ice Delineation.....	28
2.4.7	Field Observations and Measurements	29
2.4.8	Meteorological and Water Level Data	31
2.4.9	Bed Sediments	32
2.5	Analysis, Results and Discussion	33
2.5.1	Overflow Depth Data	33
2.5.2	Ice Formation and Chronology of the Ice Surface Overflow.....	36
2.5.2.1	<i>Overview.....</i>	<i>36</i>
2.5.2.2	<i>Freeze-Up and Winter Ice Conditions</i>	<i>36</i>
2.5.2.3	<i>Initial Bottomfast Ice Overflow</i>	<i>38</i>

2.5.2.4	<i>Initial Floating Sea Ice Overflow</i>	41
2.5.2.5	<i>Maximum Floating Sea Ice Overflow</i>	42
2.5.2.6	<i>Drained Overflow</i>	43
2.5.2.7	<i>Peak Freshet Arrival</i>	45
2.5.3	Timing and Extent of the Overflow.....	46
2.5.4	Interannual Variation in the Overflow Location	49
2.5.5	Predicting the Timing of the Overflow.....	51
2.5.6	Upwelling, Strudel Drains and Strudel Scours	58
2.5.6.1	<i>General</i>	58
2.5.6.2	<i>Strudel Measurement Results from Field Investigations</i>	59
2.5.6.3	<i>Upwellings</i>	62
2.5.6.4	<i>Strudel</i>	63
2.5.6.5	<i>Strudel Scours</i>	65
3.0	Physical Laboratory Model of Strudel Flow	114
3.1	Overview	114
3.2	Literature Review	115
3.2.1	Previous Physical Strudel Experiments.....	115
3.2.2	Axisymmetric Circular Turbulent Jets	116
3.2.2.1	<i>General</i>	116
3.2.2.2	<i>Free Jet Region</i>	116
3.2.2.3	<i>Impingement Region</i>	118
3.2.3	Free-Surface Vortex Flow above a Circular Drain	120
3.2.4	Free-Surface Vortex Flow below a Circular Drain	123
3.3	Materials, Methods and Data Collection	124
3.3.1	Physical Hydraulic Model.....	124
3.3.1.1	<i>Experimental Setup</i>	124
3.3.1.2	<i>Experimental Procedures</i>	126
3.3.1.3	<i>Dimensional Analysis</i>	127
3.3.2	Velocity Measurements.....	128
3.3.2.1	<i>General</i>	128
3.3.2.2	<i>Experimental Setup</i>	129
3.3.2.3	<i>Experimental Procedures and Data Collection</i>	130

3.4	Results and Discussion	132
3.4.1	Flow Visualisation of the Free-Surface Vortex Flow	132
3.4.2	Free-Surface Vortex Flow beneath the Ice Cover	134
3.4.2.1	<i>Overview</i>	134
3.4.2.2	<i>Free Jet Region</i>	134
3.4.2.3	<i>Transition Region</i>	136
3.4.2.4	<i>Impingement Region</i>	138
3.4.2.5	<i>Summary</i>	139
3.4.3	Relation between the Hydraulic Parameters of the Free-Surface Vortex Flow.....	140
4.0	Estimation of the Strudel Scour Depths in the Mackenzie Outer Delta.....	169
4.1	Overview	169
4.2	Theoretical Background	169
4.2.1	Scouring by Vertically Impinging Jets.....	169
4.2.2	Scouring Development and Scour Profile	171
4.2.3	Scours in Cohesionless Soils.....	173
4.2.4	Scours in Cohesive Soils	176
4.3	Selection of the Strudel Scour Depth Estimation Equation	178
4.4	Definition of Strudel Scour Depth Estimation Parameters	179
4.5	Estimation of the Strudel Scour Depth	182
5.0	Conclusions and Recommendations	187
6.0	References	193

Appendix A Details of Hydraulic Data Collection from Strudel Experiments

Appendix B Details of Hydraulic Data Collection from Strudel Experiments

Supplemental Collected Data and Analysis
where the Downstream Water Surface
was below the Under-Ice Surface

Appendix C Details of Velocity Data Collection from ADV Measurements

**Appendix D Complete Velocity Profiles and x-y Plane Plots
from ADV Measurements**

**Appendix E Poster Abstract, Extended Abstract and Poster
Presented at the CRIPE Conference in 2009**

Belanger, M., Hicks, F., Solomon, S., & Loewen, M. (2009). Influence of Mackenzie Delta Breakup on the Timing and Duration of Water Overflow on the Outer Delta Sea Ice Surface. Poster presented at the *CGU HS Committee on River Ice Processes and the Environment (CRIPE) - 15th Workshop on River Ice*, St. John's, Newfoundland and Labrador.

List of Tables

Table 2-1	Summarized strudel scour characteristics from a variety of publications.....	13
Table 2-2	Minimum / Average / Maximum circular strudel scour characteristics in the Alaskan Beaufort Sea from 1995 to 2007.	13
Table 2-3	Spectral band, spatial (image) resolution, delineation type, and delineation accuracy of the various satellites and instruments used in this study.	21
Table 2-4	Color appearance of the land and water features in the Mackenzie Outer Delta from the Landsat satellite images (Band 5) and modified colors resulting from the “Replace Color” Feature of Adobe Photoshop.	24
Table 2-5	Algorithm leading to the classification of the land and water features of the Mackenzie Outer Delta from the combination of high and low water level Landsat satellite images (Band 5) and final color coding of the land-water feature map.	24
Table 2-6	Date of initial overflow at key locations in the Mackenzie Outer Delta from 2006 to 2009.....	41
Table 2-7	Comparison between the ice condition of the Mackenzie Outer Delta channels and the date of peak freshet water level from the Water Survey of Canada water level gauges.	46
Table 2-8	Date of overflow stage occurrence in the Mackenzie Outer Delta at the Olivier Islands overflow region from 2002 to 2009.	48
Table 2-9	Date of overflow stage occurrence in the Mackenzie Outer Delta at the south of Garry Island overflow region from 2002 to 2009.	48
Table 2-10	Date of peak freshet arrival in the Mackenzie Outer Delta from 2002 to 2009.	48
Table 2-11	Number of days between the different overflow stages at the Olivier Islands region from 2002 to 2009.....	49

Table 2-12	Number of days between the different overflow stages south of Garry Island from 2002 to 2009.	49
Table 2-13	Methodology defining the overflow features in the Mackenzie Outer Delta from 2006 to 2009. The top overlay events have overlapping priority on the bottom events.....	51
Table 2-14	Date at which the water level increase thresholds in the Mackenzie River at Arctic Red River (Station ID 10LC014) were met from 2002 to 2009.....	54
Table 2-15	Number of days (average \pm standard deviation) between a water level increase criteria was met in the Mackenzie River at Arctic Red River (MARR) and a specified overflow stages at the Olivier Islands overflow region. The averages and standard deviations do not include the data from 2002 and 2009 as these years overflow were initiated by warm temperatures, and the year 2005 due to a gauge malfunction at MARR.	55
Table 2-16	Number of days (average \pm standard deviation) between a water level increase criteria was met in the Mackenzie River at Arctic Red River (MARR) and the specified overflow stages at the South of Garry Island overflow region. The averages and standard deviations do not include the data from 2002 and 2009 as these years overflow were initiated by warm temperatures, and the year 2005 due to a gauge malfunction at MARR.....	55
Table 2-17	Number of days between a water level increase of 30 cm/day in the Mackenzie River at Arctic Red River (MARR) and the specified overflow stages at the Olivier Islands overflow region from 2002 to 2009. The averages and standard deviations do not include the data from 2002 and 2009 as these years overflow were initiated by warm temperatures, and the year 2005 due to a gauge malfunction at MARR.	56
Table 2-18	Number of days between a water level increase of 2.0 m from the pre-breakup water level in the Mackenzie River at Arctic Red River (MARR) and the specified overflow stages at the Olivier Islands overflow region from 2002 to 2009. The averages and standard deviations do not include the data from 2002 and 2009 as these years overflow were initiated by warm temperatures, and the year 2005 due to a gauge malfunction at MARR.....	56

Table 2-19	Number of days between a water level increase of 30 cm/day in the Mackenzie River at Arctic Red River (MARR) and the specified overflow stages at the south of Garry Island overflow region from 2002 to 2009. The averages and standard deviations do not include the data from 2002 and 2009 as these years overflow were initiated by warm temperatures, and the year 2005 due to a gauge malfunction at MARR.	57
Table 2-20	Number of days between a water level increase of 2.0 m from the pre-breakup water level in the Mackenzie River at Arctic Red River (MARR) and the specified overflow stages at the south of Garry Island overflow region from 2002 to 2009. The averages and standard deviations do not include the data from 2002 and 2009 as these years overflow were initiated by warm temperatures, and the year 2005 due to a gauge malfunction at MARR.	57
Table 2-21	Cumulative mean daily degree-days above 0°C at the Inuvik climate station 1, 2, 3, 4, 5, and 10 days before the overflow began around the Olivier Islands from 2002 to 2009. The overflow process in 2002 and 2009 was initiated by warm temperatures in the Mackenzie Outer Delta.	58
Table 2-22	Summary of strudel measurements in 2008 at ST-2008.	60
Table 2-23	Summary of strudel measurements in 2009 at SL-2009 and SB-2009.	61
Table 3-1	Experimental run numbers for the ADV velocity measurements. The information in parenthesis refers to (<i>U_o</i> , <i>hod</i>).	129
Table 4-1	Strudel scour depth estimations for various parameter increase scenarios.	184

List of Figures

Figure 1-1	MODIS satellite images of the Mackenzie Delta in the Northwest Territories, Canada in a) July 2008, and b) May 2008.	5
Figure 1-2	Upwellings at the interface of the floating ice and of the bottomfast ice cover.	6
Figure 1-3	Strudel at the interface of the bottomfast ice and of the floating ice cover.	6
Figure 2-1	Topographic map of the Mackenzie Delta with the locations of the active Water Survey of Canada water level gauges (red). <i>Bottom-Right Insert:</i> Territorial map of the Northwest Territories in Canada.	67
Figure 2-2	MODIS satellite image of the Mackenzie Outer Delta with water and land features. <i>Bottom-Right Insert:</i> Mackenzie Delta.	68
Figure 2-3	a) Landsat 5 satellite image (Band 5) of the high water level on 08-June-2008, and b) Landsat 7 satellite image (Band 5) of the low water level on 18-September-2007 at the Middle Channel mouth region. c) Overlay of the high (blue) and low (red) water level Landsat satellite images. d) Land-water feature map of the Mackenzie Outer Delta (accuracy of 60 m) where the land is black, the intermittently submerged land is orange, the lakes are grey, and the ocean and rivers are white.	69
Figure 2-4	a) MODIS satellite image of Alaska, Yukon and part of the Northwest Territories on 22-May-2008. b) MODIS satellite image of the Mackenzie Outer Delta on 22-May-2008. c) MODIS satellite image of the south of Garry Island overflow region on 26-May-2008. d) Delineation of the overflow with the land-water feature map overlay (accuracy of 500 m). The green delineation represents the minimum (conservative) delineation area from personal judgement of the overflow boundaries and the combination of the red and green delineation represents the maximum (non-conservative) overflow delineation area.	70

Figure 2-5	Overflow in the Mackenzie Outer Delta at the Middle Channel mouth / Garry Island region from a) MODIS instrument (spatial resolution of 500 m), b) Landsat 5 satellite (Band 4) (spatial resolution of 30 m) on 23-May-2008. The overflow is shown as a dark color. The three pictures on the right validate the existence and the location of the overflow observed from the satellite images.....	71
Figure 2-6	a) Landsat 5 satellite image (Band 4) of the northern portion of the Mackenzie Outer Delta on 23-May-2008. b) Landsat 5 satellite image (Band 4) of the Kendall Island region on 23-May-2008. c) Delineation of the channel floating ice with the land-water feature map overlay (accuracy of 60 m). The green delineation represents the minimum (conservative) delineation area from personal judgement of the floating channel ice boundaries and the combination of the red and green delineation represents the maximum (non-conservative) channel floating ice delineation area.....	72
Figure 2-7	a) Envisat ASAR image of the northern portion of the Mackenzie Outer Delta on 02-May-2008. b) Envisat ASAR image of the south of Garry Island region on 02-May-2008. c) Delineation of the bottomfast ice with the land-water feature map overlay (accuracy of 500 m). The green delineation represents the minimum (conservative) delineation area from personal judgement of the bottomfast ice boundaries and the combination of the red and green delineation represents the maximum (non-conservative) bottomfast ice delineation area.....	73
Figure 2-8	Approximate outline of the South of Garry Island and Olivier Islands overflow regions (blue), instrument location deployed during the 2008 and 2009 field investigations, and bed sediments sampling locations in the Mackenzie Outer Delta.	74
Figure 2-9	Time-lapse picture camera and depth sensors at ST-2009 in May 2009.....	75
Figure 2-10	View from above of the strudel holes measured at ST-2008 in May 2008.....	75
Figure 2-11	View from above of the strudel drains measured at a) SL-2009 (inset: close-up view of the S2009-01 strudel) and at b) SB-2009 in May 2009.....	76

Figure 2-12	Mean daily temperature at the Inuvik climate station (ID 2202575), Norman Wells climate station (ID 2202800) and Pelly Island climate station (ID 2203095) in April and May from 2002 to 2009.....	76
Figure 2-13	Soil content at various depths from the bed surface in the Mackenzie Outer Delta at the south of Garry Island overflow region at BH4-2007, BH5-2007, and Strudel-2008.	77
Figure 2-14	Ocean water level at Tuktoyaktuk and overflow depths at BH4-2008 and ST-2008 during breakup in 2008. The ocean water level and the overflow depths are not on a common datum.	78
Figure 2-15	Ocean water level at Tuktoyaktuk, overflow depths and water depths at ST-2009 during breakup in 2009. The datum elevation of the depth sensor in Hole 1 is not fixed. The ocean water level and the water depths are not on a common datum.	78
Figure 2-16	Pictures from the time-lapse camera at ST-2008 in May 2008 showing the variation in the floating sea ice overflow depth.	79
Figure 2-17	Pictures from the time-lapse camera at ST-2008 showing the variation in the floating sea ice overflow depth on 22-May-2008. The buoy is at the same location in both pictures.	79
Figure 2-18	Pictures from the time-lapse camera at ST-2009 in May 2009 showing the variation in the floating sea ice overflow depth.	79
Figure 2-19	MODIS images, with the land-water feature map overlay, showing the progression of the nearshore ice freeze-up in the Mackenzie Outer Delta in October 2008.	80
Figure 2-20	Top view, cross-sectional view and profile view of the winter ice condition in the Mackenzie Outer Delta.	81

Figure 2-21	a) January 2008, and b) April 2009 Envisat ASAR images of the Mackenzie Outer Delta at the Shallow Bay at Reindeer Channel Mouth showing the bottomfast ice location (darker on the images). c) Chronological growth of the bottomfast ice during the 2008-2009 winter season, delineated from Envisat ASAR satellite images (accuracy of 500 m).....	82
Figure 2-22	Maximum extent of the bottomfast ice in the Mackenzie Outer Delta (orange) from 2006 to 2009 delineated from Envisat ASAR satellite images (accuracy of 500 m).....	83
Figure 2-23	Delineation of the floating channel ice location (blue) in 2008 and 2009 in the Mackenzie Outer Delta, defined from near-infrared (Band 4) Landsat images (accuracy of 60 m).	84
Figure 2-24	Top view, cross-sectional view and profile view of the initiation of the bottomfast ice overflow in the Mackenzie Outer Delta. The red arrows indicate the flow direction and the green arrow indicate the vertical ice movement direction.	85
Figure 2-25	a) Border ice and land overflow on the delta's channel's border. b) Land overflow in the outer delta. c) Flooding of the bottomfast ice surface (BFI) at the interface with the floating channel ice (FCI). d) Shallow overflow depth on the bottomfast ice surface. e) Frozen overflow on the bottomfast ice surface. f) Overflow spreading on the bottomfast ice surface.	86
Figure 2-26	MODIS images, with the land-water feature map overlay, illustrating the initial overflow on bottomfast ice in the Mackenzie Outer Delta in May 2006. The arrows indicate the first bottomfast ice overflow locations at different regions and on different dates.....	87
Figure 2-27	Top view, cross-sectional view and profile view of the initiation of the floating sea ice overflow in the Mackenzie Outer Delta. The red arrows indicate the flow direction and the green arrow indicate the vertical ice movement direction.	88
Figure 2-28	a, b & c) Overflow on the floating sea ice surface (FSI). d) Overflow draining through a strudel at the boundary between the bottomfast ice (BFI) and the floating sea ice. e) Ice ridge acting as an overflow barriers.....	89

Figure 2-29	MODIS images of the overflow expansion northwest of Olivier Islands in the Mackenzie Outer Delta on 22-May-2008. The distance between the lines averages 680 m.....	90
Figure 2-30	Top view, cross-sectional view and profile view of the maximum floating sea ice overflow in the Mackenzie Outer Delta. The red arrows indicate the flow direction and the green arrows indicate the vertical ice movement direction.	90
Figure 2-31	MODIS images, with the land-water feature map overlay, showing the flooding and the drainage of the floating sea ice overflow in the Mackenzie Outer Delta in May 2006. The arrows indicate the maximum overflow extent at different outer delta regions and on different dates.....	91
Figure 2-32	a) MODIS image of freeze-up, with the land-water feature map overlay, on 18-October-2008. b) Maximum floating sea ice overflow distance on 18-May-2007. c) Maximum floating sea ice overflow distance on 23-May-2008. The blue line refers to the freeze-up nearshore ice boundary of 18-October-2008 (accuracy of 500 m).....	92
Figure 2-33	Top view, cross-sectional view and profile view of the drained floating sea ice overflow in the Mackenzie Outer Delta. The red arrows indicate the flow direction.....	92
Figure 2-34	MODIS images, with the land-water feature map overlay, showing the drained floating sea ice overflow in the Mackenzie Outer Delta in May 2008.....	93
Figure 2-35	Overlay of the overflow area after the floating sea ice surface drained (green), defined from visible band MODIS images, over the bottomfast ice (orange) areas, defined from the Envisat ASAR images, in the Mackenzie Outer Delta from 2006 to 2009 (accuracy of 500 km).	94

Figure 2-36	a) Interface of the bottomfast ice (BFI) and of the non-flooded floating sea ice (FSI). b) Strudel drains in the shape of holes and cracks through the floating sea ice cover. c) Landsat 7 satellite image (Band 4) showing cracks in the floating sea ice cover north of Olivier Islands. d) Interface between the bottomfast ice and the floating sea ice filled with holes and cracks and having an accumulation of ice pieces. e) Ice blocks deposited on the floating sea ice surface where the overflow occurred. f) Sediment accumulation on the floating sea ice surface.	95
Figure 2-37	Top view, cross-sectional view and profile view of the peak spring freshet arrival in the Mackenzie Outer Delta.	96
Figure 2-38	a) Debris and ice pieces in the delta's channel during spring freshet. b, c & d) Flooded low-lying land in the Mackenzie Outer Delta.	96
Figure 2-39	MODIS images, with the land-water feature map overlay, showing the peak freshet arrival in the Mackenzie Outer Delta in May and June 2009. The arrows indicate the approximate location of the ice clearance front on different dates.	97
Figure 2-40	a) Landsat 5 thermal images (Band 6) of the Mackenzie Outer Delta in May 2008 showing the cold overflow. b) Landsat 5 thermal images (Band 6) of the Mackenzie Outer Delta in June 2008 showing the warm peak freshet flow. A lighter color indicates warmer water/ground temperatures. Insets: Landsat 5 images (Band 4) of the Olivier Islands and Garry Island regions on the same dates.	98
Figure 2-41	Bi-daily chronological overflow expansion in the Mackenzie Outer Delta from 2006 to 2009, defined from visible band MODIS images (accuracy of 500 m).	99
Figure 2-42	Bottomfast ice and floating ice overflow in the Mackenzie Outer Delta from 2006 to 2009, defined from visible band MODIS images (accuracy of 500 m). The green areas represent the final (drained) overflow boundaries (which correspond to the bottomfast ice location) and the red areas represent the floating sea ice cover that overflowed and drained.	100

Figure 2-43	Interannual variations in the bottomfast ice and floating sea ice overflow locations (accuracy of 500 m), and location of the floating channel ice (blue) (accuracy of 250 m) in the Mackenzie Outer Delta from 2006 to 2009, defined from visible band MODIS images.....	101
Figure 2-44	Water Level in the Mackenzie River at Arctic Red River (MARR – Station ID 10LC014) during breakup in 2008. The points indicate the dates at which the various water level thresholds were reached in 2008.....	102
Figure 2-45	Sediment-laden overflow water appearing darker on the Landsat 5 satellite images (Band 4) a) at the Kuluarpak Channel mouth and around Rae Island in June 2009, and b) at the Reindeer Channel mouth in Shallow Bay in May 2008. The red arrows indicate the flow direction.....	103
Figure 2-46	Strudel hole S2008-05 at ST-2008 on 22-May-2008.	104
Figure 2-47	Active strudel drains a) S2008-01 and b) S2008-03 at ST-2008 on 22-May-2008. The strudel drains are approximately 20 cm in diameter. Insets: Surface flow direction around the strudel drains.	104
Figure 2-48	Topographic map of strudel drain S2009-01 at SL-2009 on 26-May-2009. The dots represent the locations where data points were recorded by the total station which was located directly above the ice surface at (Easting, Northing, Elevation) = (100, 100, 100). The water was flowing from the south (bottom) towards the hole. Inset: 3D topographic map of the strudel drain.....	105
Figure 2-49	a) Sketch of the upwelling process at the interface of the floating channel ice (FCI) and the bottomfast ice (BFI). b) Sketch of the upwelling and strudel process at the interface of floating ice (FI) and of bottomfast ice (BFI). The red arrows indicate the flow direction.	105
Figure 2-50	Strip of floating ice between the strudel zone and the upwelling zone at the Middle Channel mouth region. The red arrows indicate the flow direction.	106

Figure 2-51	a & b) Upwellings with spurt diameters of approximately 3 m. c & d) Group of upwellings along cracks at the boundary between floating ice and bottomfast ice. e) Upwellings along the bottomfast ice border. f) Upwelling discharging more concentrated / darker sediments on the bottomfast ice surface.	106
Figure 2-52	Location of upwellings in the Mackenzie Outer Delta from 2007 to 2009 collected from field observations and satellite images (accuracy of 500 m). The background map identifies the regions that were bottomfast ice overflow (green) and floating sea ice overflow (red) at least two years in the 2006 to 2009 period, and the floating channel ice location (blue), presented in Figure 2-43.	107
Figure 2-53	Location of strudel / strudel drains in the Mackenzie Outer Delta from 2007 to 2009 collected from field observations and satellite images (accuracy of 500 m). The background map identifies the regions that were bottomfast ice overflow (green) and floating sea ice overflow (red) at least two years in the 2006 to 2009 period, and the floating channel ice location (blue), presented in Figure 2-43.	108
Figure 2-54	a) Drained floating sea ice strudel drains at the boundary separating the bottomfast ice from the floating sea ice. b) Strudel drain through the floating ice surface submerged by a layer of water. c) Erosion of the ice surface around an inactive strudel drain on 27-May-2008. d) Boundary strudel drains at the interface of the bottomfast ice with the floating sea ice.	109
Figure 2-55	Strudel drains a) no ID and b) S2008-10 at ST-2008 on 27-May-2008 showing cracks being part of the strudel drains.	110
Figure 2-56	a & b) Strudel drainage features observed as a water vortex swirling around a depression at its center. c) Shallow and wide strudel drain vortex on the floating sea ice. d) Narrow and deep strudel drain vortex. e) Strudel drains in small overflow depths observed as water rushing into a hole. f) Strudel drain covered by ice pieces and debris on 25-May-2009 such that no sign of drainage was observed.	111

Figure 2-57	The vortex above strudel drain S2009-04 at SB-2009 on 25-May-2009 is rotating clockwise and is not showing any significant depression. The pictures were taken at 3 seconds interval.	112
Figure 2-58	Inactive strudel drains a) S2008-05 and b) S2008-08 at ST-2008 on 27-May-2008. The areas contoured in yellow indicate the strudel hole location and the remaining flooded area consists of ice covered by a thin layer of water.	112
Figure 2-59	a) Active and b) Inactive (drained ice cover) strudel drain S2008-02 at ST-2008 in May 2008 showing erosion and thermal decay of the strudel drain.	112
Figure 2-60	Pictures from the underwater video camera inserted in strudel drain S2009-01 at SL-2009 on 26-May-2009. The camera is pointing towards the lake shore where ice is bottomfast with the bed. Steep edges with a scoured depth of approximately 30 cm are observed. The scour hole is free of vegetation and has lots of fine sediments.	113
Figure 2-61	Pictures from the underwater video camera inserted in strudel drain S2009-01 at SL-2009 on 26-May-2009. The camera is pointing towards the center of the lake where ice is not bottomfast with the bed. The original bed surface is covered by vegetation while the scour hole is free of vegetation and is covered by fine sediments. The overflow water was directed under the ice cover towards a deeper section of the lake.	113
Figure 3-1	Flow regions of a jet impinging on a perpendicular wall (adapted from Beltaos & Rajaratnam, 1977).	143
Figure 3-2	Free jet region of a circular turbulent jet (adapted from Rajaratnam, 1987).	143
Figure 3-3	Impingement region of a jet hitting a perpendicular wall at a small impingement height (adapted from Beltaos & Rajaratnam, 1977).	144
Figure 3-4	a) Top view and b) side view of a typical bathtub vortex experimental setup (adapted from Lubin and Springer, 1967).	144
Figure 3-5	Sketch of the physical experiment setup with the corresponding pipe diameters (Φ). The arrows indicate the flow direction. P is the pump, V is the valve, F1 is the flow meter measuring Q_1 , F2 is the flow meter measuring Q_2	145

Figure 3-6	a) <i>Storage Tank #2</i> (left), <i>Storage Tank #1</i> (right) and pump (center). b) Strudel hole diameter inserts of diameter 2.0 cm, 7.8 cm and 5.1 cm (from left to right).....	145
Figure 3-7	Picture of the <i>Upstream Tank</i> and of the <i>Strudel Tank</i> . The flow direction is from right to left.	146
Figure 3-8	Three-Dimensional view of the <i>Upstream Tank</i> (right) and of the <i>Strudel Tank</i> model. Bottom-left Inset: ADV probe setup under the circular strudel hole. Top-right Inset: Circular strudel hole insert.	147
Figure 3-9	Top view and side view of the <i>Upstream Tank</i> (right) and of the <i>Strudel Tank</i>	148
Figure 3-10	Air entrainment below the ice cover.	149
Figure 3-11	Top view of the circular hole and definition of the length and velocity variables in the Cartesian and the Cylindrical's global coordinate systems.	149
Figure 3-12	Vectrino ADV probe alignment below the ice surface and conversion of local (ADV) coordinate system to global coordinate system.	150
Figure 3-13	a) ADV probe below the ice cover. b) System of traverse used to position the ADV below the ice cover.	150
Figure 3-14	Axial velocity data (1-second average) collected from the ADV for Run #195b at $(x, y, z) = (0, 4, 3.3)$ and calculation of average velocities and standard deviations for various duration.....	150
Figure 3-15	Side view of a) shallow air dip, b) deep air dip above the hole entrance, and c) deep air dip penetrating inside the hole. The overflow direction is from right to left and the vortices are rotating counter-clockwise.	151
Figure 3-16	Side view of the vortex dip for small overflow depths a) above the hole entrance, and b) penetrating inside the hole. The overflow direction is from right to left and the vortices are rotating clockwise.....	151

Figure 3-17	a) Side view of a vortex dip located on the downstream side of the hole. b) Top (angled) view of the curved vortex flow streamlines using dye. The overflow direction is from right to left and the vortices are rotating counter-clockwise.....	152
Figure 3-18	a) Top (angled) view, and b) side view of the strudel vortex streamlines into a circular hole using dye. The overflow direction is from right to left and the vortices are rotating counter-clockwise.	152
Figure 3-19	Side view of the vortex flow streamlines into a circular hole using dye. The overflow direction is from right to left and the vortices are rotating counter-clockwise.....	153
Figure 3-20	Sketch of the side view of the dye streaks flowing into the circular hole.	153
Figure 3-21	Sketch of the top view of the dye streaks inserted at the upstream water surface flowing towards the counter-clockwise free-surface vortex flow. The flow direction is from right to left.....	154
Figure 3-22	Side view images of the free-surface vortex flow under the ice cover impinging on a perpendicular boundary. The time T is referenced to the instant the dye started to flow out of the hole. The under-ice flow is from right to left.	154
Figure 3-23	Dimensionless axial (U_z/U_0) and horizontal (U_{xy}/U_0) velocities in the x-y plane for run number 195b at $z/d = 0.42$. The arrows indicate the location of the ADV measurements. Each arrow shows the magnitude (colour coded) and direction of the dimensionless horizontal velocity vector, U_{xy}/U_0 . The magnitude (colour coded) of the dimensionless axial velocities were linearly interpolated / extrapolated for the entire cross-section. The hole boundary is marked by a white circle and the vortex core's location is marked by a green circle. The overflow and under-ice flow direction is towards the positive y/R direction.....	155

Figure 3-24	Dimensionless axial (U_z/U_0) and horizontal (U_{xy}/U_0) velocities in the x-y plane for run number 195b at $z/d = 0.94$. The arrows indicate the location of the ADV measurements. Each arrow shows the magnitude (colour coded) and direction of the dimensionless horizontal velocity vector, U_{xy}/U_0 . The magnitude (colour coded) of the dimensionless axial velocities were linearly interpolated / extrapolated for the entire cross-section. The hole boundary is marked by a white circle and the vortex core's location is marked by a green circle. The overflow and under-ice flow direction is towards the positive y/R direction.....	156
Figure 3-25	Dimensionless axial (U_z/U_0) and horizontal (U_{xy}/U_0) velocities in the x-y plane for run number 260 at $z/d = 0.94$. The arrows indicate the location of the ADV measurements. Each arrow shows the magnitude (colour coded) and direction of the dimensionless horizontal velocity vector, U_{xy}/U_0 . The magnitude (colour coded) of the dimensionless axial velocities were linearly interpolated / extrapolated for the entire cross-section. The hole boundary is marked by a white circle and the vortex core's location is marked by a green circle. The overflow and under-ice flow direction is towards the positive y/R direction.....	157
Figure 3-26	Dimensionless axial (U_z/U_0) and horizontal (U_{xy}/U_0) velocities in the x-y plane for run number 266 at $z/d = 0.94$. The arrows indicate the location of the ADV measurements. Each arrow shows the magnitude (colour coded) and direction of the dimensionless horizontal velocity vector, U_{xy}/U_0 . The magnitude (colour coded) of the dimensionless axial velocities were linearly interpolated / extrapolated for the entire cross-section. The hole boundary is marked by a white circle and the vortex core's location is marked by a green circle. The overflow and under-ice flow direction is towards the positive y/R direction.....	158
Figure 3-27	Dimensionless axial (U_z/U_0) velocities along the x-axis for $z/d = 0.42$	159
Figure 3-28	Dimensionless axial (U_z/U_0) velocities along the y-axis for $z/d = 0.42$	159
Figure 3-29	Dimensionless axial (U_z/U_0) velocities along the x-axis for $z/d = 0.94$	160
Figure 3-30	Dimensionless axial (U_z/U_0) velocities along the y-axis for $z/d = 0.94$	160

Figure 3-31	Dimensionless axial (U_z/U_o) velocities along the x-axis for $z/d = 1.58$	161
Figure 3-32	Dimensionless axial (U_z/U_o) velocities along the y-axis for $z/d = 1.58$	161
Figure 3-33	Dimensionless axial (U_z/U_o) and horizontal (U_{xy}/U_o) velocities in the x-y plane for run number 195b at $z/d = 1.58$. The arrows indicate the location of the ADV measurements. Each arrow shows the magnitude (colour coded) and direction of the dimensionless horizontal velocity vector, U_{xy}/U_o . The magnitude (colour coded) of the dimensionless axial velocities were linearly interpolated / extrapolated for half of the cross-section. The hole boundary is marked by a white circle. The overflow and under-ice flow direction is towards the positive y/R direction.....	162
Figure 3-34	Dimensionless axial (U_z/U_o) velocities along the x-axis for $z/d = 2.18$	163
Figure 3-35	Dimensionless axial (U_z/U_o) velocities along the y-axis for $z/d = 2.18$	163
Figure 3-36	Dimensionless lateral (U_x/U_o) / radial velocities along the x-axis for $z/d = 2.18$	164
Figure 3-37	Dimensionless longitudinal (U_y/U_o) / radial velocities along the y-axis for $z/d = 2.18$	164
Figure 3-38	Dimensionless longitudinal (U_y/U_o) / tangential velocities along the x-axis for $z/d = 2.18$	165
Figure 3-39	Dimensionless lateral (U_x/U_o) / tangential velocities along the y-axis for $z/d = 2.18$	165
Figure 3-40	Dimensionless axial (U_z/U_o) and horizontal (U_{xy}/U_o) velocities in the x-y plane for run number 195b at $z/d = 2.18$. The arrows indicate the location of the ADV measurements. Each arrow shows the magnitude (colour coded) and direction of the dimensionless horizontal velocity vector, U_{xy}/U_o . The magnitude (colour coded) of the dimensionless axial velocities were linearly interpolated / extrapolated for half of the cross-section. The hole boundary is marked by a white circle. The overflow and under-ice flow direction is towards the positive y/R direction.....	166

Figure 3-41	Graph of the Discharge Coefficient (Cd) vs. the Reynolds Number (Re). t/d is the ice thickness / hole diameter ratio.....	167
Figure 3-42	Graph of the discharge coefficient (Cd) versus the overflow depth / hole diameter (ho/d) ratio. Hd/d is the hydraulic head difference / hole diameter ratio.	167
Figure 3-43	Sketch of the profile view of the flow streamline inside the circular hole for large overflow depths, neglecting rotation of the flow.	168
Figure 3-44	Sketch of the profile view of the flow streamline inside the circular hole for small overflow depths, neglecting rotation of the flow.....	168
Figure 4-1	Half-sectional view of the eroded bed profile created by a vertical impinging jet (adapted from Rajaratnam, 1982).	185
Figure 4-2	Diagrams showing Johnson's (1985) theory on the hydraulic head difference calculation a) before overflow of the sea ice surface, and b) after overflow of the sea ice surface. The arrows indicate the flow direction.	185
Figure 4-3	Diagrams showing the maximum theoretical hydraulic head difference due to rapid overflow of the ice cover a) before overflow of the sea ice surface, and b) after overflow of the sea ice surface. The arrows indicate the flow direction.....	186
Figure 4-4	Estimation of the maximum strudel scour depth (εm) in the Mackenzie Delta for various impingement distance (H), hole diameter (d) and axial velocities (Uo) for large impingement heights ($H/d > 8.3$).	186
Figure B-1	Graph of the discharge coefficient (Cd) versus the overflow depth / hole diameter (ho/d) ratio using the collected data where the downstream water level was lower than the ice cover surface and the hydraulic head difference (Hd) was equal to the overflow depth (ho).....	1

List of Abbreviations

<u>Abbreviation</u>	<u>Definition</u>
ADV	Acoustic Doppler Velocimeter
ASAR	Advanced Synthetic Aperture Radar
AVHRR	Advanced Very High Resolution Radiometer
BFI	Bottomfast Ice
FCI	Floating Channel Ice
EOLi	Earth Observation Link
ESA	European Space Agency
FI	Floating Ice
GINA	Geographic Information Network of Alaska
Glovis	Global Visualisation Viewer
GPS	Global Positioning System
IPY	International Polar Year
LST	Local Standard Time
MARR	Mackenzie River at Arctic Red River
MRBB	Mackenzie River Basin Board
MDT	Mountain Daylight Time
MODIS	Moderate Resolution Imaging Spectroradiometer
MSC	Meteorological Service of Canada
MST	Mountain Standard Time
NASA	National Aeronautics and Space Administration
NREF	Natural Resource Engineering Facility
NSERC	Natural Sciences and Engineering Research Council of Canada
NOAA	National Oceanic and Atmospheric Administration
NPSS	Non-purely stretching-sustained
NRCan	Natural Resources Canada
PSS	Purely Stretching Sustained
PVC	Polyvinyl Chloride
SAR	Synthetic Aperture Radar
SNR	Signal-to-Noise Ratio
FSI	Floating Sea Ice
USGS	U.S. Geological Survey
UTC	Coordinated Universal Time
WSC	Water Survey of Canada

List of Symbols

<u>Symbol</u>	<u>Definition</u>	<u>Units</u>
A_1	Area of the first delineation	pixels (m ²)
A_2	Area of the second delineation	pixels (m ²)
b	Radial distance of half-velocity	m
b	Radial distance of half-scoured depth	m
C_5	Lower / upper limit constant	non-dimensional
C_d	Discharge coefficient	non-dimensional
C_u	Cohesion strength parameter	N/m ²
C_*	Variable defining the cohesive soil properties	non-dimensional
d	Hole diameter	m
d	Jet nozzle diameter	m
d_a	Arithmetic mean size of cohesive sediment	m
D_{50}	Median size of the sand particles	m
E_c	Erosion parameter	non-dimensional
F	Froude number	non-dimensional
f_b	Freeboard	m
F_o	Parameter defining the scour potential	non-dimensional
g	Gravity constant	m/s ²
g'	Effective gravity	m/s ²
h_d	Downstream water depth	m
h_o	Overflow depth	m
h_o	Depth of water above the point sink	m
h_u	Upstream water depth	m
h_w	Water depth	m
H	Impingement distance	m
H	Under-ice depth	m
H/d	Impingement height	non-dimensional
H_d	Hydraulic head difference	m
k_s	Equivalent sand roughness	m
m	Total flux from point sink	m ³ /s
P_1	Perimeter of the first delineation	m
P_2	Perimeter of the second delineation	m

<u>Symbol</u>	<u>Definition</u>	<u>Units</u>
P_c	Percentage of clay content	non-dimensional
Q_o	Flow rate into the circular strudel hole / strudel tank	L/s
Q_1	Flow rate redirected into the storage tank	L/s
Q_2	Flow rate from the pump	L/s
r	Radial direction in the cylindrical coordinate system	non-dimensional
r	Radial distance from the circular hole / jet centerline	m
r_o	Radial extent of scour hole at the original bed level	m
r_1	Radial distance of the boundary separating the potential core and the shear layer	m
r_1	Radial extent of scour hole at the top of ridge	m
r_2	Radial distance of the outer limit of the jet	m
R	Circular hole radius	m
R	Correlation Coefficient	non-dimensional
Re	Reynolds number	non-dimensional
t	Ice thickness	m
U_c	Centerline axial velocity	m/s
U_m	Maximum axial velocity	m/s
U_o	Average axial velocity at the jet nozzle / circular hole	m/s
U_x	Velocity in the x-direction of the Cartesian coordinate system	m/s
U_{xy}	Horizontal velocity vector along the xy-plane of the Cartesian coordinate system	m/s
U_y	Velocity in the y-direction of the Cartesian coordinate system	m/s
U_z	Velocity in the z-direction of the Cartesian coordinate system	m/s
U_z	Axial velocity	m/s
v_1	Radial velocity at the boundary separating the potential core and the shear layer	m/s
V_r	Radial velocity in the cylindrical coordinate system	m/s
V_z	Axial velocity in the cylindrical coordinate system	m/s
V_θ	Tangential velocity in the cylindrical coordinate system	m/s
W	Antecedent moisture content of the cohesive sediments	non-dimensional
W_*	Moisture content at saturation of the cohesive sediments	non-dimensional

<u>Symbol</u>	<u>Definition</u>	<u>Units</u>
x	x-axis in the Cartesian coordinate system	non-dimensional
X	Parameter describing the hydraulic properties of the jet	N/m^2
X_C	Parameter describing the hydraulic properties of the jet at which mass erosion first occurs	N/m^2
y	y-axis in the Cartesian coordinate system	non-dimensional
z	z-axis in the Cartesian coordinate system	non-dimensional
z	Axial distance from the jet nozzle / circular hole	m
z'	Axial distance from the impinged boundary	m
γ_d	Specific density of dry sediments	N/m^3
γ_{fw}	Specific density of fresh water	N/m^3
γ_i	Specific density of sea ice	N/m^3
γ_s	Specific density of sediments	N/m^3
γ_{sw}	Specific density of sea water	N/m^3
γ_w	Specific density of water	N/m^3
Γ	Circulation	m^2/s
$\Delta\varepsilon$	Height of ridge	m
$\Delta\rho$	Difference between the densities of sand and of the eroding fluid	kg/m^3
$\Delta\rho$	Difference in density between two liquid layers	kg/m^3
ε	Static depth of erosion	m
ε_m	Maximum static depth of erosion	m
ε'	Dynamic depth of erosion	m
ε_m'	Maximum dynamic depth of erosion	m
θ	Tangential direction in the cylindrical coordinate system	non-dimensional
μ	Dynamic viscosity of water	$N\cdot s/m^2$
ρ	A reference density	kg/m^3
ρ	Mass density of the eroding fluid	kg/m^3
ρ_s	Mass density of sediments	kg/m^3
ρ_w	Mass density of water	kg/m^3
σ	Standard Deviation	non-dimensional
φ_c	Angle of internal friction of the cohesive sediments	deg
φ_s	Angle of repose / Internal friction of the sand	deg
φ_*	Variable defining the cohesive soil properties	non-dimensional
∞	Suffix denoting asymptotical state	non-dimensional

1.0 Introduction

The Mackenzie Delta, presented in Figure 1-1, is located in the Northwest Territories, Canada, at the downstream end of a 1,760,000 km² watershed, the Mackenzie Basin (Walker, 1998; Fassnacht & Conly, 2000), which covers the northern portion of British Columbia, Alberta, Saskatchewan as well as part of Yukon and the Northwest Territories (Mackenzie River Basin Board (MRBB), 2001). It is estimated that 91 % of the freshwater discharging into the Mackenzie Delta is provided by the north flowing Mackenzie River (Fassnacht & Conly, 2000) and flows downstream into the Beaufort Sea and the Arctic Ocean. Most of the Mackenzie Delta's nearshore region is shallow (less than 2 m) (Hill, Lewis, Desmarais, Kauppaymuthoo, & Rais, 2001) such that, in winter, most of the sea water freezes to the bed and becomes bottomfast ice.

In spring, the delta receives a very large spring freshet inflow while its ice cover and the Beaufort Sea ice cover are still intact. As the under-ice flow capacity of the Mackenzie Outer Delta is too small to accommodate this increasing flow, mostly due to the extensive presence of bottomfast ice, the water level of the sea rises. As a result, the under-ice water flow is forced upwards through holes and cracks in the ice cover, a process named upwelling and presented in Figure 1-2, such that the bottomfast ice surface gets flooded by river water, thus initiating the overflow process. The upwellings are usually located near the delta's channel mouths and are observed to discharge a very large quantity of fresh water over the ice surface. This water on ice overflow phenomenon, which occurs yearly between early May and early June in the Mackenzie Delta, is also observed at the Alaskan Beaufort Sea in the United States between Smith Bay and Camden Bay (DF Dickins Associates, Coastal Frontiers Corporation, Aero-Metric Inc., & University of Alaska Fairbanks, 2009) including the mouths of the Colville River, the Kuparuk River and the Sagavanirktok River (Reimnitz, 1974), and at the Lena Delta in Russia (Reimnitz, 2002).

As the overflow onto the bottomfast ice surface progresses seaward, it reaches an ice covered region of the sea that is not frozen to the bed and also overflows on this ice surface. The overflow then infiltrates and drains through holes and cracks in the floating ice cover to flow under the ice cover and seawards towards the ocean. The flow of

water through these types of drains is called a strudel, which means “whirlpool” in German (Reimnitz & Bruder, 1972). Strudel appear as a vortex or a rushing flow of water into a hole as shown in Figure 1-3. The strong vertical flows formed in these strudel drains impinge on the sea bed because of its shallow depths creating scour holes called strudel scours. Within a month following the initiation of the overflow, the warm peak freshet reaches the outer delta and melts the entire nearshore ice cover for the summer.

Research and study of the upwelling and overflow phenomena are important for the following reasons. First, the overflow floods a large surface of ice in the Mackenzie Outer Delta in a very short period of time. As a result, ice roads and other human activities can be affected by the rapid occurrence of this overflow. For these reasons, it is important to predict the timing of the overflow. The forecasting of these events is also very useful for the planning of field investigations. Additionally, the presence of bottomfast ice at the mouth of the delta’s channels in winter creates a barrier to the river as it flows into the sea and this affects the downstream boundary conditions of the Mackenzie Delta’s river hydraulics. The overflow process can also play an important role in sediment transport towards the Beaufort Sea. Finally, the overflow event and flooding of the low-lying land surface could impact the ecosystem of the Mackenzie Delta.

Strudel are of interest mainly because of their ability to scour the sea bed to depths exceeding 1 m below the original sea bed surface (DF Dickins Associates *et al.*, 2009). Strudel scour holes up to 6.7 m deep have been recorded in the Alaskan Beaufort Sea (McClelland Engineering, 1982, reported in Coastal Frontiers, 1997, as cited in DF Dickins Associates *et al.*, 2009). Strudel scouring of the sea bed is a major concern to the energy industry because of the hazard that strudel scouring presents to existing and future pipelines buried beneath the sea bed. (Abdalla, Jukes, Eltaher, & Duron, 2008). In fact, existing pipelines have been in use in northern Alaska since 2000 (Leidersdorf *et al.*, 2006) and transport more than one million barrels of oil per day from an offshore rig (Bergman, 2010). Several strudel drains have been observed above Alaskan Beaufort Sea’s oil and gas pipelines in the Alaskan Beaufort Sea (Leidersdorf *et al.*, 2006). In Canada, a similar project, called the Mackenzie Valley pipeline project, was first proposed in the 1970s. Its objective was to build a pipeline through the Mackenzie

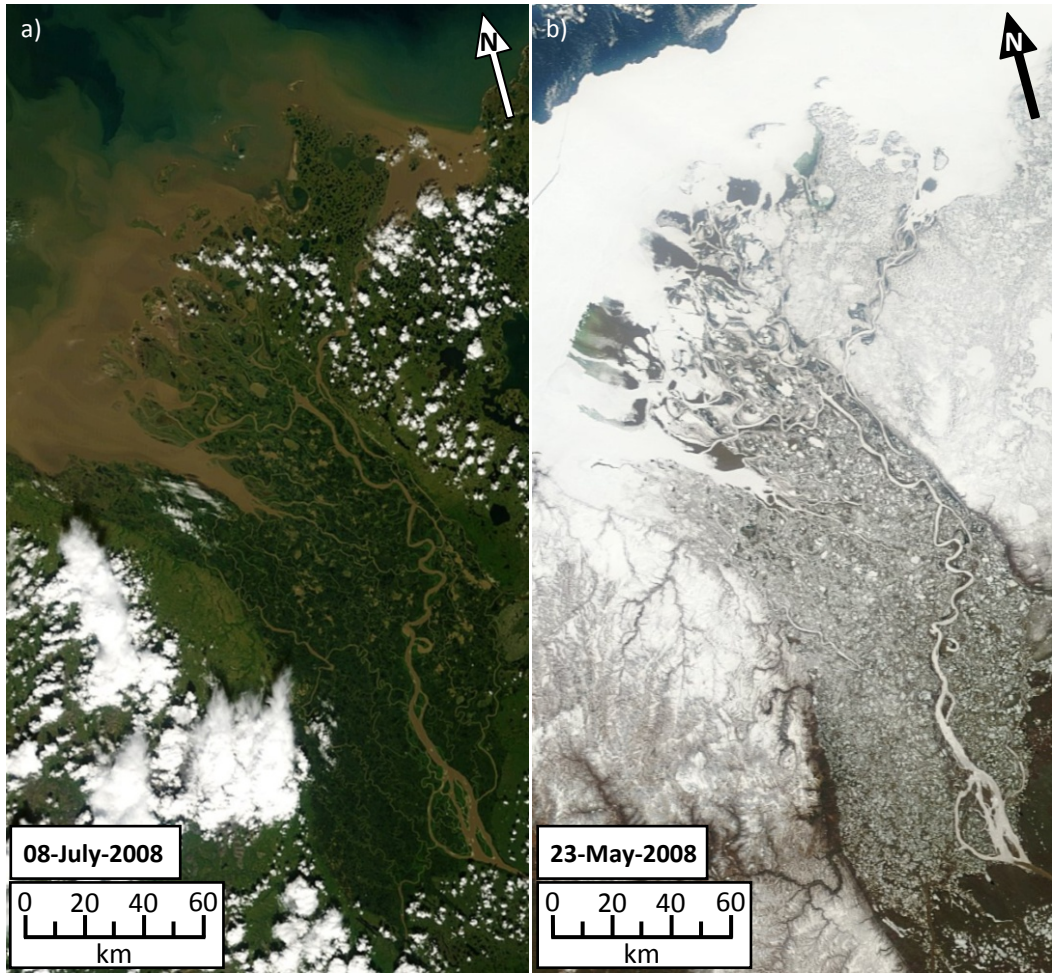
Valley and in the Beaufort Sea to exploit the vast gas and oil wealth under the sea bed in this region. The National Energy Board estimates that there are reserves of approximately 200 trillion cubic feet of natural gas below the Beaufort Sea bed surface. This project was rejected in the 1970s due to environmental and native land issues (Bergman, 2010). However, interest in this project has recently resurfaced due to the increasing demand for gas but the Conference Board of Canada predicted that the Mackenzie Valley pipeline will likely not go ahead until at least 2017 (Mackenzie Pipeline's Numbers Questioned, 2010). Therefore, a study of strudel drains and of strudel scour potential in the Mackenzie Delta is important to determine the required burial depth of proposed pipelines and could also influence pipeline routing choices.

There have been a few published studies of the overflow and strudel phenomena. However, most of these studies examined the northern shore of Alaska where overflow, strudel drains and strudel scours have been observed and quantified since the 1970s such that a strudel scour database with more than one thousand entries exists (DF Dickins Associates *et al.*, 2009). Unfortunately, only a very small amount of data has been collected for the overflow, strudel drains and strudel scours of the Mackenzie Delta. In the last few years, the Geological Survey of Canada department of NRCan started studying bottomfast ice, overflow and strudel in the outer delta and a few strudel drains and scours were observed and measured. However, the hydraulic processes leading to the upwelling, overflow and strudel events in the Mackenzie Delta were not studied in detail and are consequently not yet fully understood.

The objectives of this thesis are as follows. The first objective was to collect data regarding the upwelling, overflow, strudel drains and strudel scours in the Mackenzie Outer Delta from field investigations in spring 2008 and 2009. The plan was to analyze these data, and already published material, and to prepare detailed descriptions of the overflow processes in the Mackenzie Delta, including explanations of the upwelling and strudel events. A second objective was to provide a forecasting tool which would predict the arrival of the overflow in the outer delta. A third objective was to conduct a hydraulic model study of a strudel flow in the laboratory. This would allow relationships between the various parameters controlling the flow rate through the strudel drain to be established. From this model, it was also an objective to study the velocities below

the strudel drain to determine the influence of the free-surface vortex on the jet flow. The final objective was to identify and define the important parameters which govern the maximum strudel scour depth in the Mackenzie Outer Delta and to estimate the potential maximum strudel scour depth from published impinging jet experiments.

This thesis is divided into three main chapters and is followed by conclusions and recommendations. Chapter 2 describes the ice overflow, upwelling, strudel drains and strudel scours of the Mackenzie Outer Delta from field measurements and satellite observations taken between 2002 and 2009. Chapter 3 describes the physical scaled model of a circular strudel drain in a controlled laboratory environment. Finally, Chapter 4 presents an attempt at estimating the maximum strudel scour depth to occur in the Mackenzie Outer Delta.



University of Alaska – GINA www.gina.alaska.edu

Figure 1-1 MODIS satellite images of the Mackenzie Delta in the Northwest Territories, Canada in a) July 2008, and b) May 2008.



Figure 1-2 Upwellings at the interface of the floating ice and of the bottomfast ice cover.



Figure 1-3 Strudel at the interface of the bottomfast ice and of the floating ice cover.

2.0 Ice Overflow, Upwellings, Strudel Drains and Strudel Scours in the Mackenzie Outer Delta

2.1 Overview

The main goal of this chapter is to increase our understanding of ice overflow, upwelling and strudel events in the Mackenzie Outer Delta. A specific objective was to provide an explanation of overflow initiation and progression in the Mackenzie Outer Delta including a chronology of the ice surface overflow stages and a summary of the timing and inter-annual variability of the overflow extent. A second objective is to study the inter-annual variability of the overflow initiation such that its arrival in the outer delta could be accurately predicted a few days in advance. A third objective is to describe the upwelling, strudel drains and strudel scour phenomena as they are an integral part of the overflow process.

It should be noted that the dates and times presented throughout this chapter refer to the Coordinated Universal Time (UTC) unless otherwise specified. During breakup, the Mackenzie Delta follows the Mountain Daylight Time (MDT) which is 6 hours earlier than UTC.

2.2 Literature Review

2.2.1 Ice Overflow Descriptions and Observations

Nearly 25% of the major river-drainage systems on the globe, including the Mackenzie Delta watershed, discharge their water supply northward into the Arctic Ocean (Milliman & Meade, 1983, as cited in Reimnitz, 2002). In spring, the river ice and snow from the southern regions of the rivers' watersheds melts and flows towards the ocean. This increase in discharge from northward-flowing rivers occurs in advance of break-up of the nearshore Arctic ice cover (Reimnitz, Rodeick & Wolf, 1974; Arctec Newfoundland Limited, 1987; Dey, 1980). This ice cover typically freezes to a thickness approaching 2 m such that the ice bonds to the bed if the water depth is small, thus forming bottomfast ice (Hill *et al.*, 2001), also called grounded ice (Hirose, Kapfer, Bennett, Cott, Manson, & Solomon, 2008). Early in the Alaskan Beaufort sea overflow, flood water passes over the zone of bottomfast ice located near the shore to flood the surface of the floating ice further offshore (Leidersdorf, Hearon, Vaudrey, & Swank, 2006; Reimnitz & Kempema,

1983). This overflow typically occurs in late May or early June and lasts for 7 to 10 days following peak water depths on the ice before completely draining through holes and cracks (DF Dickins Associates *et al.*, 2009; Reimnitz & Kempema, 1983). Once the water drains through the holes, the ice is lifted vertically by the resulting rise in water levels (Kane *et al.*, 1975, as cited in Dey, 1980).

Yearly overflow of freshwater on top of vast expanses of shorefast ice, including bottomfast ice and some floating ice, has been observed and studied for three north flowing river regions of the Arctic: along the Alaskan Beaufort Sea in the United States of America; the Mackenzie River Delta in Canada; and the Lena Delta in Russia. In the Alaskan Beaufort Sea, the large amount of nearshore bottomfast ice creates a dam effect at the channel mouth and forces the water to flood the sea ice surface (Leidersdorf *et al.*, 2006). The depth of this overflow is said to vary between 0.5 and 1.5 m for distances up to 15 km seaward from the river mouth (Reimnitz *et al.*, 1974; Reimnitz & Bruder, 1972). In the Mackenzie Delta, shorefast ice flooding occurs indicating that the sub-ice channels are inadequate to accommodate all of the river flow during this seasonal discharge pulse (Dickins Associates Ltd., 1987, as cited in Reimnitz, 2002). It was speculated by Hill, Blasco, Harper and Fissel (1991) that submarine extensions of some delta distributaries may accommodate part of the flow or that delta-front ice may be lifted off the bottom to allow discharge beneath. In the outer delta, the overflow was observed to extend up to 30 km off the shore (Pilkington *et al.*, 1988, as cited in Forbes & Taylor, 1994). Finally, off the Lena Delta, the bottomfast ice is said to be submerged by about 1 m of river water (Reimnitz, 2002).

Reimnitz and Bruder (1972) clarify that most of the sediment carried by the river onto the ice is deposited close to the river mouths, or flushed through the ice at strudel drains. However, Reimnitz (2002) stated that there is no sediment deposit on the Alaskan Beaufort Sea or the Lena Delta floating ice surface after it has drained, even if it was flooded with sediment laden water. The Mackenzie River carries a large sediment load which significantly affects coastal processes. However, the Mackenzie Outer Delta's ice surface was also observed to be clean after the overflow drained (Arctec Newfoundland Limited, 1987).

The overflow does not usually happen during winter months because the discharge of all northern Alaska's rivers stops entirely in winter, while the Mackenzie River and many of the Siberian rivers continue to flow but at a greatly reduced rate (Reimnitz, 2002). However, storm surges have been observed to create some sea ice overflow on the ice surface during winter months in both the Alaskan Beaufort Sea (Reimnitz, 2002) and the Mackenzie Delta (Solomon, Fraser, & Whalen, 2007). These winter surges could result in the formation of strudel scour craters at small sea water depths (Reimnitz, 2002).

2.2.2 Strudel Drains Definitions and Observations

'Strudel' (singular and plural (Reimnitz *et al.*, 1974)) is defined as a violent and powerful vertical drainage of water through holes and cracks in an ice cover. Strudel flows produce local scour depressions in the underlying sediments, defined as strudel scours (Reimnitz & Bruder, 1972; Reimnitz *et al.*, 1974; Reimnitz & Kempema, 1983). Strudel form in seal breathing holes, cracks developed in the floating ice due to the water load (Reimnitz *et al.*, 1974), and older ice fractures such as tidal cracks, thermal cracks, and stress cracks (Leidersdorf *et al.*, 2006). Strudel holes can be of two types: Widely spaced circular holes or connected holes trending along a line (Reimnitz *et al.*, 1974). The earliest report of river overflow onto sea ice and its drainage through cracks and seal holes was published by Kindle (1924, as cited in Reimnitz *et al.*, 1974) for the Greenland and the Canadian Archipelago regions.

Three strudel zones were defined for the Alaskan overflow. Strudel form initially at and seaward of the bottomfast ice contour (Reimnitz *et al.*, 1974) defined as the "Primary Strudel Zone" where the scouring tends to be stronger and more frequent since it happens during the peak overflow discharge (Leidersdorf *et al.*, 2006). Later, as the bond between the bottomfast ice and the sea bottom deteriorates, the ice breaks free and floats such that strudel can develop inside the formerly bottomfast region (Reimnitz *et al.*, 1974; Reimnitz, 2002) defined as the "Secondary Strudel Zone" where the scouring tends to be milder as the peak discharge is said to have subsided by the time strudel developed here (Leidersdorf *et al.*, 2006). DF Dickins Associates *et al.* (2009) defined a "Tertiary Strudel Zone" which is located beyond the 6.1 m (20 ft) water depth region where the potential for strudel scour formation diminishes compared to shallower water depths.

Multiple strudel drain observations were performed in the Arctic as summarized below. Walker (1972, as cited in Reimnitz *et al.*, 1974) studied the 1971 overflow and its drainage in the Colville River Delta of Alaska. One week after sea ice flooding began, the author counted 140 strudel along the outer margin of the overflow. In the Alaskan Beaufort Sea, most strudel drains were semicircular with estimated diameters of 15 m; others were elongated with long axes measuring 30 m (Reimnitz & Bruder, 1972). The spacing of strudel drains was irregular such that the larger ones were from 100 m to several kilometres apart (Reimnitz & Bruder, 1972). In the Mackenzie Delta, early studies reported that no large strudel were observed on the ice surface, only drainage through small cracks (Arctec Newfoundland Limited, 1987; Forbes & Taylor, 1994). However, Solomon, Forbes, Fraser, Moorman, Stevens, Whalen and ASME (2009) observed several strudel drains at the south of Garry Island overflow region in 2007 with estimated diameters of 1 to 3 m and several instances of multiple drainage features were observed within metres of each other. Once the floating sea ice overflow drained, the authors observed that the strudel drains were less than 1 m in diameter with pools of dirty water obscuring them. They also observed that all of the strudel drainage features were found on the floating sea ice within a narrow (< 1 km) band from the edge of the bottomfast ice.

2.2.3 Strudel Scour Descriptions and Observations

Two types of strudel scours are defined in the literature. Most are described as roughly circular depressions with a ridge around part of the rim; these are referred to as *Circular Scours* and are formed from circular strudel drains (Reimnitz *et al.*, 1974). Others are described as scour depressions arranged along a line; these are referred to as *Linear Scours* which form from strudel drains at cracks. These scours are either spaced so closely that individual craters are in contact or spaced tens of meters apart but connected by a shallow, linear and narrow scour depression (Reimnitz *et al.*, 1974; DF Dickins Associates *et al.*, 2009).

Diving observations of two strudel scours were performed in the overflow area of the Kuparuk River in the Alaskan Beaufort Sea (Reimnitz *et al.*, 1974). The first strudel scour was partly bordered by a 40 cm wide ridge while the second strudel scour was bordered by a 60 cm ridge partly surrounding the hole. The ridges consisted of muddy sand and

gravel. The flanks were as steep as 35° for the first strudel scour while the depression of the second scour was described as having nearly vertical walls with small terraces and undercut locally. The observation of the second strudel scour revealed the composition of the bed which was comprised of layers of different materials such as loose sandy gravel at the base, and sandy silt to silty sand at the surface. No radial channel patterns were seen on the sea floor around a scour depression, as might be expected from sub-ice flow away from the strudel.

Diving observations of two strudel scours in the Alaskan Beaufort Sea were performed from 1978 to 1980 by Reimnitz and Kempema (1983) to calculate the infill rate of the scour holes and to define the scoured bed and infill composition. For the strudel scour at the mouth of the Sagavanirktok River, they observed ledges of rich fibrous organic matter 50 to 80 cm high, overhanging in places by as much as 50 cm. Two years later, that strudel scour was nearly filled with fine sand. The authors calculated an average of 60 cm depth of infill per month for the 4 months of open water and sediment transport conditions and state that all scours should be filled with sediments after 2 to 3 years. This rapid infilling rate implies that the chances of seeing a strudel scour without fill and, therefore, measuring its maximum depth are small.

Reimnitz and Bruder (1972) studied a strudel scour, observed as a conical depression in the sea bed, in the lagoon near Point McIntyre in Alaska. Along the flanks of this depression the sediment felt hard as if frozen. At its center, the bottom appeared soft, indicating either deposition of sediments or that the sediments did not freeze at this depth.

In general, the depth of strudel scours today is limited by the depth to the pre-Holocene materials (Reimnitz *et al.*, 1974). The stiff, over-consolidated, silty clay found in extensive areas of the inner shelf below Holocene marine sediments offers considerable resistance to scour by vertical jet flows. In one of the strudel scours studied by diving, this layer marked the bottom of the scour and was apparently slightly affected (Reimnitz *et al.*, 1974). Gravel offers significantly greater resistance to strudel scouring than the sands and silts typically encountered in the Beaufort Sea (Leidersdorf, Gadd, & Vaudrey, 1996). However, the influence of soil type is relatively minor, amounting on average to a

0.3 m depth difference between required cover depths between sand and clay (King, Phillips & Barrett, 2009).

2.2.4 Strudel Scour Measurements and Statistics

A list of publications presenting strudel scour measurements is summarised in Table 2-1. In this table, the *strudel scour depth* is defined as the vertical distance from the average elevation of the surrounding sea bottom to the deepest point in the scour depression and the *maximum horizontal dimension* is defined as the largest horizontal dimension of a circular scour or linear scour depression at the average elevation of the surrounding sea bottom. (DF Dickins Associates *et al.*, 2009).

In the Mackenzie Delta, early studies revealed no seabed strudel craters (Arctec Newfoundland Limited, 1987; Forbes & Taylor, 1994). However, a recent publication by Solomon *et al.* (2009) reports that strudel bed scours are, in fact, present in the outer delta where the maximum measured strudel scour depth was 0.8 m. The majority of strudel scour studies were performed in the Alaskan Beaufort Sea where strudel scours were found to occur as much as 30 km from the river mouths and in water depths between 0.6 and 8.1 m (Reimnitz *et al.*, 1974). A recent report published by DF Dickins Associates *et al.* (2009) provides the largest strudel scour database, regrouping data from approximately 1,100 scours from the Alaskan Beaufort Sea; this is summarized in Table 2-2. The study area went from Smith Bay to Camden Bay and covered a 13-year period between 1995 and 2007. In this study, a lot more circular drains ($\approx 1,100$) were observed compared to linear drains (≈ 15).

The density of strudel drains on the ice surface varies substantially from river to river in any given year, and from year to year at a given river. As an example, the strudel drain density ranged between 0.6 and 7.1 drains/km² between 1996 and 2007 at the Kuparuk River in Alaska (DF Dickins Associates *et al.*, 2009). The highest frequency of scours occurs within the Primary Strudel Zone with the greatest scour depths occurring in water depths of 2 to 4 m. No significant correlations between strudel scour depth and water depth, or between strudel scour maximum dimensions and water depth were identified for any of the river data sets investigated (DF Dickins Associates *et al.*, 2009).

Table 2-1 Summarized strudel scour characteristics from a variety of publications.

Publication	Number Of Scours	Water Depth (m)	Strudel Scour Depth (m)	Maximum Horizontal Dimension (m)
Reimnitz <i>et al.</i> , 1974	4	3 - 3.5	1.2 - 4.3	3 - 12
McClelland Engineering, 1982 (reported in Coastal Frontiers, 1997, as cited in DF Dickins Associates <i>et al.</i> , 2009)	613		Max. 6.7 (Four > 4.5)	
Reimnitz & Kempema, 1983	2	2.5	3.1 - 3.5	
Harding Lawson Associates, 1986 (reported in Coastal Frontiers, 1997, as cited in DF Dickins Associates <i>et al.</i> , 2009)	46	2.1 - 8.1	0.1 - 1.7	
Coastal Frontiers Corporation, 1996 (as cited in DF Dickins Associates <i>et al.</i> , 2009)	7	≈2.0	Max. 2.8	
Solomon <i>et al.</i> , 2009			Max. 0.8	Max. 20
DF Dickins Associates <i>et al.</i> , 2009	≈1,100	0.61 – 6.65	0.09 - 4.27	1.5 – 70.4

Table 2-2 Minimum / Average / Maximum circular strudel scour characteristics in the Alaskan Beaufort Sea from 1995 to 2007.

	Water Depth (m)	Strudel Scour Depth (m)	Maximum Horizontal Dimension (m)
Primary Strudel Zone	1.31/3.00/6.07	0.09/0.48/4.27	1.5/11.4/70.4
Secondary Strudel Zone	0.61/1.54/3.41	0.09/0.40/2.29	1.5/13.6/50.3
Tertiary Strudel Zone	5.98/6.31/6.65	0.37/0.38/0.40	4.0/5.2/6.4

2.2.5 Risk Assessment to Man-Made Structures

Both the sea ice overflow and the strudel scours can potentially damage structures or increase risks to human activities. The sea ice overflow can impact nearshore facilities by causing premature closure of ice roads. The sea ice in the Alaskan Beaufort Sea is usually strong enough to support the weight of heavy equipment into June (DF Dickins Associates *et al.*, 2009). Ice roads that extend above the ice surface have been observed to contain or deflect the overflow (Leidersdorf *et al.*, 2006). Strudel scours also impose a significant threat to manmade installations (Abdalla *et al.*, 2008) such that the oil industry considers them to be one of the most serious geologic hazards to pipelines in shallow-shelf areas (Reimnitz & Kempema, 1983). A strudel scour forming just above a

pipeline could expose it to an unacceptable span by removing the supporting soil. The velocity of the strudel flow can also impose vortex-induced vibrations (King *et al.*, 2009) which potentially lead to upheaval buckling of the pipe and to ice keel damages (DF Dickins Associates *et al.*, 2009). These two factors could rupture a pipe and cause a gas/oil spill to flow below the ice sheet towards the ocean (King *et al.*, 2009; DF Dickins Associates *et al.*, 2009).

The ice cover overlying two 9.6 km long gas and oil pipelines, installed under the Alaskan Beaufort Sea bed in 2000, is being studied to determine the effect of these pipelines on the ice deterioration. Both pipelines were installed in the seabed and backfilled with native materials with a minimum cover depth of 1.8 m. The radiant heat released by the pipelines was observed to propagate through the backfill and cause thermal decay of the overlying bottomfast ice of the Secondary Strudel Zone to occur faster than it would naturally. Such premature melting promoted early strudel drainage and preferential scour formation over the pipelines, a phenomenon called the “strudel magnet” effect. However, no such thermal decay was observed above the pipeline in the Primary Strudel Zone (Leidersdorf *et al.*, 2006).

From 2002 to 2007, three strudel scours formed directly above the pipeline in the primary strudel zone while six others were encountered in the secondary zone. Three of the encounters in the secondary zone formed within a lateral distance of 1,524 m (5,000 ft) from the pipe. Fortunately, these strudel encounters did not pose a significant threat to the integrity of the pipelines (DF Dickins Associates *et al.*, 2009). In the Primary Strudel Zone, the arithmetic probability for three years of strudel encounter directly above the pipeline in a period of six years is only 7% (DF Dickins Associates *et al.*, 2009). Therefore, it is likely that the presence of the warm pipelines are increasing the probability of strudel forming above them either directly (early deterioration of the ice cover), indirectly (increased biological activity in the warmer water), or a combination of both (Leidersdorf *et al.*, 2006). Leidersdorf *et al.* (2006) proposed mitigation measures to reduce the risk of strudel scour occurring over both present and future underground pipelines. These measures include routing of the pipelines into shallow water depths (< 1.5 m) as strudel scour processes are milder in this zone; reduction in the radiant heat from the pipeline to prevent early melting of the ice cover; increasing the depth of

burial to prevent undermining by strudel scour; erosion-resistant backfill such as gravel or cobble which offer significantly greater resistance to scouring, and; deflection of flood water using ice roads or ice berms to move the zone of strudel drainage a safe distance away from the pipelines.

2.2.6 Interannual Variability of the Overflow and Strudel Events

The complex inter-annual variability of the overflow extent and of strudel properties appears to be governed by complex interactions between a variety of environmental factors (DF Dickins Associates *et al.*, 2009). First, the discharge of the river, judged to be the most promising parameter for the purpose of establishing a positive correlation with river overflow on the sea ice (DF Dickins Associates *et al.*, 2009), is controlled by precipitation, by the depth of snowpack in the drainage basin and by the nature of breakup (Reimnitz & Bruder, 1972; Leidersdorf *et al.*, 2006; King *et al.*, 2009). High air temperatures promote strong and defined overflow events while intermittent periods of thawing and freezing produces low rates of river discharge which extend over a longer period of time (Leidersdorf *et al.*, 2006). Wind can control the speed and direction of the overflow spread (Leidersdorf *et al.*, 2006). Ice features such as drainage cracks, fissures and pressure ridges govern the location of strudel drains. The snow cover and man-made features such as ice roads can impede the spread of the overflow water and create ice insulation. Frazil ice and buoyancy of the sea ice surface can also play a part in the overflow process (Reimnitz & Bruder, 1972; Leidersdorf *et al.*, 2006; King *et al.*, 2009; DF Dickins Associates *et al.*, 2009). The sea water level controls the impingement distance to the bed and the bottomfast ice location (Reimnitz & Bruder, 1972). The sea level fluctuations, tides and surges can flood the ice surface in winter (Reimnitz & Bruder, 1972; Reimnitz, 2002; Solomon *et al.*, 2007). Properties of the strudel scours depend mostly on the bed sediments size and type and are also affected by the properties of the vertical flow in the strudel hole (Reimnitz *et al.*, 1974; Arctec Newfoundland Limited, 1987).

2.3 Study Area – The Mackenzie Delta

The Mackenzie Delta, presented in Figure 2-1, is located in the Northwest Territories in Canada. The delta is bordered to the north by the Beaufort Sea, to the west by the Richardson mountain range, to the east by the Caribou Hills, and to the south by the Mackenzie River, the Arctic Red River and the Peel River. The delta measures more than 210 km from Point Separation to the Beaufort Sea and has a mean width of 62 km (Hill *et al.*, 2001) such that it covers an area of 13,000 km² (Fassnacht & Conly, 2000). The Mackenzie Delta is the termination of the 1,760,000 km² Mackenzie River Basin (Walker, 1998) which is the biggest watershed in Canada, covering approximately 20 % of the country (Fassnacht & Conly, 2000), and the second largest in North America after the Mississippi-Missouri system (Walker, 1998). The southern part of the delta, known as the upper delta, is composed of several rivers, lakes and ponds that are connected together in a maze-like pattern (MacKay, 1963, as cited in Walker, 1998). The delta has three primary navigable channels: the Middle Channel which carries the main outflow towards the Beaufort Sea; the East Channel which runs along the east of the delta and flows beside Inuvik; and the Peel/West Channel which runs to the west of the delta beside Aklavik. The upper delta is mostly covered by black spruce trees which decrease in density towards the north (The Canadian Encyclopaedia, 2010). The northern part of the delta, known as the outer delta (Figure 2-2), is composed of low-lying tundra covered land, islands, lakes, channels, bays and the Beaufort Sea. The delta has a low gradient that continues offshore in the form of a subaqueous delta (Walker, 1998) such that the average 2 m depth bathymetric contour line is located at distances in excess of 15 km from the delta's shore line (Solomon *et al.*, 2009). The nearshore region of the Mackenzie Delta, with a water depth less than 6 m, extends about 50 km offshore (Whalen, Solomon, Forbes, Beaver, Nelson, & Travaglini, 2007).

The delta discharges its water northwards towards the Beaufort Sea through 57 active channel outputs (Lewis, 1988, as cited in Hill *et al.*, 2001) and eventually to the Arctic Ocean at a mean annual discharge of 8 980 m³/s (Fassnacht & Conly 2000). Its peak discharge can be as high as 34,000 m³/s during the spring freshet in May/June (Fassnacht & Conly 2000) while the average winter discharge is less than 5,000 m³/s (Dean, Stringer, Ahlnas, Searcy, & Weingartner, 1994). The Mackenzie Delta receives

more than 91 % of its flow from the Mackenzie River, 8% from the Peel River, and less than 1 % from the Arctic Red River. The majority of the Mackenzie River, 80 % during peak flow and 95 % in the winter, flows in the Middle Channel while 3 % of its summer flow and 1 % of its winter flow is carried into the East Channel. At the Middle Channel trifurcation, 40 % of the remaining Middle Channel water flows to the west into the Reindeer Channel, 25 % to the east into the East Channel, and the remaining 35 % flows north into the Middle Channel (Fassnacht & Conly, 2000).

2.4 Data Collection and Methodology

2.4.1 General

A variety of publicly available data from governmental agencies, such as meteorological data, water levels, and satellite images were obtained in order to explain and describe the overflow process that leads to the presence of upwellings and strudel in the Mackenzie Outer Delta. Bed sediment information was collected and analysed by NRCan as it is an important factor in determining the scour potential of strudel drains. For this study, water depth and strudel dimension data were collected with the collaboration of Natural Resources Canada (NRCan) during field investigations in 2008 and 2009.

Some overflow, floating channel ice and bottomfast ice delineations using satellite images are presented in the study. The delineations were done manually using a PC pointing device (i.e. mouse) to identify the edges. The delineations were performed by clicking on each pixel of the boundary using the PC pointing device. The delineation methodologies are described in detail in the sections below. Furthermore, the creation of a land-water feature map is also presented. All the satellite images, the delineations and the strudel and upwelling location map presented in this thesis were prepared using Adobe Photoshop CS3, a graphics editing program.

The accuracies of these delineations and maps were usually limited by the spatial resolution of the satellite images, but in some cases by the image resolution defined in the Adobe Photoshop software. Errors in the delineations were usually the result of incorrectly identifying features in the images. For example, overflow may be mistaken for floating ice or vice versa. The different features (e.g. overflow) in the images were identified visually based on their brightness, or grey scale value, and this method relies

on the judgement of the person performing the delineation. The accuracy of the overflow delineations was assessed as follows and the same methodology was used estimating the accuracies of the floating channel ice and the bottomfast ice delineations. Delineation of the overflow regions within the same satellite image were performed using two different approaches. In the first approach, the overflow regions were conservatively delineated, that is, minimizing the area identified. In the second approach, the overflow regions were delineated non-conservatively, that is, attempting to maximize the areas identified. The number of pixels between the two delineation boundaries were calculated and converted to distances and areas. The accuracy of the delineation in meters was then defined as,

$$\text{Delineation Accuracy} = \frac{A_2 - A_1}{(P_2 + P_1)/2} \quad [2-1]$$

where:

- A_2 = the area of the second delineation;
- A_1 = the area of the first delineation;
- P_2 = the perimeter of the second delineation; and
- P_1 = the perimeter of the first delineation.

Adobe Photoshop does not have the capability to directly calculate distances and areas. To calculate the area, the delineated pixels were selected using the “Magic Wand Tool” and the number of pixels was collected from the Histogram. This number was then multiplied by the pixel area to obtain an area. To calculate the perimeter, the delineated pixels were selected using the “Magic Wand Tool”, the “Stroke” feature was used to create a one pixel wide line along the inside edge of the delineated overflow, and the number of pixels was collected from the Histogram. This number was then multiplied by the pixel size to obtain a perimeter. In addition to the delineation accuracy, the error associated with the manual delineations was also assessed and was calculated as

$$\text{Percent Error} = \frac{A_2 - A_1}{(A_2 + A_1)/2} * 100 (\%) \quad [2-2]$$

2.4.2 Satellite Images

Satellite images are a useful tool for breakup observations in the Mackenzie Delta. An advantage of using satellite images over field observations is that they provide entire coverage of the study area. The ice overflow and floating channel ice in the Mackenzie Outer Delta can be observed in images from satellites that collect reflected radiation in the visible wavelength spectrum including MODIS, AVHRR/3, SPOT and Landsat. A major disadvantage of using visible spectrum images is that clouds can limit visibility of the overflow during breakup. Synthetic Aperture radar (SAR) satellites, such as Radarsat, Envisat and ERS-2, can also be used to map the overflow extent with the advantage that the radar backscatter is not affected by the presence of clouds (DF Dickins Associates *et al.*, 2009).

In the Alaskan Beaufort Sea, DF Dickins Associates *et al.* (2009) showed that Landsat, MODIS and ERS-2 satellite images provide the most accurate depiction of the ice overflow extent when compared to direct observations from a helicopter. They also concluded that Radarsat SAR and SPOT images provided the least accurate overflow mapping. Hirose *et al.* (2008) showed that bottomfast ice can be detected using active radar satellites (i.e. Radarsat SAR and Envisat ASAR) images using the fact that the radar backscatter from the bottomfast ice is much lower than from the floating ice.

In this study, satellite images were used to delineate bottomfast ice, floating channel ice and the ice overflow. Visible spectrum MODIS, AVHRR/3 and Landsat satellite images were used to create a land-water feature map and to delineate the overflow and the floating channel ice, and ASAR Envisat satellite images were used to delineate the bottomfast ice, as presented in Table 2-3.

The Moderate Resolution Imaging Spectroradiometer (MODIS) instrument is part of two different satellites, Terra and Aqua. These two satellites individually orbit the Earth every 99 minutes (NASA, 2010a) and the pair of MODIS sensors provides global coverage every one to two days (NASA, 2010b). The Mackenzie Delta is actually covered about twice a day by each satellite around 10:30am LST by Terra and around 1:30pm LST by Aqua (NASA, 2010b). MODIS is designed to collect reflected radiation from the earth's surface in 36 spectral bands ranging from wavelengths of 0.405 to 14.385 μm

with a spatial resolution ranging between 250 and 1,000 m. The visible spectral band (0.4 μm to 0.7 μm) MODIS images have a maximum spatial resolution of 500 m (NASA, 2010b). Geometrically corrected true-color MODIS images from 2003 to 2009 were downloaded free of charge from the University of Alaska's GINA (2010) website. Visible band MODIS images were used to visually identify and then delineate the overflow progression on the outer delta's sea ice surface.

The Advanced Very High Resolution Radiometer/3 (AVHRR/3) is a six-channel imaging radiometer instrument aboard several NOAA satellites and more recently aboard the MetOp-A satellite (ESA, 2010c). It collects reflected radiation from the earth's surface in the wavelength range of 0.58 to 12.50 μm at a maximum spatial resolution of 1.09 km (NOAA, 2010). Geometrically corrected true-color AVHRR/3 images of year 2002 were downloaded free of charge from the University of Alaska's GINA (2010) website. The AVHRR/3 images were used to track the progression of the overflow on the outer delta's sea ice surface for the earlier years when MODIS was not yet in orbit.

The Landsat 5 and Landsat 7 satellites orbit the Earth about 14 times a day around 10:00 am LST and they each have a 16-day orbit cycle. The Thematic Mapper sensor of both satellites collect reflected radiation from the earth's surfaces in seven spectral bands ranging from wavelengths of 0.45 to 2.35 μm at a maximum spatial resolution of 30 m for Band 1 to 5 and Band 7, and 60-120 m for Band 6 (NASA, 2005; NASA, 2009). Geometrically corrected greyscale Landsat images from 2002 to 2009 were downloaded free of charge from the U.S. Geological Survey's Glovis (2010) website. For this study, the near-infrared band (Band 4 – 0.76 μm to 0.90 μm) of Landsat was found to be better than the visible spectrum bands (Band 1-2-3 – 0.45 μm to 0.69 μm) for identifying and delineating the overflow and floating channel ice. The mid-infrared band (Band 5 – 1.55 μm to 1.75 μm) was used to create the land-water feature map. The thermal band (Band 6 – 10.4 μm to 12.5 μm) was used to follow the relative changes in water and ground temperature (i.e. warmer surface temperatures appear as a lighter color than colder temperatures). No attempt was made to convert colors into absolute temperature values.

Envisat, an active radar satellite, cycles the earth about 14 times a day with a 35-day repeat cycle. The Envisat Advanced Synthetic Aperture Radar (ASAR) has a C Band microwave radar that has 37 operating modes (ESA, 2010b). The Image mode and Alternate Polarization mode geometrically corrected images of Envisat ASAR from 2006 to 2009, having a maximum spatial resolution of 30 m, were used. Envisat ASAR images were downloaded from the ESA's Earth Observation Link (2010a) image collection software and were used to delineate the bottomfast ice in the outer delta.

Table 2-3 Spectral band, spatial (image) resolution, delineation type, and delineation accuracy of the various satellites and instruments used in this study.

Satellite / Instrument	Spectral Band	Spatial (Image) Resolution	Delineation Type	Delineation Accuracy
MODIS	Visible	500 m	Overflow Observation	
			Overflow Delineation	500 m
AVHRR/3	Visible	1.09 km	Overflow Observation	
Landsat 5 & 7	Near-Infrared (Band 4)	30 m	Overflow Observation	
			Floating Channel Ice Delineation	60 m
	Mid-Infrared (Band 5)	30 m	Land-Water Feature Map	60 m
	Thermal (Band 6)	60 - 120 m	Spring Freshet and Overflow Temperature	
Envisat	ASAR	30 m Downloaded Image Resolution: 250 m	Bottomfast Ice Delineation	500 m

2.4.3 Land-Water Feature Map

It is important to define the location of the land and water in the Mackenzie Outer Delta. An accurate electronic version of such a map could not be found and, therefore, the creation of a land and water feature map was necessary. Two recent Landsat images (Band 5 with image preset # 65011) of high (08-June-2008 in Figure 2-3a) and low (18-September-2007 in Figure 2-3b) water levels in the Mackenzie Outer Delta, at a spatial resolution of 30 m, were downloaded and opened in the Adobe Photoshop software at an image resolution of 30 m. It can be seen in Figure 2-3b that the low water level

satellite image has some black lines due to a failure in the scan line corrector of the Landsat 7 satellite (NASA, 2009) but it was the best recent image of the outer delta when the water levels were very low.

In the greyscale Band 5 images, the water and the ice features appear as a dark grey color, the land appear as a white or light grey color, and the scan line corrector failure lines are black, as presented in Table 2-4 and shown in Figure 2-3a & b. The color of both images was modified using the “Color Balance” function of Adobe Photoshop as follow. The white and grey areas that correspond to the land in the images were transformed to red (+100 red) and blue (+100 blue) composite colours in the low and high water level images, respectively, as presented in Table 2-4 and shown in the insets of Figure 2-3a & b. The two images were then overlaid with the low water level image (red) as the bottom layer at opacity of 100%, and the high water level image (blue) as the top layer at opacity of 50%. The two layers were merged together using the “Flatten Image” function, resulting in the red and blue composite image presented in Figure 2-3c.

Table 2-5 defines how the overlapping pixels of both images were interpreted to identify the water, land, and intermittently submerged land regions of the outer delta. The intermittently submerged land is defined as the land that was visible on the low water level image but was covered with water (or not visible due to any other reason) on the high water level image. These water and land features were then transformed into different colors, identified in the last column of Table 2-5, by using the “Replace Color” function to create Figure 2-3d. For example, the land features, observed as a light blue, light red or white color on Figure 2-3c, was replaced by a white color.

Note that the scan line corrector failure lines in the low water level satellite image are black and when they were overlaid on top of water in the high water level image, some regions of intermittently submerged land were incorrectly identified as water. At some regions of the outer delta, these errors were corrected manually by visually interpolating the intermittently submerged land location with the surrounding land and converting the colour from white (water) to orange (intermittently submerged land) using the “Pencil Tool”. It should also be noted that when land on the high water level image was overlapping water in the low water level image, the pixel was defined as water because of its resemblance with the water color (dark red) and also because this

should not happen. Furthermore, it should be noted that when land on the high water level image was overlapping on a scan line corrector failure line on the low water level image, the pixel was defined as land as land should also have been observed at this pixel location on the low water level image.

The opacity of the intermittently submerged land layer was reduced to 80% by selecting the “Magic Eraser Tool”, setting its opacity to 20%, giving a tolerance value of approximately 50, unselecting the “Contiguous” box so all the orange coloured pixels of the map were affected, and clicking on the orange intermittently submerged land. The water layer was set to a transparency of 100% by selecting the “Magic Eraser Tool”, setting its opacity to 100%, giving a tolerance value of approximately 10, unselecting the “Contiguous” box so all the white pixels of the map were affected, and clicking on the water. To represent the lakes, a grey layer was added behind the land layer where lakes were observed. The lakes were defined as the water features that were surrounded by land.

It should be noted that the intermittently submerged land features may have been incorrectly identified in regions where the scan line corrector failure lines were located as they were interpolated manually. Furthermore, depending on the sample color criteria and the fuzziness value when using the “Replace Color” step of the delineation, some pixels may be identified incorrectly (e.g. land defined as water). To avoid these types of errors the “Replace Color” function had to be used carefully. The delineation errors of the land-water feature map were not rigorously quantified. However, the errors appear to be small when the map is qualitatively compared with the original satellite images.

This land-water feature map was created with both a satellite spatial resolution and an Adobe Photoshop image resolution of 30 m. A comparison between the processed and unprocessed images revealed that the accuracy of the delineation is approximately 2 pixels, therefore, 60 m. However, in some cases, this map was slightly rotated and reduced in size and quality (image resolution of 250 m) to overlay on the MODIS satellite images. Consequently, some of the land-water feature maps, presented below, have an accuracy and a resolution of 250 m.

Table 2-4 Color appearance of the land and water features in the Mackenzie Outer Delta from the Landsat satellite images (Band 5) and modified colors resulting from the “Replace Color” Feature of Adobe Photoshop.

High Water Level (Figure 2-3a)			Low Water Level (Figure 2-3b)		
Feature	Color	Modified Color	Feature	Color	Modified Color
Water / Ice	Dark Grey	Dark Blue	Water	Dark Grey	Dark Red
Land	White / Light Grey	White / Light Blue	Scan Line Corrector Failure Lines	Black	Black
			Land	White / Light Grey	White / Light Red

Table 2-5 Algorithm leading to the classification of the land and water features of the Mackenzie Outer Delta from the combination of high and low water level Landsat satellite images (Band 5) and final color coding of the land-water feature map.

High Water Level (Red Composite) (Figure 2-3a)		Low Water Level (Blue Composite) (Figure 2-3b)		Combined Composite Image	Overlay of Low and High Water Level Images (Figure 2-3c)	Land-Water Feature Map (Figure 2-3d)
Feature	+	Feature	=	Feature	Color	Modified Color
Water Ice	+	Water	=	Water (Sea / Rivers)	Dark Red Dark Blue	White (Transparent)
				Water (Lakes)	Dark Red Dark Blue	Grey
Land	+	Water	=	Water (Sea / Rivers)	Dark Red	White (Transparent)
				Water (Lakes)	Dark Red	Grey
Water Ice	+	Scan Line Corrector Failure Lines	=	Water (Sea / Rivers)	Dark Blue	White (Transparent)
				Water (Lakes)	Dark Blue	Grey
				Intermittently Submerged Land	Dark Blue	Orange (80 % Opacity)
Land	+	Scan Line Corrector Failure Lines	=	Land	Blue	Black
Water Ice	+	Land	=	Intermittently Submerged Land	Red	Orange (80 % Opacity)
Land	+	Land	=	Land	White Light Red Light Blue	Black

2.4.4 Overflow Delineation

The methodology used to delineate the overflow is described below. First, daily MODIS satellite images (spatial resolution of 500 m) of the Mackenzie Delta region during the overflow periods from 2006 to 2009 were downloaded and opened in Adobe Photoshop at an image resolution of 250 m. The downloaded images, covering the same predefined area of approximately 2,500 km x 2,500 km, shown in Figure 2-4a, were cropped to cover only the Mackenzie Outer Delta region, as shown by the red outline in Figure 2-4b. For consistency in the cropped selection of the satellite images, the “Save/Load Selection” feature of Adobe Photoshop was used. These cropped images were then overlaid by the land-water feature map presented in Section 2.4.3. As this map was geometrically adjusted to overlay on the cropped MODIS images, no MODIS satellite image adjustment was required.

In these visible spectrum band images, the overflow appears as a grey or brown color and the ice and snow surface appears white, as shown in Figure 2-4c. The overflow locations were delineated manually using a PC pointing device, using a method similar to the one described by DF Dickins Associates *et al.* (2009), by clicking on each pixel of the sharp boundary between the overflow and the ice cover, as illustrated in Figure 2-4d. In some cases, especially in the earlier overflow stages, the brightness/contrast of the satellite images was adjusted to better define the overflow boundaries. The overflow was delineated using this method on each day where clouds or fog were not covering and obscuring the overflow regions.

Field investigations in the Mackenzie Outer Delta, performed in 2008 and 2009, confirmed the existence and accuracy of the overflow boundary location that were determined from the satellite images. As observed from Figure 2-5, the MODIS image has a smaller resolution (500 m) than the Landsat image (30 m). As a result, smaller ice and overflow features observed on the Landsat images, especially along the interface of the overflow and of the floating ice cover, are not observed on the MODIS images. However, the general shape of the overflow is the same in both images. The overflow boundaries and the ice features observed from the georeferenced pictures taken during field investigations (Pictures 1, 2 and 3 in Figure 2-5) are all clearly observed on the Landsat satellite images and to a much lesser extent in the MODIS images. To conclude,

the overflow boundaries observed in the field correspond reasonably with the overflow observed on the satellite.

As the delineations were performed manually, some human errors and inaccuracies were introduced. These errors were usually introduced when the observed features on the satellite images could subjectively be identified as either ice or overflow due to their similar colors. For the 26-May-2008 image, the accuracy of the overflow delineations was assessed at the south of Garry Island region, using the methodology presented in section 2.4.1. The delineation is presented in Figure 2-4d. From this analysis, it was found that the edges of the overflow were on average accurate within 1 to 3 pixels (250 m to 750 m) with a maximum deviation of up to 6 pixels. This accuracy varied because of the sharpness of the overflow boundary and the difficulty in correctly identifying the overflow regions in some outer delta locations. From equation 2-1, using $A_1 = 68.4 \text{ km}^2$, $P_1 = 41.5 \text{ km}$, $A_2 = 85.6 \text{ km}^2$, and $P_2 = 41.3 \text{ km}$, the delineation accuracy of the overflow south of Garry Island was calculated as 415 m. Consequently, the accuracy of the manual overflow delineations performed using Adobe Photoshop is approximately 500 m (2 pixels) and equal to the spatial resolution of the MODIS satellite images. From equation 2-2, the maximum error of this delineation was calculated as 22 %. For a better assessment of the overflow delineation accuracies and errors, this analysis could be performed for each region of the Mackenzie Outer Delta and for each satellite image used, but this was not done due to time constraints.

2.4.5 Floating Channel Ice Delineation

The methodology of the delineation of the floating channel ice is described below. First, Landsat satellite images (spatial resolution of 30 m) of the Mackenzie Outer Delta (Band 4 with image preset #65011) during the overflow period on 23-May-2008 and 19-May-2009 were downloaded and opened in Adobe Photoshop at an image resolution of 30 m. These downloaded images covered the same region of the Mackenzie Outer Delta and no image cropping or adjustment was required.

In these visual spectral band images, the floating channel ice cover is observed as the white coloured regions in the channels and sub-channels of the Mackenzie Delta extending into the sea and bordered by the dark coloured overflow, as shown in Figure

2-6a, and that was observed to be floating both in 2008 and in 2009. The sharp transition between the overflow and the floating channel ice cover was delineated manually using a PC pointing device, as shown in Figure 2-6b. At the Reindeer Channel Mouth and in Kittigazuit Bay, Canadian Hydrographic Service charts presented by Hill *et al.* (2001) were used to assist with the delineation of the sub-ice channels. The images were imported into Adobe Photoshop and the delineation of the sub-ice channels were performed from these charts. The delineation of floating channel ice was abruptly stopped seawards of the overflow region because it is unknown if the sub-channels extend further towards the sea.

As the delineations were performed manually, some human errors and inaccuracies were introduced. These errors were usually introduced when the observed features on the satellite images could be either defined as floating channel ice or water due to their similar colors. For the 23-May-2008 image, the accuracy and error of the floating channel ice delineations were assessed at the Kendall Island region, using the methodology presented in section 2.4.1. The delineation is presented in Figure 2-6c. From this analysis, it was found that the edges of the floating channel ice were on average accurate within 1 to 2 pixels (30 m to 60 m) with a maximum error of up to 4 pixels (120 m) in a few cases. This accuracy varied because of the sharpness of the floating channel ice boundary and the difficulty of identifying the floating channel ice in some outer delta locations. From equation 2-1, using $A_1 = 6.01 \text{ km}^2$, $P_1 = 31.6 \text{ km}$, $A_2 = 7.14 \text{ km}^2$, and $P_2 = 30.5 \text{ km}$, the delineation accuracy of the floating channel ice at the Kendall Island region was calculated to be 36 m. Consequently, the accuracy of the manual floating channel ice delineations performed using Adobe Photoshop is approximately 60 m (2 pixels). This accuracy is twice the spatial resolution of the Landsat satellite images. In some figures, the floating channel ice delineation was rotated and reduced in size and quality (image resolution of 250 m) to be combined with the overflow delineations. From equation 2-2, the maximum error of this delineation was calculated as 17 %.

2.4.6 Bottomfast Ice Delineation

The methodology of the delineation of the bottomfast ice is described below. First, Envisat ASAR satellite images (spatial resolution of 30 m, downloaded at an image resolution of 250 m) of the Mackenzie Outer Delta between 2006 and 2009 were downloaded and opened in Adobe Photoshop at an image resolution of 250 m. As the collected Envisat images did not all cover the same outer delta regions, the images were rotated and resized to overlap with the land-water feature map and the MODIS images.

In these ASAR images, the bottomfast ice appears darker than the floating ice, as shown in Figure 2-7a & b, as it has a smaller radar backscatter because the SAR microwave radiation penetrates through the ice and into the bed sediments (Hirose *et al.*, 2008). The bottomfast ice boundaries were delineated manually by contouring the boundary, using the PC pointing device, between the dark bottomfast ice and the light floating ice cover, as shown in Figure 2-7c. It is observed that the ice cover further offshore is also dark but was not defined as bottomfast ice as the water at this distance is too deep for bottomfast ice to form. Additionally, land also appears darker than the floating ice cover such that the land-water feature map overlay helped to differentiate between land and bottomfast ice.

As the delineations were performed manually, some human errors and inaccuracies were introduced. These errors were usually introduced when the observed features on the ASAR satellite images could be either defined as bottomfast ice or floating ice due to the grey color of the radar backscatter at some locations. For the 02-May-2008 image, the accuracy and error of the bottomfast ice delineations were assessed at the south of Garry Island region, using the methodology presented in section 2.4.1. The delineation is presented in Figure 2-7c. From this analysis, it was found that the edges of the bottomfast ice were on average accurate within 1 to 2 pixels (250 m to 500 m) with some exceptions where the deviation was larger (up to 4 pixels). From equation 2-1, using $A_1 = 61.6 \text{ km}^2$, $P_1 = 45.5 \text{ km}$, $A_2 = 77.1 \text{ km}^2$, and $P_2 = 43.0 \text{ km}$, the delineation accuracy of the bottomfast ice at the south of Garry Island region was calculated as 350 m. Consequently, the accuracy of the manual bottomfast ice delineations performed using Adobe Photoshop is approximately 500 m (2 pixels). This accuracy is 16.7 times the spatial resolution (2 times the downloaded image resolution) of the

Envisat satellite images. From equation 2-2, the maximum error of this delineation was calculated as 22 %.

2.4.7 Field Observations and Measurements

Multiple helicopter flights were performed in 2008 and 2009 in order to collect data and take pictures of the Mackenzie Outer Delta during breakup. To collect data on a continuous basis, some time-lapse cameras and water depth pressure sensors were installed prior to the arrival of the overflow at some key locations in the Mackenzie Outer Delta. Strudel drain dimensions and scour depths were measured at some strudel sites. Survey of the topography and bathymetry of one strudel hole region was attempted using a total station, which is an electronic/optical instrument used in modern surveying, and an underwater video camera.

The data collection sites during the field surveys are shown in Figure 2-8. Two prioritized overflow regions are identified: *Olivier Islands* and *South of Garry Island*. These two regions were chosen as the overflow covers a larger ice surface area in comparison to the other outer delta regions. The sites ST-2008 and ST-2009 are located on the floating sea ice of the South of Garry Island overflow region, about 600 m to the west and 1,600 m to the northwest of the nearest bottomfast ice respectively.

Several observation flights between 17-May and 08-June 2008 and between 06-May and 08-June 2009 were performed in order to locate strudel drains and upwellings. During these flights, strudel drains and upwellings of different flow strength, size and shape were photographed using still cameras and video and located using GPS coordinates. 60 strudel drains and 115 upwellings were identified in 2008 and 20 strudel drains and 65 upwellings were found in 2009.

Time-lapse cameras (Cuddeback model Expert) were installed in the Mackenzie Outer Delta by NRCan in 2008 and 2009 to observe the arrival, extent and depth of the overflow. Hourly photos were obtained at ST-2008 from 08-May to 21-May 2008 and at ST-2009 (Figure 2-9) from 09-May to 17-May 2009 at ST-2009. NRCan also installed time-lapse cameras on the low-lying land of the outer delta at locations H01-2009, K30-2009 and B19-2009 to observe flooding.

Water pressure depth sensors were installed in some key regions of the Mackenzie Delta both in 2008 and 2009. These sensors were used to obtain overflow depth information and also to determine the effect of increasing water level in the outer delta on the overflow. The water depths were corrected for the atmospheric pressure as the pressure sensors were unvented and thus measured total pressure. In March 2008, NRCan installed water pressure depth sensors, which collected the depth of overflow at 15-minute intervals, on the floating sea ice surface at ST-2008 and another one 15 cm below the bottomfast ice surface at BH4-2008. Overflow depth data were collected at ST-2008 from 21-April to 27-May 2008 and at BH4-2008 from 21-April to 05-June 2008. For the 2009 overflow period, a total of four water depth pressure sensors were installed at ST-2009 and BH4-2009. At BH4-2009, a pressure sensor was put on the ice surface on 08-May 2009 to measure the overflow depth on the bottomfast ice but attempts at locating the pressure sensor in late May were unsuccessful and no depth data were retrieved. At ST-2009, a Levellogger Model 3001 pressure sensor, which recorded water depth at 5-minute intervals from 08-May to 29-May, was inserted inside the ice cover on 08-May 2009 (Hole 1 in Figure 2-9) at a depth of about 1.1 m from the ice surface. At ST-2009, on 08-May 2009, a pressure sensor was fixed at the base of the time-lapse camera pole to measure the overflow depth but unfortunately the overflow was too small to be measured by the sensor. At ST-2009, on 17-May 2009, after the floating sea ice overflow covering the ice surface had drained, a second Levellogger Model 3001 pressure sensor was inserted into an auger hole (Hole 2 in Figure 2-9), about 5 m away from Hole 1. This time, the depth sensor, recording water depth at 5-minute intervals from 17-May to 29-May, was laid on the bed.

Strudel drains were observed and measured in the outer delta in both 2008 and 2009. In 2008, strudel drains were present at the ST-2008 site and a total of 13 strudel holes, presented in Figure 2-10, were measured for their horizontal dimension and depth of scour. The scour depths were measured manually by using a weight attached at the bottom of a rope and measuring the submerged portion of the rope using a measuring tape. Both the hole diameters and the overflow depths were estimated from field observations, pictures and videos. Strudel investigations at this site were made between 19:50 and 22:00 on 22-May 2008 while some strudel drains were still active and from 19:20 to 21:15 on 27-May 2008 when the overflow had drained and all strudel were

inactive. During the 2009 field investigation, no strudel were observed at ST-2009. At SB-2009, 11 active strudel drains, presented in Figure 2-11, were observed and measured between 23:15 on 25-May 2009 and 00:45 on 26-May 2009. The hole diameters of these strudel drains could not be accurately measured as the drains were completely covered by overflow and could not be reached. At SL-2009, near the border of a lake, another active strudel drain, presented in Figure 2-11, was observed and measured on 25-May 2009 from 21:55 to 22:35 and on 26-May 2009 from 20:10 to 23:00. This lake strudel hole did not have any ice cracks around it suggesting that it was formed by muskrats, as explained in Great Canadian Rivers (2007). At both these sites, the water depths and the overflow depths were both measured using a Schlumberger Mini-Diver pressure sensor (Houston, Texas, United States).

The ice surface topography and the scour bathymetry of the S2009-01 lake strudel at SL-2009 were measured on 26-May 2009 using a Trimble S Series total station. This total station was set on the ice surface about 7 m to the east of the strudel hole. On the same day, an Aqua-Vu underwater video camera (Crosslake, Minnesota, United States) was inserted into this strudel hole. This video was then analysed for bed scour and ice structure observations.

2.4.8 Meteorological and Water Level Data

Meteorological data collected by the Meteorological Service of Canada (MSN), including air temperatures and atmospheric pressures, were obtained in order to analyse various parameters related to the overflow process of the Mackenzie Delta's ice surface. Furthermore, ocean and the delta channel water levels, collected by the Water Survey of Canada (WSC), were obtained to help to quantify their effect on the overflow process.

Air temperature data was used to determine whether a temperature increase in the Mackenzie Outer Delta could result in the initiation of the overflow on the ice surface. Daily air temperatures at Inuvik (Station ID 2202575 at 68.30°N 133.48°W), Norman Wells (Station ID 2202800 at 65.28°N 126.80°W) and Pelly Island (Station ID 2203095 at 69.63°N 135.44°W) from 2002 to 2009 were downloaded from the Environment Canada (2010a) website. The air temperature at Inuvik, for the month of April and May, is indicative of the average temperature of the delta as it was located near the center of

the delta along the north-south axis of the delta. As shown in Figure 2-12, during these two months, the recorded temperatures at Inuvik were on average 6°C higher than at Norman Wells, located 460 km to the southeast of Inuvik, and 4°C lower than at Pelly Island, located 155 km north of Inuvik in the outer delta. An increase in the average air temperature during breakup can be observed from Figure 2-12 and on average, in the last eight years, the average air temperature at Inuvik crossed 0°C on 17-May. However, the mean temperature varies daily and yearly such that it can deviate significantly from this average.

Atmospheric pressures from Environment Canada's (2010a) station no. 2203095 on Pelly Island (69.63°N 135.44°W) were used to correct the measured water depths deduced from the pressure sensors installed throughout the outer delta in 2008 and 2009. The Pelly Island station data were chosen as this was the closest climate station to the installed pressure sensors.

Water level data for the Mackenzie Delta from 2002 to 2009 were downloaded from Environment Canada's WSC (2010b) website for the twelve gauges indicated on the map in Figure 2-1. Water levels for the Mackenzie Delta's channels, the Mackenzie River and the Peel River were analysed to determine the effect of the increase of water level (discharge) on the ice overflow timing, its depth of overflow, and the rate at which it spreads.

The ocean water level at the Tuktoyaktuk station no. 6485 (69.43°N 133.02°W), downloaded from the Fisheries and Oceans Canada (2010) website, were used to determine the effect of tides and storm surges on the overflow depth. The tidal range of the Beaufort Sea has a mean of 30 cm and a maximum of 50 cm at Tuktoyaktuk (Hill *et al.*, 2001). Therefore, the tides could be of sufficient height to affect the overflow and the strudel process. Storm surges which can significantly increase the sea water level in a short time (Hill *et al.*, 2001) were also observed in the data.

2.4.9 Bed Sediments

Knowledge of the bed sediment characteristics is important to predict the potential scouring of the Mackenzie Outer Delta seabed caused by vertical strudel flows. In the shallow-water facies of the Mackenzie Outer Delta in water depths up to 2 m, Hill *et al.*

(2001) observed that the dominant lithology is fine to very fine sand with concentrations of detritus organic matter and small tabular mud clasts. Sediments from three locations (BH4-2007, BH5-2007 and Strudel-2008) at the Mackenzie Outer Delta were collected and analysed by NRCan for grain size distribution, water content and material density.

The grain size distribution analysis is described as follow (D. Whalen, personal Communication, July 2010). The grain size sub-samples were transferred into a test tube from the frozen and non-frozen samples. Peroxide (35% H₂O₂) was added to each sample to burn off any excess organics that may have skewed the resulting grain size data. The sample was dried at 60°C for at least 24 hours. Each sample was centrifuged at 1500 rpm, and the final sample was freeze dried. The resultant powder was poured into a Coulter Laser model LS230 for grain size analysis. All of the samples used in this study had a grain size of less than 1 mm so the Coulter laser could be used for the entire grain size spectrum at each site. However, as a precaution, all samples were passed through a 1 mm sieve before being poured into the instrument.

Based on the Udden-Wentworth scale grain-size classification scheme, the bed material at these three location, presented in Figure 2-13, is composed of 5 to 20 % clay (< 3.9 µm), 45 to 70 % silt (> 3.9 µm & < 62.5 µm), and 10 to 50 % sand (>62.5 µm & <2 mm). At BH-2007 and BH5-2007, the soil relative density varied from 2.65 to 2.75 and the water content varied from 20.3 to 28.0 % for depths up to 4 m. For the first 2.5 m depth from the surface, the median size of the sand particles was 75 µm and the arithmetic mean size of the cohesive sediment was 35 µm.

2.5 Analysis, Results and Discussion

2.5.1 Overflow Depth Data

The data collected from the water pressure depth gauges installed throughout the Mackenzie Outer Delta in 2008 and 2009 are presented below with the help of time-lapse camera photos. The measured overflow depths from the water level gauges at the BH4-2008 and ST-2008 sites in 2008 are presented in Figure 2-14 and explained in the following two paragraphs. The overflow depths and water depths measured from the water level gauges installed in two adjacent holes at ST-2009 in 2009 are presented in

Figure 2-15 and explained in the subsequent three paragraphs. The purpose of this section is to present and explain how the collected data from the pressure depth sensors were analysed and resulted into overflow depth and water depth measurements.

The overflow arrived very quickly at site BH4-2008 on 18-May-2008 such that the water depth over the sensor increased to 54 cm in a 15-minute interval between 18:15 and 18:30. Since the depth sensor was installed 15 cm under the ice surface, the overflow depth at BH4-2008 was 39 cm. The overflow depth rose at a rate of 1 to 5 cm/hr until a local maximum overflow depth of about 1.05 m above the ice surface was reached 24 hours later. The overflow depth remained mostly constant until 27-May after which it started to slowly drop and reached a minimum value of 0.85 m on 30-May. A few days later, the water level increased once more to reach a maximum of 1.25 m on 03-June which corresponds to the peak freshet arrival. The jump in the overflow depth on 03-June was probably caused by a gauge movement. In fact, a comparison between the deployment and the pickup coordinates suggests that the depth sensor had moved about 400 m to the north-north-west (S. Solomon, Personal Communication, January 2009). During the entire overflow process, the ocean tides and water level variations observed at Tuktoyaktuk did not affect the overflow depth over the bottomfast ice surface.

At ST-2008, the floating sea ice overflow arrived abruptly on 20-May-2008 such that the overflow depth increased from 0 to 15 cm in a 15-minute interval between 00:00 and 00:15, reaching a depth of 34 cm one hour later. The overflow arrival was confirmed by the time-lapse camera's pictures presented in Figure 2-16. The overflow depth reached a maximum of 48 cm on 20-May at 19:00. A slight variation in the overflow depth was noticed on 21-May but the maximum overflow depth remained fairly constant. The overflow depth started to drop rapidly at 01:00 on 22-May which was confirmed by the pictures presented in Figure 2-17. No water was covering the depth sensor by 20:00 on 22-May but it was observed that overflow was still present in the surrounding regions. This rapid drop in water level at ST-2008 did not coincide with any water level decrease at BH4-2008 (measured by the other depth sensor) suggesting the entire floating sea ice cover was rising under buoyant forces.

The water depth pressure sensor installed at ST-2009 on 08-May-2009 was inserted at the vertical centre of the ice cover in an auger hole (Hole 1) such that the initial water depth over the sensor was 92 cm. The water level increased suddenly by 19 cm in a 5-minute period between 21:25 and 21:30 on 10-May. However, what seemed to be a large increase in overflow depth in such a small time was actually water that filled the freeboard portion of the hole, measured as 18 cm. The water depth reached a maximum of 35 cm at 23:30 on 10-May. The time-lapse camera pictures presented in Figure 2-18 show that the overflow did not fully drain from the ice surface but instead froze due to the low air temperatures. Additionally, a visit on site on 17-May revealed that 8 cm of overflow ice was frozen over the original ice surface. As a result, it is estimated that 8 of the 35 cm depth increase over the sensor was overflow depth, 18 cm was the freeboard, and the depth sensor dropped inside the ice cover by the remaining 9 cm possibly due to erosion of the ice cover inside the auger hole. The overflow depth started to decrease at 20:00 on 11-May such that the water depth over the sensor rapidly decreased by 14 cm which was equal to the new ice freeboard measured on 17-May. Starting on 17-May, the depth sensor slowly dropped into the hole as the ice deteriorated, such that an increase in water depth over the sensor was recorded. At 20:00 on 24-May, the depth sensor reached the bottom of the 2.0 m thick ice cover and fell onto the sea bed surface at a depth of 2.65 m.

The water depth pressure sensor laid on the bed surface at ST-2009 under Hole 2 on 17-May 2009, which was drilled approximately 5 m away from Hole 1, revealed that the sea water depth was 2.04 m. The under ice water depth at this hole was measured as 0.28 m from the field investigation. The sea water depth slowly increased with time such that it rose by 15 cm in 13 days, at a rate of approximately 1.2 cm/day, indicating that the water level and the floating sea ice were continuously rising due to the increase in water discharge from the delta. The spring peak freshet discharge reached the area on 05-June after the depth sensors were retrieved such that its effect on the variation of the sea water depth is unknown.

The difference in recorded water levels between the depth sensors in Hole 1 and Hole 2 at ST-2009, after both sensors were sitting on the bed (25-May and beyond), suggests that a 45 cm deep strudel scour formed below Hole 1 during the overflow process. A

scour formed even though a strudel was not observed and the hole was not augered completely through the ice cover. However, this depth variation between the two depth sensors could be non-scour related. Furthermore, on both depth sensors, it is possible to see the small tidal effect on the sea water level which is dampened such that the tides are about 5 cm instead of the 40 cm recorded at Tuktoyaktuk. However, the variation in the average ocean water level observed at Tuktoyaktuk did not affect the overflow depth on the Mackenzie Outer Delta sea ice surface.

2.5.2 Ice Formation and Chronology of the Ice Surface Overflow

2.5.2.1 Overview

The ice cover of the Mackenzie Outer Delta forms during freeze-up and thickens during the winter. When breakup arrives, the outer delta ice cover goes through four main water overflow stages: the initial bottomfast ice overflow, the initial floating sea ice overflow, the maximum floating sea ice overflow, and the draining of the floating sea ice surface. These overflow stages are followed by the peak freshet overflow arrival which rapidly melts the entire outer delta ice cover. The objective of this section is to provide brief but detailed explanation of these six stages. These explanations are of great importance as the overflow has never been thoroughly documented in the past for the Mackenzie Delta or for the Alaskan Beaufort Sea where the majority of the ice overflow and strudel research was completed.

2.5.2.2 Freeze-Up and Winter Ice Conditions

The Mackenzie Delta's ice and snow cover are completely melted by the end of June such that a new ice cover is formed in the Beaufort Sea every October. The freeze-up of the Mackenzie Outer Delta's water surface into an ice cover begins in the nearshore regions of the outer delta and expands towards the sea, as shown in Figure 2-19. Two weeks after the initiation of the ice cover formation, the shorefast ice cover has expanded approximately 18 kilometres towards the sea. As the nearshore sea ice cover is in place before a strong and established ice cover is present over the delta's channels, some ice floes are discharged from those channels towards the sea thus creating some freeze-up ice jams. With time, the ice cover continues to grow both in surface area and in thickness such that by late October, the Mackenzie Bay is completely ice covered

(Dey, 1980). By the end of winter, the shorefast ice of the Mackenzie Outer Delta extends between 50 and 65 kilometres offshore such that a continuous sheet exists up to the 18-20 m isobath line (Stringer, 1974 and Cooper, 1975 as cited in Dey, 1980). In May, the ice thickness of the Mackenzie Outer Delta channels, lakes and nearshore floating sea ice cover measured between 1.6 and 1.9 m, but may reach up to 2 m (Hill *et al.*, 2001).

Three types of ice covers form in the Mackenzie Outer Delta throughout the winter season: bottomfast ice, floating channel ice and floating sea ice. Solomon *et al.* (2009) consider another type of ice cover, transitional ice, characterized by floating ice with intermittently bottomfast ice areas. For simplicity, transitional ice is categorized as either floating sea ice or bottomfast ice throughout this report. Descriptions of the three types of ice cover, illustrated in Figure 2-20, are presented in the next three paragraphs.

Bottomfast ice (BFI) is defined as ice which freezes and bonds to the bed sediments and vegetation (Hill *et al.*, 2001) and is present in shallow water depths of rivers, lakes and nearshore sea regions. With time, the ice increases in thickness such that the bottomfast ice region expands into deeper water (Solomon *et al.*, 2007). The annual progression of the bottomfast ice during the 2008-2009 winter season is presented in Figure 2-21. As observed from this figure, some bottomfast ice was in place very early in the freeze-up season in October and the bottomfast ice expansion was observed until breakup in May. In the Mackenzie Outer Delta, the location of the bottomfast ice slightly changes each year depending on a variety of factors such as the bathymetry, the sea water level, the ice thickness and the sediment transport effects (Solomon *et al.*, 2007). In fact, the bottomfast ice distribution at the south of Garry Island overflow region greatly changed since 1993 (Solomon *et al.*, 2007). The final bottomfast ice locations in the Mackenzie Outer Delta from 2006 to 2009, presented in Figure 2-22, were delineated from Envisat ASAR satellite images. The delineations show that the bottomfast ice extent is in fact varying every year at some outer delta regions such as south of Garry Island, north of Olivier Islands and around Rae Island. However, extents of the bottomfast ice at other regions such as in the Shallow Bay at the Reindeer Channel Mouth and at the Middle Channel Mouth were observed to be steadier.

Floating channel ice (FCI) is defined as ice that is not frozen to the bed and which covers the deep primary channels of the delta and the sub-ice channels extending into the sea. Contrary to the Alaskan Beaufort Sea (Leidersdorf *et al.*, 2006), the delta's channels extend into the sea such that they provide conduits for winter flow through the bottomfast ice zone (Hill *et al.*, 2001). The locations of the floating channel ice covering the channel and sub-channels of the Mackenzie Outer Delta are shown in Figure 2-23. Contrary to the bottomfast ice, the location of the floating channel ice on the delta's channels is usually the same every year. However, some temporal variations in the location of the floating channel ice covering the sub-channels of the sea were observed because of the interannual variability in the bottomfast ice location.

The last ice type, *floating sea ice (FSI)*, is defined as the shorefast sea ice that is not categorized as bottomfast ice or floating channel ice. In the Mackenzie Outer Delta, most of the ice cover is floating sea ice. The floating sea ice is said to vary in elevation with the sea water level changes such that tidal cracks form at its interface with the bottomfast ice (Reimnitz, 2002).

Storm surges were observed to cause overflow of the bottomfast ice surface of the Mackenzie Outer Delta in winter. Solomon *et al.* (2007) studied the effect of a storm surge of 1.3 m above the normal tide range in January 2005. They observed a dramatic increase in radar backscatter on the bottomfast ice from the Envisat ASAR and Radarsat satellite images during the storm surge period, caused by overflow onto ice and overlying snow. Winter storm surges are not uncommon and were also documented to happen in the Alaskan Beaufort Sea (Reimnitz, 2002). Even months after a storm surge overflow occurred on bottomfast ice, the refrozen overflow was sometimes visible on the Landsat satellite images (Band 4).

2.5.2.3 Initial Bottomfast Ice Overflow

The first of the four main overflow stages of the Mackenzie Outer Delta is the initial overflow of water on the bottomfast ice surface, illustrated in Figure 2-24. In spring, the Mackenzie Delta receives a very large amount of water discharge, called the spring freshet, caused by the melting of snow and ice in the upstream regions of the watershed. This north flowing water reaches the delta when the delta's channels are still

covered by a thick and strong ice cover, and when air temperatures are usually below the freezing point. As the under ice flow capacity of the delta's channels is too small to accommodate this increasing water discharge, the water level rises such that some bottomfast border ice and some land floods in the delta (Figure 2-25a). In the outer delta, the increasing water level rise combined with the ice buoyancy led to a flexure of the ice surface and eventually to a rupture between the floating channel ice, which is mobile, and the bottomfast ice, which is frozen to the sea bed (Hill *et al.*, 2001). As a result, the under-ice water flows upwards through these new formed cracks, a process called upwelling, such that it overflows onto the bottomfast ice surface (Figure 2-25c) and floods some low-lying land along the sea shore (Figure 2-25b). It was observed that a rise in water level between 0.0 m and 0.6 m in the outer delta's channels was enough to initiate this overflow process. However, most of the discharge continues to flow through the sub-ice channels of the Mackenzie Outer Delta, bypassing the bottomfast ice (Hill *et al.*, 2001). The shallow initial bottomfast ice overflow is initiated near the channel's mouth (Figure 2-25d) and can freeze onto the ice surface when the air temperature is below the freezing point (Figure 2-25e). Shortly after the initiation of the overflow, the water provided from the continuously discharging upwellings rapidly spreads onto the surrounding bottomfast ice (Figure 2-25f) which acts as an effective surface to carry the river flow towards the sea. From 2002 to 2009, the initial bottomfast ice overflow south of Garry Island and at the Olivier Island region happened on 13-May \pm 7.6 days and 09-May \pm 7.8 days respectively. These uncertainties are the standard deviation of the overflow stage dates between 2002 and 2009.

In May 2008, the local maximum overflow depth on bottomfast ice at BH4-2008 reached a value of 1.05 m one day after the overflow was initiated at this location. When this maximum water depth was reached, the overflow expanded in surface area instead of increasing in depth such that the water depth on the bottomfast ice was mostly constant. Twelve days later, coinciding with the date of drained floating sea ice, the overflow depth at BH4-2008 decreased to a minimum of 0.85 m. This decrease occurred even though the water level increased continuously in the outer delta's channels throughout the breakup period. The overflow depth on the bottomfast ice surface southwest of Rae Island (69.517120°N, 135.244910°W) was measured as 54 cm on 21-May 2009.

In the Mackenzie Outer Delta, the initial overflow location on a regional level is variable from year to year, as presented in Table 2-6. In 2008, the overflow at the mouth of Harry Channel was initiated on 01-May while the overflow at Shallow Bay at Reindeer Channel Mouth and at the Olivier Island region did not start until 16 days later. Conversely, in Figure 2-26, it is evident that the overflow was initiated simultaneously at all the regions in 2006. No attempt was made to find the reasons causing the interannual variability in the initial overflow location. However, the flow rate in each of the delta channels of the Mackenzie Delta possibly varies yearly depending on the channel's ice condition.

The spring freshet flows from the upstream Mackenzie River and Peel River are not the only factors initiating the overflow. Occasionally, consecutive days of warm temperatures in the delta are responsible for the initiation of this overflow process, such as in 2002 and 2009. It is thought that air temperatures above the freezing point can melt a large quantity of snow and ice throughout the delta which translates into a local rise in discharge in the delta's channels. Consequently, the bottomfast ice surface floods but the overflow depths are small compared to a freshet initiated overflow.

As they have been observed to overflow the ice surface in winter, storm surges are considered as potential overflow instigators. However, storm surges were not observed to initiate the overflow process between 2002 and 2009. Tides are not expected to initiate or affect the overflow process as they were observed from depth sensor gauges to be dampened by the nearshore ice cover presence (5 cm tides compared to 40 cm in Tuktoyaktuk). Additionally, no winter overflow from tidal action was observed from satellite images in the years studied.

During the overflow period, the albedo of the flooded ice surface decreases significantly to as little as 1/7 of its initial value and the albedo of the non-flooded ice decreases down to 1/3 of its initial value (Dean *et al.*, 1994). As a result, the Mackenzie Outer Delta ice cover is absorbing more heat from the solar radiation such that the melting process is accelerated (Dey, 1980). The temperature of the under ice flow in the outer delta was measured to be approximately $0.0^{\circ}\text{C} \pm 0.1^{\circ}\text{C}$ in 2008 and therefore it does not seem to greatly contribute to the melting of the ice. Dean *et al.* (1994) measured the overflow to be a few tenths of a degree above 0°C and the water flowing beneath the ice to be within a few hundredth of a degree from 0°C .

Table 2-6 Date of initial overflow at key locations in the Mackenzie Outer Delta from 2006 to 2009.

Year	Shallow Bay at Reindeer Channel Mouth	Around Olivier Island	Middle Channel Mouth	Harry Channel Mouth
2009	30-April	29-April	01-May	05-May
2008	17-May	18-May	11-May	01-May
2007	02-May	02-May	12-May	02-May
2006	14-May	16-May	14-May	14-May

2.5.2.4 Initial Floating Sea Ice Overflow

The second main overflow stage in the Mackenzie Outer Delta is the initiation of the floating sea ice overflow, illustrated in Figure 2-27. About 2 to 5 days after the bottomfast ice overflow initiated, the overflow wave reaches the floating sea ice, depresses the floating ice cover due to its weight and forms cracks (Reimnitz *et al.*, 1974), and spreads on its surface thus covering more surface area (Figure 2-28a, b & c). The overflow then percolates through holes and cracks at the boundary between the bottomfast ice and the floating sea ice as well as through the floating sea ice cover, a phenomenon called strudel (Figure 2-28d). Additionally, the floating ice surface in the strudel zone was observed to be porous thus facilitating the flow of water through the ice cover. Pressure ridges, rising up to 5 m above the average sea ice surface, were observed to act as overflow barriers (Figure 2-28e). Furthermore, an ice road constructed in northern Alaska effectively halted the progression of the river overflow (DF Dickins Associates *et al.*, 2009). From 2002 to 2009, the initial floating sea ice overflow south of Garry Island and at the Olivier Island region happened on 16-May \pm 6.4 days and 14-May \pm 7.6 days respectively.

In May 2008, the local maximum overflow depth on the floating sea ice at ST-2008 reached a value of 48 cm about 19 hours after the overflow was initiated at this location. This overflow depth remained constant and maximum for two consecutive days after which it decreased rapidly as the ice surface was draining due to the buoyant rise of the floating ice cover. In May 2009, the overflow depth on the floating sea ice at ST-2009 reached a maximum of 8 cm about 2 hours after the overflow was initiated at this location and the ice cover was drained 24 hours later.

The velocity of the leading edge of the overflow on the floating sea ice was quantified in 2008 using visible spectral band MODIS satellite images, presented in Figure 2-29. In the Alaskan Beaufort Sea, the front of the freshwater was said to intermittently advance in individual lobes, progressing at a rate of about 2 to 3 m/s (Reimnitz & Bruder, 1972). Hourly MODIS images of the peak floating sea ice expansion period in May 2008 revealed that the overflow front north of Olivier Islands was progressing at a speed of approximately 12 ± 9 cm/s. The standard deviation of this velocity comes from the accuracy (spatial resolution) of the MODIS images, which is 500 m. At the south of Garry Island overflow region, the depth sensors recorded that it took 29.75 hours for the overflow wave to travel the 9.85 km distance between BH4-2008 and ST-2008 for an average velocity of 9.2 cm/s. This overflow front velocity was not directly measured during the field investigations.

2.5.2.5 Maximum Floating Sea Ice Overflow

The third main overflow stage in the Mackenzie Outer Delta occurs when the floating sea ice overflow extent is a maximum, as illustrated in Figure 2-30. About 3 or 4 days after the floating ice overflow begins, the overflow reaches a maximum distance from the shore, depending on the region and the year. In 2008, the overflow south of Garry Island extended to a maximum of 20.2 km from the shore and 4.6 km of this overflow was on floating ice. In 2009, the overflow reached a maximum of 18.6 km and 4.1 km was floating ice overflow. At the Olivier Islands region, the overflow in 2008 reached a maximum distance of 14 km from the shore and 12.7 km of this overflow was on floating ice and it reached a maximum of 13.4 km from the shore in 2009 where 12.3 km was floating ice overflow. From 2002 to 2009, the maximum floating sea ice overflow south of Garry Island and north of Olivier Islands happened on 19-May ± 5.4 days and 18-May ± 5.7 days respectively.

The date of maximum overflow extent and of maximum overflow depths on the floating sea ice does not coincide with the occurrence of maximum water levels or water discharge in the Mackenzie Delta channels. Actually, in 2002, the maximum overflow extent was reached when the water level of the outer delta channels had increased by only 0.2 m out of the peak freshet maximum water level increase of 1.3 m at the WSC station ID 10MC011. In 2009, the maximum overflow extent was reached when the

water level of the outer delta channels had increased by only 0.3 m out of the peak freshet maximum water level increase of 1.1 m at the WSC station ID 10MC011. The optimal overflow distances and depths were usually reached when the freshet peak water level and peak discharge were still upstream of Tsiigehtchic (Mackenzie River at Arctic Red River); therefore approximately 15 days before the peak freshet reached the outer delta.

The maximum floating sea ice overflow extent does not happen on the same date in different outer delta regions. As illustrated in Figure 2-31, the maximum floating sea ice overflow in 2006 was reached south of Garry Island on 20-May while the overflow northwest of the Olivier Islands had barely started to flood onto the floating sea ice surface. The maximum overflow extent at the Olivier Island was reached four days later when the floating ice surface south of Garry Island was drained from its overflow. The maximum floating ice overflow depth also varies with the regions and with the years. The maximum floating sea ice overflow depth was about 48 cm at ST-2008 in 2008 while this depth was only 8 cm at the same location (ST-2009) in 2009.

It appears that the maximum distance of overflow in some years is controlled by the maximum extent of the nearshore ice cover observed at freeze-up, presented in Figure 2-32a. The outer edge of the overflow generally is located just seaward of the two metre isobath, as observed from the bathymetry of the sea delineated by Hill *et al.* (2001). When the overflow reaches this limit distance, it abruptly stops expanding suggesting the ice surface has a ridge forming at that location every year (Figure 2-32b & c). This hypothesis on the existence of a ridge was not confirmed as field observations were not performed at these locations. The maximum extent of the nearshore ice cover observed at freeze-up in October 2008 is seen to correspond closely with the maximum overflow extent in spring 2007 and 2008.

2.5.2.6 Drained Overflow

The drained overflow, illustrated in Figure 2-33, is the final overflow stage in the Mackenzie Outer Delta. Once the maximum distance of floating sea ice overflow is reached, the water drains from its surface and the floating sea ice rises due to buoyancy forces and the unloading of the ice as the water drains. Once drained, the floating sea

ice surface will not be flooded again for the remainder of the breakup, as presented for the year 2008 in Figure 2-34 and also observed by Kane *et al.* (1975) for the Alaskan Beaufort Sea overflow (as cited in Dey, 1980). However, the water level in the Mackenzie Outer Delta, measured at site ST-2009, still rises at a rate of approximately 1.2 cm/day while the average rise is 5 cm/day in the channel near the mouth of Reindeer Channel (WSC station ID 10MC011). However, the overflow depth on the bottomfast ice surface decreases, as measured by the pressure depth sensor at BH4-2008 in May 2008. The duration between the initiation of the floating sea ice overflow to its complete drainage is typically 8 or 9 days. From 2002 to 2009, the drained floating sea ice overflow south of Garry Island and at the Olivier Islands region happened on 24-May \pm 4.8 days and 23-May \pm 5.0 days respectively.

Bottomfast ice is the only type of ice that stays flooded throughout the entire duration of the overflow, until the entire sea ice surface melts. In fact, the overlay of the final drained overflow areas onto the bottomfast ice outline earlier defined from Envisat ASAR images (Figure 2-22), presented in Figure 2-35, clearly shows that the majority of the ice surface still flooded by water is the bottomfast ice. Conversely, the floating channel ice surface never floods during the overflow period as it rises with the increase in the channel's water level (Reimnitz, 2002). Also, some of the floating sea ice adjacent to the bottomfast ice does not flood (Figure 2-36a).

Once the floating sea ice surface is drained, strudel holes and cracks in the ice surface are visible from a helicopter (Figure 2-36b) and even from satellite images (Figure 2-36c). The boundary between the bottomfast ice and the drained floating sea ice is observed to be sharp and filled with cracks and holes (Figure 2-36d). An accumulation of ice pieces is also observed at the boundary, indicating that the overflow is directed towards that boundary such that strudel drains are likely present along this border. Additionally, ice blocks are deposited onto the floating sea ice surface where the overflow occurred (Figure 2-36e). In 2008, about 5 mm of fine sediments accumulated in small patches on the floating sea ice surface (Figure 2-36f) but the majority of the ice surface was white and not covered by sediments.

In the Alaskan Beaufort Sea, the bottomfast ice often detaches from the bed and floats to the surface (Reimnitz *et al.*, 1974; Reimnitz, 2002) potentially creating strudel in the

smaller sea water depth regions (< 2 m). The reasons for these detachments are unknown. In the Mackenzie Outer Delta, the bottomfast ice either rarely or never detaches from the bed as this separation was not observed to happen from field observations or from satellite images between 2006 and 2009. Therefore, it is possible that the majority of the Mackenzie Delta's bottomfast is well bonded to the sea bed such that it melts in place below the overflow.

2.5.2.7 Peak Freshet Arrival

Before the ice surface in the nearshore Beaufort Sea melts and about 10 days after the floating sea ice has completely drained, the spring freshet reaches the Mackenzie Outer Delta, as illustrated in Figure 2-37. The peak freshet, which is filled with debris (Figure 2-38a), corresponds to the highest water levels and the highest discharges in the delta for the entire year with a water level increase varying between 1.2 and 2.5 m at the outer delta channel's mouth. Consequently, the majority of the low-lying land of the outer delta floods due to the peak freshet (Figure 2-38b, c & d). From 2002 to 2009, the peak spring freshet reached the outer delta at the southern end of Shallow Bay and at the Middle Channel Mouth on 01-June \pm 3.1 days and 04-June \pm 3.4 days respectively.

An analysis was made to determine the location of the peak freshet with respect to the ice clearance location and its date of arrival in the outer delta using time-lapse camera pictures, water pressure depth sensor data, water level data and satellite images. A comparison between the ice conditions of the delta's channels, shown for the year 2009 in Figure 2-39, and the freshet peak location is presented in Table 2-7. The analysis shows that the maximum water level in the delta's channels, the peak freshet, is located at the interface of the ice free freshet water with the floating channel ice. Furthermore, these results are consistent with Hill *et al.* (2001) who showed from data acquired by Lewis (1988) that in the East Channel at Inuvik, the maximum daily water levels occurred very close to the date of ice clearance. Additionally, the depth sensor installed at BH4-2008 recorded that the maximum overflow depth occurred on 03-June in 2008, which agrees with the above results.

Satellite observations by Dean *et al.* (1994) revealed that approximately a week after the water level peaked in the Mackenzie River at Arctic Red River, the appearance of warm

water in the delta arises. From Landsat thermal images (Band 6) presented in Figure 2-40, it was observed that the water temperature of the peak freshet was warmer (lighter color) than the water temperature of the overflow (darker color). Therefore, the warmer river water appears to become a dominant contributor of heat such that the ice cover melts rapidly.

Table 2-7 Comparison between the ice condition of the Mackenzie Outer Delta channels and the date of peak freshet water level from the Water Survey of Canada water level gauges.

Year	Date when the WSC Water Level Gauge Station was Free of Ice			Date of Peak Freshet from the WSC Water Level Gauge Data		
	10MC023	10MC011	10LC019	10MC023	10MC011	10LC019
2009	31-May	05-June	04-June	31-May	04-June	04-June
2008	31-May	02-June	02-June	-	02-June	02-June
2007	02-June	04-June	03-June	02-June	03-June	-
2006	30-May	01-June	31-May	30-May	-	31-May

2.5.3 Timing and Extent of the Overflow

The chronological events leading to the overflow of the ice surface in the Mackenzie Outer Delta were described in detail in the previous sections and a summary of the overflow extent and of the timing of this overflow is presented in this section. Visible spectral band MODIS satellite images from 2006 to 2009 were analysed on a daily basis to follow the chronology of the overflow extent in the Mackenzie Outer Delta, presented in Figure 2-41. The illustrations of Figure 2-42 present the final drained overflow on bottomfast ice throughout the outer delta in which the drained floating sea ice regions are also identified. In the years when clouds were present in the outer delta at the time when the maximum floating sea ice overflow extent was reached, the maximum extent could still be defined a few days later because the drained floating sea ice surface was still appearing darker than the surrounding ice surface.

The dates at which the four main overflow stages were reached in the Mackenzie Outer Delta from 2002 to 2009, defined from the observation of MODIS images, are shown in Table 2-8 for the overflow at the Olivier Islands region and in Table 2-9 for the overflow south of Garry Island. The dates at which the peak freshet reached the outer delta, acquired from the analysis of both MODIS satellite images and WSC water level gauges,

are shown in Table 2-10 for the regions at the mouth of Napoiak Channel at Shallow Bay and at the Middle Channel mouth. As observed from the standard deviation values in these tables, the accuracy in the overflow timing prediction increases for the later stages. For example, the initial bottomfast ice overflow in the region south of Garry Island occurred on average on 13-May \pm 7.6 days while the drained floating sea ice overflow usually occurred on 24-May \pm 4.8 days. The durations between the four main overflow stages were derived from Table 2-8 and Table 2-9 and the results are presented in Table 2-11 and Table 2-12 respectively for the overflow regions around the Olivier Islands and south of Garry Island. For example, it took 3.0 ± 1.6 days between the initial bottomfast ice overflow and the initial floating ice overflow stages at the south of Garry Island overflow region.

The effects of the type of breakup (thermal vs. dynamic) and overflows initiated by warm temperatures on the duration of the overflow was studied by Bélanger, Hicks, Solomon, & Loewen (2009), as presented in Appendix E. The type of breakup can be determined from field observations and Landsat satellite images (Band 4). The floating sea ice overflow at the Olivier Islands region and especially south of Garry Island had a longer duration when the breakup in the Mackenzie Delta at Point Separation was thermal compared to dynamic which happened both in 2003 and in 2007 (Bélanger *et al.*, 2009). At the Olivier Islands overflow region, the floating sea ice overflow lasted 9 and 14 days respectively in 2003 and 2007 while the average is 9.3 days. South of Garry Island, the floating sea ice was flooded for 12 days in 2003 and 14 days in 2007 while the average is 7.8 days. From the few collected years of data, no relationship was found between the overflow initiated by warm temperatures which happened in 2002 and 2009 and the duration and rate of the overflow spread.

Table 2-8 Date of overflow stage occurrence in the Mackenzie Outer Delta at the Olivier Islands overflow region from 2002 to 2009.

	2009	2008	2007	2006	2005	2004	2003	2002	Average Date	Standard Deviation (Days)
Initial Bottomfast Ice Overflow	30-April	18-May	02-May	14-May	05-May	21-May	04-May	12-May	09-May	7.8
Initial Floating Ice Overflow	02-May	20-May	12-May	20-May	12-May	27-May	10-May	14-May	14-May	7.6
Maximum Floating Ice Overflow Extent	12-May	23-May	18-May	23-May	16-May	29-May	14-May	16-May	18-May	5.7
Drained Floating Ice	16-May	25-May	26-May	27-May	25-May	01-June	19-May	21-May	23-May	5.0

Table 2-9 Date of overflow stage occurrence in the Mackenzie Outer Delta at the south of Garry Island overflow region from 2002 to 2009.

	2009	2008	2007	2006	2005	2004	2003	2002	Average Date	Standard Deviation (Days)
Initial Bottomfast Ice Overflow	04-May	16-May	12-May	16-May	13-May	27-May	03-May	16-May	13-May	7.6
Initial Floating Ice Overflow	08-May	20-May	14-May	18-May	16-May	28-May	09-May	18-May	16-May	6.4
Maximum Floating Ice Overflow Extent	12-May	22-May	19-May	20-May	19-May	30-May	14-May	19-May	19-May	5.4
Drained Floating Ice	16-May	24-May	28-May	23-May	26-May	01-June	21-May	23-May	24-May	4.8

Table 2-10 Date of peak freshet arrival in the Mackenzie Outer Delta from 2002 to 2009.

	2009	2008	2007	2006	2005	2004	2003	2002	Average Date	Standard Deviation (Days)
Shallow Bay at Napoiak Channel Mouth	01-June	31-May	03-June	31-May	27-May	06-June	-	01-June	01-June	3.1
Middle Channel Mouth	05-June	03-June	05-June	02-June	29-May	-	07-June	08-June	04-June	3.4

Table 2-11 Number of days between the different overflow stages at the Olivier Islands region from 2002 to 2009.

	2009	2008	2007	2006	2005	2004	2003	2002	Average	Standard Deviation
Initial Bottomfast Ice Overflow to Initial Floating Ice Overflow	2	2	10	6	7	6	6	2	5.1	2.9
Initial Floating Ice Overflow to Maximum Floating Ice Overflow Extent	10	3	6	3	4	2	4	2	4.3	2.7
Maximum Floating Ice Overflow Extent to Drained Floating Ice Overflow	4	2	8	4	9	3	5	5	5.0	2.4

Table 2-12 Number of days between the different overflow stages south of Garry Island from 2002 to 2009.

	2009	2008	2007	2006	2005	2004	2003	2002	Average	Standard Deviation
Initial Bottomfast Ice Overflow to Initial Floating Ice Overflow	4	4	2	2	3	1	6	2	3.0	1.6
Initial Floating Ice Overflow to Maximum Floating Ice Overflow Extent	4	2	5	2	3	2	5	1	3.0	1.5
Maximum Floating Ice Overflow Extent to Drained Floating Ice Overflow	4	2	9	3	7	2	7	4	4.8	2.6

2.5.4 Interannual Variation in the Overflow Location

As both the bottomfast ice location and the extent of the floating sea ice overflow varies yearly, an analysis was made to determine which ice covered regions of the Mackenzie Outer Delta were flooded by overflow between 2006 and 2009. Figure 2-43 shows the interannual variations in the bottomfast ice and floating sea ice overflow locations in the four year period from 2006 to 2009, which are individually presented in Figure 2-42.

The methodology of the creation of Figure 2-43 is described as follow. First, the bottomfast ice and floating sea ice overflow boundaries from 2006 to 2009, presented in Figure 2-42, were opened in Adobe Photoshop and their overflow delineations were modified into 8 distinct colors using the “Hue/Saturation” function (4 floating sea ice colors and 4 bottomfast ice colors). These four overflow delineations were then overlaid with opacities of 20%, 40%, 70% and 100% from top to bottom respectively and merged into a single image using the “Flatten Image” function. The resulting image is comprised of many different colors due to the color combinations produced by the overlaying layers. These colour combinations were then modified into distinct colors using the “Replace Color” feature of Adobe Photoshop using the methodology presented in Table 2-13. For example, in the case where the four floating ice overflow layers were overlaid on top of each other, the corresponding color was replaced by a dark red color. These delineations were performed automatically using several features of Adobe Photoshop and the delineations were verified manually for inaccuracies or inconsistencies. The accuracy of the overflow delineations presented in this figure is the same as the overflow delineations that were used to produce this figure, therefore 500 m.

From the illustration of Figure 2-43, it is observed that all the intermittently submerged land areas of the outer delta are covered by bottomfast ice which overflowed in the four studied years. Furthermore, the majority of the bottomfast ice surface overflowed all four years as most of the bottomfast ice forms at the same locations every year. Conversely, the floating sea ice overflow location is more variable such that it seldom happens at the same place every year. However, some sea ice and floating sea ice regions were seen to overflow every year including at the south of Garry Island, the Olivier Islands and the Rae Island overflow regions. It is important to note that the majority of the floating sea ice overflow regions are located directly seaward of the bottomfast ice as the river and the overflow water is flowing towards the ocean.

Table 2-13 Methodology defining the overflow features in the Mackenzie Outer Delta from 2006 to 2009. The top overlay events have overlapping priority on the bottom events.

Overlay Event	Recurrence of Overlay Event	Resulting Color Coding
Bottomfast ice overflow	4 years	Dark Green
Floating sea ice overflow	4 years	Dark Red
Sea ice overflow	4 years	Orange
<i>Bottomfast ice overflow</i>	1 to 3 years	
<i>Floating ice overflow</i>	Remaining 1 to 3 years	
Bottomfast ice overflow	2 or 3 years	Light Green
Floating sea ice overflow	2 or 3 years	Light Red
Sea ice overflow	2 years	Pink
<i>Bottomfast ice overflow</i>	1 year	
<i>Floating ice overflow</i>	1 year	

2.5.5 Predicting the Timing of the Overflow

Despite the fact that the various regions of the Mackenzie Outer Delta overflow at different dates during the same year, a prediction of the timing of the four main overflow stages at the south of Garry Island region and at the Olivier Islands region was attempted using data from 2002 to 2009. The initiation and progression of the ice overflow can be affected by several factors as mentioned in the Literature Review. Unfortunately, an attempt to correlate the interannual variability of the Alaskan Beaufort Sea ice overflow found no correlation between the studied variables and the overflow extent (DF Dickins Associates *et al.*, 2009). However, this study revealed that the initiation of the overflow process and of its progression in the Mackenzie Outer Delta depended on two major variables; air temperatures and the increase in water level (discharge) from the Mackenzie River.

The prediction of the overflow timing south of Garry Island and at the Olivier Islands overflow region was done using the Water Survey of Canada (WSC) (Environment Canada, 2010b) water level data from the Mackenzie River at Arctic Red River (MARR) gauge ID 10LC014. The MARR water level station is located just upstream of the delta and it provides a good indication of the increasing river discharge that eventually spreads throughout the delta's channels. Also, the water level gauge at MARR was one of the only water level gauges in the delta that provided continuous and useful data

during breakup. For simplicity, the discharge of the Peel River into the delta (station ID 10MC002) was ignored because it comprises only 8 % of the total flow (Fassnacht and Conly, 2000).

Attempts were made to predict the timing of the overflow using two criteria. The first criteria used threshold values of the daily water level increase at MARR and the second used threshold values of the total water level increase with respect to the pre-breakup water level at MARR. The pre-breakup water level was defined as the water level ten days before a 3 cm/day increase was first observed which typically occurred from late April to early May. Daily water level change thresholds of 3 cm/day, 10 cm/day, and 30 cm/day, total water level increases of 1.0 m, 2.0 m, 4.0 m, and the peak increase were tested. An example of the water level thresholds being met during the year 2008 at MARR is presented in Figure 2-44. These thresholds were evaluated by recording the date on which the threshold was met, presented in Table 2-14, and comparing these to the dates when the four main overflow stages occurred at Olivier Islands and south of Garry Island, presented in Table 2-8 and Table 2-9 respectively. The hypothesis being tested here is that one or more of these seven thresholds will be reached each year at MARR a fixed number of days prior to the occurrence of the various stages of overflow. If this hypothesis is correct, the timing of the overflow could be predicted each year with reasonable accuracy by applying this threshold to the MARR water level data. It should be noted that this analysis is not based on a statistical model but on a simple calculation and standard deviation analysis.

The results of this analysis are presented in Table 2-15 for the overflow at the Olivier Islands and in Table 2-16 for the overflow south of Garry Island. Two of those seven thresholds revealed to be the most accurate (smallest standard deviation) at predicting the timing of the overflow caused mainly by an increase in discharge from the Mackenzie River which happened from 2003 to 2008. In 2002 and 2009, it is thought that the overflow was initiated by warm temperatures, as discussed below. The two selected criteria are the 30 cm/day rate of increase in water level and the water level increase of 2.0 m with respect to the pre-breakup water level. The yearly results of the prediction using the 30 cm/day rate of increase in water level criteria and the 2.0 m water level increase with respect to the pre-breakup water level criteria are presented

in Table 2-17 and Table 2-18 respectively for the overflow prediction at the Olivier Island overflow region, and in Table 2-19 and Table 2-20 respectively for the overflow prediction at the South of Garry Island overflow region. The peak water level was the worst predictor as all four overflow stages were usually completed before the peak water level was reached at MARR.

For the 30 cm/day rate of increase criteria, the analysis suggests that the overflow stages can be predicted with accuracy (standard deviation) of 1.5 to 4.5 days at Olivier Island, and 0.5 to 3.7 days south of Garry Island. For example, the initial floating sea ice overflow south of Garry Island is predicted to occur 8.2 ± 1.1 days after a 30 cm/day increase is first recorded by the MARR water level gauge. Using the 2.0 m total increase in water level threshold, the overflow stages can be predicted with accuracy (standard deviation) of 1.1 to 4.4 days at Olivier Island, and 1.7 to 4.0 days south of Garry Island. The occurrence of the maximum floating sea ice overflow is the overflow stage that is predicted most accurately using these two thresholds since the standard deviation is less than 2 days at both locations. To conclude, this overflow prediction scheme is more accurate than predicting the overflow timing using the average overflow stage dates, presented in Table 2-8 and Table 2-9. These historical averages provide accuracies (standard deviations) of 5.0 to 7.8 days at the Olivier Islands and 4.8 to 7.6 days at Garry Island.

In year 2002 and 2009, warm air temperature in the Mackenzie Delta occurred in advance of the increase in discharge from the Mackenzie River into the delta. Warm temperatures can melt the snow and ice cover of the delta such that this water flows towards the sea and causes an early initiation of the ice overflow. It is observed from Table 2-17 to Table 2-20 that when warm delta temperatures occurs in advance of the increase in discharge from the Mackenzie River, the timing of the overflow cannot be predicted by the water level at MARR as the time interval is usually negative indicating the overflow stage occurred prior to the threshold being exceeded. Therefore, an attempt was made to predict the overflow initiation using cumulative degree days at the Inuvik Climate Station for both these years.

Both in 2002 and 2009, the initial bottomfast ice overflow was observed at the Olivier Island overflow region four days before it was observed south of Garry Island, as

observed from Table 2-8 and Table 2-9. Therefore, the Olivier Islands region is more sensitive to a small discharge increase from local melting and this region was selected to predict the overflow initiation from an increase in air temperature. The cumulative degree days above 0°C at the Inuvik climate station, summed from 1 to 10 days before the initiation of the bottomfast ice overflow, are presented in Table 2-21. The data indicate that warm delta air temperatures may initiate the bottomfast ice overflow if the cumulative degree-day total in Inuvik, preceding the initial overflow at the Olivier Islands, exceeds 10°C in 3 days or if it exceeds 16°C in 5 days.

Table 2-14 Date at which the water level increase thresholds in the Mackenzie River at Arctic Red River (Station ID 10LC014) were met from 2002 to 2009.

Water Level Threshold	2009	2008	2007	2006	2005	2004	2003	2002	Average	Standard Deviation (days)
3 cm/day	01-May	06-May	23-Apr	28-Apr	-	04-May	28-Apr	11-May	01-May	6.0
10 cm/day	03-May	09-May	01-May	06-May	-	08-May	30-Apr	14-May	05-May	4.9
30 cm/day	14-May	11-May	07-May	09-May	-	19-May	02-May	15-May	11-May	5.6
1.0 m	08-May	11-May	04-May	08-May	-	11-May	03-May	17-May	08-May	4.7
2.0 m	11-May	13-May	08-May	11-May	-	17-May	04-May	19-May	11-May	5.1
4.0 m	17-May	15-May	12-May	14-May	11-May	23-May	17-May	23-May	16-May	4.5
Peak Water Level	26-May	23-May	21-May	22-May	19-May	29-May	24-May	28-May	24-May	3.5

Table 2-15 Number of days (average \pm standard deviation) between a water level increase criteria was met in the Mackenzie River at Arctic Red River (MARR) and a specified overflow stages at the Olivier Islands overflow region. The averages and standard deviations do not include the data from 2002 and 2009 as these years overflow were initiated by warm temperatures, and the year 2005 due to a gauge malfunction at MARR.

	3 cm/day	10 cm/day	30 cm/day	1.0 m	2.0 m	4.0 m	Peak Water Level
Initial Bottomfast Ice Overflow	12.0 \pm 4.6	7.0 \pm 4.6	2.2 \pm 4.5	4.4 \pm 4.8	1.2 \pm 4.4	-4.4 \pm 6.8	-12.0 \pm 7.0
Initial Floating Ice Overflow	18.0 \pm 4.8	13.0 \pm 3.7	8.2 \pm 2.2	10.4 \pm 3.6	7.2 \pm 2.4	1.6 \pm 5.3	-6.0 \pm 5.3
Maximum Floating Ice Overflow Extent	21.6 \pm 4.7	16.6 \pm 2.9	11.8 \pm 1.5	14.0 \pm 2.7	10.8 \pm 1.1	5.2 \pm 4.8	-2.4 \pm 4.5
Drained Floating Ice	26.0 \pm 5.8	21.0 \pm 3.7	16.2 \pm 2.6	18.4 \pm 3.4	15.2 \pm 2.2	9.6 \pm 4.7	2.0 \pm 4.1

Table 2-16 Number of days (average \pm standard deviation) between a water level increase criteria was met in the Mackenzie River at Arctic Red River (MARR) and the specified overflow stages at the South of Garry Island overflow region. The averages and standard deviations do not include the data from 2002 and 2009 as these years overflow were initiated by warm temperatures, and the year 2005 due to a gauge malfunction at MARR.

	3 cm/day	10 cm/day	30 cm/day	1.0 m	2.0 m	4.0 m	Peak Water Level
Initial Bottomfast Ice Overflow	15.0 \pm 7.3	10.0 \pm 5.9	5.2 \pm 2.7	7.4 \pm 5.8	4.2 \pm 4.0	-1.4 \pm 7.2	-9.0 \pm 7.2
Initial Floating Ice Overflow	18.0 \pm 5.3	13.0 \pm 4.2	8.2 \pm 1.1	10.4 \pm 4.0	7.2 \pm 2.3	1.6 \pm 5.5	-6.0 \pm 5.5
Maximum Floating Ice Overflow Extent	21.2 \pm 5.0	16.2 \pm 3.8	11.4 \pm 0.5	13.6 \pm 3.4	10.4 \pm 1.7	4.8 \pm 4.4	-2.8 \pm 4.2
Drained Floating Ice	25.8 \pm 6.3	20.8 \pm 4.9	16.0 \pm 3.7	18.2 \pm 4.4	15.0 \pm 3.7	9.4 \pm 4.3	1.8 \pm 3.6

Table 2-17 Number of days between a water level increase of 30 cm/day in the Mackenzie River at Arctic Red River (MARR) and the specified overflow stages at the Olivier Islands overflow region from 2002 to 2009. The averages and standard deviations do not include the data from 2002 and 2009 as these years overflow were initiated by warm temperatures, and the year 2005 due to a gauge malfunction at MARR.

	2009	2008	2007	2006	2004	2003	2002	Average	Standard Deviation
Initial Bottomfast Ice Overflow	-14	7	-5	5	2	2	-3	2.2	4.5
Initial Floating Ice Overflow	-12	9	5	11	8	8	-1	8.2	2.2
Maximum Floating Ice Overflow Extent	-2	12	11	14	10	12	1	11.8	1.5
Drained Floating Ice	2	14	19	18	13	17	6	16.2	2.6

Table 2-18 Number of days between a water level increase of 2.0 m from the pre-breakup water level in the Mackenzie River at Arctic Red River (MARR) and the specified overflow stages at the Olivier Islands overflow region from 2002 to 2009. The averages and standard deviations do not include the data from 2002 and 2009 as these years overflow were initiated by warm temperatures, and the year 2005 due to a gauge malfunction at MARR.

	2009	2008	2007	2006	2004	2003	2002	Average	Standard Deviation
Initial Bottomfast Ice Overflow	-11	5	-6	3	4	0	-7	1.2	4.4
Initial Floating Ice Overflow	-9	7	4	9	10	6	-5	7.2	2.4
Maximum Floating Ice Overflow Extent	1	10	10	12	12	10	-3	10.8	1.1
Drained Floating Ice	5	12	18	16	15	15	2	15.2	2.2

Table 2-19 Number of days between a water level increase of 30 cm/day in the Mackenzie River at Arctic Red River (MARR) and the specified overflow stages at the south of Garry Island overflow region from 2002 to 2009. The averages and standard deviations do not include the data from 2002 and 2009 as these years overflow were initiated by warm temperatures, and the year 2005 due to a gauge malfunction at MARR.

	2009	2008	2007	2006	2004	2003	2002	Average	Standard Deviation
Initial Bottomfast Ice Overflow	-10	5	5	7	8	1	1	5.2	2.7
Initial Floating Ice Overflow	-6	9	7	9	9	7	3	8.2	1.1
Maximum Floating Ice Overflow Extent	-2	11	12	11	11	12	4	11.4	0.5
Drained Floating Ice	2	13	21	14	13	19	8	16.0	3.7

Table 2-20 Number of days between a water level increase of 2.0 m from the pre-breakup water level in the Mackenzie River at Arctic Red River (MARR) and the specified overflow stages at the south of Garry Island overflow region from 2002 to 2009. The averages and standard deviations do not include the data from 2002 and 2009 as these years overflow were initiated by warm temperatures, and the year 2005 due to a gauge malfunction at MARR.

	2009	2008	2007	2006	2004	2003	2002	Average	Standard Deviation
Initial Bottomfast Ice Overflow	-7	3	4	5	10	-1	-3	4.2	4.0
Initial Floating Ice Overflow	-3	7	6	7	11	5	-1	7.2	2.3
Maximum Floating Ice Overflow Extent	1	9	11	9	13	10	0	10.4	1.7
Drained Floating Ice	5	11	20	12	15	17	4	15.0	3.7

Table 2-21 Cumulative mean daily degree-days above 0°C at the Inuvik climate station 1, 2, 3, 4, 5, and 10 days before the overflow began around the Olivier Islands from 2002 to 2009. The overflow process in 2002 and 2009 was initiated by warm temperatures in the Mackenzie Outer Delta.

Year	1 day	2 days	3 days	4 days	5 days	10 days
2009	3.6 °C	8.4 °C	18.5 °C	21.6 °C	22.3 °C	22.5 °C
2008	2.5 °C	5.1 °C	7.9 °C	11.5 °C	13.4 °C	13.4 °C
2007	0.0 °C	0.0 °C	0.0 °C	0.0 °C	0.0 °C	0.3 °C
2006	4.8 °C	4.8 °C	4.8 °C	6.6 °C	8.9 °C	11.5 °C
2005	0.0 °C	0.0 °C	0.0 °C	1.0 °C	5.9 °C	8.1 °C
2004	1.6 °C	1.7 °C	1.7 °C	1.7 °C	1.7 °C	5.5 °C
2003	0.0 °C	0.0 °C	0.0 °C	0.0 °C	0.0 °C	8.2 °C
2002	0.0 °C	3.7 °C	10.0 °C	13.3 °C	16.5 °C	16.5 °C

2.5.6 Upwelling, Strudel Drains and Strudel Scours

2.5.6.1 General

Upwelling and strudel are two distinct features that occur simultaneously in the Mackenzie Outer Delta. The positions of upwellings and strudel drains in the Mackenzie Delta are usually found from field observations using a GPS instrument. Nonetheless, satellite images can also be used to determine the location of these features even though most satellite images do not have a good enough resolution to see them directly. From the visible spectrum Landsat satellite images (Band 4), presented in Figure 2-45, some dark water streamlines are clearly observed to flow seawards from the region of upwelling near the land and along the floating channel ice, towards the region of strudel along the floating sea ice surface. These dark streamlines are considered to be sediment-laden water as darker sediment-laden water was in fact observed to spout onto the ice surface by upwelling. From these images, the upwelling zones are located at the region where the sediment-laden water streamlines meet with the floating ice surface near the land. The strudel zones are located at the opposite end (seawards) of the sediment-laden water streamlines, at the interface with the floating ice surface. Consequently, some strudel drains and upwellings which were not observed during the field observations can be roughly located from those images. This method was observed

to work as the extremities of the sediment-laden streamlines are both located where upwelling and strudel are expected to occur and were observed to occur.

2.5.6.2 Strudel Measurement Results from Field Investigations

Measurements of strudel drain dimensions and strudel scour depths were performed during the spring 2008 and 2009 field investigations in the Mackenzie Outer Delta. These measurements are unique as they were taken while some strudel were still active and ice was still covering the outer delta. Until now, measurements like these have not been reported in the literature. Additionally, in 2009, an attempt was made to measure the ice topography around a strudel drain using a total station, which is also unique.

A summary of the collected water depth, overflow depth, scoured depth and hole dimensions collected in May 2008 at ST-2008 is presented in Table 2-22. At ST-2008, the strudel drain hole sizes varied between 0.1 and 3.5 m in dimension and the maximum measured scoured depth was 0.87 m. It should be noted that there was no correlation between the strudel drain size and the strudel scour depth. On 22-May-2008, it was observed that the overflow depth on the floating sea ice surface at ST-2008 decreased rapidly such that some active strudel became inactive during a time interval of two hours, including strudel drain S2008-05 presented in Figure 2-46. Two other active strudel drains which were observed and measured at ST-2008 are shown in Figure 2-47.

A summary of the collected water depth, overflow depth, scoured depth and hole dimensions collected in May 2009 at SL-2009 and at SB-2009 is presented in Table 2-23. The diameter of the lake strudel at SL-2009 was 1.6 m in diameter with a scour depth of 30 cm. At SB-2009, the strudel drains were not measured but most of the holes seemed to be between 0.3 and 5.0 m in dimension with scour holes varying between 0.18 and 1.38 m. The ice topography and scour hole bathymetry of the lake strudel drain S2009-01 at SL-2009 was surveyed using a total station, and the results are presented in Figure 2-48. The illustration shows that the bottomfast ice surface at the south of the strudel drain, where the water is flowing from, is greatly eroded while the ice surface that is not flooded is flat and not eroded. The figure also shows that the strudel drain walls are very steep such that they seem vertical.

Table 2-22 Summary of strudel measurements in 2008 at ST-2008.

Strudel (S) / Auger (A) Hole ID	Date and Time (2008-UTC)	Water Depth (m)	Scoured Depth ¹ (m)	Overflow Depth (m)	Hole Size / Diameter (m)	Geographic Coordinate
S2008-01	22-May (20:07)	2.68		0.2	0.2	69.428116° N 135.900757°
S2008-02	22-May (20:14)	2.27		0.2	0.2	69.428186° N 135.901286°
S2008-03	22-May (21:13)			0.05	0.1	69.428051° N 135.899768°
S2008-04	22-May (19:50)			0.2		69.428898° N 135.899845° W
	22-May (21:35)	3.17		Drained		
	27-May	2.90	0.81	Drained	3.5 x 2.5	
S2008-05	22-May (19:50)			0.2		69.428908° N 135.899992° W
	22-May (21:35)			Drained		
	27-May	2.58	0.49	Drained	3.0	
S2008-06	27-May	2.95	0.86	Drained		69.429136° N 135.900177°
S2008-07	27-May	2.87	0.78	Drained	1.0 x 0.6	69.429380° N 135.899525°
S2008-08	27-May	2.48	0.39	Drained	0.2 x 0.1	69.429328° N 135.899344°
S2008-09	27-May			Drained	0.5 x 0.1	69.429328° N 135.899113°
S2008-10	27-May	2.96	0.87	Drained	0.4	69.429337° N 135.898830°
S2008-11	27-May	2.13	0.04	Drained	0.2	69.429130° N 135.898524°
S2008-12	27-May			Drained		69.428842° N 135.899594°
S2008-13	27-May			Drained		69.428666° N 135.898711°
A2008-04	27-May	2.09	-	Drained	-	69.428875° N 135.899892°

¹ The scoured depth at ST-2008 on 27-May-2008 was calculated by subtracting the water depth of the strudel by the water depth at the augered hole A2008-04, 2.09 m, assumed to be the average undisturbed bed elevation in the region.

Table 2-23 Summary of strudel measurements in 2009 at SL-2009 and SB-2009.

Strudel Hole ID	Date (2009-UTC)	Water Depth (m)	Scoured Depth ¹ (m)	Overflow Depth (m)	Hole Size / Diameter (m)	Geographic Coordinate
S2009-01	25-May	1.65		0.2 to 0.5	1.6	69.192362° N 134.797420° W
	26-May	1.79	0.30 ²	0.2 to 0.5	1.6	
S2009-02	25-May					69.386214° N 135.797082° W
S2009-04	25-May	2.89	1.38	0.2 to 0.4		69.385963° N 135.797463° W
S2009-05	25-May	2.19	0.68	0.22		69.386428° N 135.796734° W
S2009-06	25-May			0.46		69.386626° N 135.796255° W
S2009-07	25-May			0.21		69.386700° N 135.795600° W
S2009-08	25-May	1.69	0.18			69.387137° N 135.795515° W
S2009-09	25-May	1.51	-			69.387117° N 135.795549° W
S2009-10	25-May	1.87	0.36			69.387234° N 135.796628° W
S2009-11	25-May	1.80	0.29			69.387222° N 135.796640° W
S2009-15	25-May	1.89	0.38	0.24		69.386499° N 135.796559° W
S2009-17	25-May	1.82	0.31	0.23		69.387337° N 135.796943° W

¹ The scoured depth at SB-2009 (S2009-02 to S2009-17) on 25-May-2009 was calculated by subtracting the water depth at the strudel by the smallest measured water depth, 1.51 m at S2009-09, which is assumed to be water depth at the average undisturbed bed in the region.

² The scoured depth of S2009-01 (at SL-2009) on 26-May-2009 was estimated from underwater videos.

2.5.6.3 Upwellings

Upwellings are defined as an upward flow of water through holes and cracks in the ice cover which act as a passage for the under-ice river flow to overflow the sea ice surface. The main factor driving the upwelling flow upwards is thought to be the hydraulic head that develops due to an increase in the pressure head below the ice cover, caused by an increasing discharge into the outer delta (Figure 2-49a), or due to an elevation head difference between the upstream and downstream overflow water levels (Figure 2-49b). This latter case may have been observed in the field at various locations including near the Middle Channel mouth as shown in Figure 2-50.

In the Mackenzie Outer Delta, upwellings are present and active from the initiation of the overflow until the freshet arrival. No publications related to upwelling either in the Mackenzie Delta or in the Alaskan Beaufort Sea could be found even though upwellings are an important factor governing the overflow of the sea ice surface. In the Mackenzie Outer Delta, most of the observed upwellings had a spout diameter of less than one metre. However, some large upwelling spouts were observed to be about three metres in diameter (Figure 2-51a & b).

The locations of the upwellings in the Mackenzie Delta from 2007 to 2009, observed from satellite images and from the field investigations, are presented in Figure 2-52. Most upwellings were located near the channel mouths at the boundary between the floating channel ice and the bottomfast ice where water overflows onto the bottomfast ice surface. Most of the observed upwellings were located in the overflow region within 10 m of the floating ice surface. The largest upwelling density was observed at the southern edge of the south of Garry Island overflow region as well as on the southeastern edge of the Olivier Island overflow region.

Field observations of upwellings in 2008 and 2009 indicate that they can be of different sizes and of different flow strength and are often grouped together and/or along cracks (Figure 2-51c & d). The discharge of the upwelling flow mostly depends on the hydraulic head difference such that a larger head difference would increase the intensity of the upwelling flow strength and it will spurt higher above the overflow surface. The highest observed spurt was surfacing at approximately 10 cm above the average overflow

surface. Some upwellings which did not spurt water high above the overflow surface were still noticeable as the outflow of water caused turbulence in the surrounding water (Figure 2-51e) or involved water with a more concentrated / darker sediment content (Figure 2-51f).

2.5.6.4 Strudel

Strudel are defined as the drainage of overflow water through holes and cracks in the ice surface, defined as strudel drains, which can produce scour depressions in the underlying sediments (Reimnitz *et al.*, 1974), defined as strudel scours. The main factor driving the strudel flow downwards is thought to be the hydraulic head that develops due to an elevation head difference between the upstream and downstream overflow water levels (Figure 2-49b) which was observed in the field near the Middle Channel mouth as shown in Figure 2-50, or between the overflow water level and the sea water level. Strudel formation could also be caused by the rising of the floating ice cover due to buoyancy (Reimnitz, 2002).

Strudel flows are an important part of the overflow process and they have already been studied to some extent in the Mackenzie Delta and in the Alaskan Beaufort Sea, where multiple observations and measurements are presented in the Literature Review. In the Mackenzie Outer Delta, during field investigations in 2008 and 2009, the average observed vortex dip diameter, which rotated either clockwise or counter-clockwise, measured approximately 2 m in diameter with a maximum of about 5 m. Strudel drains were measured to vary between 0.1 m and 3.5 m in diameter (horizontal extent) with possibly some drains exceeding more than 5.0 m in diameter (horizontal extent). These are much smaller than the 15 to 30 m diameter strudel drains reported by Reimnitz and Bruder (1972) in the Alaskan Beaufort Sea.

The locations of the strudel drains in the Mackenzie Outer Delta from 2007 to 2009, observed from satellite images and from the field investigations, are presented in Figure 2-53. Strudel drains were categorized into two main groups: *floating sea ice strudel drains* and *bottomfast ice strudel drains*. The *floating sea ice strudel drains* occur through cracks and holes in the floating sea ice which floods during the overflow process. Most of these strudel form within a kilometre of the boundary separating the

bottomfast ice and the floating sea ice as this is where the majority of cracks are formed (Figure 2-54a) (Solomon *et al.*, 2009). With time, the floating sea ice rises due to buoyancy (Figure 2-54b) as the overflow drains completely from its surface and the strudel drains become inactive (Figure 2-54c). *Bottomfast ice strudel drains* form in the overflow region less than about 10 m away from the boundary between the bottomfast ice and the floating sea ice surface (Figure 2-54d). As these strudel drains are always covered by overflow, they are active throughout the overflow season. The largest strudel density was observed at the north-western edge of the south of Garry Island overflow region and at the Middle Channel mouth.

The overflow water initially infiltrates through cracks that formed or were already present on the ice surface. In fact, all strudel drains measured in the field had at least one longitudinal crack crossing through them, as observed in Figure 2-55, such that the drainage probably initiated at those cracks. Eventually, these cracks increase in size due to thermal decay and erosion of the ice cover caused by the draining of the floodwaters such that they become holes (Leidersdorf *et al.*, 2006). Additionally, the floating ice cover could already have holes at its surface, such as seal breathing holes (Reimnitz *et al.*, 1974) or man-made holes, such that the overflow water drains through them.

It was observed from field investigations that the surface overflow water was directed towards the strudel drains. Higher discharge strudel drainage features were observed as a water vortex swirling around a depression at its center (Figure 2-56a & b). These vortices varied in size such that their depression could be wide and shallow (Figure 2-56c) or narrow and deep (Figure 2-56d). In smaller overflow depths, these strudel drainage features were observed as water rushing into a hole (Figure 2-56e). Strudel drains with larger vortex depressions were usually observed earlier in the overflow season until the complete drainage of the floating sea ice surface. Smaller discharge strudel drains were dominant after the floating sea ice surface was drained as the hydraulic head difference driving the strudel flow was smaller and only appeared as an irrotational flow of water without a noticeable surface depression (Figure 2-57). Some strudel drains were even covered by ice pieces and other debris such that it was not possible to see any sign of strudel drainage (Figure 2-56f). No ice pieces or debris were

ever seen to be entrained below the ice surface due to a strudel flow but the hypothesis of their entrainment is reasonable for strudel with large vertical flows.

During physical measurements of inactive strudel drains at ST-2008, it was observed that part of what seemed to be a single large strudel hole was actually one or multiple smaller holes as illustrated in Figure 2-58. The remaining area was ice covered by a thin layer (approximately 5 cm depth) of water. Therefore, strudel drain dimensions could easily be overestimated from helicopter observations. It is thought that thermal erosion of the ice surface in the vicinity of the strudel hole was the responsible factor for this misinterpretation. For example, as observed from Figure 2-59, strudel drain S2008-02 which was only 20 cm in diameter during its final active hours on 22-May-2008 could easily be misinterpreted to be more than 5 m x 3 m in dimension when it was flown over only 5 days later.

2.5.6.5 Strudel Scours

Strudel drainage features in the Mackenzie Outer Delta have the potential to scour the sea bed. Strudel scour measurements were performed in both 2008 and 2009 in the outer delta where the scour depth varied between 0.04 m and 1.38 m.

In the Mackenzie Outer Delta, at the south of Garry Island overflow region, boat surveys were performed by NRCan from 2007 to 2009 to detect strudel scours. In summer 2007, an interferometric side-scan sonar boat survey successfully mapped three strudel scours, the largest scour being 20 m wide and 0.8 m in depth (Whalen *et al.*, 2007). In June 2008, a side-scan sonar and single beam echo sounder boat survey detected multiple strudel scours in the outer delta such that a scour that formed about 125 m to the northwest of ST-2008 had a maximum scoured depth of 1.5 m and a diameter of 20 m (S. Solomon, Personal Communication, November 2009). In June 2009, a side-scan sonar and multi-beam echo sounder boat survey detected multiple strudel scours in the outer delta. The largest scour, located at the geographic coordinate 69.39215°N 135.78268°W, which is about 850 m to the northeast of SB-2009, had a maximum scoured depth of 5.2 m and a diameter of 24 m (D. Forbes, Personal Communication, 2009). This scour depth is unusually deep compared to previously measured depths and it is possible that it might not have been formed due to a strudel flow.

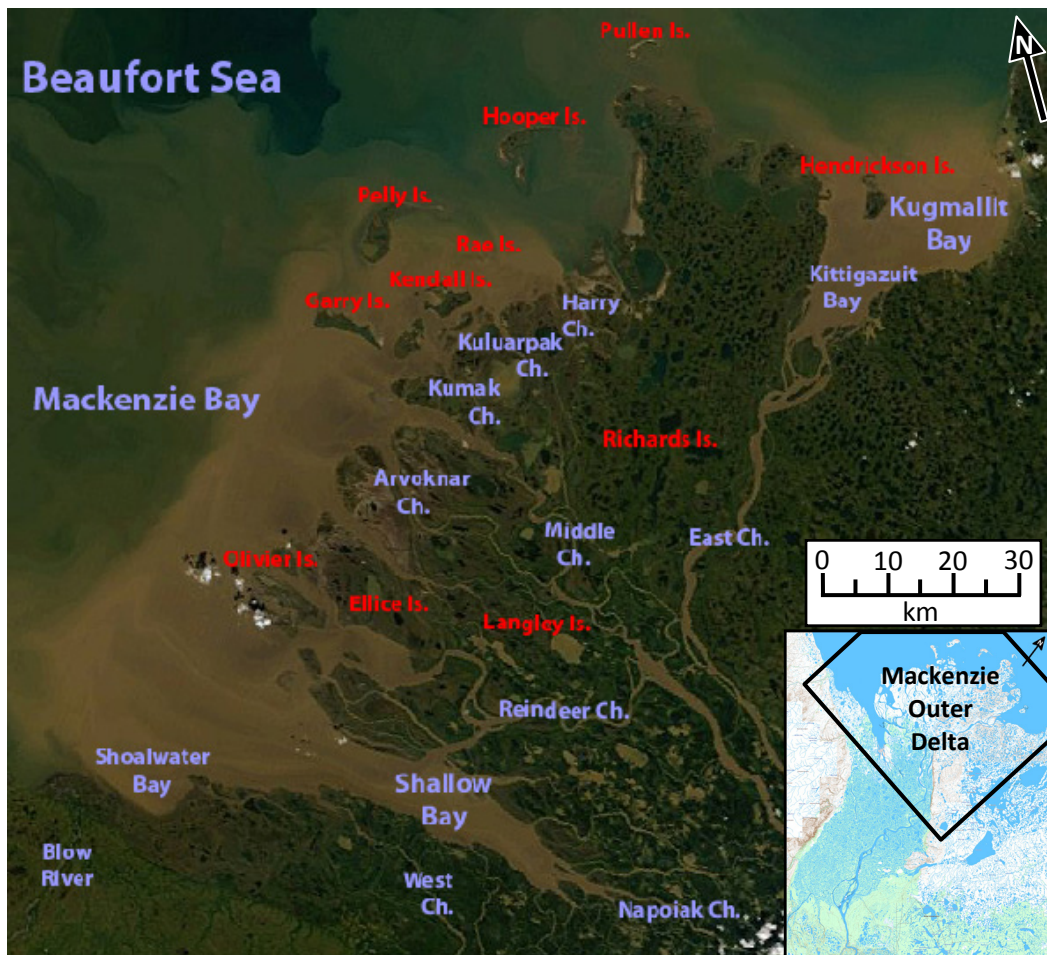
Reimnitz and Bruder (1972) observed during field investigations in the Alaskan Beaufort Sea that sediments were harder along the flanks and softer at the bottom of the strudel scour. During field investigations on 27-May-2008 at ST-2008, it was observed that the bed sediments on the surface of the strudel scour were soft and not frozen such that some cohesive soil particles were collected. Five metres away from the strudel drain, a hole (A2008-04) was augered through the ice cover. The bed sediments under the augered hole were frozen such that a thumping sound was heard when hitting the bed, a sound that was not heard when hitting the soft strudel scour sediments. This suggests that the strudel scour sediments thawed because of the strudel jet flow impinging on the bed surface.

An underwater video camera was inserted into the S2009-01 lake strudel on 26-May-2009 to observe the strudel scour that formed at that location. As observed from video images presented in Figure 2-60, a steep edge strudel scour of about 30 cm depth was formed. The vegetation on the original bed surface was completely removed and the bottom of the scoured hole was flat and composed of fine sediments. For about half of the strudel hole circumference, located on the shore side of the lake, the ice was frozen to the bed. The other half of the circumference, located towards the center of the lake as presented in Figure 2-61, was actually deeper than the scour itself and the overflow water was directed under the ice surface in that direction. Video observations were found to be a good tool to observe strudel scours.



© Department of Natural Resources Canada. All rights reserved. (NRCan – The Atlas of Canada, 2010)

Figure 2-1 Topographic map of the Mackenzie Delta with the locations of the active Water Survey of Canada water level gauges (red). *Bottom-Right Insert:* Territorial map of the Northwest Territories in Canada.



University of Alaska – GINA www.gina.alaska.edu

© Department of Natural Resources Canada. All rights reserved.

Figure 2-2 MODIS satellite image of the Mackenzie Outer Delta with water and land features. *Bottom-Right Insert:* Mackenzie Delta.

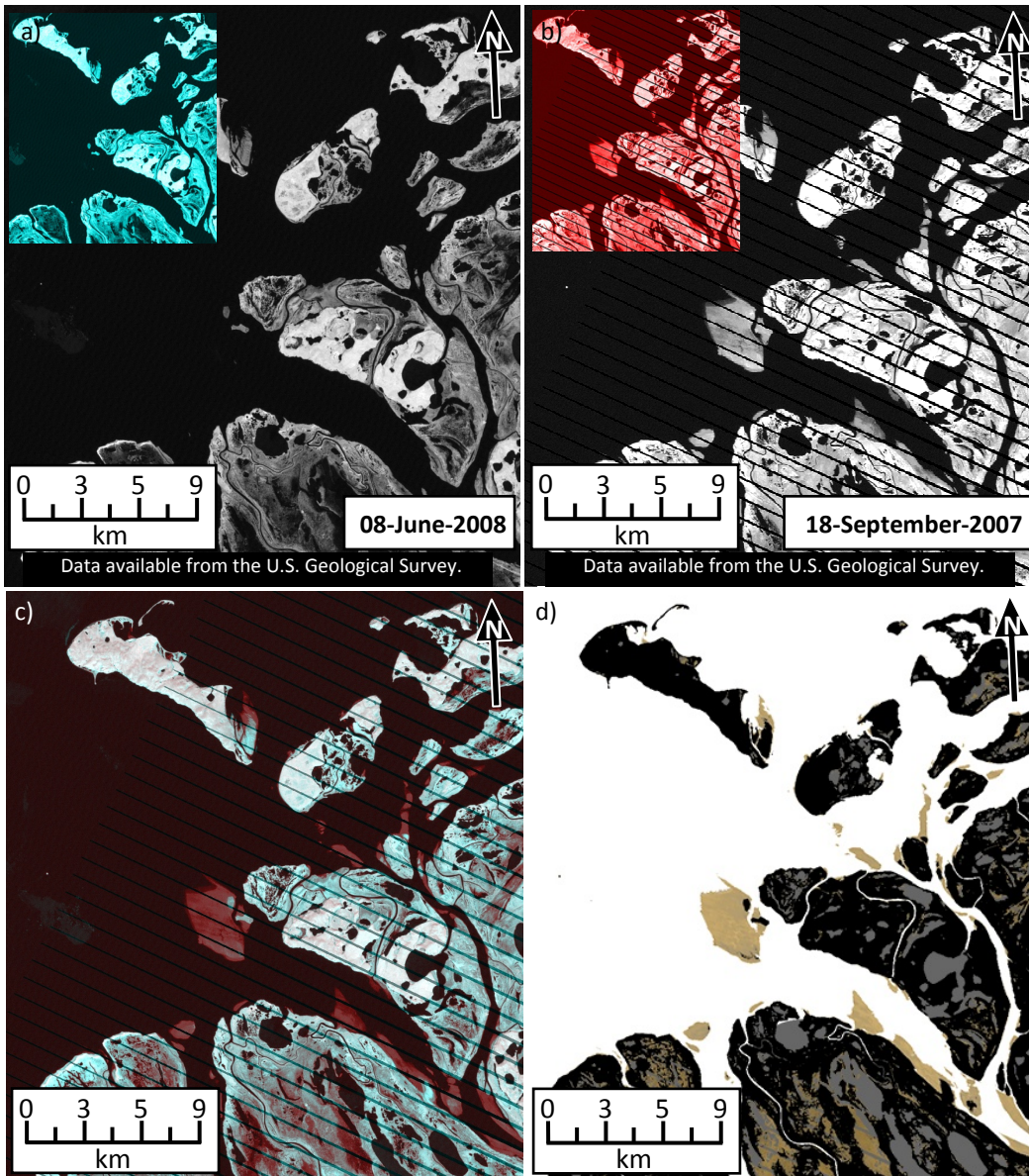
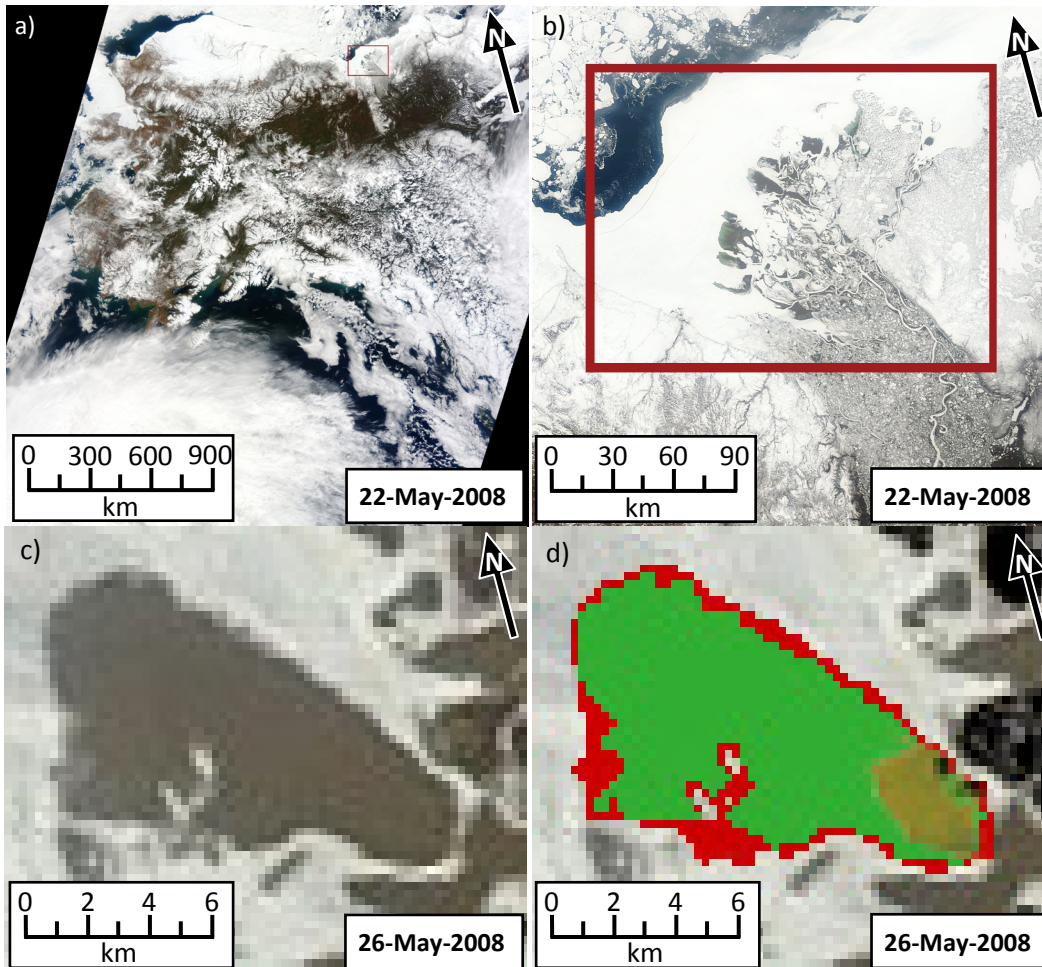


Figure 2-3 a) Landsat 5 satellite image (Band 5) of the high water level on 08-June-2008, and b) Landsat 7 satellite image (Band 5) of the low water level on 18-September-2007 at the Middle Channel mouth region. c) Overlay of the high (blue) and low (red) water level Landsat satellite images. d) Land-water feature map of the Mackenzie Outer Delta (accuracy of 60 m) where the land is black, the intermittently submerged land is orange, the lakes are grey, and the ocean and rivers are white.



University of Alaska – GINA www.gina.alaska.edu

Figure 2-4 a) MODIS satellite image of Alaska, Yukon and part of the Northwest Territories on 22-May-2008. b) MODIS satellite image of the Mackenzie Outer Delta on 22-May-2008. c) MODIS satellite image of the south of Garry Island overflow region on 26-May-2008. d) Delineation of the overflow with the land-water feature map overlay (accuracy of 500 m). The green delineation represents the minimum (conservative) delineation area from personal judgement of the overflow boundaries and the combination of the red and green delineation represents the maximum (non-conservative) overflow delineation area.

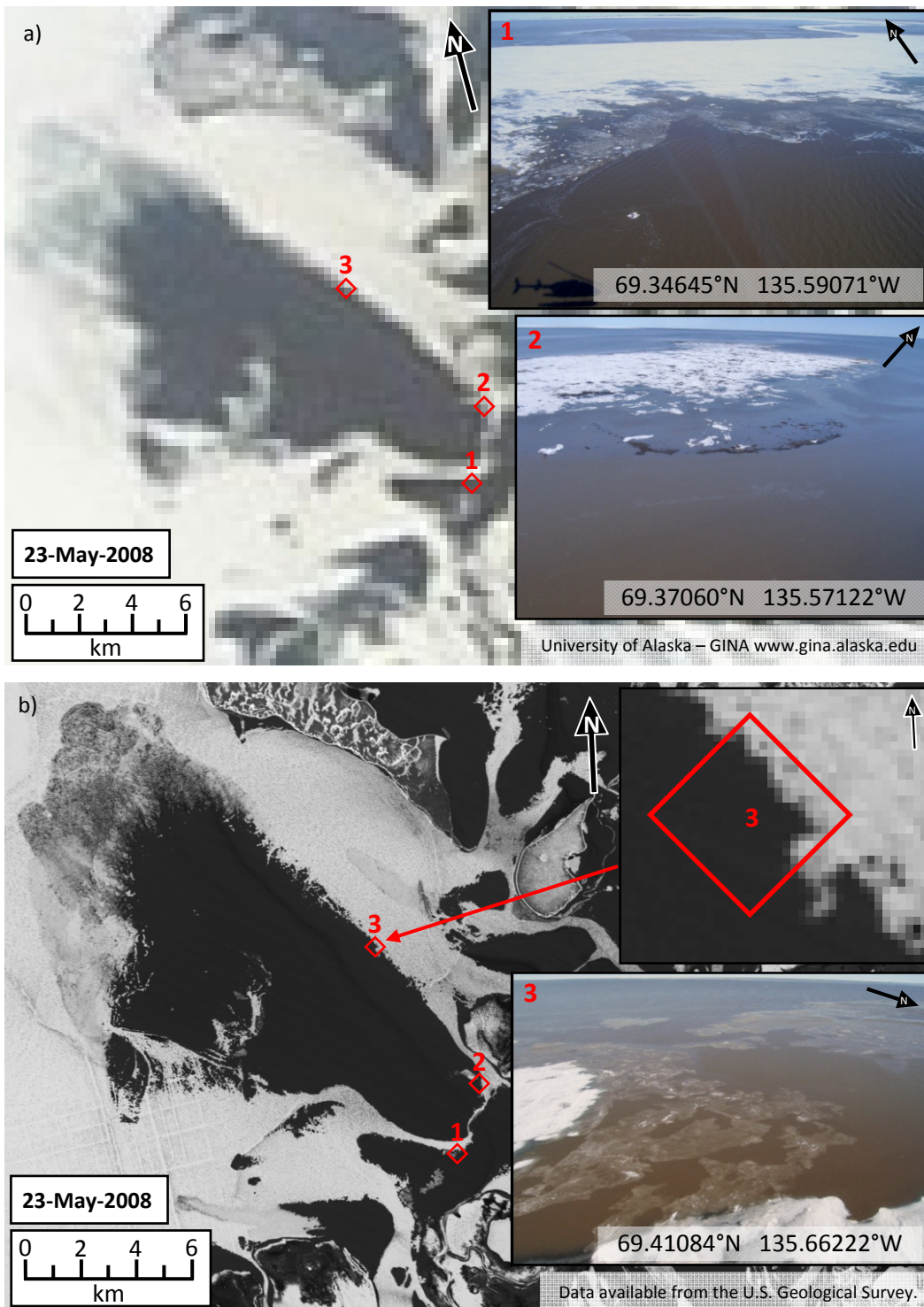
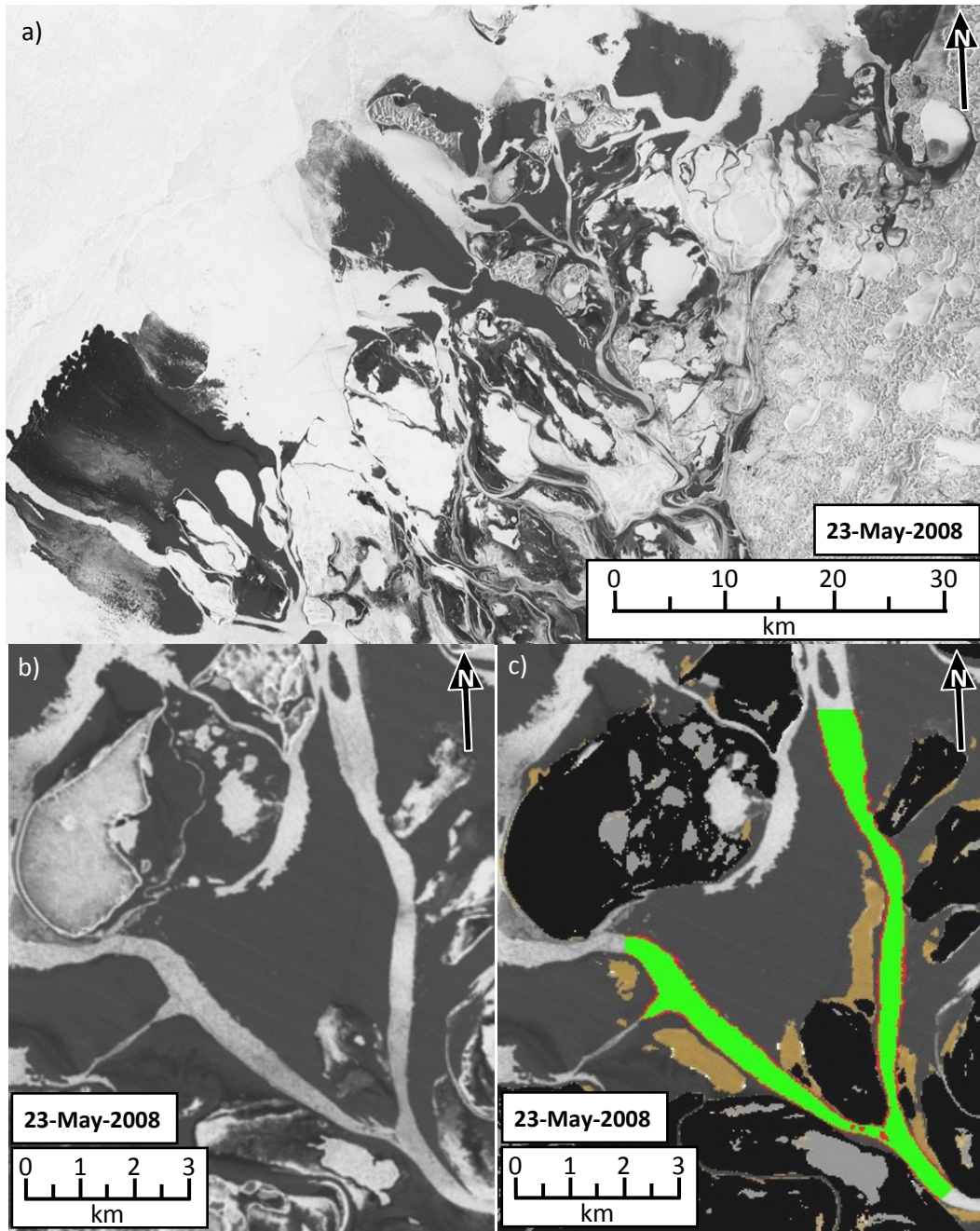
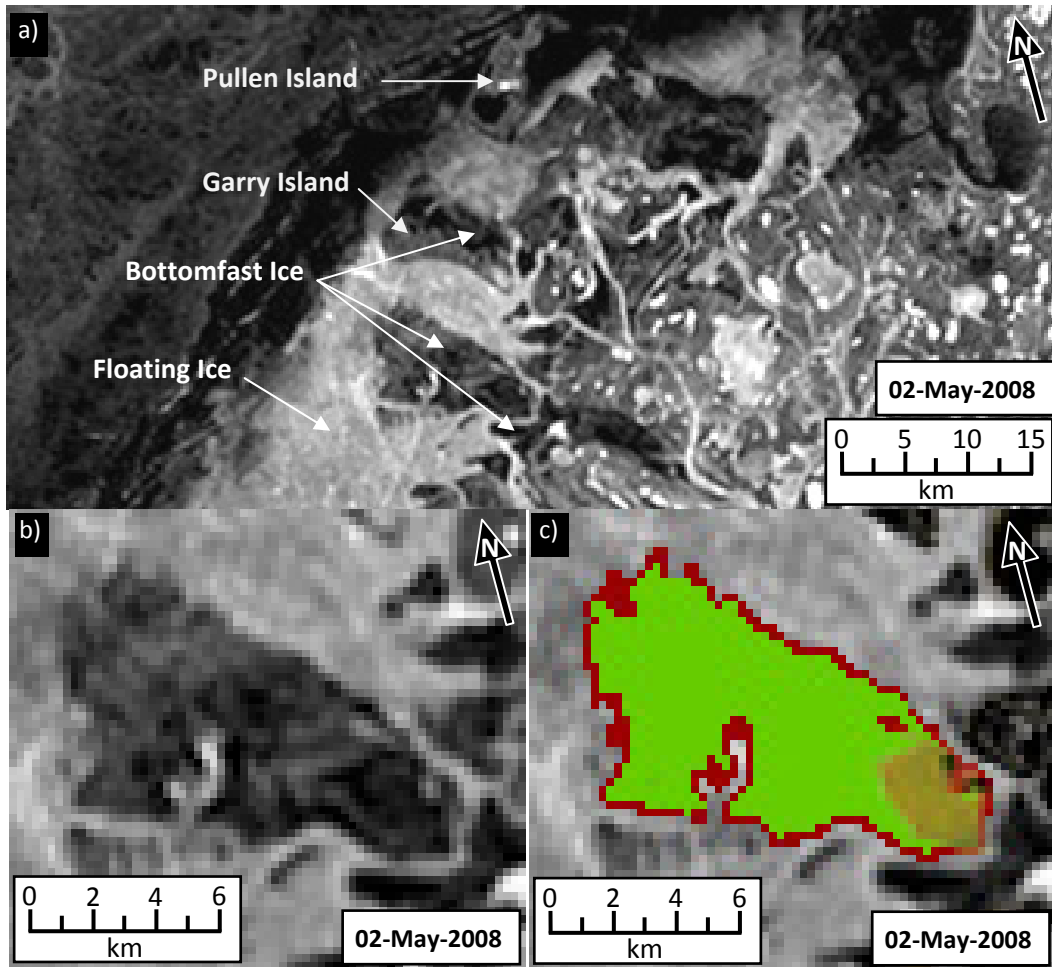


Figure 2-5 Overflow in the Mackenzie Outer Delta at the Middle Channel mouth / Garry Island region from a) MODIS instrument (spatial resolution of 500 m), b) Landsat 5 satellite (Band 4) (spatial resolution of 30 m) on 23-May-2008. The overflow is shown as a dark color. The three pictures on the right validate the existence and the location of the overflow observed from the satellite images.



Data available from the U.S. Geological Survey.

Figure 2-6 a) Landsat 5 satellite image (Band 4) of the northern portion of the Mackenzie Outer Delta on 23-May-2008. b) Landsat 5 satellite image (Band 4) of the Kendall Island region on 23-May-2008. c) Delineation of the channel floating ice with the land-water feature map overlay (accuracy of 60 m). The green delineation represents the minimum (conservative) delineation area from personal judgement of the floating channel ice boundaries and the combination of the red and green delineation represents the maximum (non-conservative) channel floating ice delineation area.



Envisat ASAR satellite image, courtesy of ESA – European Space Agency

Figure 2-7 a) Envisat ASAR image of the northern portion of the Mackenzie Outer Delta on 02-May-2008. b) Envisat ASAR image of the south of Garry Island region on 02-May-2008. c) Delineation of the bottomfast ice with the land-water feature map overlay (accuracy of 500 m). The green delineation represents the minimum (conservative) delineation area from personal judgement of the bottomfast ice boundaries and the combination of the red and green delineation represents the maximum (non-conservative) bottomfast ice delineation area.

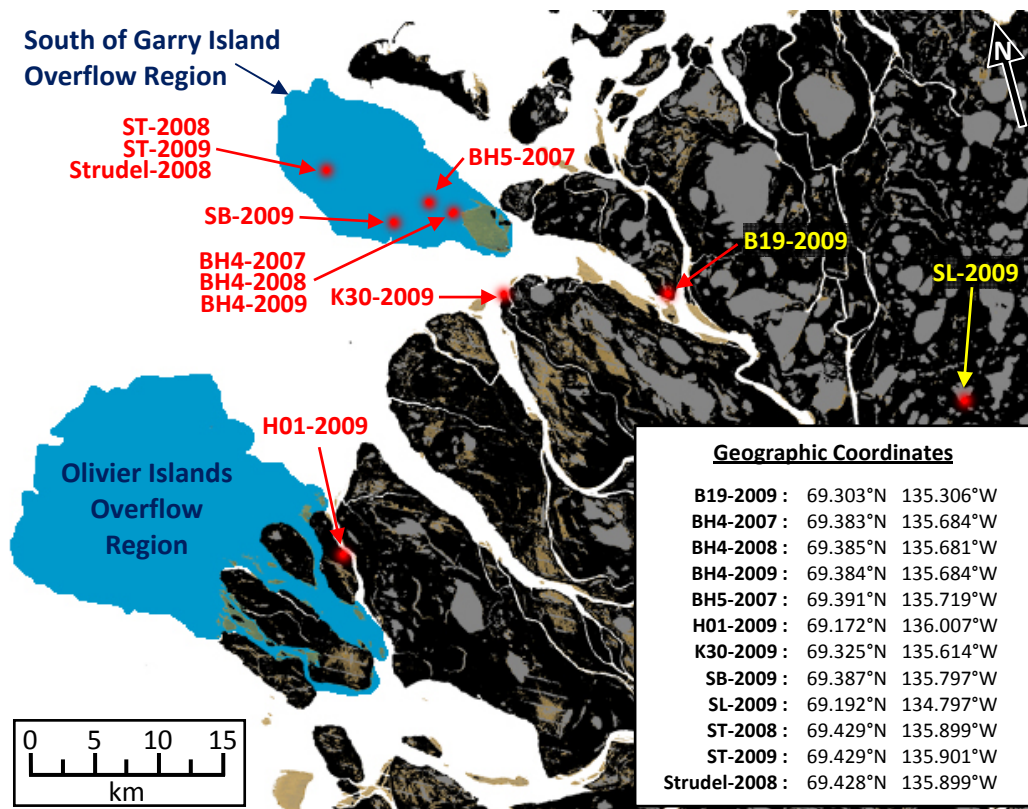


Figure 2-8 Approximate outline of the South of Garry Island and Olivier Islands overflow regions (blue), instrument location deployed during the 2008 and 2009 field investigations, and bed sediments sampling locations in the Mackenzie Outer Delta.

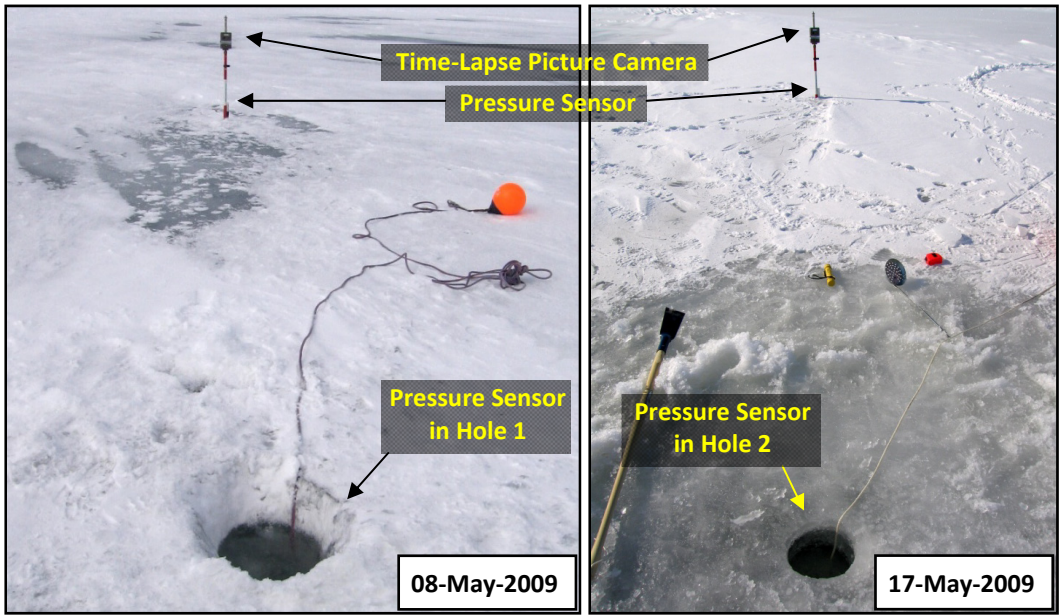


Figure 2-9 Time-lapse picture camera and depth sensors at ST-2009 in May 2009.

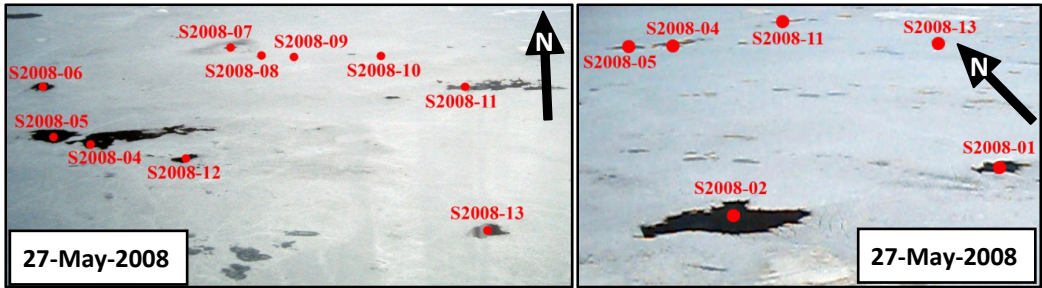


Figure 2-10 View from above of the strudel holes measured at ST-2008 in May 2008.

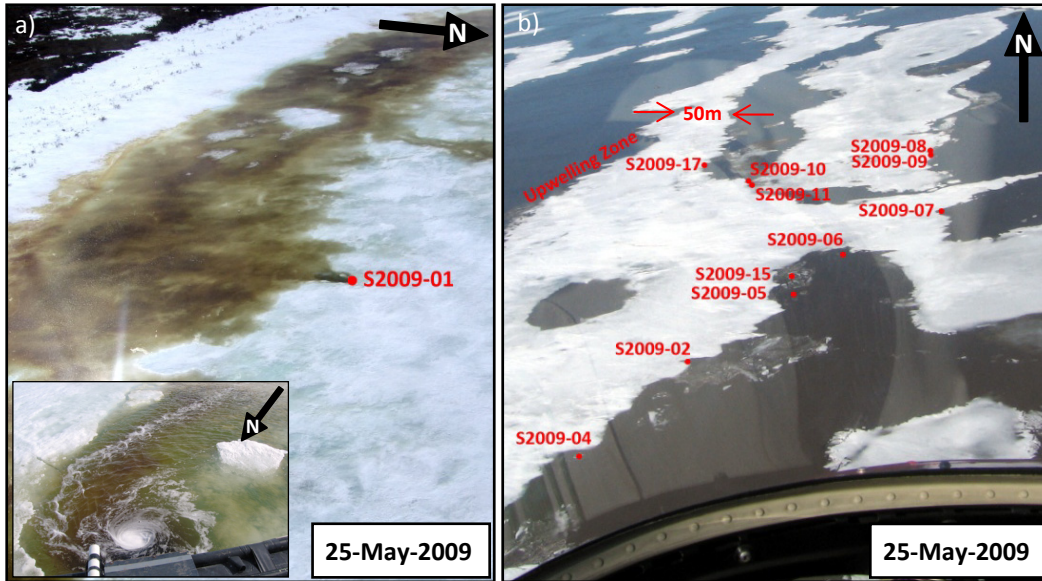


Figure 2-11 View from above of the strudel drains measured at a) SL-2009 (inset: close-up view of the S2009-01 strudel) and at b) SB-2009 in May 2009.

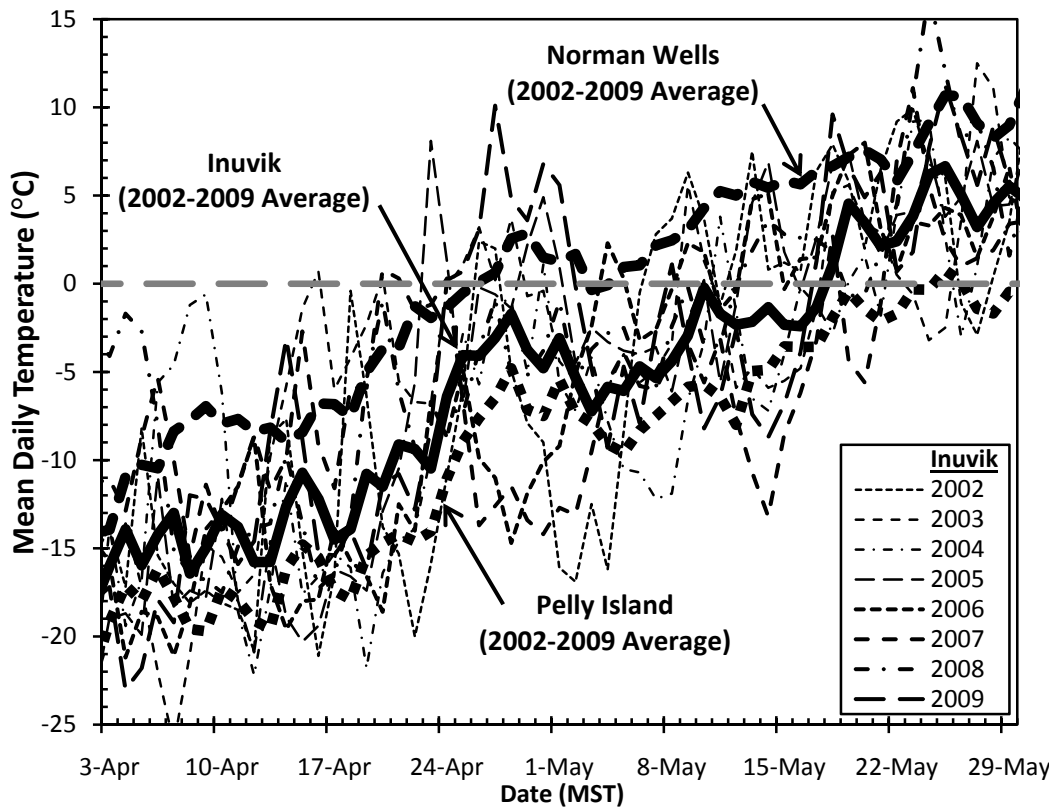


Figure 2-12 Mean daily temperature at the Inuvik climate station (ID 2202575), Norman Wells climate station (ID 2202800) and Pelly Island climate station (ID 2203095) in April and May from 2002 to 2009.

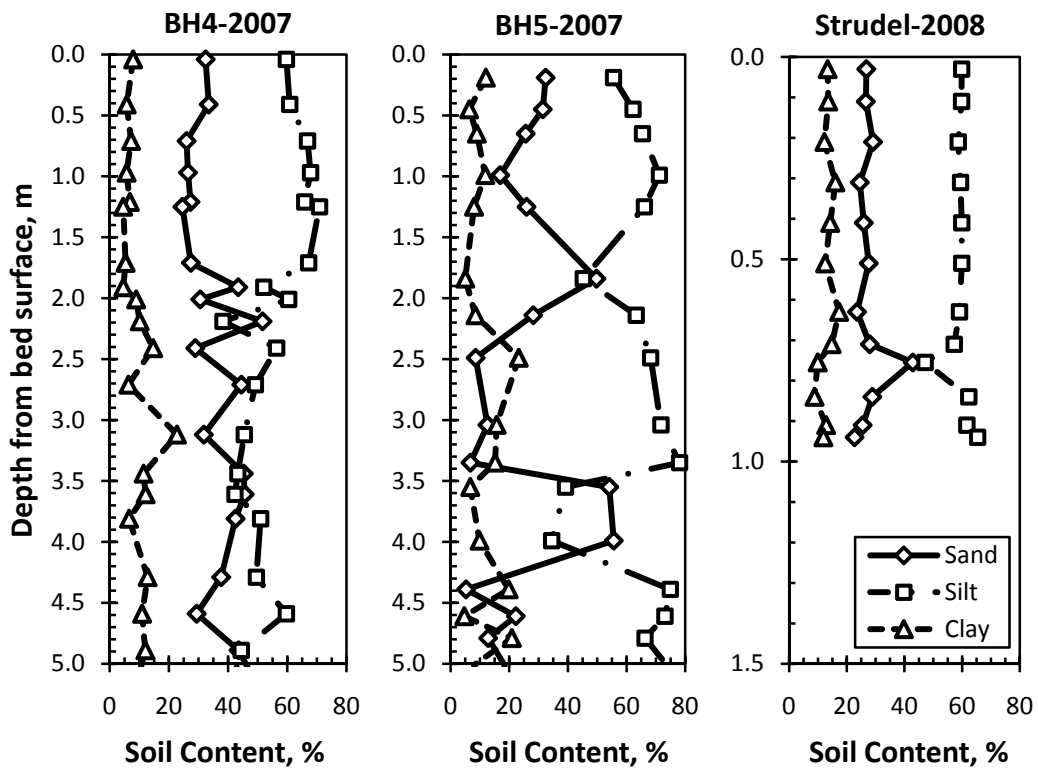


Figure 2-13 Soil content at various depths from the bed surface in the Mackenzie Outer Delta at the south of Garry Island overflow region at BH4-2007, BH5-2007, and Strudel-2008.

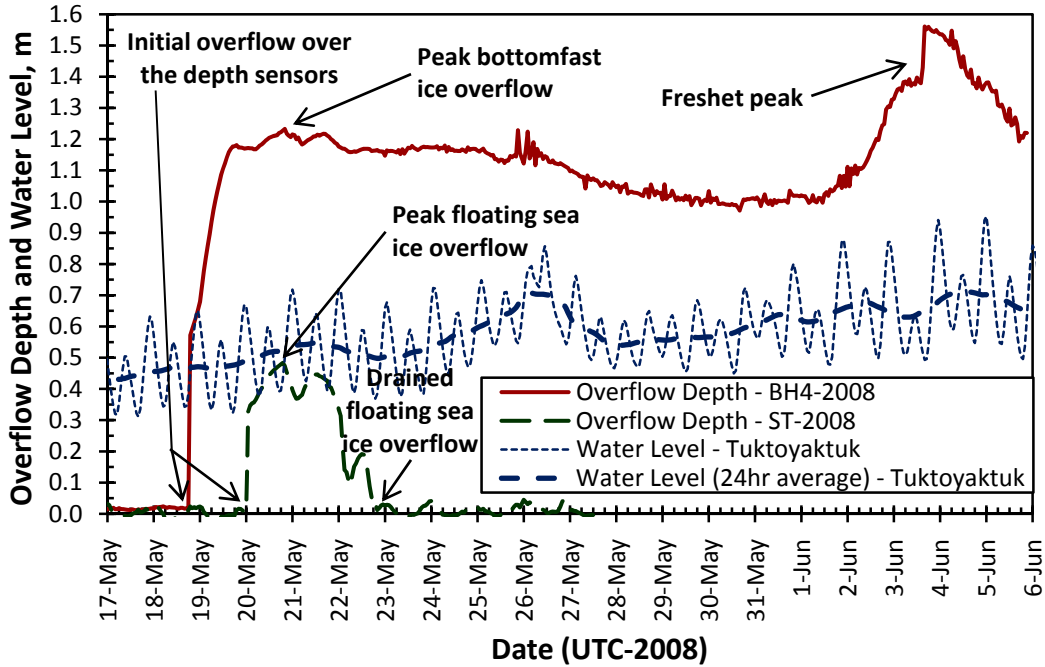


Figure 2-14 Ocean water level at Tuktoyaktuk and overflow depths at BH4-2008 and ST-2008 during breakup in 2008. The ocean water level and the overflow depths are not on a common datum.

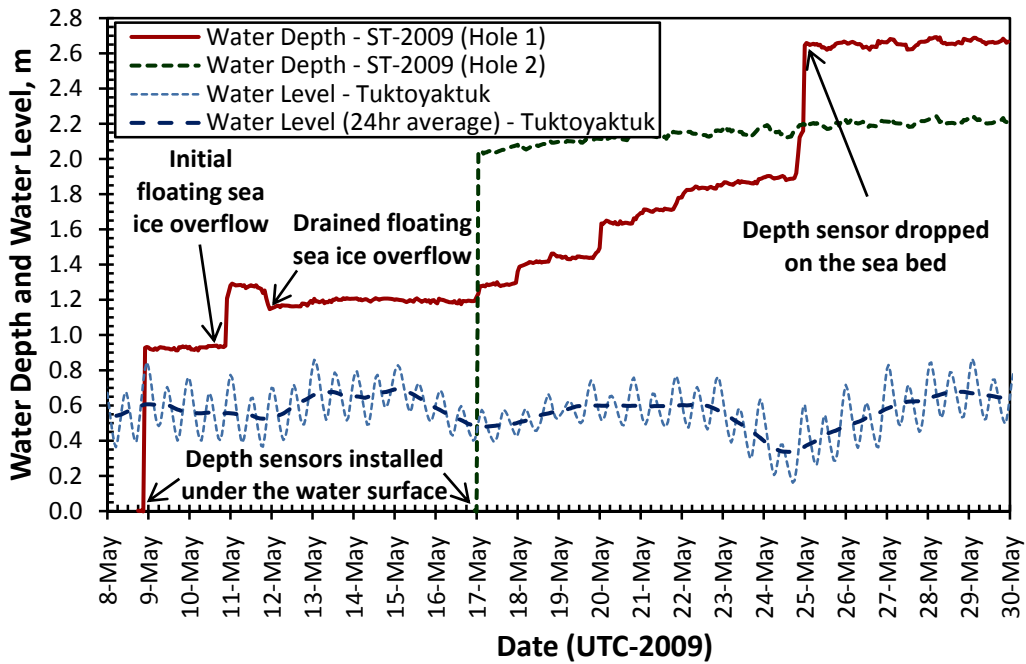


Figure 2-15 Ocean water level at Tuktoyaktuk, overflow depths and water depths at ST-2009 during breakup in 2009. The datum elevation of the depth sensor in Hole 1 is not fixed. The ocean water level and the water depths are not on a common datum.

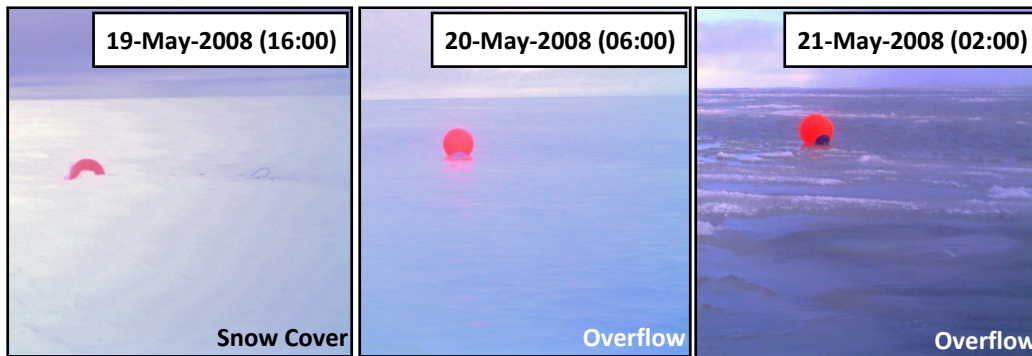


Figure 2-16 Pictures from the time-lapse camera at ST-2008 in May 2008 showing the variation in the floating sea ice overflow depth.

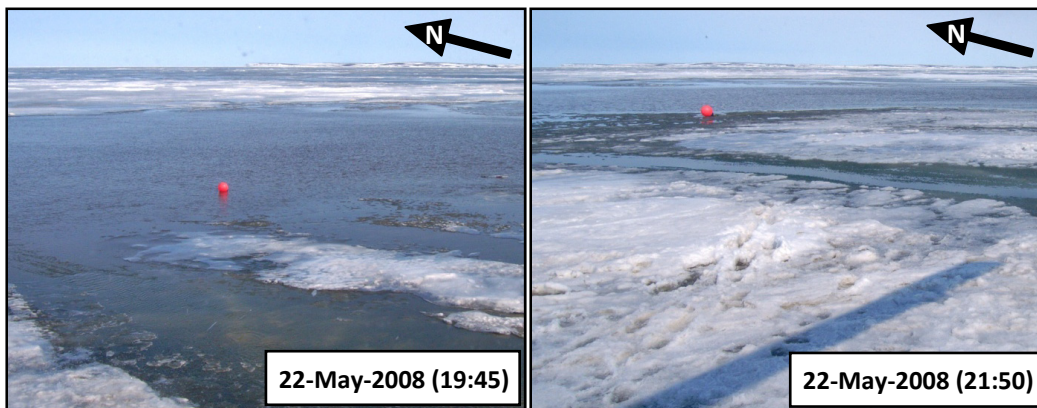
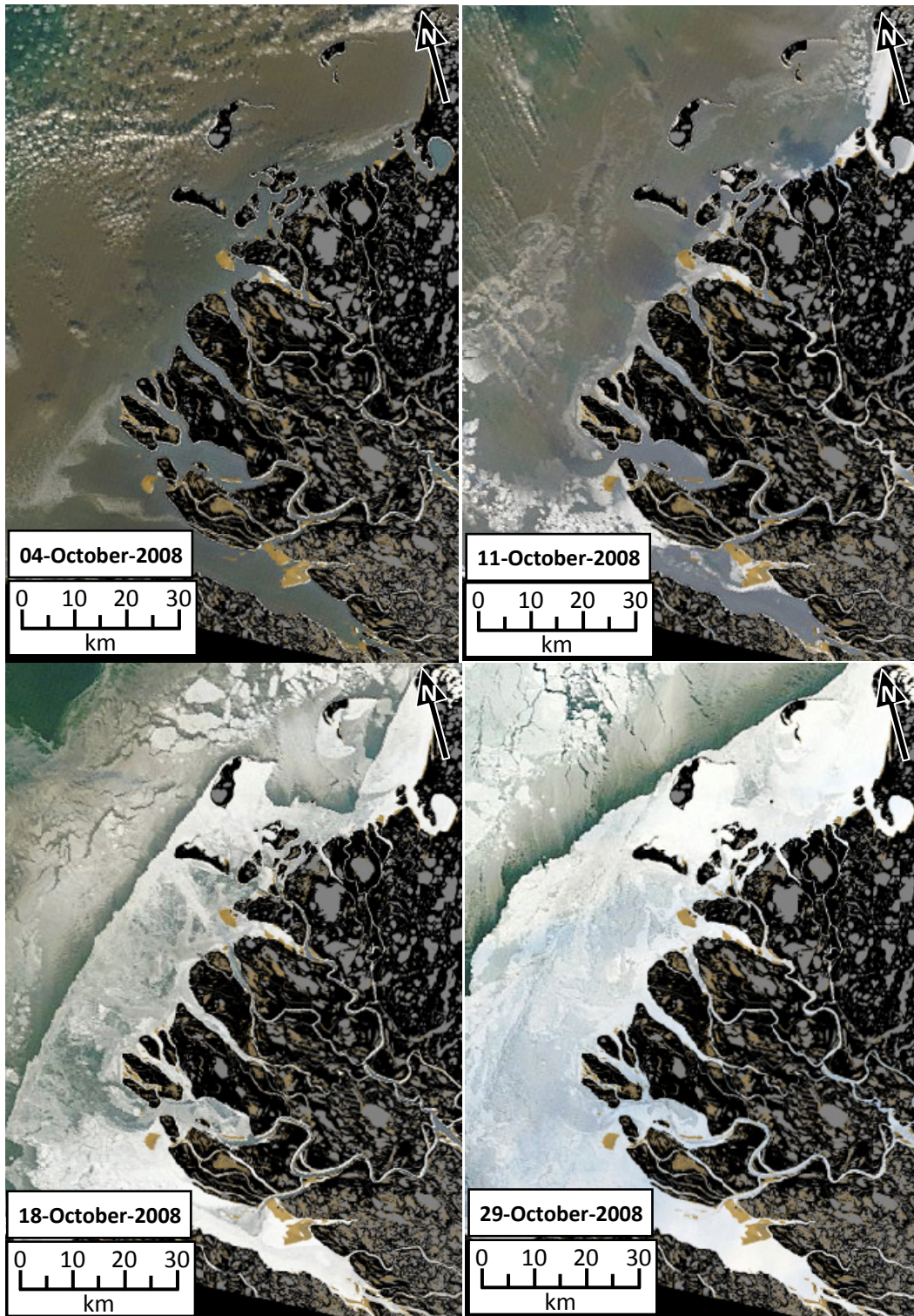


Figure 2-17 Pictures from the time-lapse camera at ST-2008 showing the variation in the floating sea ice overflow depth on 22-May-2008. The buoy is at the same location in both pictures.



Figure 2-18 Pictures from the time-lapse camera at ST-2009 in May 2009 showing the variation in the floating sea ice overflow depth.



University of Alaska – GINA www.gina.alaska.edu

Figure 2-19 MODIS images, with the land-water feature map overlay, showing the progression of the nearshore ice freeze-up in the Mackenzie Outer Delta in October 2008.

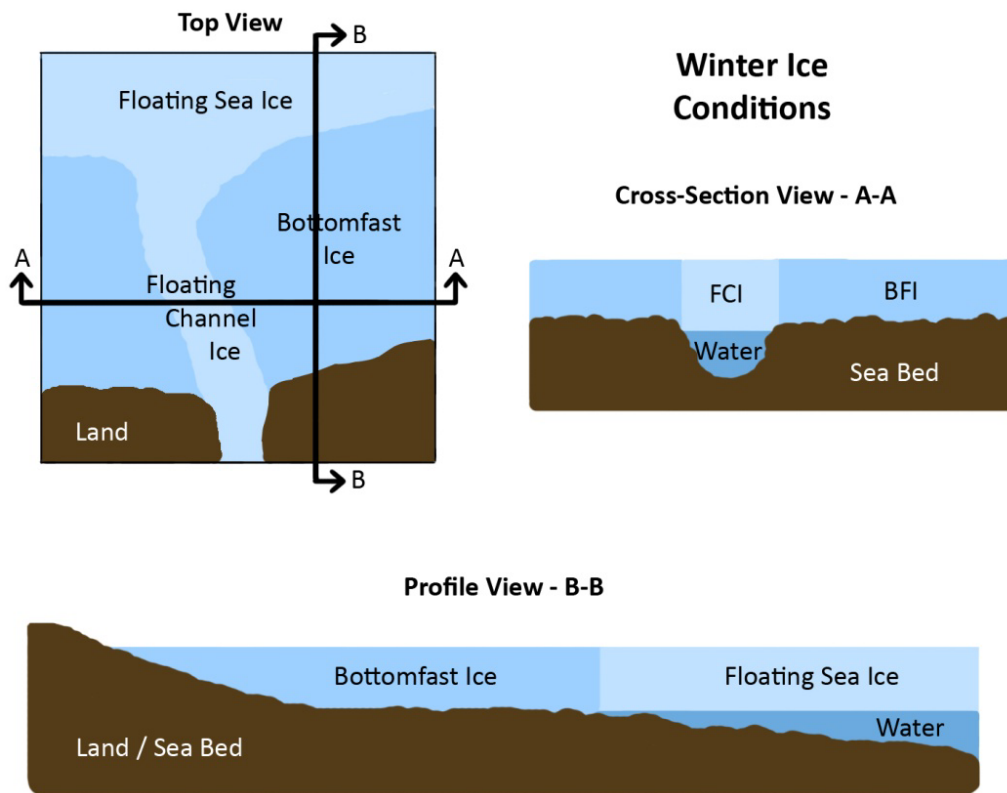
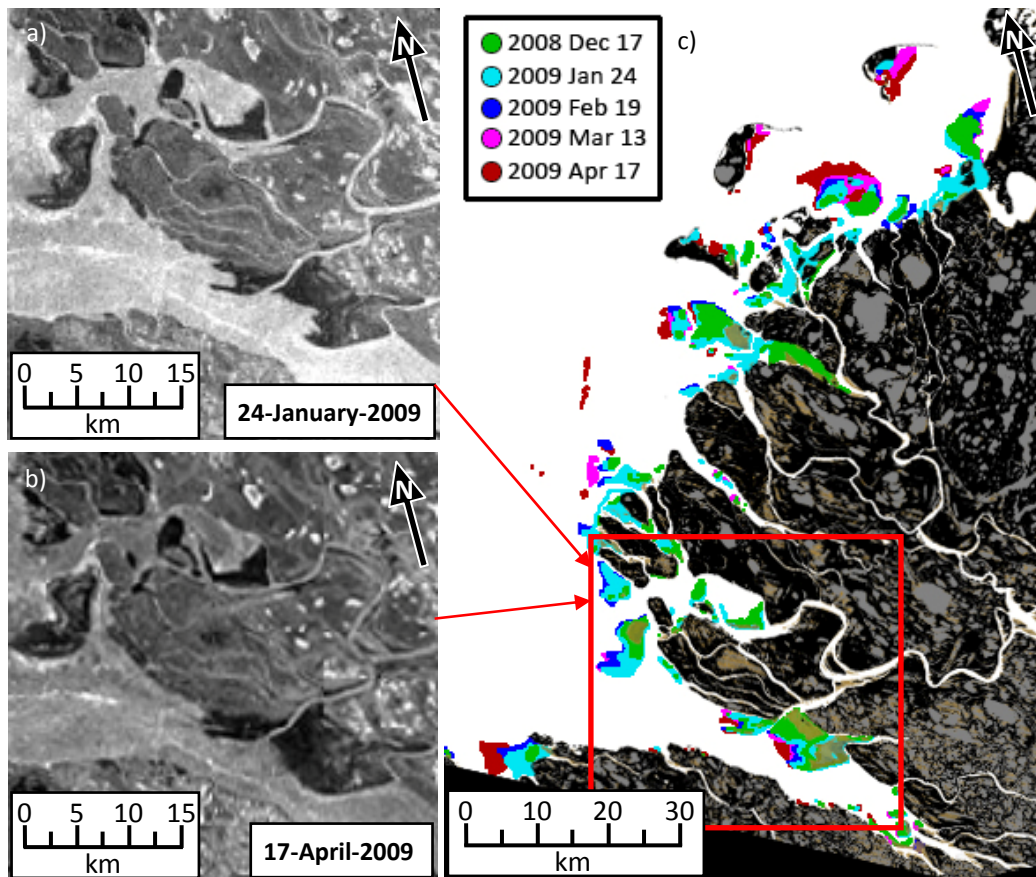


Figure 2-20 Top view, cross-sectional view and profile view of the winter ice condition in the Mackenzie Outer Delta.



Envisat ASAR satellite images
courtesy of ESA – European Space Agency

Figure 2-21 a) January 2008, and b) April 2009 Envisat ASAR images of the Mackenzie Outer Delta at the Shallow Bay at Reindeer Channel Mouth showing the bottomfast ice location (darker on the images). c) Chronological growth of the bottomfast ice during the 2008-2009 winter season, delineated from Envisat ASAR satellite images (accuracy of 500 m).

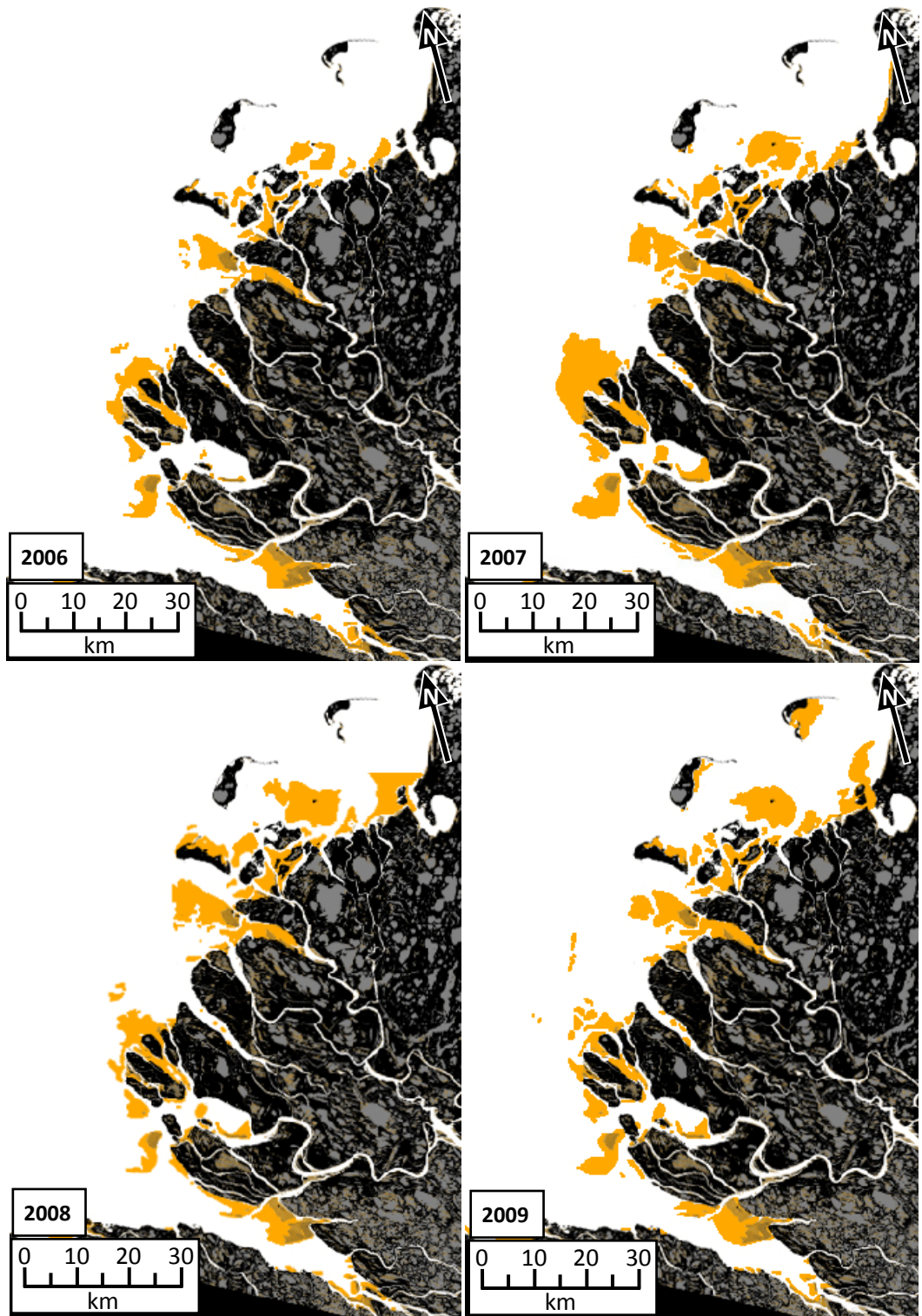


Figure 2-22 Maximum extent of the bottomfast ice in the Mackenzie Outer Delta (orange) from 2006 to 2009 delineated from Envisat ASAR satellite images (accuracy of 500 m).

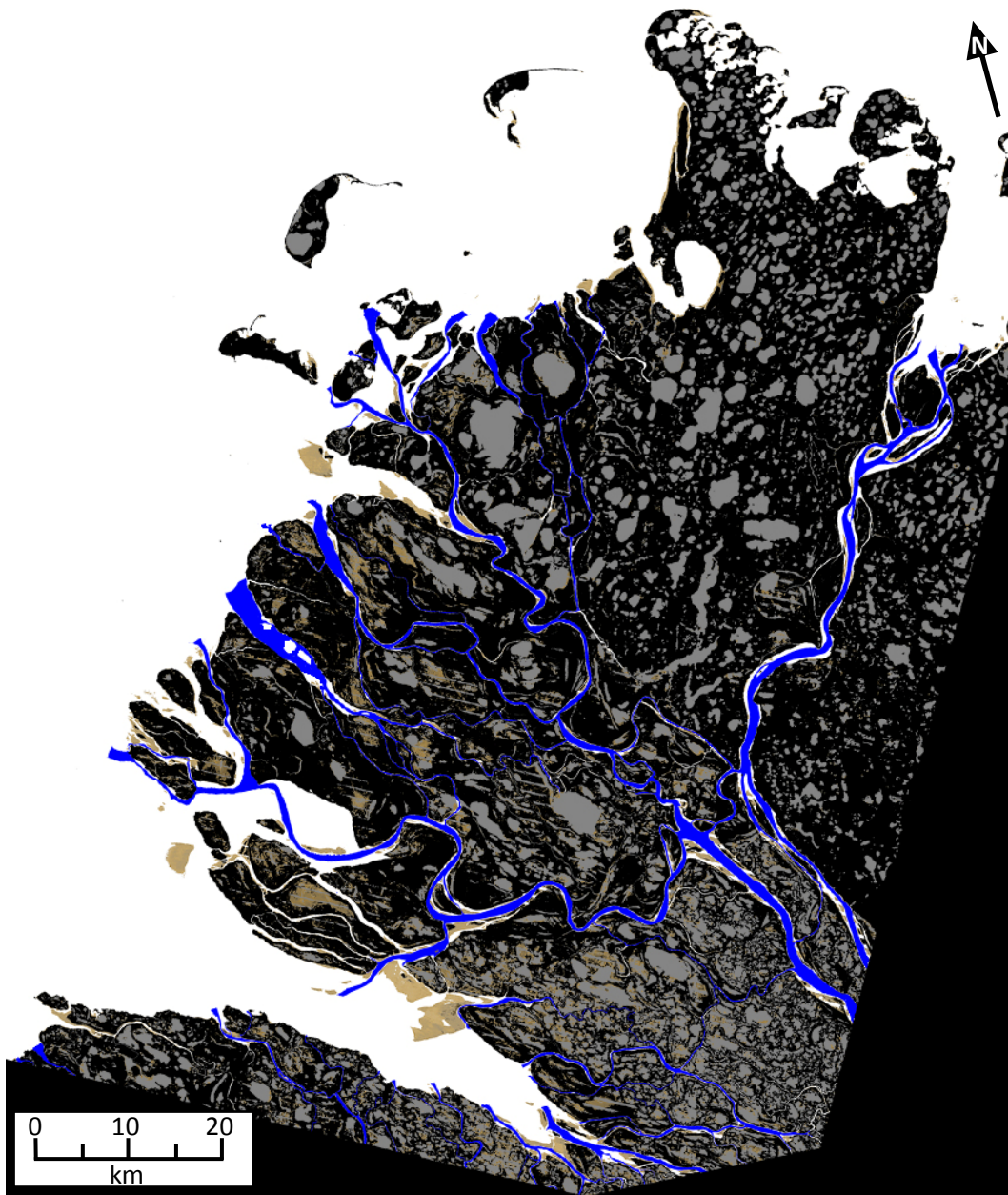


Figure 2-23 Delineation of the floating channel ice location (blue) in 2008 and 2009 in the Mackenzie Outer Delta, defined from near-infrared (Band 4) Landsat images (accuracy of 60 m).

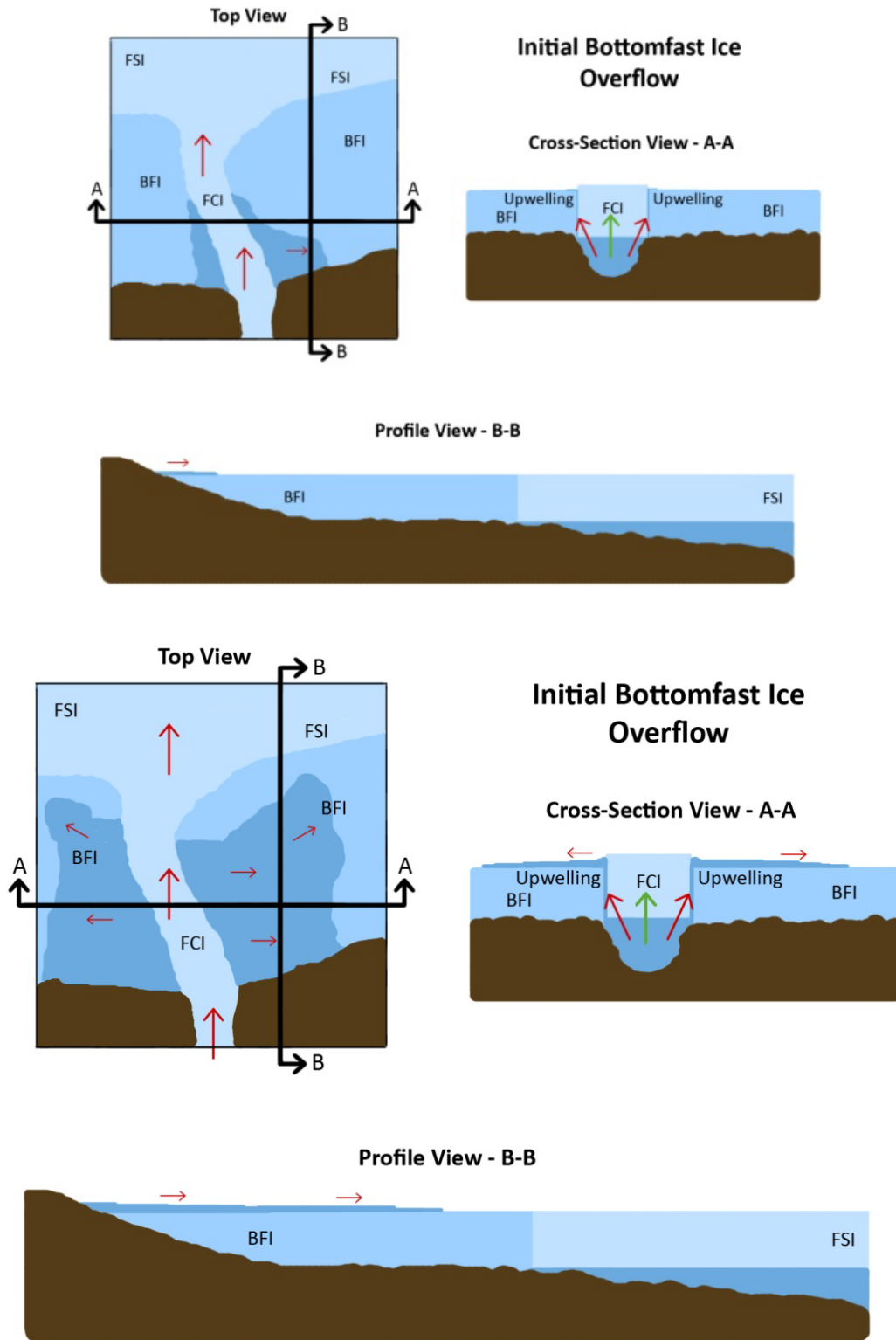


Figure 2-24 Top view, cross-sectional view and profile view of the initiation of the bottomfast ice overflow in the Mackenzie Outer Delta. The red arrows indicate the flow direction and the green arrow indicate the vertical ice movement direction.

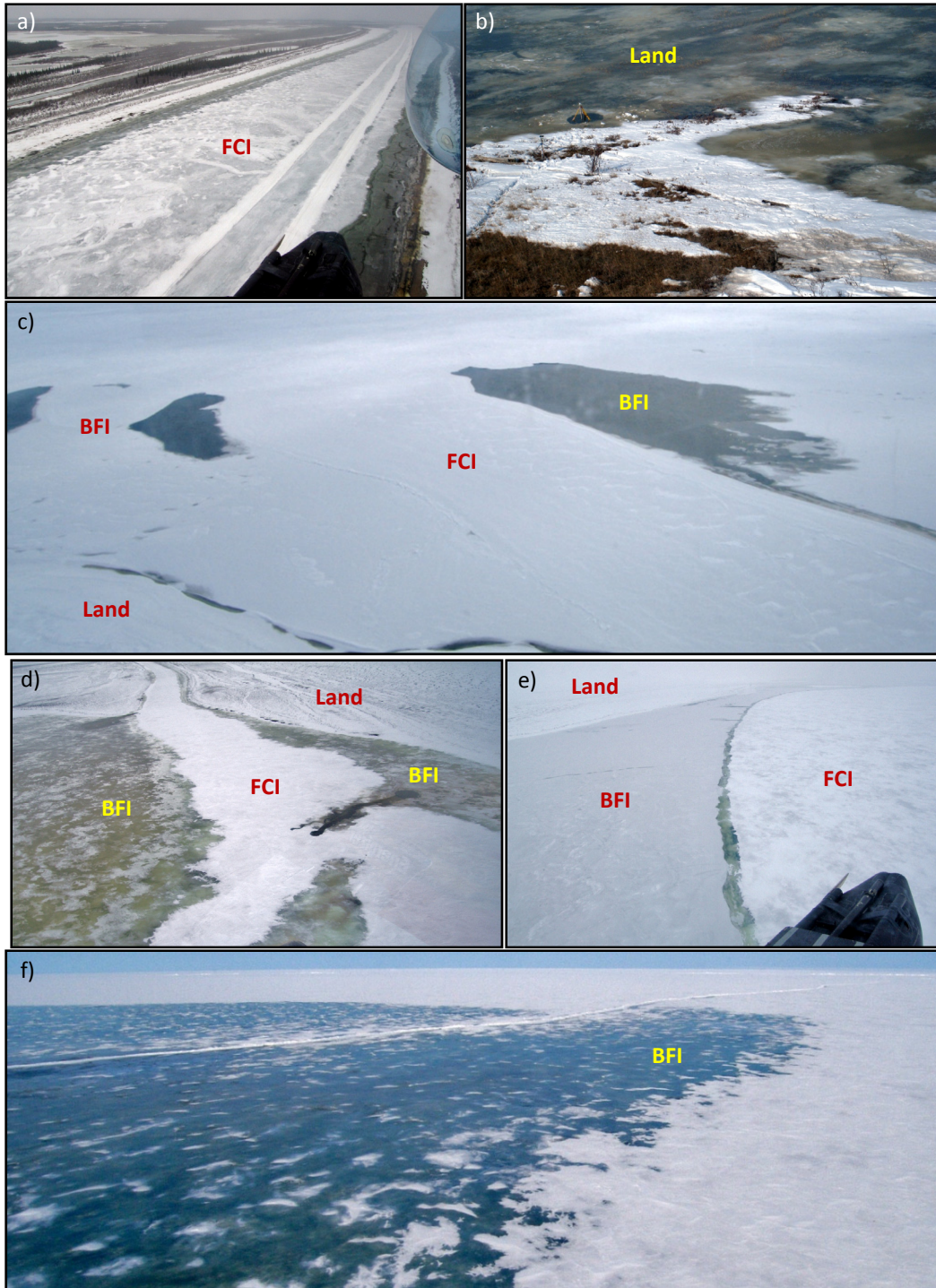
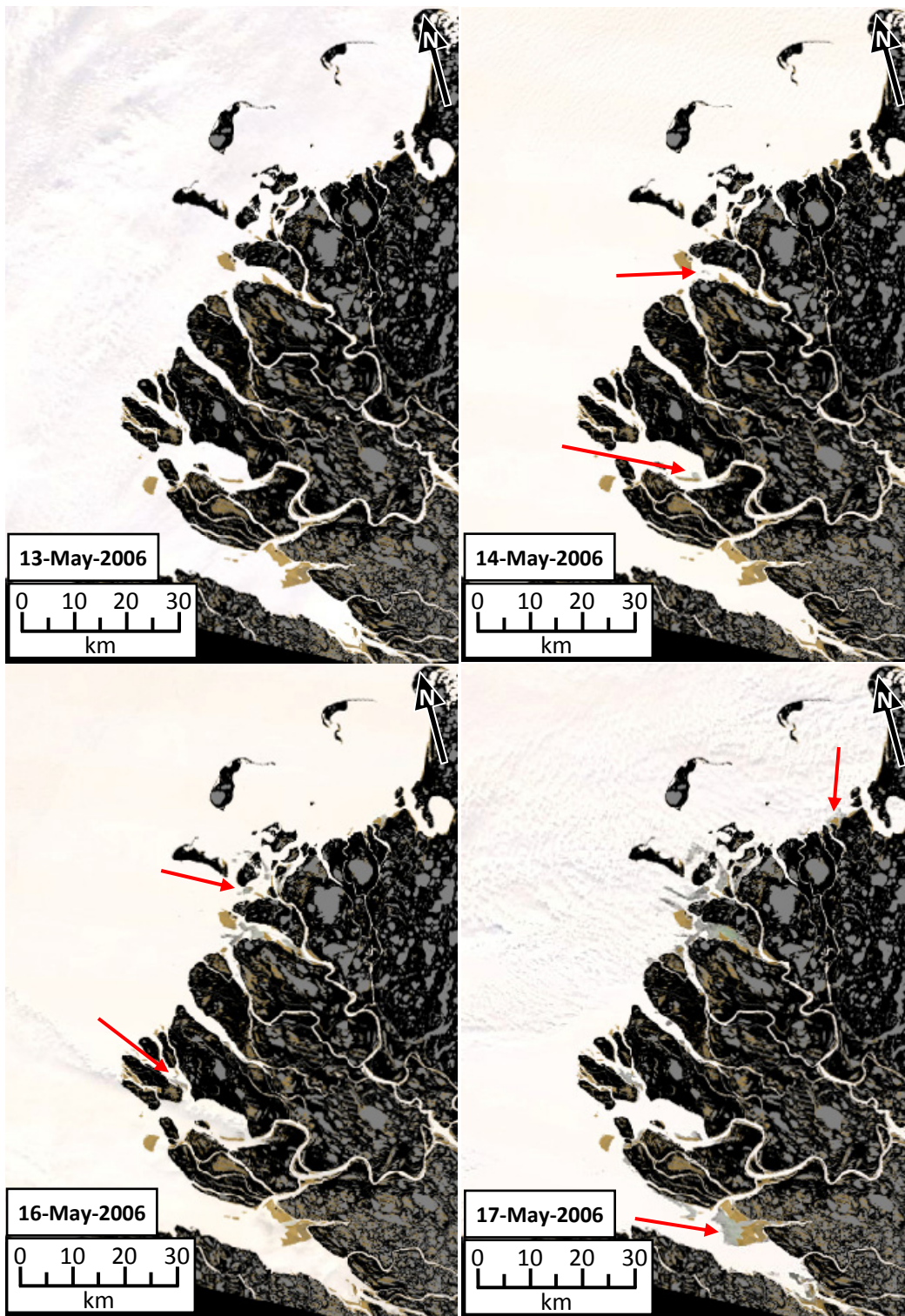


Figure 2-25 a) Border ice and land overflow on the delta's channel's border. b) Land overflow in the outer delta. c) Flooding of the bottomfast ice surface (BFI) at the interface with the floating channel ice (FCI). d) Shallow overflow depth on the bottomfast ice surface. e) Frozen overflow on the bottomfast ice surface. f) Overflow spreading on the bottomfast ice surface.



University of Alaska – GINA www.gina.alaska.edu

Figure 2-26 MODIS images, with the land-water feature map overlay, illustrating the initial overflow on bottomfast ice in the Mackenzie Outer Delta in May 2006. The arrows indicate the first bottomfast ice overflow locations at different regions and on different dates.

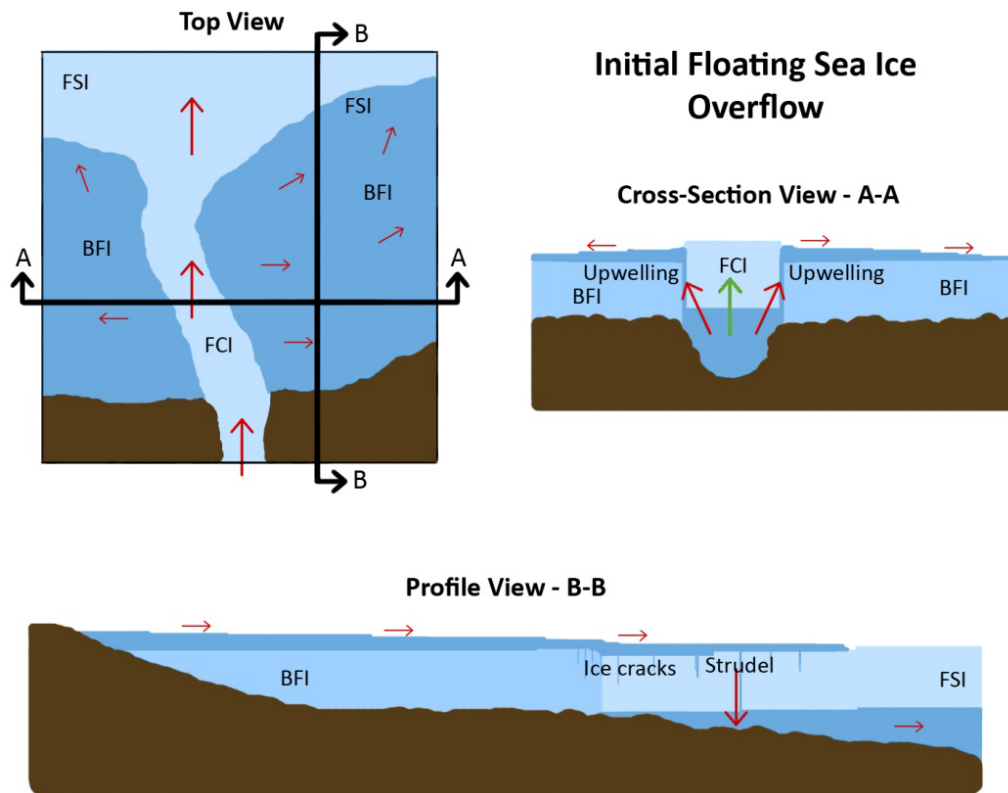


Figure 2-27 Top view, cross-sectional view and profile view of the initiation of the floating sea ice overflow in the Mackenzie Outer Delta. The red arrows indicate the flow direction and the green arrow indicate the vertical ice movement direction.

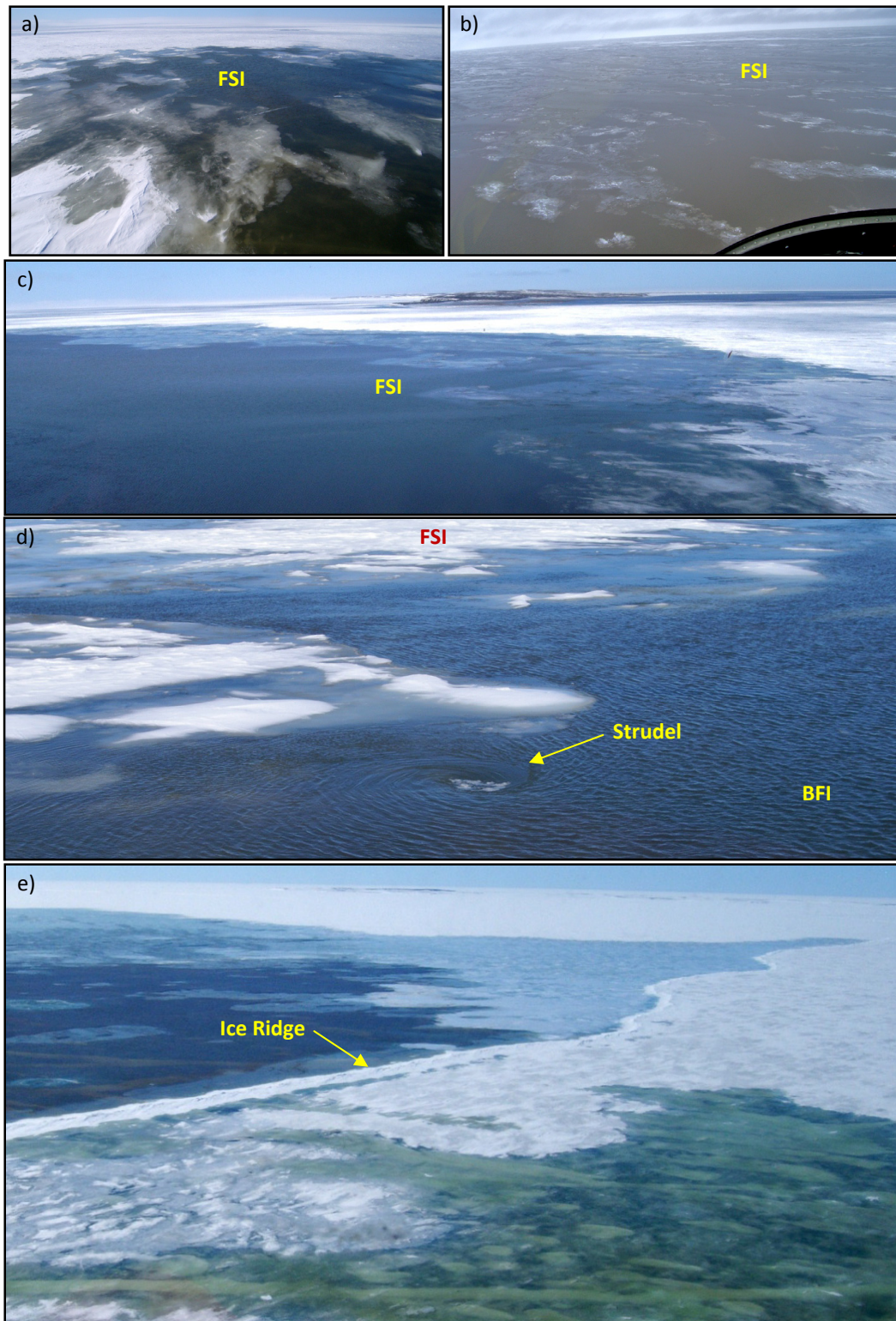


Figure 2-28 a, b & c) Overflow on the floating sea ice surface (FSI). d) Overflow draining through a strudel at the boundary between the bottomfast ice (BFI) and the floating sea ice. e) Ice ridge acting as an overflow barriers.

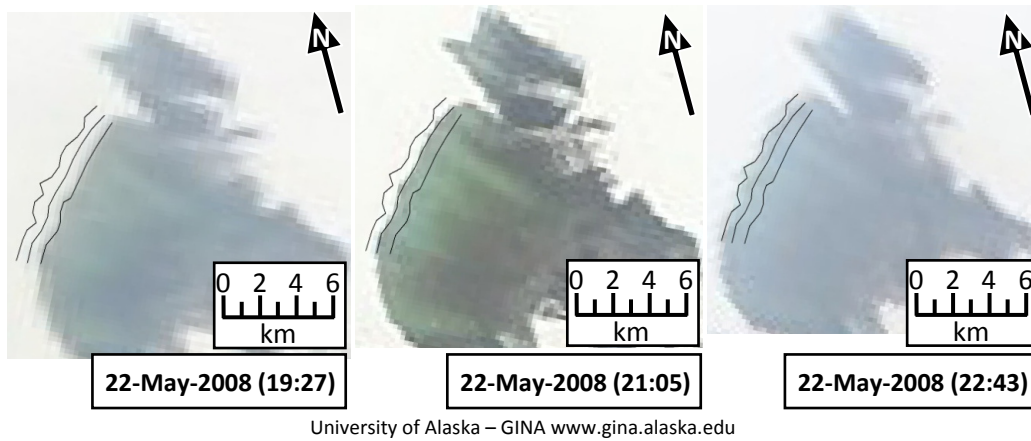


Figure 2-29 MODIS images of the overflow expansion northwest of Olivier Islands in the Mackenzie Outer Delta on 22-May-2008. The distance between the lines averages 680 m.

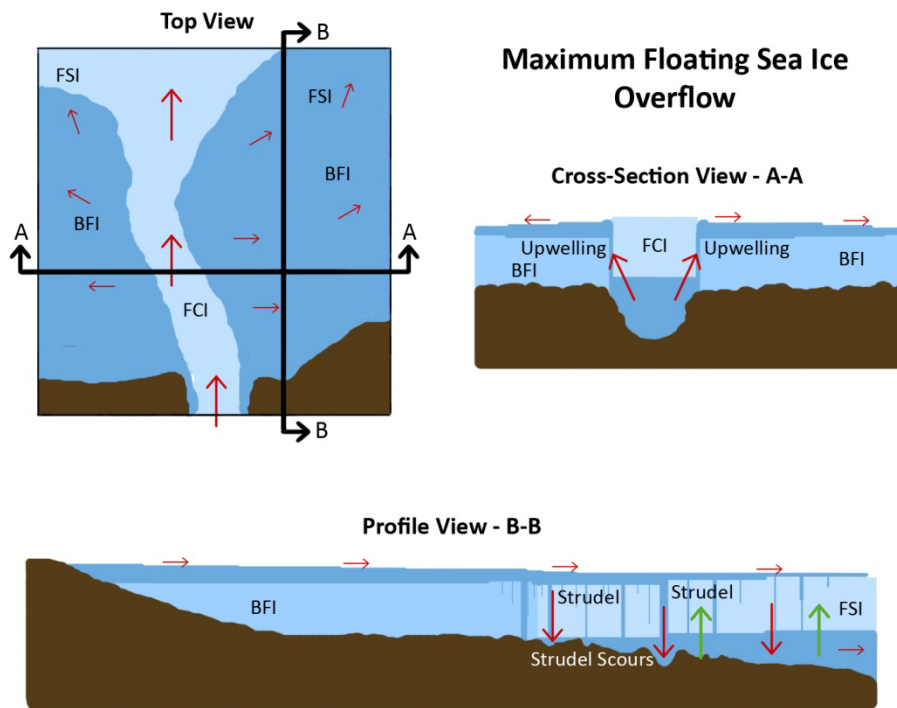
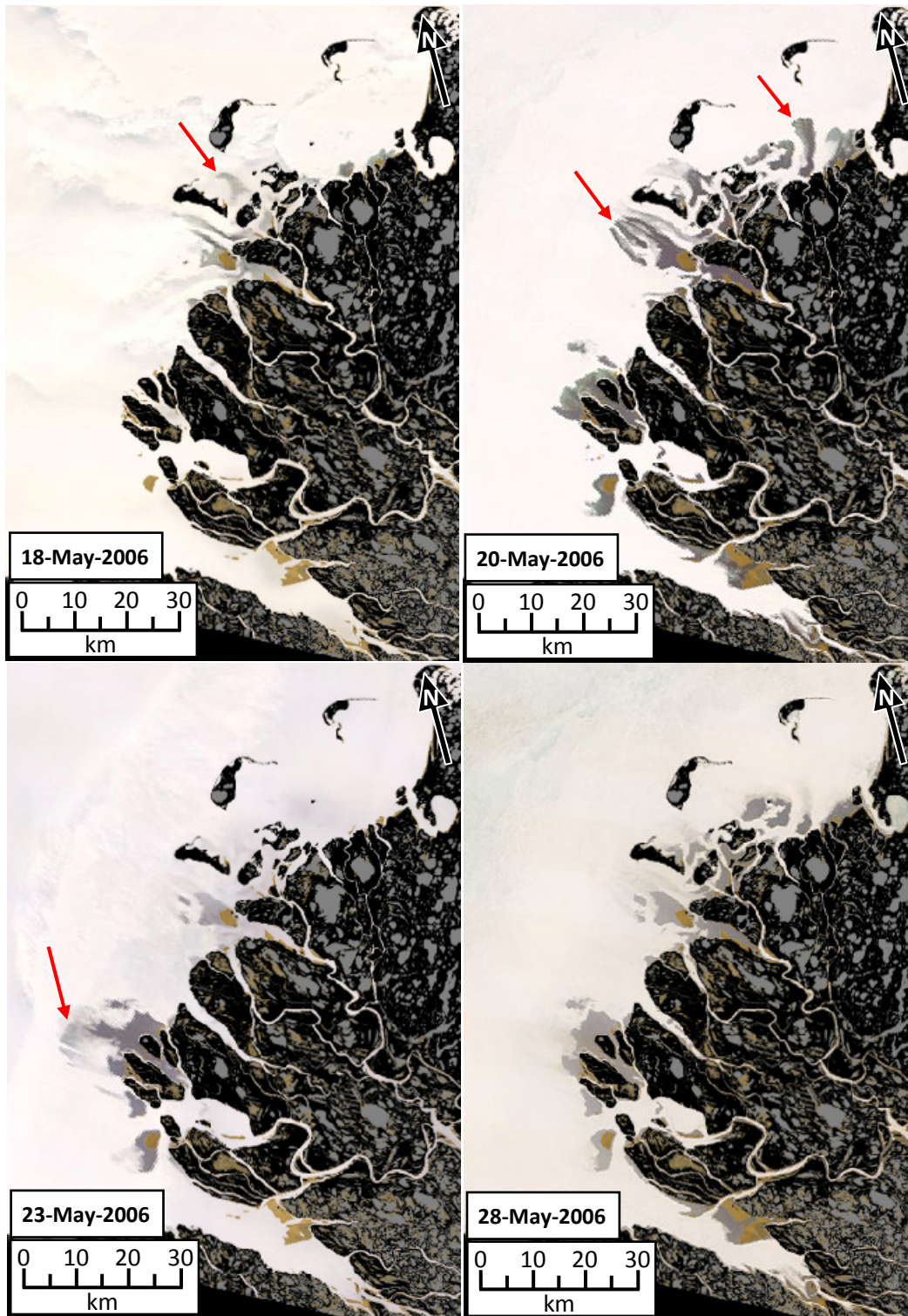


Figure 2-30 Top view, cross-sectional view and profile view of the maximum floating sea ice overflow in the Mackenzie Outer Delta. The red arrows indicate the flow direction and the green arrows indicate the vertical ice movement direction.



University of Alaska – GINA www.gina.alaska.edu

Figure 2-31 MODIS images, with the land-water feature map overlay, showing the flooding and the drainage of the floating sea ice overflow in the Mackenzie Outer Delta in May 2006. The arrows indicate the maximum overflow extent at different outer delta regions and on different dates.

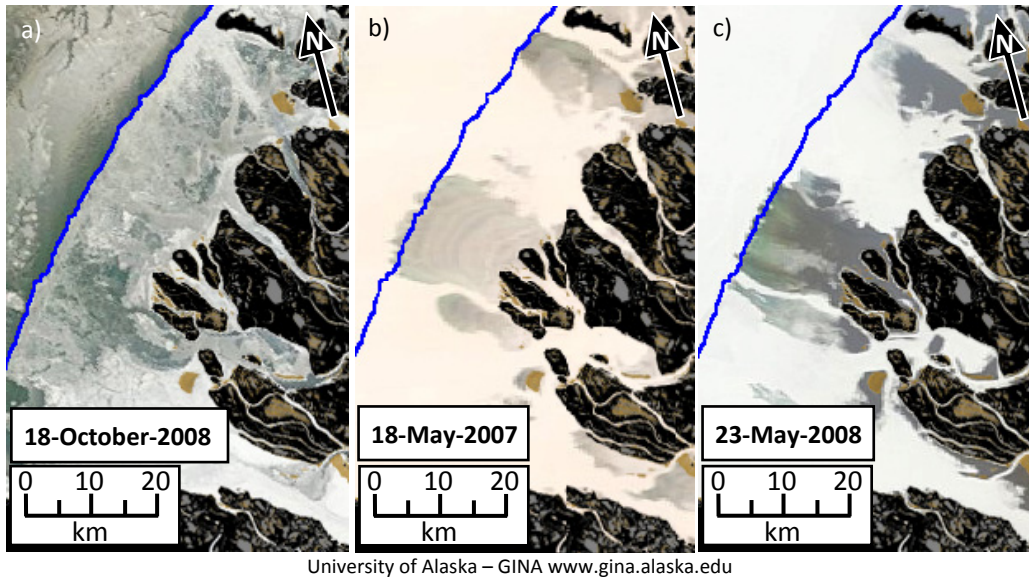


Figure 2-32 a) MODIS image of freeze-up, with the land-water feature map overlay, on 18-October-2008. b) Maximum floating sea ice overflow distance on 18-May-2007. c) Maximum floating sea ice overflow distance on 23-May-2008. The blue line refers to the freeze-up nearshore ice boundary of 18-October-2008 (accuracy of 500 m).

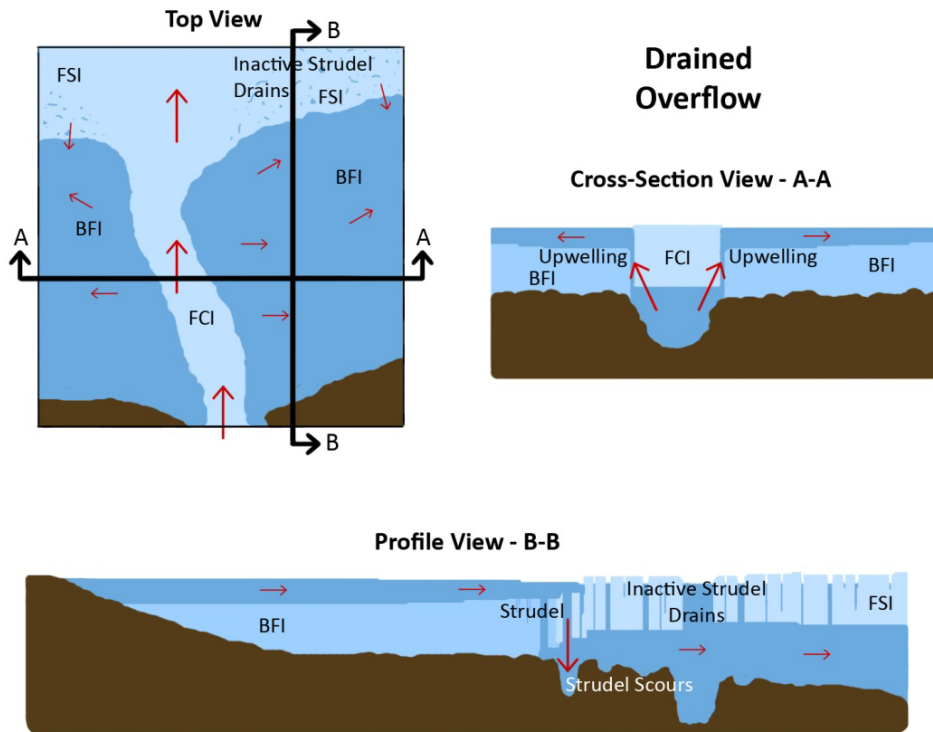
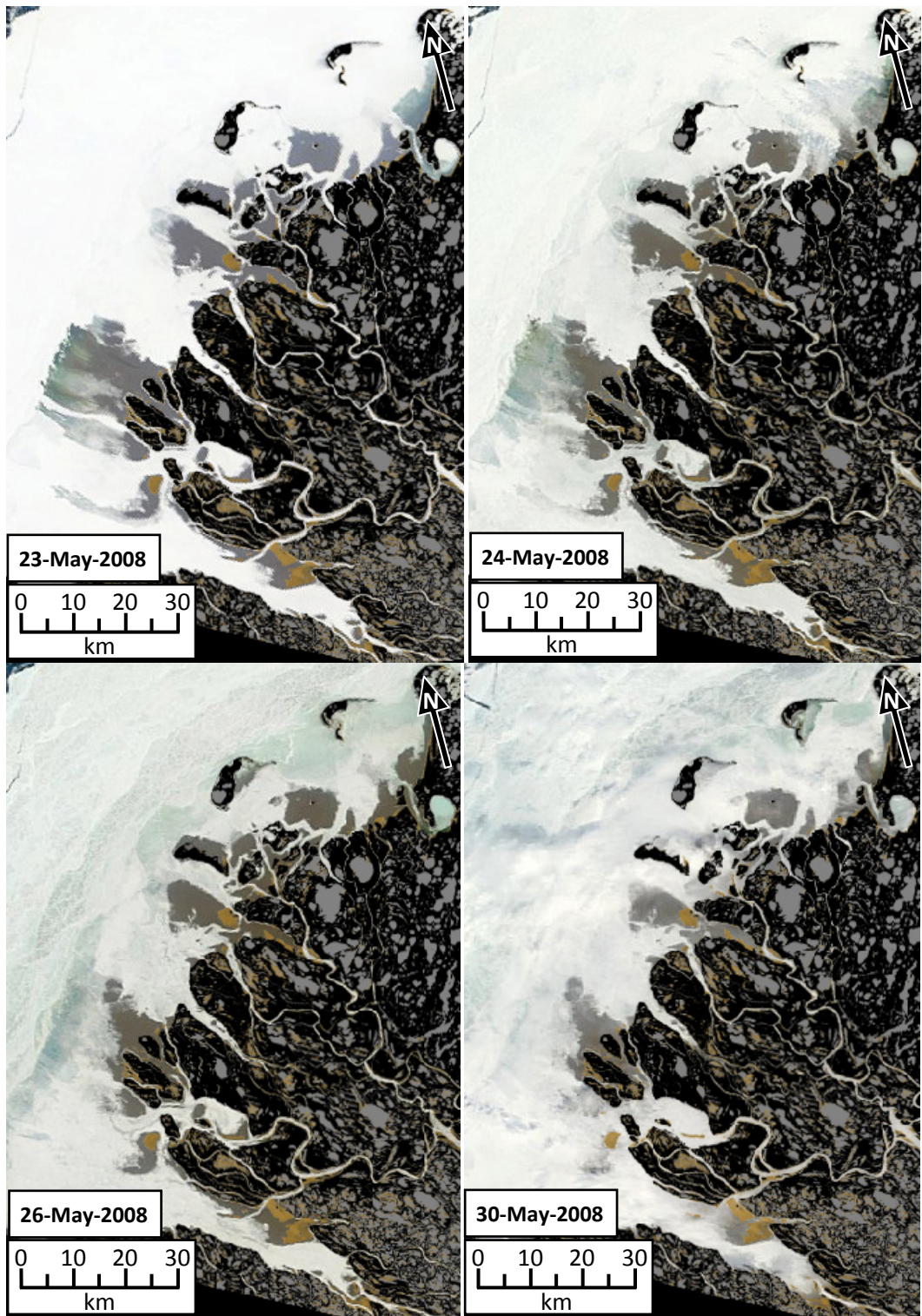


Figure 2-33 Top view, cross-sectional view and profile view of the drained floating sea ice overflow in the Mackenzie Outer Delta. The red arrows indicate the flow direction.



University of Alaska – GINA www.gina.alaska.edu

Figure 2-34 MODIS images, with the land-water feature map overlay, showing the drained floating sea ice overflow in the Mackenzie Outer Delta in May 2008.

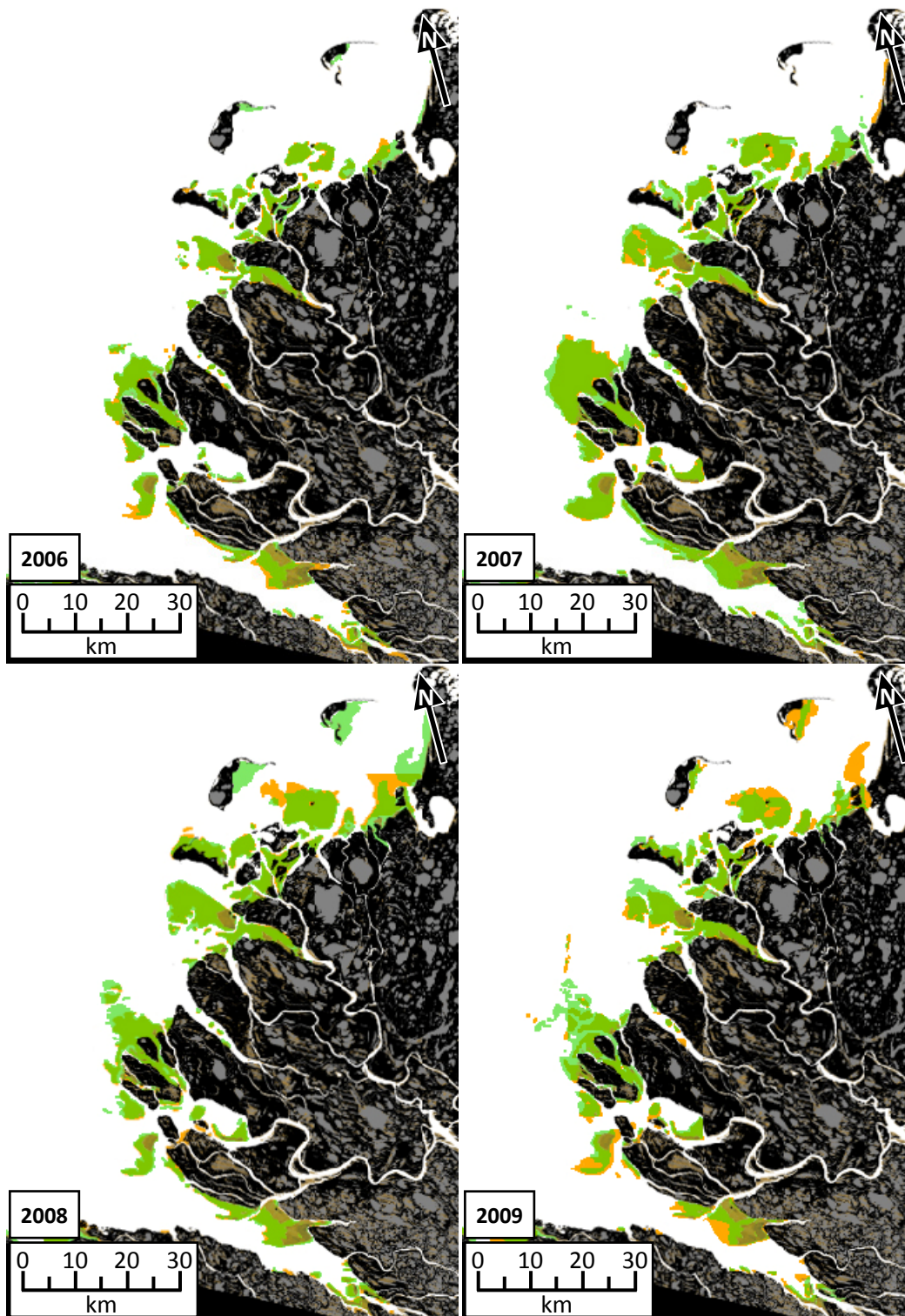


Figure 2-35 Overlay of the overflow area after the floating sea ice surface drained (green), defined from visible band MODIS images, over the bottomfast ice (orange) areas, defined from the Envisat ASAR images, in the Mackenzie Outer Delta from 2006 to 2009 (accuracy of 500 km).

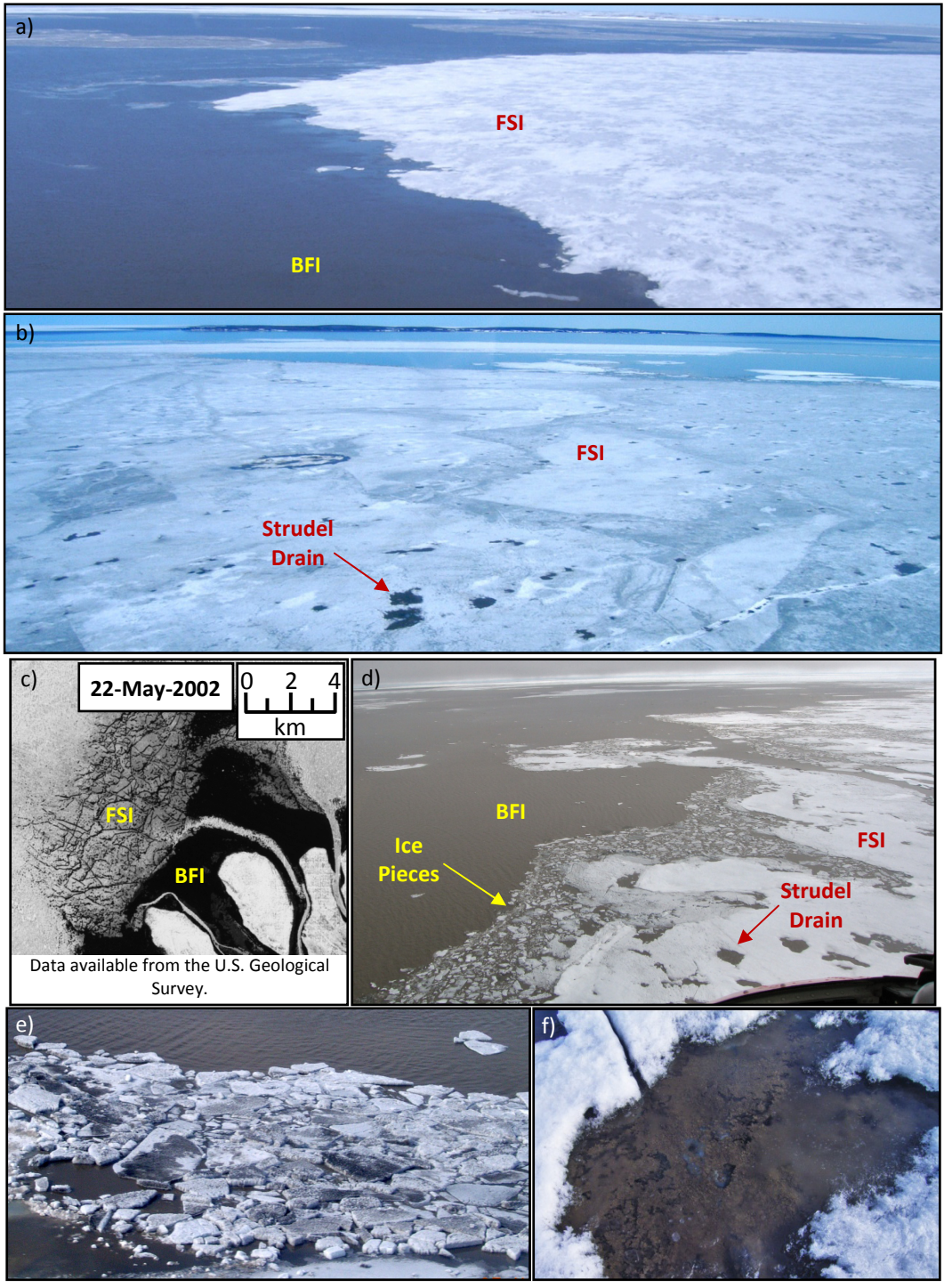


Figure 2-36 a) Interface of the bottomfast ice (BFI) and of the non-flooded floating sea ice (FSI). b) Strudel drains in the shape of holes and cracks through the floating sea ice cover. c) Landsat 7 satellite image (Band 4) showing cracks in the floating sea ice cover north of Olivier Islands. d) Interface between the bottomfast ice and the floating sea ice filled with holes and cracks and having an accumulation of ice pieces. e) Ice blocks deposited on the floating sea ice surface where the overflow occurred. f) Sediment accumulation on the floating sea ice surface.

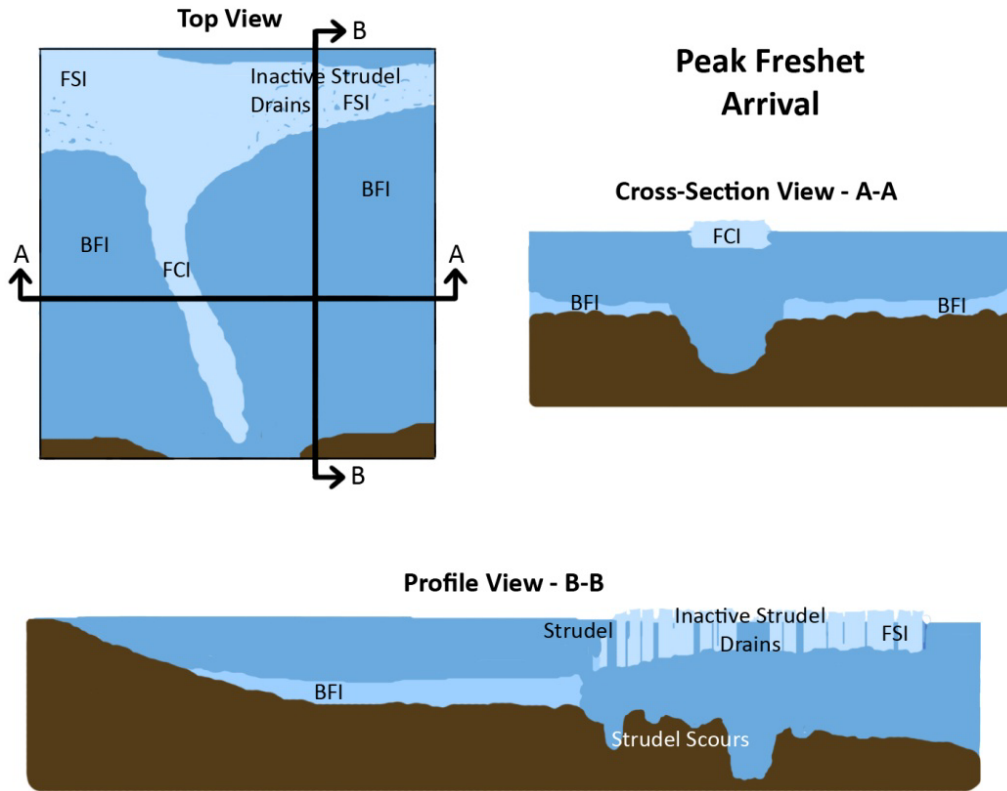


Figure 2-37 Top view, cross-sectional view and profile view of the peak spring freshet arrival in the Mackenzie Outer Delta.

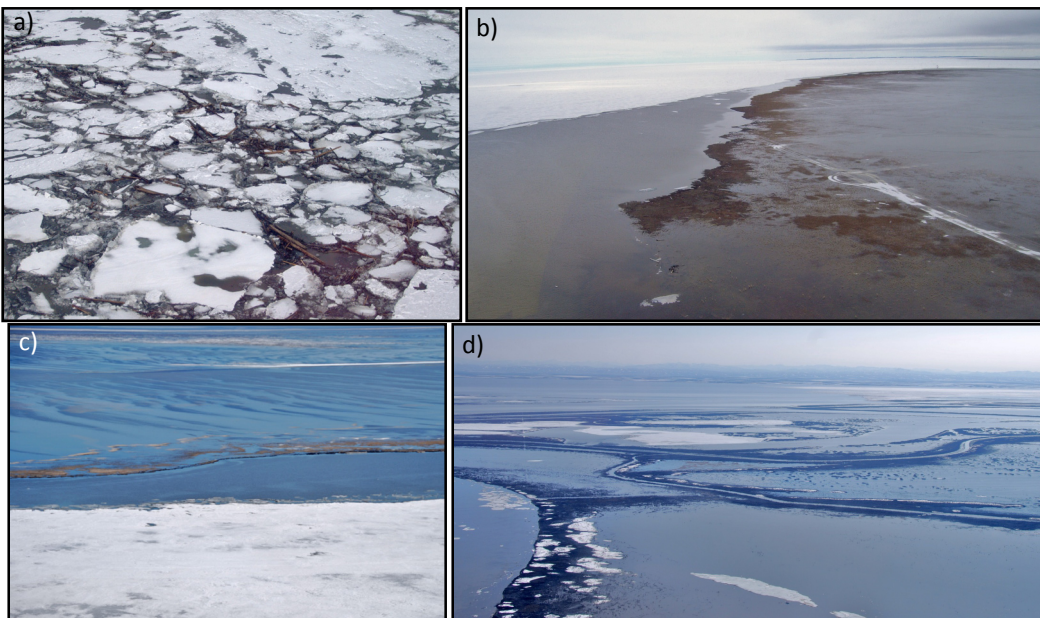
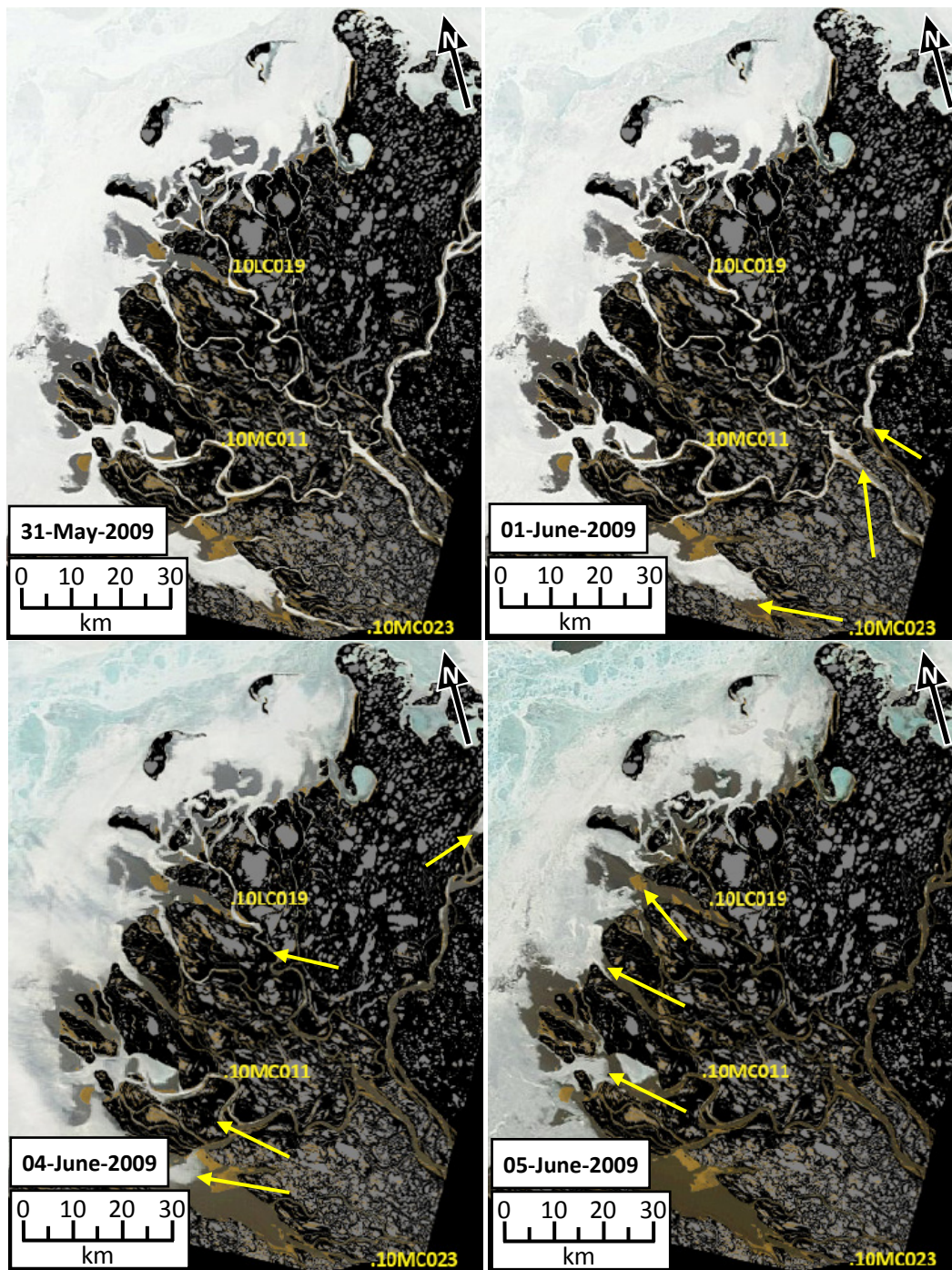
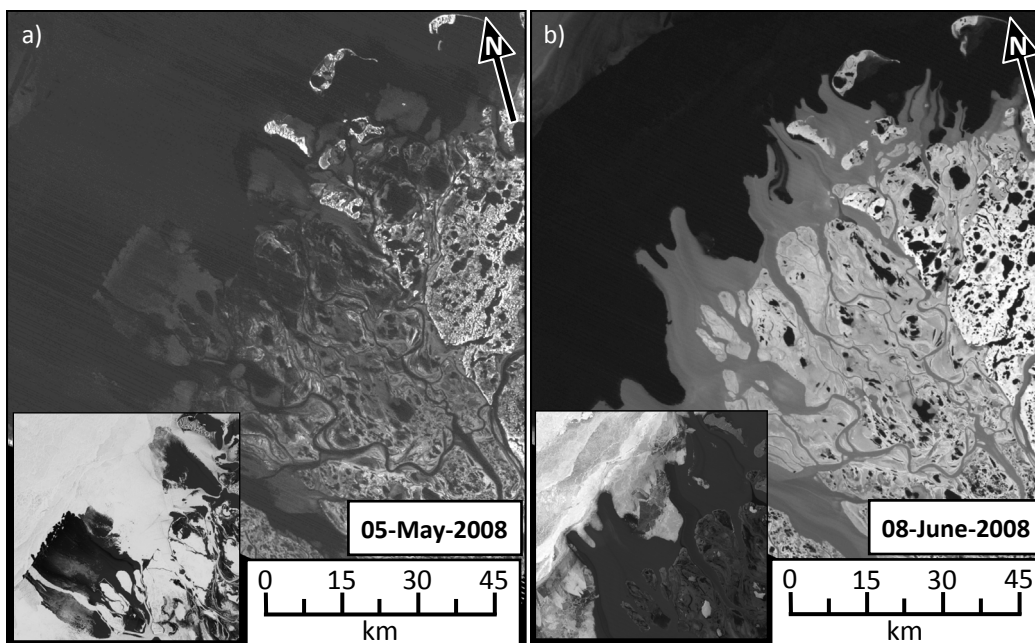


Figure 2-38 a) Debris and ice pieces in the delta's channel during spring freshet. b, c & d) Flooded low-lying land in the Mackenzie Outer Delta.



University of Alaska – GINA www.gina.alaska.edu

Figure 2-39 MODIS images, with the land-water feature map overlay, showing the peak freshet arrival in the Mackenzie Outer Delta in May and June 2009. The arrows indicate the approximate location of the ice clearance front on different dates.



Data available from the U.S. Geological Survey.

Figure 2-40 a) Landsat 5 thermal images (Band 6) of the Mackenzie Outer Delta in May 2008 showing the cold overflow. b) Landsat 5 thermal images (Band 6) of the Mackenzie Outer Delta in June 2008 showing the warm peak freshet flow. A lighter color indicates warmer water/ground temperatures. Insets: Landsat 5 images (Band 4) of the Olivier Islands and Garry Island regions on the same dates.

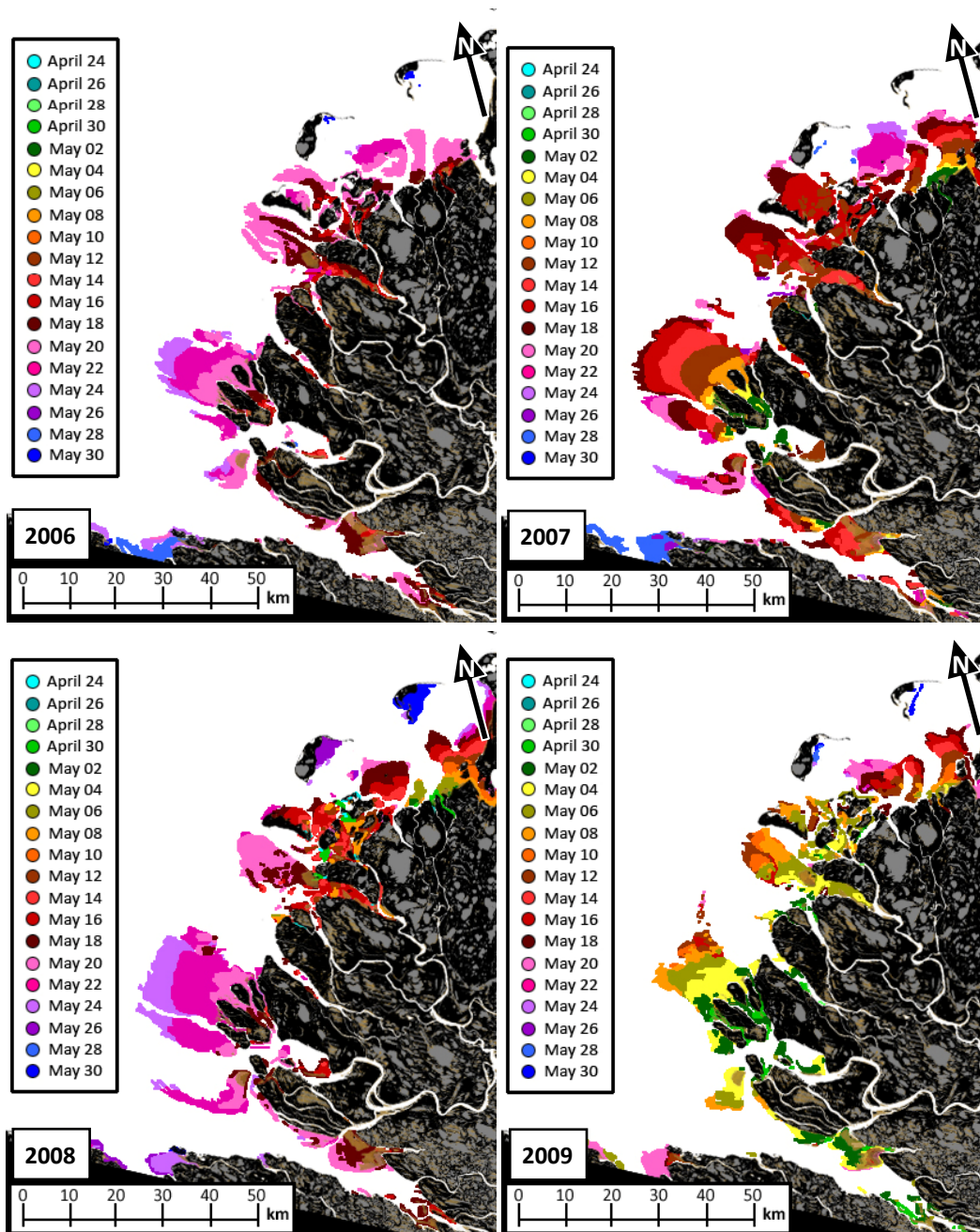


Figure 2-41 Bi-daily chronological overflow expansion in the Mackenzie Outer Delta from 2006 to 2009, defined from visible band MODIS images (accuracy of 500 m).

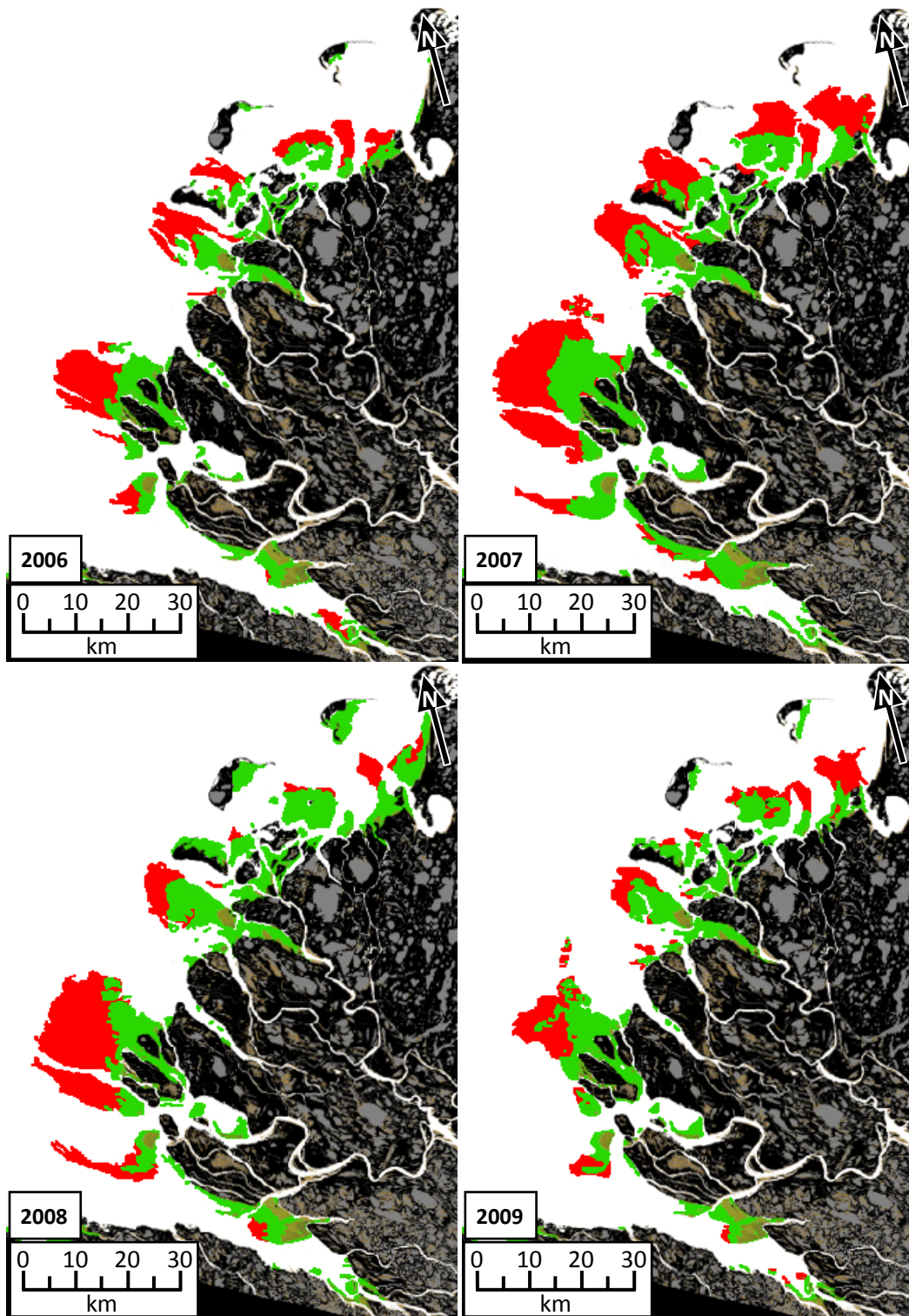


Figure 2-42 Bottomfast ice and floating ice overflow in the Mackenzie Outer Delta from 2006 to 2009, defined from visible band MODIS images (accuracy of 500 m). The green areas represent the final (drained) overflow boundaries (which correspond to the bottomfast ice location) and the red areas represent the floating sea ice cover that overflowed and drained.

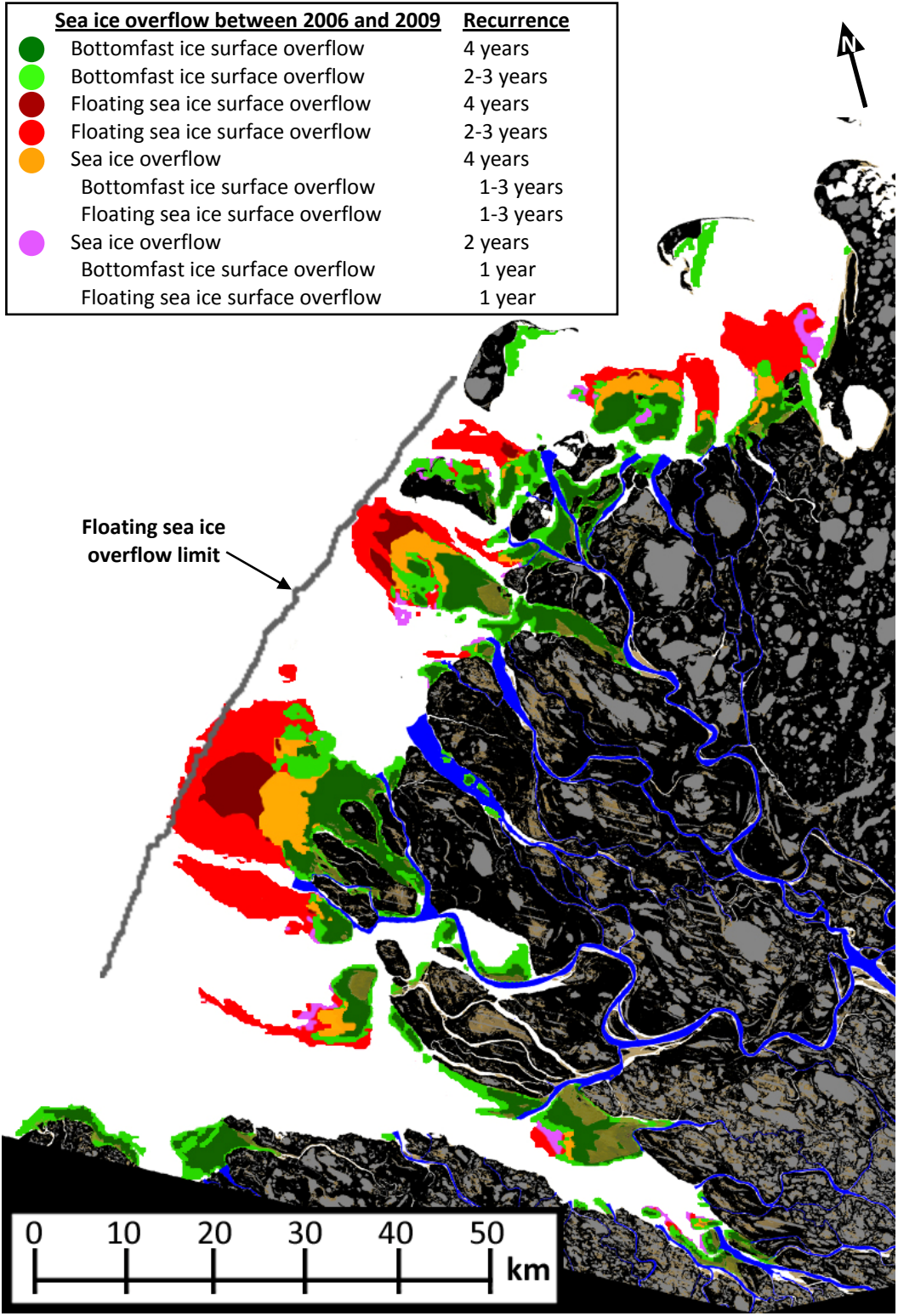


Figure 2-43 Interannual variations in the bottomfast ice and floating sea ice overflow locations (accuracy of 500 m), and location of the floating channel ice (blue) (accuracy of 250 m) in the Mackenzie Outer Delta from 2006 to 2009, defined from visible band MODIS images.

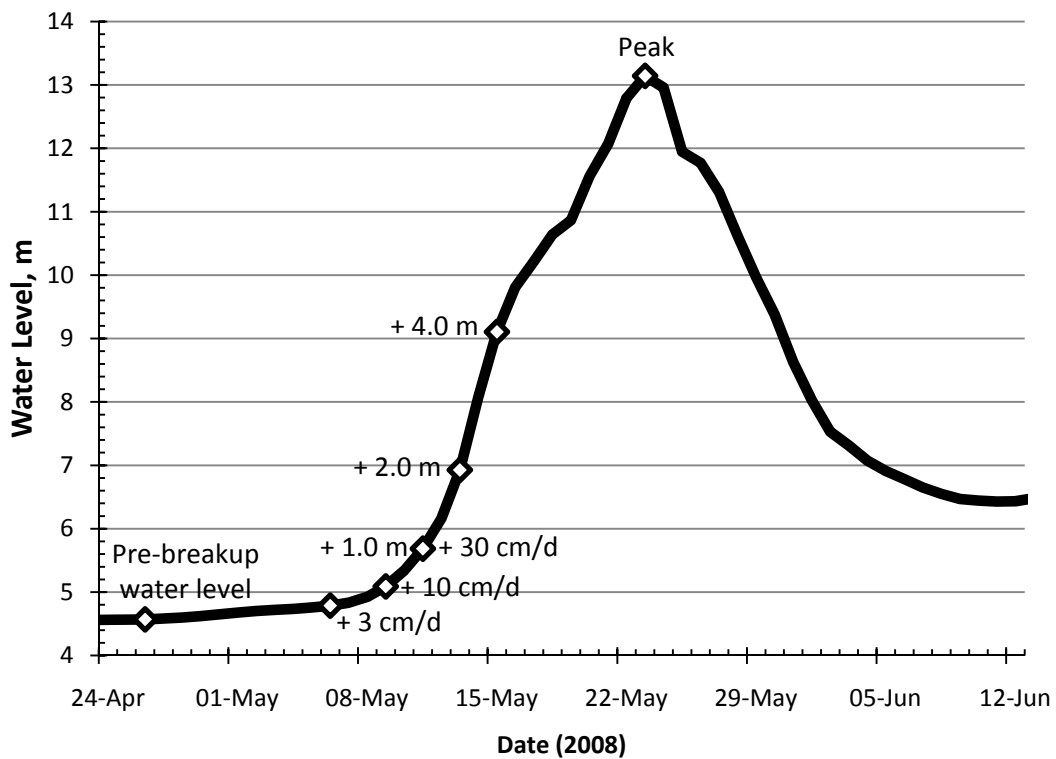
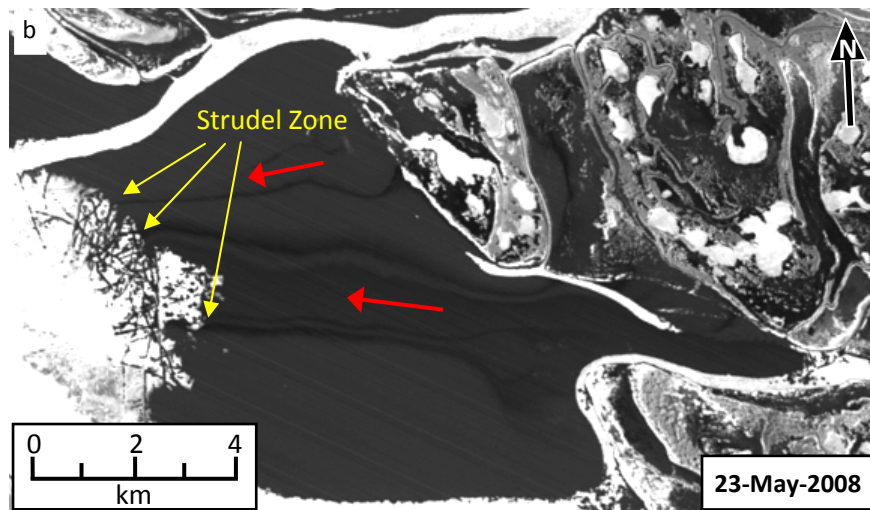
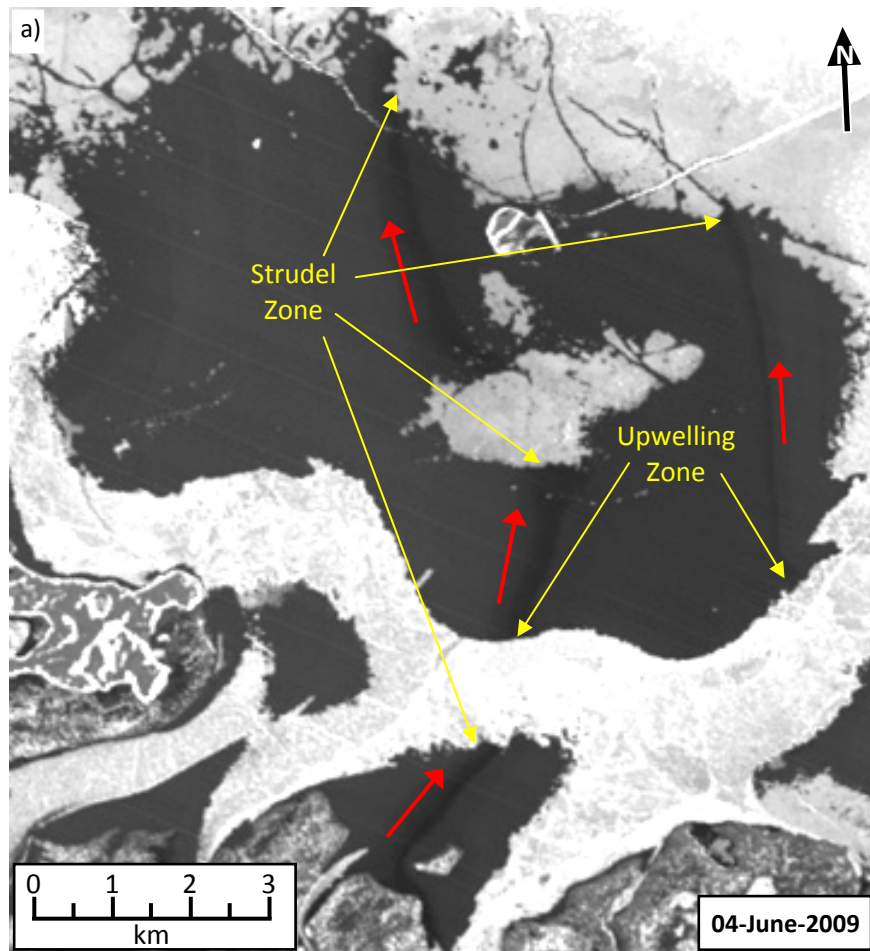


Figure 2-44 Water Level in the Mackenzie River at Arctic Red River (MARR – Station ID 10LC014) during breakup in 2008. The points indicate the dates at which the various water level thresholds were reached in 2008.



Data available from the U.S. Geological Survey.

Figure 2-45 Sediment-laden overflow water appearing darker on the Landsat 5 satellite images (Band 4) a) at the Kuluarpak Channel mouth and around Rae Island in June 2009, and b) at the Reindeer Channel mouth in Shallow Bay in May 2008. The red arrows indicate the flow direction.

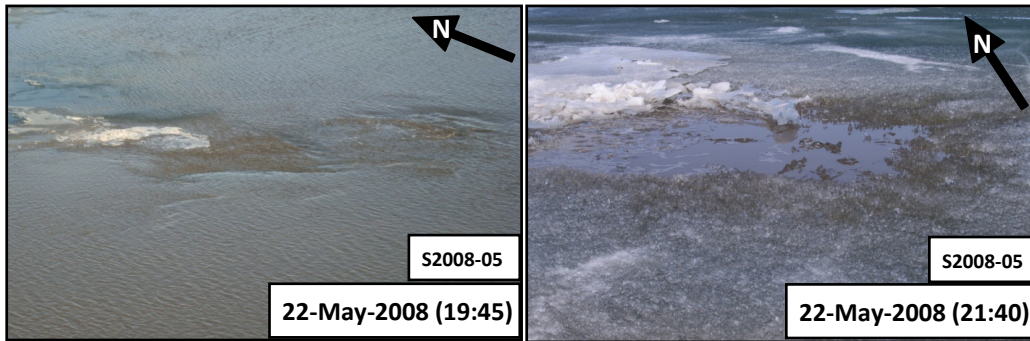


Figure 2-46 Strudel hole S2008-05 at ST-2008 on 22-May-2008.

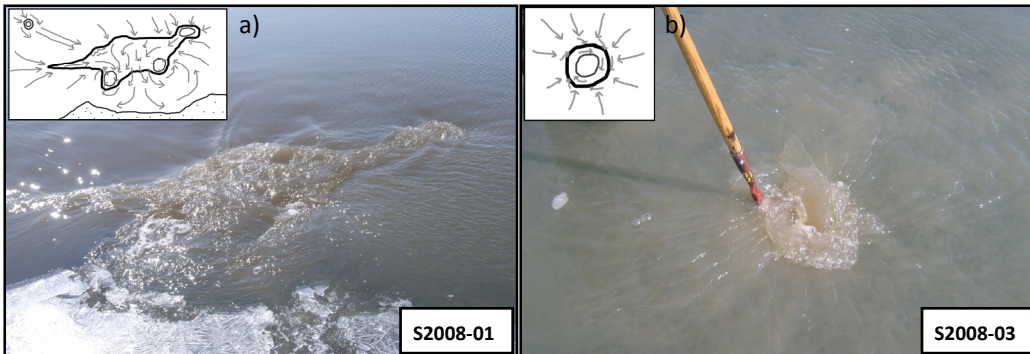


Figure 2-47 Active strudel drains a) S2008-01 and b) S2008-03 at ST-2008 on 22-May-2008. The strudel drains are approximately 20 cm in diameter. Insets: Surface flow direction around the strudel drains.

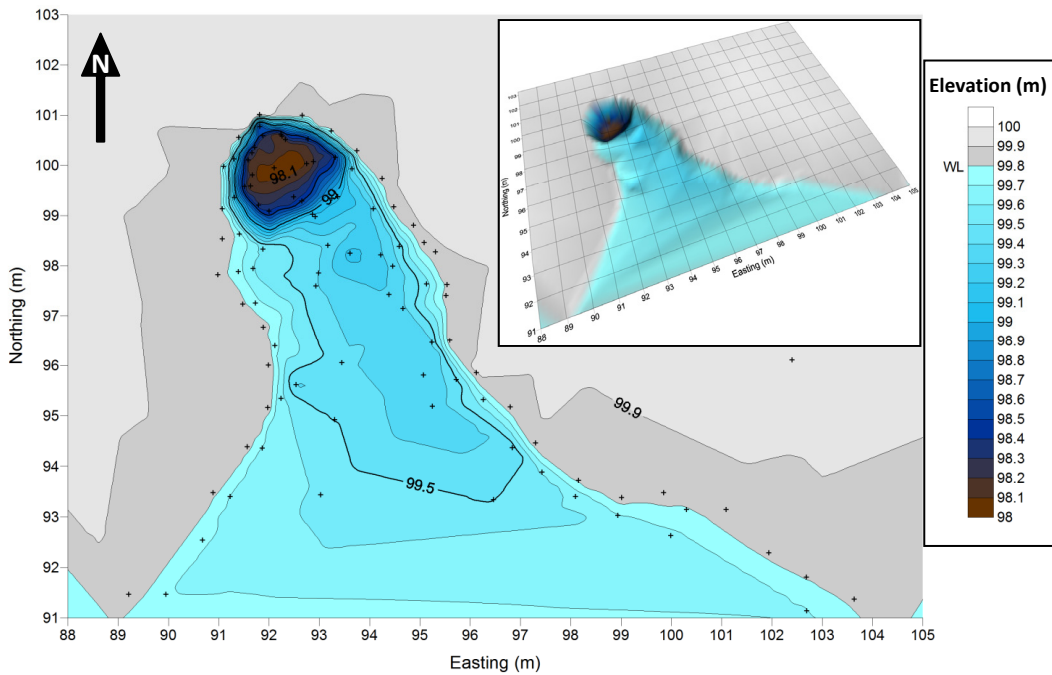


Figure 2-48 Topographic map of strudel drain S2009-01 at SL-2009 on 26-May-2009. The dots represent the locations where data points were recorded by the total station which was located directly above the ice surface at (Easting, Northing, Elevation) = (100, 100, 100). The water was flowing from the south (bottom) towards the hole. Inset: 3D topographic map of the strudel drain.

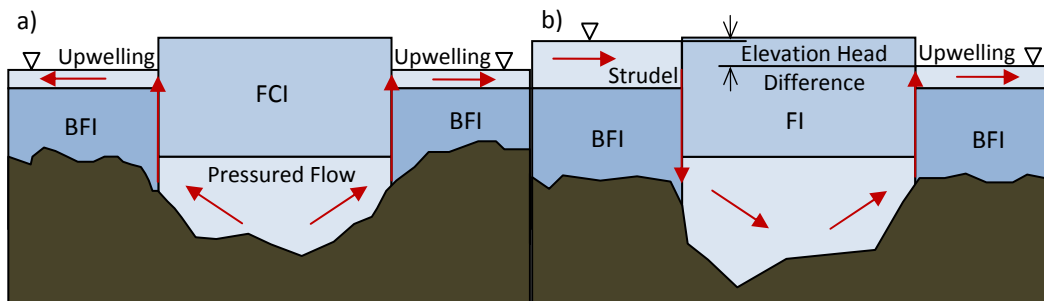


Figure 2-49 a) Sketch of the upwelling process at the interface of the floating channel ice (FCI) and the bottomfast ice (BFI). b) Sketch of the upwelling and strudel process at the interface of floating ice (FI) and of bottomfast ice (BFI). The red arrows indicate the flow direction.

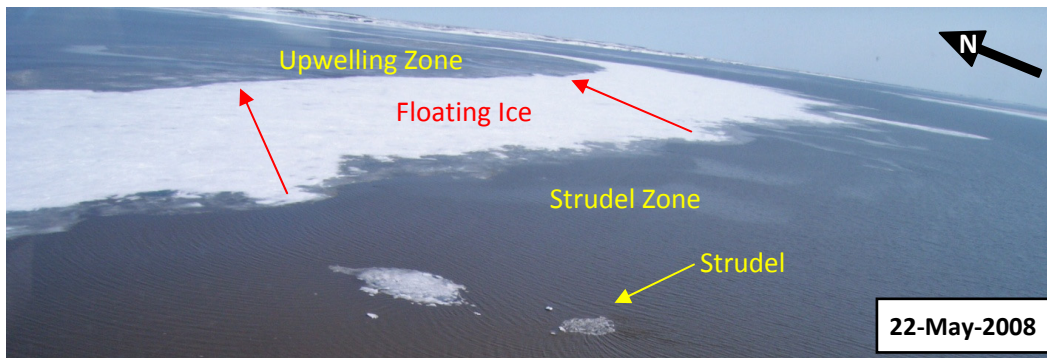


Figure 2-50 Strip of floating ice between the strudel zone and the upwelling zone at the Middle Channel mouth region. The red arrows indicate the flow direction.

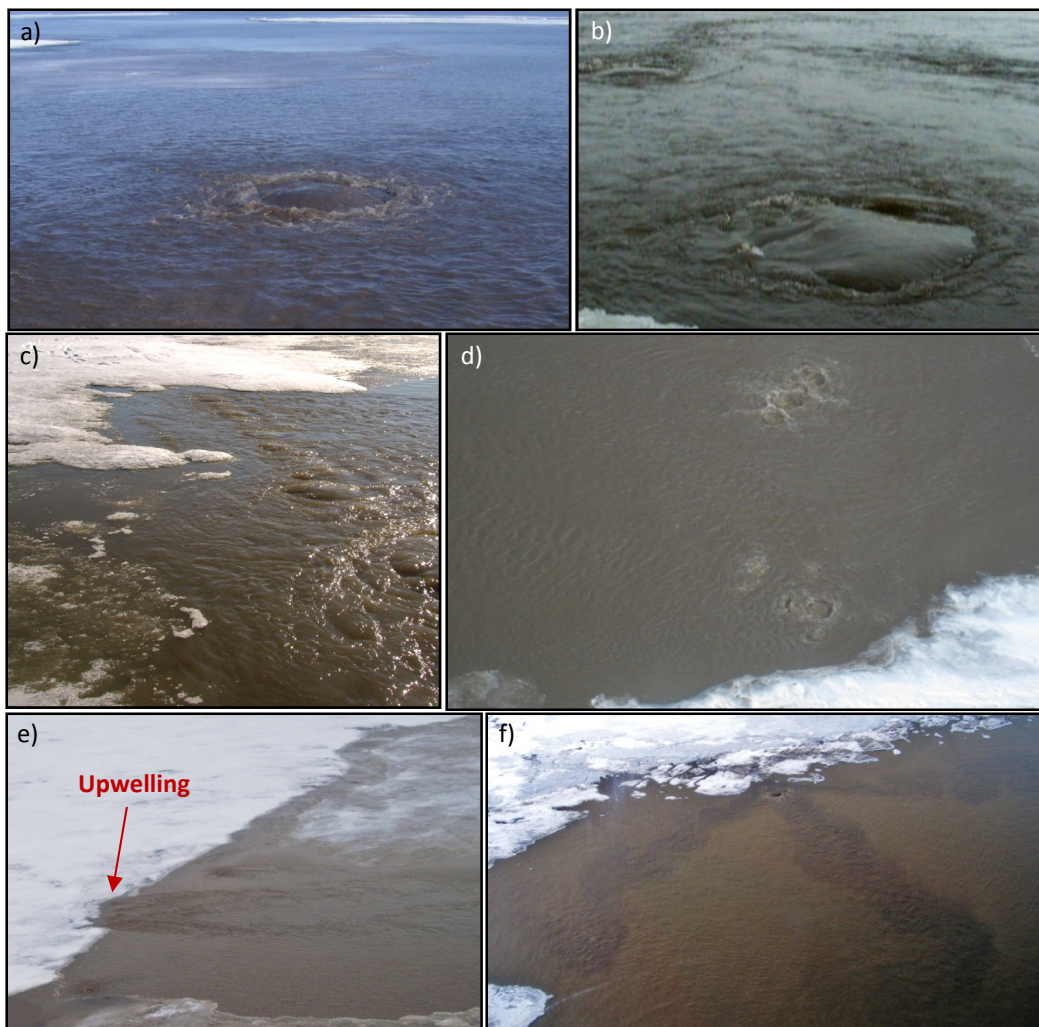


Figure 2-51 a & b) Upwellings with spurt diameters of approximately 3 m. c & d) Group of upwellings along cracks at the boundary between floating ice and bottomfast ice. e) Upwellings along the bottomfast ice border. f) Upwelling discharging more concentrated / darker sediments on the bottomfast ice surface.

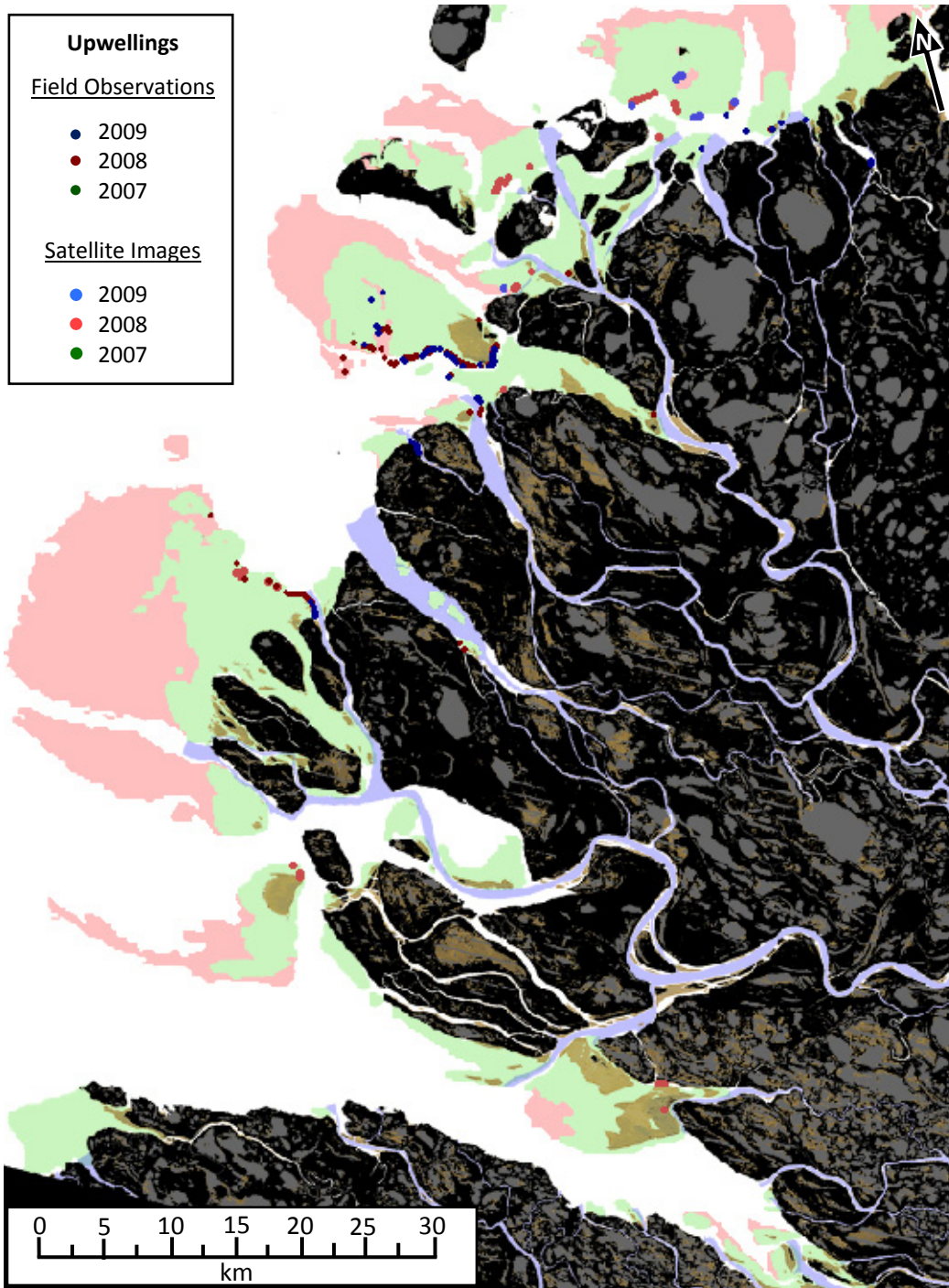


Figure 2-52 Location of upwellings in the Mackenzie Outer Delta from 2007 to 2009 collected from field observations and satellite images (accuracy of 500 m). The background map identifies the regions that were bottomfast ice overflow (green) and floating sea ice overflow (red) at least two years in the 2006 to 2009 period, and the floating channel ice location (blue), presented in Figure 2-43.

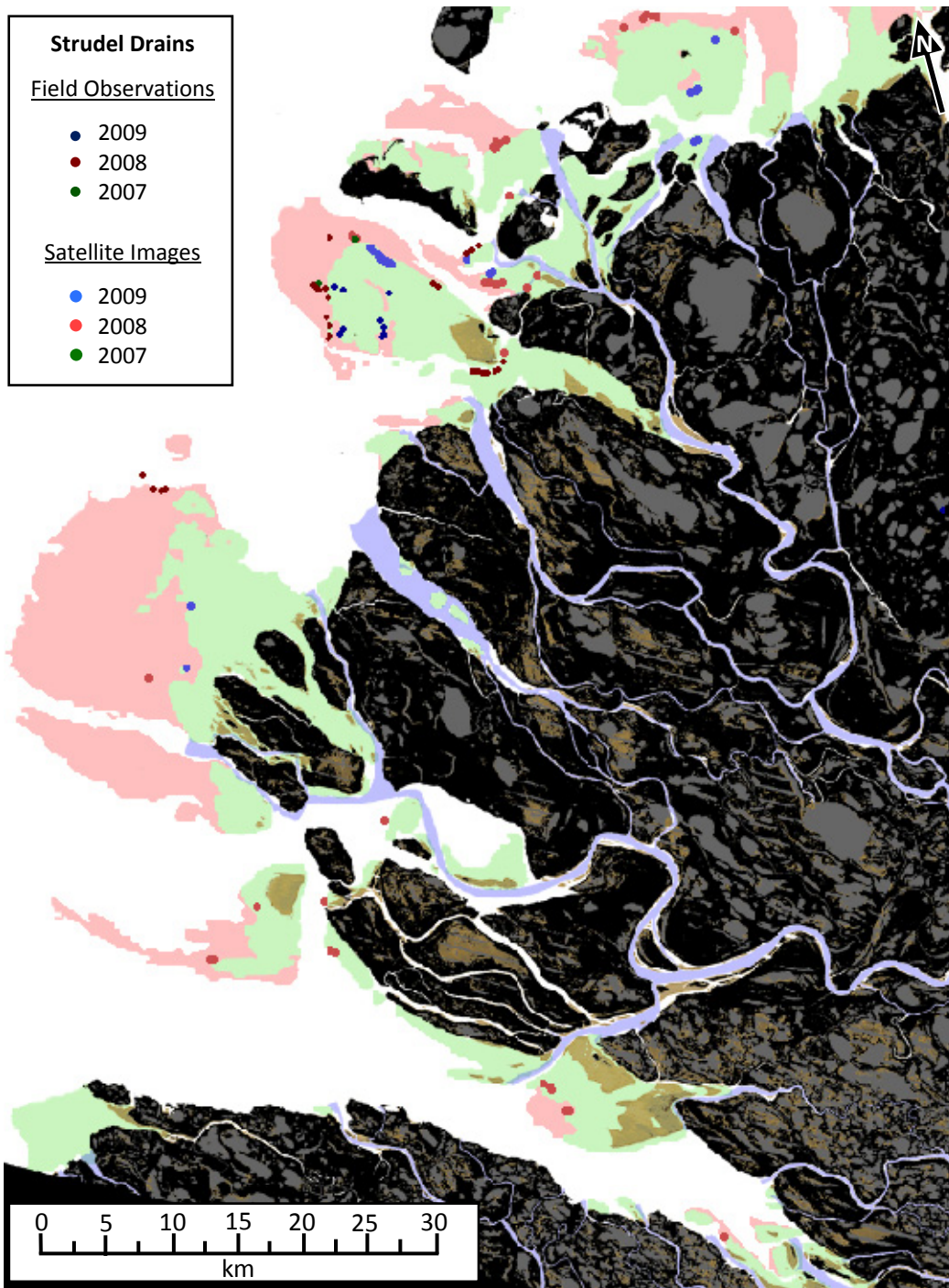


Figure 2-53 Location of strudel / strudel drains in the Mackenzie Outer Delta from 2007 to 2009 collected from field observations and satellite images (accuracy of 500 m). The background map identifies the regions that were bottomfast ice overflow (green) and floating sea ice overflow (red) at least two years in the 2006 to 2009 period, and the floating channel ice location (blue), presented in Figure 2-43.

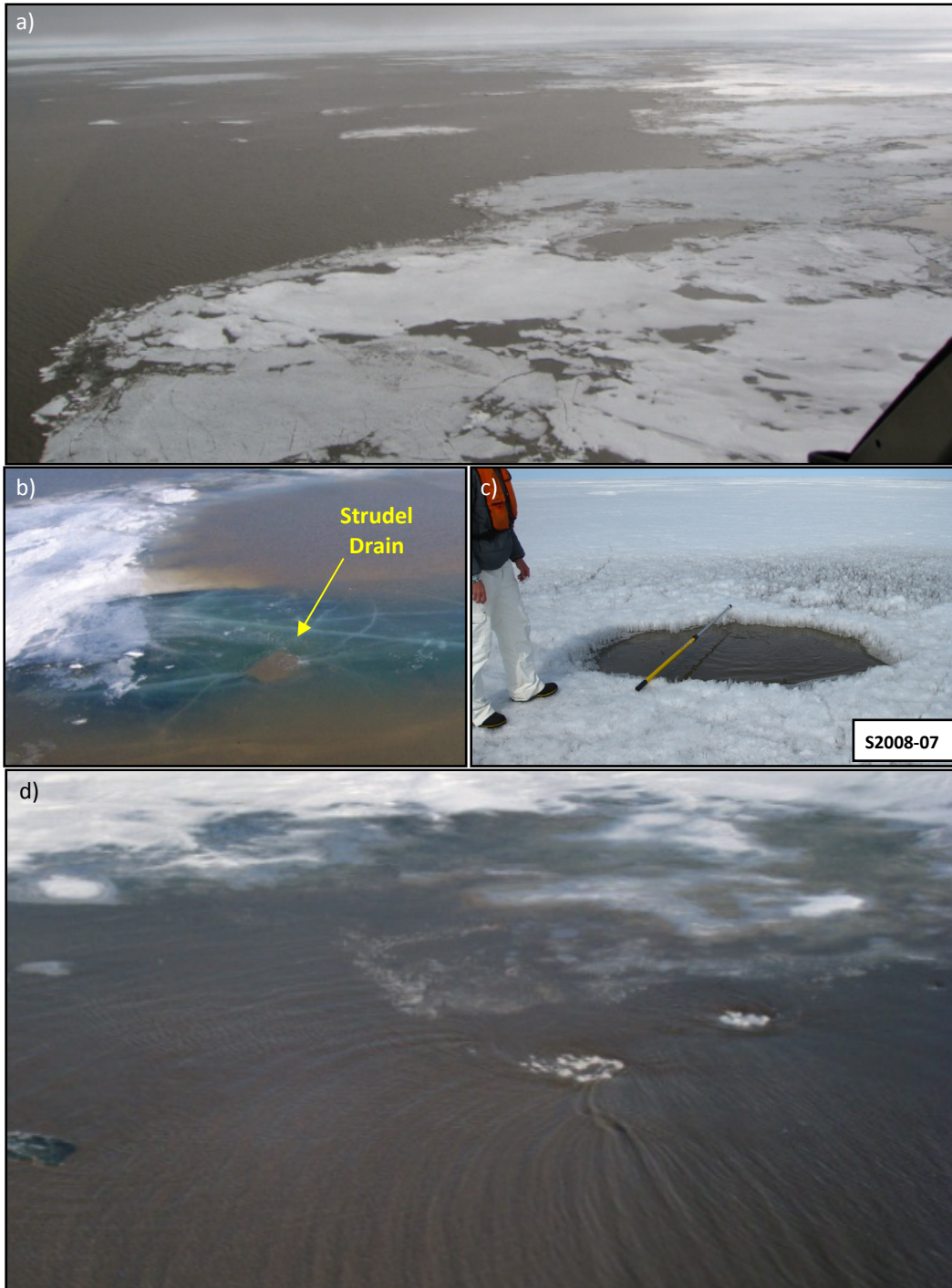


Figure 2-54 a) Drained floating sea ice strudel drains at the boundary separating the bottomfast ice from the floating sea ice. b) Strudel drain through the floating ice surface submerged by a layer of water. c) Erosion of the ice surface around an inactive strudel drain on 27-May-2008. d) Boundary strudel drains at the interface of the bottomfast ice with the floating sea ice.

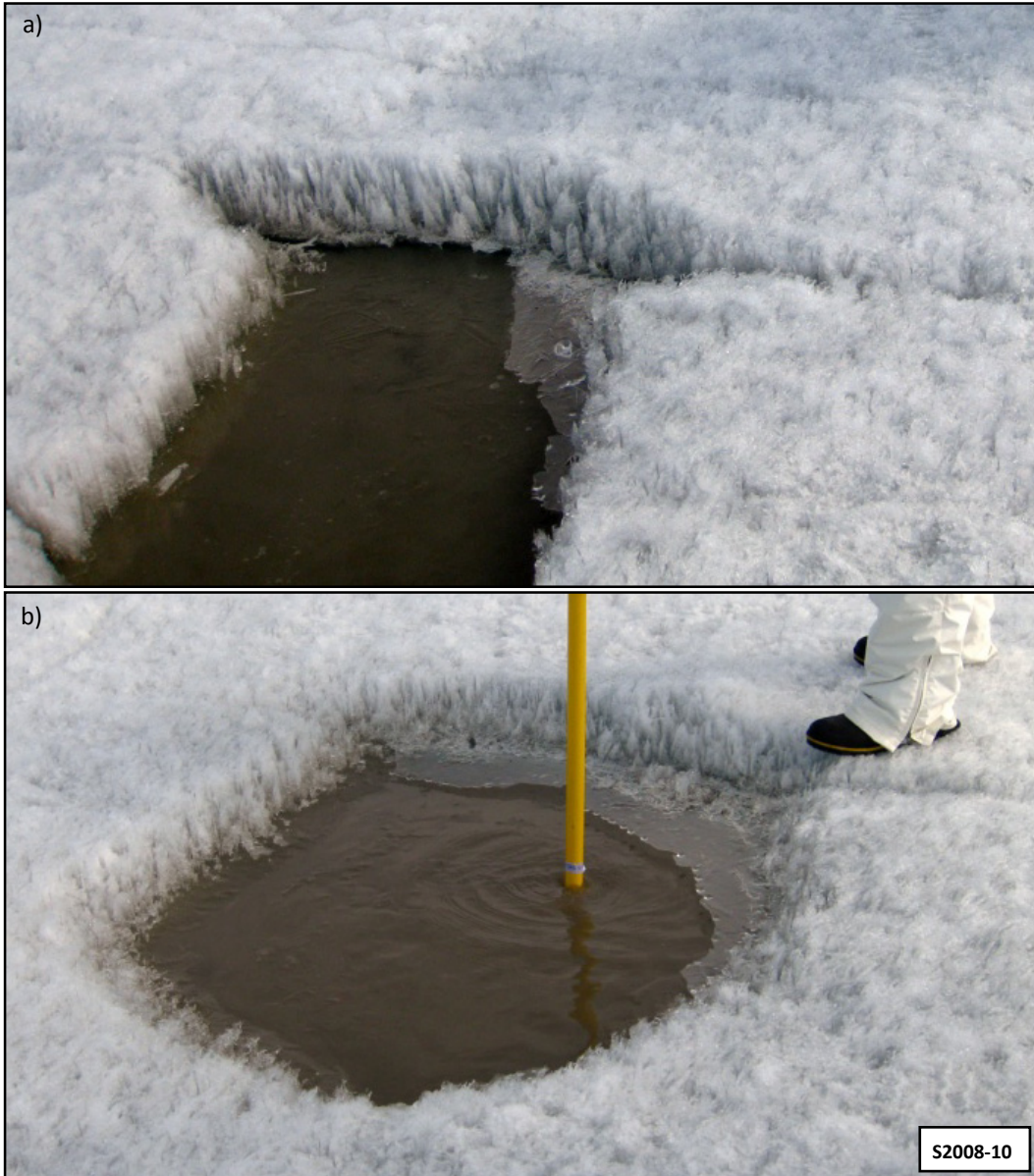


Figure 2-55 Strudel drains a) no ID and b) S2008-10 at ST-2008 on 27-May-2008 showing cracks being part of the strudel drains.

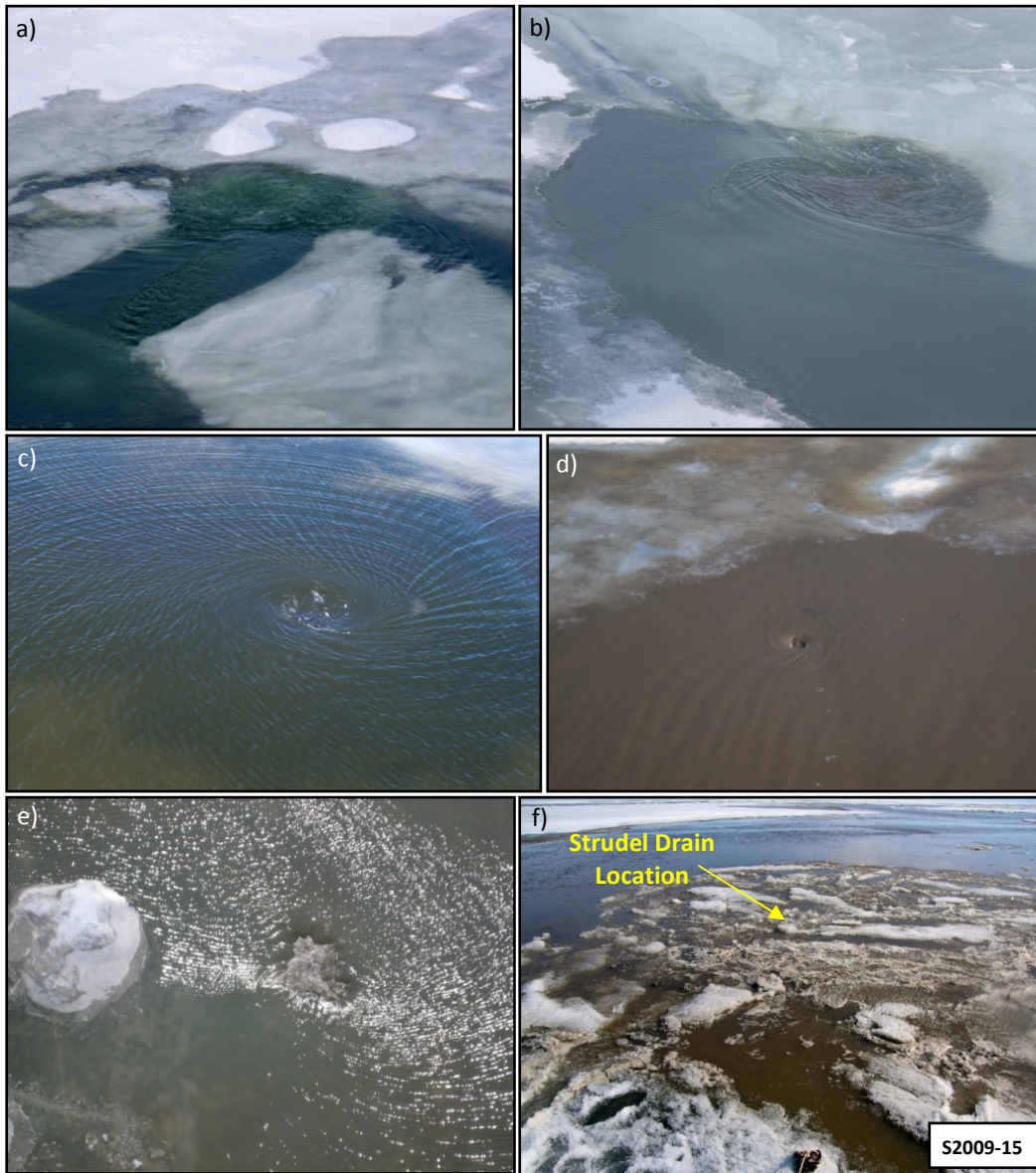


Figure 2-56 a & b) Strudel drainage features observed as a water vortex swirling around a depression at its center. c) Shallow and wide strudel drain vortex on the floating sea ice. d) Narrow and deep strudel drain vortex. e) Strudel drains in small overflow depths observed as water rushing into a hole. f) Strudel drain covered by ice pieces and debris on 25-May-2009 such that no sign of drainage was observed.



Figure 2-57 The vortex above strudel drain S2009-04 at SB-2009 on 25-May-2009 is rotating clockwise and is not showing any significant depression. The pictures were taken at 3 seconds interval.

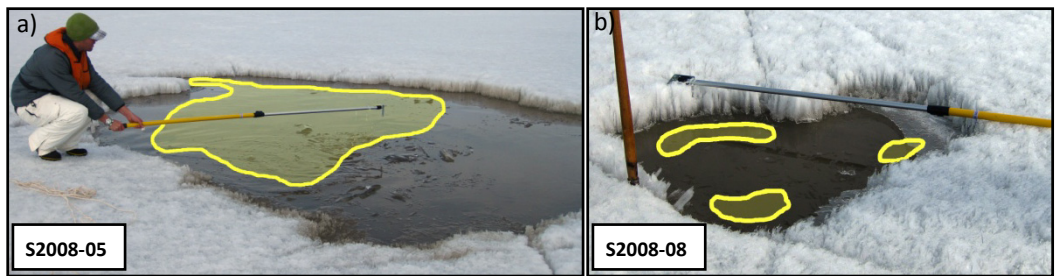


Figure 2-58 Inactive strudel drains a) S2008-05 and b) S2008-08 at ST-2008 on 27-May-2008. The areas contoured in yellow indicate the strudel hole location and the remaining flooded area consists of ice covered by a thin layer of water.

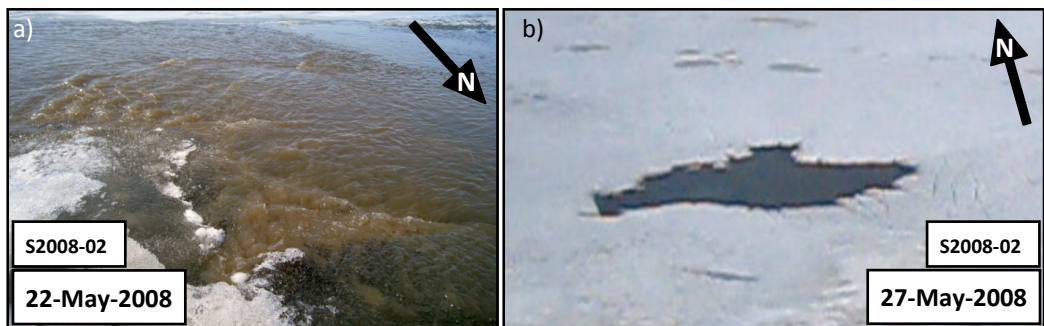


Figure 2-59 a) Active and b) Inactive (drained ice cover) strudel drain S2008-02 at ST-2008 in May 2008 showing erosion and thermal decay of the strudel drain.



Figure 2-60 Pictures from the underwater video camera inserted in strudel drain S2009-01 at SL-2009 on 26-May-2009. The camera is pointing towards the lake shore where ice is bottomfast with the bed. Steep edges with a scoured depth of approximately 30 cm are observed. The scour hole is free of vegetation and has lots of fine sediments.

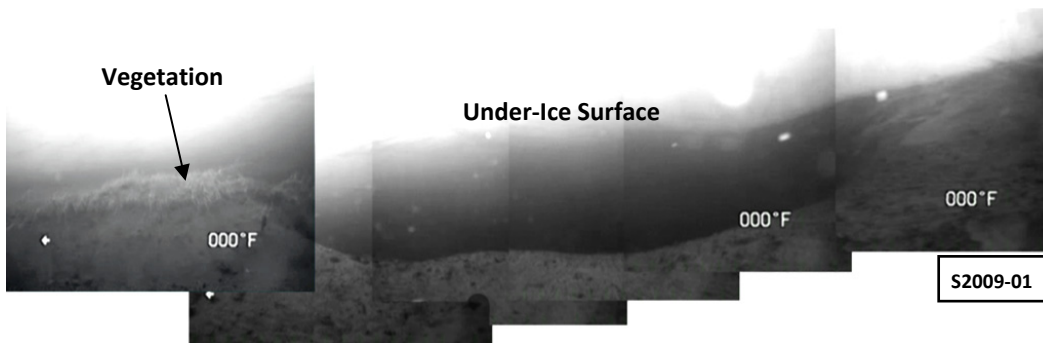


Figure 2-61 Pictures from the underwater video camera inserted in strudel drain S2009-01 at SL-2009 on 26-May-2009. The camera is pointing towards the center of the lake where ice is not bottomfast with the bed. The original bed surface is covered by vegetation while the scour hole is free of vegetation and is covered by fine sediments. The overflow water was directed under the ice cover towards a deeper section of the lake.

3.0 Physical Laboratory Model of Strudel Flow

3.1 Overview

It is of great importance to understand the hydraulic processes which drive the overflow water on the Mackenzie Outer Delta sea ice surface into strudel drains and under the ice cover. This is because the vertical flow through strudel drains impinges on the sea bed and creates strudel scours. It is also important to study the effect of the free-surface vortex on the vertical strudel flow because it may affect the hydraulic and impinging properties of the flow. Unfortunately, detailed experiments investigating strudel flows and their properties are rare. The only study found in the literature was by Johnson (1985) who performed laboratory experiments in an attempt to quantify the discharge coefficient of a strudel flow through a circular orifice. Furthermore, studies of the free-surface vortex flow under a strudel drain have not yet been completed.

It was initially thought that strudel flows in the Mackenzie Outer Delta were caused primarily by the rising floating sea ice cover. However, this hypothesis was rejected because multiple strudel were observed at locations where the ice surface was not rising or could not rise due to its bottomfast properties. A second hypothesis that the strudel flows were induced by a hydraulic head difference between the overflow water level and the sea water level was proposed. This hypothesis is the most plausible explanation for the origin of strudel flows. Therefore, the experimental setup was built and experiments were conducted to assess the validity of this hypothesis.

Physical experiments were performed in a controlled laboratory environment in order to accurately model a strudel flow and to observe and measure its properties. Strudel flows through a circular hole were created using a hydraulic head difference to drive the flow into the hole and under the ice surface. The main objective of these experiments was to determine if a hydraulic head difference between the overflow water level and the downstream water level was sufficient to produce strudel flows that were similar to those observed in the Mackenzie Outer Delta. Relationships between the physical parameters affecting the strudel flow, such as the overflow depth and the hydraulic head difference, were examined. A second objective was to study the effect of the free-surface rotating flow (i.e. vortex), present above the strudel hole, on the jet flow impinging on the bed below the hole by measuring velocities using an Acoustic Doppler

Velocimeter (ADV). The velocity profiles of the free-surface vortex jet in the free jet region and the impinging region of the jet measured by the ADV were compared with the calculated results of published fully turbulent jet equations. These ADV measurements are of great value for future work as they can be used to calibrate numerical models of a strudel flow under an ice cover. Some qualitative observations of the free-surface vortex flow above the strudel drain were also performed during the experiments.

3.2 Literature Review

3.2.1 Previous Physical Strudel Experiments

Only one study regarding the hydraulics of strudel flow was found in the literature. Johnson (1985) performed laboratory experiments in an attempt to quantify the discharge coefficient of a strudel flow through a circular orifice. Johnson (1985) found that the discharge coefficient (C_d) increases with an increase in the Reynolds Number (Re). The author concluded that above a critical Reynolds Number of 25,000, the viscous effects of the water are negligible and the discharge coefficient is a constant. This value varied depending on the ice thickness / hole diameter (t/d) ratio. Johnson (1985) found that, for a Reynolds Number above 25,000 and for $t/d = 1$ and 1.3, the discharge coefficient varies between a value of 0.75 and 0.80. For $t/d = 2$ and 4, the discharge coefficient was not constant but it appeared to be converging to a value greater than one. Johnson (1985) did not find any correlation between the discharge coefficient (C_d) and the hydraulic head difference / impingement distance (H_d/H) ratio, and he concluded that the scale of his experimental setup was insufficient to find a correlation between the discharge coefficient (C_d) and the hydraulic head difference / hole diameter ratio (H_d/d).

Johnson (1985) also performed a qualitative flow visualisation study of the strudel orifice flow using dye. He observed that the water entered the hole radially in the ponded cases and mostly through the upstream edge in the flowing cases. Johnson stated that when vortices formed, they were strong whirlpools which entrained air into and sometimes through the hole, to the underside of the ice sheet.

3.2.2 Axisymmetric Circular Turbulent Jets

3.2.2.1 General

Axisymmetric circular turbulent jets have been studied extensively in the past. Turbulent jets occur when the Reynolds Number at the jet exit is more than a few thousand (Crow & Champagne, 1971; Rajaratnam, 1981a). For turbulent jets impinging on a solid boundary, the flow is divided into three regions as illustrated in Figure 3-1. The *free jet region* where the flow behaves as if there were no boundary; the *impingement region* where the boundary affects the flow behaviour, the jet begins to stagnate and is redirected to flow radially along the boundary; and the *wall jet region* where the flow behaves as a radial wall jet (Beltaos & Rajaratnam, 1977). The wall jet region of the flow does not contribute greatly to the strudel scouring of the sea bed because the flow in this region is parallel to the bed. Therefore, this region was not examined in this study.

3.2.2.2 Free Jet Region

The free jet region consists of a *flow development region* and a *fully developed flow region* as shown in Figure 3-2. Beltaos and Rajaratnam (1977) studied the flow development region of the jet which extends up to an axial distance of approximately $6d$ from the jet nozzle, where d is the jet nozzle diameter. The flow development region contains a *potential core* and a *shear layer*. The potential core extends from the jet centreline to a radial distance of r_1 as shown in Figure 3-2. In the core, the axial velocity (V_z) is equal to the velocity at the jet nozzle (U_o) and the radial velocity (V_r) is negligible. The potential core is surrounded by a shear layer, where for $r > r_1$, the axial velocity decreases to zero with increasing radial distance from the jet centerline while the radial velocity takes on non-zero values. In general, the axial velocity is larger than the radial velocity both in the potential core and in the shear layer (Beltaos & Rajaratnam, 1977). Beltaos and Rajaratnam (1977) found that the radius of the potential core could be estimated using the following empirical equation,

$$\frac{r_1}{d} = 0.39 - 0.065 \frac{z}{d} \quad [3-1]$$

where:

z = the axial distance from the jet nozzle; and

r_1 = the radial distance of the boundary separating the potential core and the shear layer.

The radial distance of half-velocity from the jet centerline was defined by Beltaos and Rajaratnam (1977) to be estimated by the following empirical equation,

$$\frac{b}{d} = 0.115 + 0.087 \frac{z}{d} \quad [3-2]$$

where:

b = the radial distance of half-velocity,

and the radial distance of the outer limit of the jet where the axial velocity is approximately equal to zero ($u \approx 0$) can be estimated as

$$r_2 \cong r_1 + 2.25b \quad [3-3]$$

where:

r_2 = the radial distance of the outer limit of the jet.

Finally, Beltaos and Rajaratnam (1977) found that the velocity in the shear layer could be modelled using the following exponential equation,

$$\frac{v_z}{U_o} = \exp\left(-0.693 \left[\frac{(r-r_1)}{b}\right]^2\right) \quad \text{valid for } r \geq r_1 \quad [3-4]$$

where:

r = the radial distance from the jet centerline;

V_z = the axial velocity; and

U_o = the average axial velocity at the jet nozzle.

Boguslawski and Popiel (1979) studied the *fully developed flow region* of the jet which extends beyond $6d$ from the jet nozzle (Beltaos & Rajaratnam, 1977). In this region, the velocity profile was observed to be self-similar and described well by the following equation,

$$\frac{v_z}{U_c} = \exp\left(-108 \left[\frac{r}{(z-0.5d)}\right]^2\right) \quad [3-5]$$

where:

U_c = the centerline axial velocity.

Boguslawski and Popiel (1979) also found that the decay of the center-line velocity with increasing axial distance could be approximated by the following equation,

$$\frac{U_c}{U_o} = \frac{5.9d}{z-0.5d} \quad [3-6]$$

3.2.2.3 Impingement Region

Beltaos and Rajaratnam (1974) and Mazurek, Rajaratnam and Seago (2001) found that the behaviour of turbulent jets impinging on solid boundaries varied with the impingement height. For a *small impingement height*, $H/d < 5.5$ where H is the impingement distance, the jet is not fully developed. In this case the potential core of the jet impinges on the boundary and the characteristic length is the jet nozzle diameter. For a *large impingement height*, $H/d > 8.3$, the jet is fully developed before it impinges on the boundary and the characteristic length is the impingement distance. In the *transition region* defined as, $5.5 < H/d < 8.3$, there is a rapid increase in the turbulence intensity due to the extension of the mixing subregion over the whole cross-section of the jet (Boguslawski & Popiel, 1979). In this case both the jet nozzle diameter and the impingement height are characteristic lengths. The effect of the nozzle geometry on the potential core of the jet was studied by Ashforth-Frost and Jambunathan (1996) where they measured that the length of the potential core increases by 7% for fully developed jets compared to flat jets.

The flow in the *impingement region* of a jet impinging on a perpendicular boundary at a small impingement height, illustrated in Figure 3-3, has been investigated in numerous studies. It was found that the impingement region extends to an axial distance of about $1.2d$ from the boundary and about $1.4d$ radially from the stagnation point (Beltaos & Rajaratnam, 1977). For an impingement height ranging between $4d$ and $12d$ (small to large impingement heights), Tani and Komatsu's (1964) measurements show that this region extends to an axial distance between $1.6d$ and $2.2d$ from the boundary. For small impingement heights, Beltaos and Rajaratnam (1977) observed that the centerline axial velocity decreased as the flow approached the boundary and that it was a maximum at a

radial distance r_1 from the jet centerline such that $U_m \cong 1.15U_c$, where U_m is the maximum axial velocity. For small impingement heights, Beltaos and Rajaratnam (1977) found that the centerline axial velocity in the impingement region for $z'/d \leq 0.14$ is approximated by

$$\frac{U_c}{U_o} = 2 \frac{z'}{d} \quad [3-7]$$

where:

z' = the axial distance from the impinged boundary.

For $0.1 < z'/d < 0.8$, the centerline axial velocity could be approximated as

$$\frac{U_c}{U_o} = 1.07 \sqrt{\frac{z'}{d} - 0.07} \quad [3-8]$$

The centerline axial velocity can also be approximated in the entire impingement region at small impingement heights using the following slightly less accurate empirical equation defined by Beltaos & Rajaratnam (1977) as

$$\frac{U_c}{U_o} = \frac{z'/d}{1.1} \left(2 - \frac{z'/d}{1.1} \right) \quad [3-9]$$

Beltaos and Rajaratnam (1977) formulated the following equation for the radial velocity in the impingement region,

$$\frac{V_r}{V_{r_1}} = \frac{r/r_1}{1.15} \left[1 + 0.15 \left(\frac{r}{r_1} \right)^2 \cdot \left(2 - \left(\frac{r}{r_1} \right)^2 \right) \right] \quad \text{valid for } r \leq r_1 \quad [3-10]$$

valid for small impingement heights, where:

V_r = the radial velocity; and

V_{r_1} = the radial velocity at the boundary separating the potential core and the shear layer.

In equation 3-10, r_1 is calculated as

$$\frac{r_1}{d} = \left(0.50 - 0.069 \frac{H}{d} \right) \cdot \left(\frac{z'}{d} \right)^{-1/4} \quad [3-11]$$

and V_{r_1} is calculated as

$$\frac{V_{r_1}/U_0}{r_1/d} = \frac{0.294}{\sqrt{(z'/d)-0.07}} \quad [3-12]$$

The peak radial velocity is reached at a radial distance away from the jet centerline between $1.0d$ and $1.8d$ (Tani & Komatsu, 1964). In the impingement region, the decay of the velocity in the shear layer was well described by

$$\frac{V_z}{U_m} = \exp\left(-0.693 \left[\frac{(r-r_1)}{b}\right]^2\right) \quad \text{valid for } r \geq r_1 \quad [3-13]$$

where b can be approximated by equation 3-2 (Beltaos & Rajaratnam, 1977).

Rajaratnam and Mazurek (2005) studied the impingement of a jet on a rough boundary, having an equivalent sand roughness (k_s) between 1.73 and 15.18 mm, at large impingement heights. The pressure acting on the boundary is a maximum at the stagnation point and decreases with increasing radial distance and the pressure reaches the ambient value at approximately $r/H = 0.22$. The shear stress at the jet centerline is zero and increases with increasing radial distance and reaches a maximum at a distance of $r/H = 0.12$ for rough boundaries, compared to 0.14 for smooth boundaries (Beltaos & Rajaratnam, 1974). The shear stress then decreases with increasing radial distance from the stagnation point. For the same jet characteristics as smooth boundaries experiments, the maximum shear stress is a factor of 2.5 to 5.0 times higher for rough boundaries but the radial extent of the impingement region might be slightly smaller. Nonetheless, the velocity distribution in the wall jet region is similar for both rough and smooth boundaries.

3.2.3 Free-Surface Vortex Flow above a Circular Drain

The free-surface vortex that occurs above a drain, including the strudel drain hole, is also referred to as a bathtub vortex, whirlpool, point sink, intake vortex and sometimes drainpipe in the literature. The bathtub vortex, illustrated in Figure 3-4, is defined as the flow of water draining through a drain hole by gravity which is accompanied by a circulation induced rotation and in some cases, by a dip in the free surface above the drain.

Carriveau, Kopp and Baddour (2009) defined two types of vortex. The *non-purely stretching-sustained (NPSS)* vortex occurs for large overflow depths. In this case vorticity needs to be constantly supplied in order for the vortex to be sustained. The *purely stretching sustained (PSS)* vortex occurs at smaller overflow depths and larger withdrawal rates. In this case vorticity does not need to be constantly supplied for the vorticity to be sustained.

There have been a number of previous studies that have examined the effect of Coriolis forces on the direction of rotation of the vortex. In a typical experiment a circular container of water was allowed to rest for several hours or days to ensure that the water was completely stagnant and then drained through a small hole in the bottom. Experimental (Sibulkin, 1962) and analytical (Tyvand & Haugen, 2005) studies revealed that the Coriolis effect due to the Earth's rotation has a negligible influence on the bathtub vortex. It was found that other environmental factors such as residual fluid motion in the vessel, pressure variations caused by air flow and asymmetry in the initial or boundary conditions are leading factors in determining the direction of rotation (Stepanyants & Yeoh, 2008). Carriveau et al. (2009) provide a thorough review of the many previous bathtub vortex studies.

Sibulkin (1962) performed "bathtub vortex" experiments in a circular tank and observed that when the tank was initially filled in a clockwise direction, a clockwise vortex tended to form and vice versa. However, on some occasions he observed that the vortex flow changed direction and he named this phenomenon vortex reversal. Kelly, Martin and Taylor (1964) performed experiments using the same apparatus as Sibulkin (1962) and studied flow reversal in some detail. They observed that reversal mostly occurred when the circular tank was filled counter-clockwise initially and also observed a secondary reversal to the original induced direction.

Bathtub vortex experiments in a rotating container by Andersen, Bohr, Stenum, Rasmussen and Lautrup (2003 & 2006), and by Bergmann, Andersen, van der Meer and Bohr (2009) investigated the effect of the rotation rate on the free surface dip. These studies showed that for an increasing rotation rate, the dip increased in depth and the shape became more needle-like. At a critical rotation rate, air bubbles detached from the dip and got entrained into the downward flow inside the orifice while the radius of

the dip stayed constant (Andersen *et al.*, 2006). It was found that as the rotation rate increased, the volumetric flow rate through the orifice or drain decreased (Andersen *et al.*, 2006).

A large number of vortex studies have been conducted to establish guidelines that would aid hydraulic designers in avoiding the problematic formation of vortices at municipal hydraulic intake, industrial cooling intake or in hydroelectric dam head-race channels. Vortices forming in intakes are problematic because they can lead to air and debris entrainment in the pipe thus reducing efficiency or causing damage to the structures (Carriveau *et al.*, 2009). When withdrawal occurs through a circular orifice at the bottom of a fluid consisting of two layers of different density, such as air and water, buoyancy forces ensure only fluid from the lower layer is drawn through the orifice. As the depth of the lower layer decreases, it reaches a critical value at which the interface is pulled down so the fluid from the upper layer also flows through the orifice (Hocking, Vanden-Broeck & Forbes, 2002). Hocking *et al.* (2002) observed that this dip formation process occurred in a matter of seconds. An early attempt to predict sudden dip formation in a two layer flow was carried out by Lubin and Springer (1967). They observed that the flow rate through the orifice was related to the critical depth of the bottom layer. Hocking *et al.* (2002) present a summary of studies that examined the critical drawdown Froude number for a point sink, defined as

$$F = (m^2/g'h_o^5)^{1/2} \quad [3-14]$$

where:

- F = the Froude number;
- m = the total flux from the point sink;
- g' = the effective gravity defined as $(\Delta\rho/\rho)g$ where $\Delta\rho$ is the difference in density between two liquid layers and ρ is a reference density; and
- h_o = depth of water above the point sink.

The critical drawdown Froude Number was found to vary between 0.3 and 6.4. Carriveau *et al.* (2009) reviewed a large number of previous studies in order to identify the main criteria defining the safe normalized depth, also called the critical formation submergence and defined as h_o/d , to minimize threats to structures.

3.2.4 Free-Surface Vortex Flow below a Circular Drain

The vortex jet flow formed under a strudel drain, below the ice cover, is a rather unique flow because its vorticity is induced by a free surface vortex. This type of flow is often modelled as an irrotational vortex in which the tangential velocity is inversely proportional to the radius. In this case the tangential velocity is given by Kundu, Cohen and Hu (2002) as,

$$V_{\theta} = \Gamma/2\pi r \quad [3-15]$$

where:

V_{θ} = the tangential velocity; and

Γ = the circulation.

No studies of irrotational vortex jets resulting from a free surface vortex flow were found in the literature. Numerous jet experiments with swirl have been published but unfortunately, the rotating flow induced by swirl is different than the flow induced by a free surface vortex. The tangential velocity (w) in a swirling flow increases with radial distance from the centreline and is negligible at its center (Mak & Balabani, 2007; Alekseenko, Dulin, Kozorezov, & Markovich, 2008). Nonetheless, results regarding vortices induced by swirl are presented below for comparison purposes with free-surface vortex flow.

The effects of a swirl induced by pipe rotation (Örlü & Alfredsson, 2008) and by a swirler device (Mak and Balabani, 2007; Alekseenko *et al.*, 2008) on the jet flow have been studied. It was found that the distance of the shear boundary from the jet centerline increases faster and the centerline velocity decays more quickly than in fully developed non-swirling jets due to the increased turbulence created by the swirl (Örlü & Alfredsson, 2008; Mak & Balabani, 2007). Jets with weak swirl (i.e. small tangential velocities) were only observed to have slightly modified flow pattern. In jets with strong swirl, a vortex breakdown, which is characterised by a wake-like velocity profile with a stagnation point and a subsequent flow reversal at the jet centerline, was observed (Mak & Balabani, 2007).

3.3 Materials, Methods and Data Collection

3.3.1 Physical Hydraulic Model

3.3.1.1 Experimental Setup

The strudel laboratory experiments were performed in the Wind Wave Laboratory located in the Natural Resource Engineering Facility (NREF) building at the University of Alberta. The laboratory apparatus was designed such that the model (laboratory) to prototype (field) ice thickness, under-ice depth and strudel hole diameter were approximately at a 1 to 10 ratio. A narrow rectangular channel was chosen for modelling strudel flows for two primary reasons. First, for convenience as it was already owned by the University of Alberta and it could be easily and quickly modified to model the strudel flows. Secondly, even though this narrow tank may not be suitable for modelling strudel completely surrounded by overflow it can be used to accurately model strudel flows that are fed by channelled overflow which are often observed in the field (see Figure 2-56a & b). Flow visualizations confirmed that the flow was not unduly influenced by the side walls. Additionally, the strudel flow was observed to be rotating in the laboratory model similar to in the field, indicating that the basic pattern of the strudel flow was being modelled correctly.

In order to simplify the laboratory study while still providing a realistic model of strudel flow, only the essential and most significant elements of the strudel flows observed in the field were retained. As a result, a non-eroding and smooth Styrofoam (ice) surface, a circular non-eroding hole, a constant ice thickness, a constant under-ice depth, a non-eroding smooth bed surface, and a steady flow were used. The ice thickness and the under-ice depth were held constant throughout the experiments at 0.152 m and 0.201 m, respectively. The strudel hole diameter was offset at 2.0 cm, 5.1 cm and 7.8 cm. These diameters were chosen to represent strudel holes varying between 20 cm and 78 cm in the field. 96 % of the laboratory experiments were conducted with jet Reynolds Number between 5,070 and 62,120 to ensure that the flow was fully turbulent (Crow & Champagne, 1971; Rajaratnam, 1981a). However, a few measurements were performed at Reynolds number as low as 1,260.

The experimental apparatus consists of four tanks connected together as sketched in Figure 3-5. The dimensions of the tanks listed below are stated as (Length x Width x Height). Two water storage tanks were used in this experiment. *Storage Tank #1* (304 x 48 x 40 cm) and *Storage Tank #2* (165 x 98 x 98 cm) were both connected to the pump inlet by a 5.1 cm (2 in) diameter pipe (Figure 3-6a). The ¼ hp electric pump (Monarch Model BVE-S75) provided a maximum water discharge of 3.87 L/s to the *Upstream Tank*. The flow rate from the pump (Q_2) could be systematically varied by a ball valve and was measured using a 5.1 cm (2 in) diameter magnetic flow tube and transducer (Foxboro Model IMT25).

Photographs of the *Strudel Tank* and *Upstream Tank* laboratory setup are presented in Figure 3-7. A three-dimensional scale drawing of the *Upstream Tank* and of the *Strudel Tank* is presented in Figure 3-8 and Figure 3-9. The role of the *Upstream Tank* (26.8 x 49.7 x 35.9 cm), which could be moved vertically, was to reduce the turbulence from the high velocity pipe inflow and to allow the upstream water level to be systematically varied. Inside the *Upstream Tank*, an overflow pipe redirected the excess flow of water, Q_1 , into *Storage Tank #1*, measured using a 2.0 cm (1 in) diameter magnetic flow tube and transducer (Foxboro Model IMT25). The remaining flow from the *Upstream Tank*, Q_0 , was directed into the deep upstream section of the *Strudel Tank* (6,100 x 49.2 x 51.0 cm) where the velocity head was negligible.

Once inside the upstream end of the *Strudel Tank*, the water flowed downstream over the 0.0 % \pm 0.1 % slope 0.152 m thickness Styrofoam cover which modelled an ice cover, and into a circular strudel hole. Three sharp edge circular holes of 2.0, 5.1 and 7.8 cm diameter were fabricated from PVC pipes to model strudel holes of three different sizes (Figure 3-6b). Once under the ice cover, the water flowed downstream into another deep area of the tank where the velocity head was again negligible. The downstream water depth was systematically controlled by a sharp-crested hinged weir (Figure 3-7). After flowing over the weir, the water exited the *Strudel Tank* via the 7.7 cm diameter outlet pipe and then flowed into *Storage Tank #1*.

3.3.1.2 Experimental Procedures

Four measuring tapes, named from upstream to downstream as U tape, I Tape, S Tape and D Tape as presented in Figure 3-9, were installed on the *Strudel Tank* walls to measure the water levels. Visual water level readings from the measuring tapes had a precision of ± 1 mm. The water level tapes were calibrated by introducing water into the *Strudel Tank* while all exits were blocked and a common datum was established when the water was still. The upstream (h_u) and downstream (h_d) water levels were measured from Tape U and Tape D respectively. The downstream water level, controlled by the weir, varied depending on the flow rate such that defining a predetermined downstream water level using the weir was difficult. The hydraulic head difference (H_d) was calculated as the difference between the upstream depth and the downstream depth, $H_d = h_u - h_d$. Collected values of H_d varied between 0.001 m and 0.138 m. The overflow depth (h_o) was taken as the average reading from Tape I and Tape S, the tapes located 50 cm upstream and directly in line with the strudel hole, respectively. Collected values of h_o varied between 0.003 m and 0.139 m.

The discharge into the strudel hole (Q_o) was induced by a hydraulic head difference between the upstream (h_u) and the downstream (h_d) water levels. The discharge flowing into the *Strudel Tank*, and therefore through the strudel hole (Q_o), was calculated as the difference between the inflow into the Upstream Tank and the outflow into the overflow pipe, therefore $Q_o = Q_2 - Q_1$. The inflow rate into the Upstream Tank (Q_2) and out of the Upstream Tank into the overflow pipe (Q_1) were calculated using magnetic flow meters. The magnetic flow meters were calibrated by the manufacturer, Foxboro. However, a calibration check of both flow meters was performed in the laboratory by diverting the entire flow entering the *Upstream Tank* into the overflow pipe such that $Q_1 = Q_2$. This calibration revealed that both flow meters recorded the same discharge rate to a precision of ± 0.01 L/s. Due to equipment availability and for simplicity of the experimental setup, the flow meters were installed in the pipes going from and into the *Storage Tanks* instead of directly measuring the flow rate going into the *Strudel Tank*. It should be noted that for the majority of the experiments, the overflow pipe of the Upstream Tank was not used to convey flow such that Q_1 was 0. Even if this method resulted in a more stable discharge and upstream water level, a

predetermined discharge was difficult to obtain. Collected values of Q_o varied between 0.02 L/s and 3.82 L/s. The average velocity through the circular strudel hole was calculated as $U_o = \frac{Q_o}{\pi d^2/4}$. Calculated values of U_o varied between 0.02 m/s and 1.27 m/s.

The following describes the experimental procedures during a typical experimental run. First, one of the three strudel hole insert was selected and installed in the Styrofoam cover. The weir was then adjusted to obtain a constant downstream water depth and the pump was started and its flow into the *Strudel Tank* was adjusted using the valve. The water level and the flow rates were given time to stabilize and then measurements of the water levels at each tape and of the discharges from the two flow meters were recorded. In the case where a predetermined hydraulic head difference, overflow depth or discharge was required, adjustments to the weir position and to the valve were performed manually by trial and error.

The above mentioned measurements were collected for a total of 176 different runs where the downstream water surface was above the under-ice surface and the results are presented in Appendix A. In addition, for each run it was recorded whether or not the downward flow entrained air under the ice cover, as observed in Figure 3-10. For some of these runs, ADV velocity measurements were performed. Experimental runs were conducted with the downstream water surface below the bottom of the ice cover and this data is tabulated in Appendix B. As strudel are not observed under the latter circumstance in the field, it was not an objective of this thesis to study this flow. However, comparisons of the hydraulics of that flow with empirical equations developed in this study are presented in Appendix B.

3.3.1.3 Dimensional Analysis

The average axial velocity in the hole (U_o) is a function of the hole diameter (d), the ice thickness (t), the hydraulic head difference (H_d), the overflow depth (h_o), the impingement distance (H), the density of water (ρ), the dynamic viscosity (μ), and the gravity (g) such that

$$U_o = f_1(d, t, H_d, h_o, H, \rho, \mu, g) \quad [3-16]$$

The dynamic viscosity (μ), density (ρ) and gravity (g) are all assumed to be constant ($\mu = 1.002 \times 10^{-3} \text{ N} \cdot \text{s}/\text{m}^2$, $\rho = 998.2 \text{ kg}/\text{m}^3$ and $g = 9.81 \text{ m}/\text{s}^2$). The ice thickness and the impingement distance were held constant at 0.152 m and 0.201 m respectively for all the experimental runs. The independent variables that were varied were the hole diameter (d), the hydraulic head difference (H_d) and the overflow depth (h_o).

The Buckingham II theorem was applied with the hole diameter, the dynamic viscosity and the gravity selected as the repeating variables such that,

$$\frac{U_o}{\sqrt{gd}} = f_2 \left(\frac{t}{d}, \frac{H_d}{d}, \frac{h_o}{d}, \frac{H}{d}, \frac{\rho\sqrt{gd^3}}{\mu} \right) \quad [3-17]$$

Manipulation of the variables results in common non-dimensional variables defined as

$$C_d = \frac{U_o}{\sqrt{2gH_d}} = f_3 \left(\frac{t}{d}, \frac{H_d}{d}, \frac{h_o}{d}, \frac{H}{d}, Re = \frac{\rho U_o d}{\mu} \right) \quad [3-18]$$

where:

C_d = the discharge coefficient; and

Re = the Reynolds number.

These non-dimensional parameters were calculated for all the collected data and are presented in Appendix A and Appendix B.

3.3.2 Velocity Measurements

3.3.2.1 General

The ADV was used to measure the three-dimensional, counter-clockwise, free-surface vortex jet velocities below the ice cover for nine different runs, identified in

Table 3-1. These runs were carefully selected in order to obtain measurements for a large range of axial velocities (U_o) varying between 0.126 and 0.345 m/s and a range of overflow depth / hole diameter (h_o/d) ratios varying between 0.26 and 1.78. All the velocity measurements were performed with a 7.8 cm diameter hole giving an impingement distance of $2.58d$ which is defined as a short impingement distance. Additionally, the ice thickness / hole diameter (t/d) ratio was constant and equal to 1.95. The main objective of these measurements was to identify the effects of the free-

surface vortex's vorticity on the strudel flow behaviour below a circular hole both in the free jet region and the impingement region of the flow development region of the jet.

Any reference to the coordinate system, including the experimental data in all appendices, refers to the global coordinate system presented in Figure 3-11, and not the local (ADV) coordinate system, unless otherwise noted. In the global coordinate system, the x-axis is the lateral direction, the y-axis is the longitudinal direction, and the z-axis is the vertical direction (Figure 3-12). In the local coordinate system, the x-axis is the vertical direction, the y-axis is the lateral direction, and the z-axis is the longitudinal direction (Figure 3-12). The origin of the global coordinate system is located on the centerline of the circular hole in the x-y plane at the bottom of the ice cover as shown in the bottom-left inset of Figure 3-8. The corresponding velocities in the (x, y, z) direction are (U_x, U_y, U_z). In some cases, the velocities were transformed into the cylindrical coordinate system (Figure 3-11) and were kept at the same centerline origin such that the corresponding velocities in the (r, θ , z) direction are (V_r, V_θ, V_z).

Table 3-1 Experimental run numbers for the ADV velocity measurements. The information in parenthesis refers to ($U_o, h_o/d$).

Average Axial Velocity, U_o (m/s)	Overflow Depth / Hole Diameter ratio, h_o/d		
	0.26 – 0.55	1.09 – 1.13	1.63 – 1.78
0.126	Run no. 207 (0.126, 0.26)	Run no. 268 (0.126, 1.12)	Run no. 269 (0.126, 1.63)
0.226	Run no. 261 (0.226, 0.55)	Run no. 260 (0.226, 1.13)	Run no. 267 (0.226, 1.67)
0.337 - 0.345	Run no. 205 (0.337, 0.45)	Run no. 195b (0.345, 1.09)	Run no. 266 (0.345, 1.78)

3.3.2.2 Experimental Setup

The Vectrino (Nortek) is a high resolution Acoustic Doppler Velocimeter (ADV) that measures the three-dimensional water velocity using the Doppler effect. It transmits a short pulse of sound, receives its echo, and converts the change in pitch or frequency of the echo into a velocity (Vectrino Velocimeter's User Guide, 2009). The Vectrino ADV probe, which is made of titanium and contains a central transmitting transducer and four receive transducers, can sample the velocities at rates up to 200 Hz. The ADV has a

measurement range varying between 0.01 and 4 m/s and has a velocity measurement accuracy of $\pm 0.5\%$ of the measured value ± 1 mm/s (Vectrino Velocimeter's User Guide, 2009). Seed (Dirt or small particles) is usually added to the water to increase the signal-to-noise ratio (SNR) and the correlation coefficient, therefore, the quality of the collected data. It is important to obtain a large correlation coefficient during the data collected such that the velocities are precise and accurate.

For this study, the ADV was used to obtain a three-dimensional structure of the velocity field of the strudel flow below the ice cover. The ADV probe, pictured in Figure 3-13a, was mounted on a two dimensional traverse (Figure 3-13b) that allowed it to be positioned in the lateral (x) and vertical (z) directions with an accuracy of 0.01 mm. The entire traverse was mounted on aluminum (Minitec) rails which allowed it be positioned in the longitudinal (y) direction to an accuracy of ± 1 mm using a tape measure. The ADV probe was installed under the ice surface in a horizontal position such that the red receiver was pointing upwards and towards the upstream end of the tank. In that orientation, the ADV's x-, y- and z-axis are defined as illustrated in Figure 3-12. Accurate positioning and alignment of the ADV and of its sampling volume was essential to obtain accurate measurements of the three-dimensional velocities under the ice cover.

3.3.2.3 Experimental Procedures and Data Collection

The ADV velocity measurements were recorded using the *Vectrino Plus* software. During the data collection, the ADV sampling rate was set to 200 Hz and the transmit length to 1.8 mm. The diameter of the sampling volume was fixed at 6 mm and its height was varied from 3 to 15 mm. Addition of SPHERICEL[®] Hollow Glass Spheres (Potters Industries Inc., Valley Forge, PA, USA) to the water, with a mean diameter of approximately 15 microns, was done to increase the quality of the collected data. These settings resulted in correlation factors exceeding 80 %. Experiments using the ADV were performed without air entrainment as air bubbles significantly decreased the correlation below 80 %.

All velocity measurements were collected for the 7.8 cm diameter hole such that the cross-sectional area of the ADV sampling volume was much smaller (less than 2%) than the cross-sectional area of the circular hole. First a steady flow was established as

described above. The sampling volume of the ADV was then moved to a specified position. A minimum of three minutes of ADV data was collected at each position to ensure that accurate time-averaged values of the three velocity components were obtained. It was found that a time period of three minutes was sufficient to obtain accurate measurements of the mean velocities and standard deviations, as presented in Figure 3-14. For selected fixed z-distances, velocity measurements were made along the x- and y-axis of the coordinate system. For some runs, velocity measurements were collected on the entire x-y plane. In the x-y plane, the lateral (x) and longitudinal (y) velocities were transformed into horizontal velocity vectors (U_{xy}). The magnitude of the horizontal velocity vector can be computed in two ways as shown below,

$$U_{xy} = \sqrt{V_{\theta}^2 + V_r^2} \qquad U_{xy} = \sqrt{U_x^2 + U_y^2} \qquad [3-19]$$

where:

- U_{xy} = the horizontal velocity vector along the xy-plane;
- U_x = the velocity in the x-direction; and
- U_y = the velocity in the y-direction.

The measured velocities were analysed using the *Explore V* software and data that deviated from the average velocity by more than three standard deviations were rejected. About 0.3 % of the collected data were rejected using this criterion. The remaining velocity data were time-averaged over the sampling duration and the time-averaged velocities are presented in Appendix C. Near the vortex centerline, the velocities in the x- and y-direction were often observed to switch from negative to positive due to slight radial movements of the vortex caused by instabilities in the flow. Therefore, the average velocities in the x- and y- direction, less than approximately 0.3 R from the typical vortex centerline location, may be slightly less accurate. In order to facilitate comparisons, the ADV velocity measurements were transformed into non-dimensional variables, also presented in Appendix C. The x- and y-distances were divided by the circular hole radius (R), and the z-distance was divided by the hole diameter (d). The lateral, longitudinal, axial and horizontal velocities were divided by the average axial velocity in the strudel hole (U_o).

3.4 Results and Discussion

3.4.1 Flow Visualisation of the Free-Surface Vortex Flow

Digital images and videos of the strudel vortices, both above and below the ice cover, were taken during several experimental runs. For some of these runs, red dye was used as a tracer so that the flow streamlines could be observed. The purpose of the flow visualisation experiments was to improve our understanding of the behaviour and properties of this irrotational flow both above and below a fixed ice cover. It was a concern in the selection of the tank that the channel width might have been too small such that the tank walls might have been too close to the strudel hole, therefore affecting the flow pattern towards the strudel. From qualitative observations, the walls of the tank did not seem to greatly affect the flow pattern around and into the strudel hole.

For larger overflow depths, the free surface signature / dip of the vortex was observed to be of different sizes and shapes such that the vortices were classified into four vortex types. The first vortex type did not produce a dip even though a flow rotation was observed. This type was observed for the smallest flows and at larger overflow depths. The second vortex type was observed to have a shallow dip which did not entrain air under the ice cover (Figure 3-15a). The third vortex type had a deeper and wider dip which did not penetrate into the hole but sometimes entrained air under the ice cover (Figure 3-15b). The fourth type had a very deep dip which stretched inside the hole and air bubbles were continuously entrained under the ice cover (Figure 3-15c). For smaller overflow depths, the bottom of the dip was observed to be either above (Figure 3-16a) or extend into the hole such that it fills the majority of the hole width (Figure 3-16b). It was observed that the dip became deeper and tended to produce more air entrainment as the flow rate increased, and the overflow depth decreased. For most of the runs, the vortex was shifted slightly towards the downstream side of the hole, and to the left side with respect to the flow direction (for counter-clockwise vortices) as shown in Figure 3-17a). This is likely due to the fact that as the counter-clockwise water flowed from the upstream portion of the tank into the hole, it had a significant velocity component in the downstream and left direction. In some few cases, the vortex was pushed so far downstream that the core of the vortex was curved (Figure 3-17b).

For most of the runs, the vortex was rotating counter clockwise. However, for smaller overflow depths, the rotation was often clockwise. In one case (Run no.261), the vortex changed direction three times in a time period of only one minute. The reason for the change in rotation direction is unknown and was not studied for this thesis but is hypothesised to be caused by the geometry of the strudel tank apparatus and by changing conditions at the upstream end of the tank. Additionally, the vortex rotation direction could easily be changed by stirring the flow in the opposite direction. However, after being forced to reverse direction, the vortex would eventually reverse and rotate in the original direction.

The flow visualisation revealed that the largest tangential velocities were concentrated near the core of the vortex, as shown in Figure 3-18. Away from the vortex centerline, the water flowed towards the strudel hole without much rotation as shown in Figure 3-19. This flow behaviour is consistent with the velocity distribution in an irrotational vortex where the tangential velocity is inversely proportional to the radius (Kundu *et al.*, 2002). Observations of dye streaks injected near the strudel hole are sketched in Figure 3-20. This sketch suggests that at the vortex core, the water rotates rapidly as it flows into and through the hole and that away from the core and near the ice surface, the water flows into the hole radially without much rotation. Observation of dye streaks injected at the water surface at the upstream end of the tank, sketched in Figure 3-21, indicate that the flow near the water surface was influenced to a much greater extent by the vortex. That is, the flow was observed to be rotating significantly at larger radial distances.

The free surface vortex flow beneath the ice cover was also visualized using dye. Figure 3-22 shows that the free-surface vortex jet outflow beneath the ice cover increases in diameter with increasing axial distance such that the shear layer at the interface of the vertical flow (red water) and the ambient water (clear water) was well defined. Additionally, the dye which was inserted into the core of the vortex at the water surface was well mixed when it exited the strudel hole below the ice cover. As the jet approached the perpendicular boundary, it entered in the flow impingement region and was redirected radially as a wall jet.

3.4.2 Free-Surface Vortex Flow beneath the Ice Cover

3.4.2.1 Overview

Velocity measurements were collected at four different axial distances below the strudel hole exit at $z = 3.3$ cm, 7.3 cm, 12.3 cm and 17.0 cm. The first two correspond to $z/d = 0.42$ and $z/d = 0.94$ which are in the free jet region. The third location is in the transition region at $z/d = 1.58$ ($z'/d = 1.00$) and the fourth is in the impingement region of the jet at $z/d = 2.18$ ($z'/d = 0.40$). The majority of the velocity measurements were collected along the x- and y-axis of the hole at each axial distance. However, at six occasions, the measurements were collected over the x-y plane in order to obtain a more complete picture of the flow field. In two of those occasions, only half of the plot is presented in the figures as the velocities were only measured in the positive (downstream) y-direction. In these x-y plots, the axial velocities were linearly interpolated / extrapolated by the Origin Pro software and the position of the vortex core was approximated from the rotation direction and magnitude along the horizontal plane. The complete set of profile and x-y plane plots are included in Appendix D.

It should be noted that due to the small impingement height, the velocity measurements in the flow development region were only measured up to a z/d value of 0.94 before the jet entered the transition region and the impingement region. Some scatter is observed in the profile plots discussed below and presented in Appendix D due to instability of the vortex position and of the flow inside the strudel hole. However, velocity measurements were collected for more than three minutes at each data point and averaged to limit this effect. This scatter could also result from the variation of the overflow depths and axial velocities between experimental runs.

3.4.2.2 Free Jet Region

Immediately below the hole exit is the free jet region of the flow where velocity measurements were collected at z/d distances of 0.42 and 0.94. First, as observed from the x-y plots of Figure 3-23, Figure 3-24, Figure 3-25 and Figure 3-26, the vortex core in the free jet region was located slightly to the left side of the hole, with respect to the overflow direction, and slightly downstream of the hole centerline at an average coordinate of $(x/R, y/R) = (-0.3 \pm 0.1, 0.2 \pm 0.2)$. These observations correlate with the

observed vortex position above the ice surface. As the centerline of the vortex was not at the centerline of the hole, the interpretation of the velocity profiles in this region must be made carefully. In the axial velocity profiles, presented below, the theoretical fully turbulent jet Equation 3-4 was plotted for comparison.

For $z/d = 0.42$, the axial velocities in the jet core ($r < 0.8R$), presented in Figure 3-27 and Figure 3-28, had average magnitudes varying between $0.9 U_o$ and $1.1 U_o$ with a minimum of $0.65 U_o$ (Run no. 260) and a maximum of $1.15 U_o$ (Run no. 195b). From the fully turbulent jet theory, these average velocities were expected to be $1.0 U_o$. Beyond the shear layer ($r > 0.8R$), the axial velocities decreased rapidly for an increasing radial distance such that they had magnitudes of approximately $0.1 U_o$ at $r = 1.25R$. Along the lateral (x) axis, the spread of the flow in the radial direction was slightly less than estimated by the fully turbulent jet equation 3-4. Along the longitudinal (y) axis, the velocity profile was observed to be skewed towards the downstream edge of the hole. This skew might have been caused by precision error in positioning the ADV probe during the initial setup, but was most likely caused by the flow direction both above and below the ice cover which was towards the positive y-direction.

For $z/d = 0.94$, the axial velocities in the jet core ($r < 0.8R$), presented in Figure 3-29 and Figure 3-30, were measured to have an average magnitude varying between $0.8 U_o$ and $1.0 U_o$. From the theory, these average velocities were expected to be $1.0 U_o$. Smaller axial velocities along the x-axis were observed between distances of $-0.8R$ and $-0.1R$ where a minimum velocity of $0.4 U_o$ (Run no. 195b) was recorded. The maximum axial velocities were measured near the downstream edge of the hole at approximately $y = 0.8R$ with a magnitude of $1.15 U_o$ (Run no. 266). Beyond the shear layer ($r > 0.8R$), the axial velocities decreased rapidly such that they varied between $0.15 U_o$ and $0.35 U_o$ at $r = 1.25R$. Once again, for the majority of the runs, the axial velocities along the x-axis were smaller than estimated from equation 3-4. Along the y-axis, the flow was observed to spread more rapidly and a skew was again observed towards the downstream edge of the hole.

Observations of the four velocity plots along the x-y plane for $z/d = 0.42$ in Figure 3-23 and for $z/d = 0.94$ in Figure 3-24, Figure 3-25 and Figure 3-26 show that the axial velocities at the vortex core, which has a diameter of approximately $0.5R$, were usually

significantly less than the surrounding flow. The minimum axial velocities at the vortex core varied between $0.5 U_o$ ($z/d = 0.42$ for Run no. 195b) and $0.9 U_o$ ($z/d = 0.94$ for Run no. 195b). From the theory of the fully turbulent jet, these velocities would have been expected to have magnitudes of $1.0 U_o$ as they are located in the core of the jet. The smaller axial velocities at the vortex core explain the scatter in the velocities presented in the profile figures mentioned earlier. From these x-y plots, the maximum axial velocities, varying between $1.0 U_o$ (Run no. 260) and $1.15 U_o$ (Run no. 195b), were mostly located along the downstream edge of the hole at approximately $y = 0.7R$. From those plots, the axial flow was again observed to spread more rapidly in the y-direction, especially downstream of the hole, compared to the x-direction. The rapid decrease in velocity beyond the shear layer ($r > 0.8R$) is also well observed from those plots.

The counter-clockwise rotation of the free-surface vortex flow is clearly observed in the x-y plots presented in Figure 3-23, Figure 3-24, Figure 3-25 and Figure 3-26. This rotation was even observed to extend outside the hole boundary. From these plots and from horizontal velocity profiles presented in Appendix D, the maximum horizontal velocities were mostly observed at the proximity of the vortex core with maximum magnitudes ranging from $0.45 U_o$ (Run no. 267) to $0.65 U_o$ (Run no. 260) at $z/d = 0.42$ and from $0.20 U_o$ (Run no. 267) to $0.45 U_o$ (Run no. 195b) at $z/d = 0.94$. At the center of the vortex core, horizontal velocities were observed to be of smaller magnitudes, possibly due to instability in the vortex location which caused lateral and longitudinal velocities to transition back and forth from positive to negative. Due to the averaging method used, a positive and negative velocity of the same magnitude cancelled each other, thus the reason for the smaller presented velocities. Away from the vortex core, the horizontal velocity vectors were generally of smaller magnitudes. These velocities decreased with increasing radial distance from the hole boundary with an average magnitude of $0.04 U_o$ to $0.12 U_o$ at $r = 1.25R$.

3.4.2.3 Transition Region

The velocity measurements made at $z/d = 1.58$ ($z'/d = 1.00$) are described to be in the transition region. Even if the impingement region of the jet is said to start between a z'/d value of 1.2 (Beltaos & Rajaratnam, 1977) and 2.2 (Tani & Komatsu, 1964), the

impinging boundary did not seem to affect the free jet flow behaviour until a z'/d distance between 1.00 and 1.64. As the empirical equations describing the impingement region of the fully turbulent jet are only valid for $z'/d < 0.8$, no comparisons with these equations were made. For that reason, the axial velocities were compared with equation 3-4 developed for the fully turbulent jet in the free jet region.

For $z/d = 1.58$, the axial velocities in the core region of the jet ($r < 0.6R$), presented in Figure 3-31 and Figure 3-32, had scattered magnitudes varying between $0.35 U_o$ (Run no. 260) and $0.95 U_o$ (Run no. 267). The smallest velocities, which were in majority located along the negative x-axis, were significantly smaller than the velocities of $1.0 U_o$ estimated by the theory of fully turbulent jets in the free jet region. These smaller axial velocities could result from both the effect of the impinging boundary which redirected the flow radially, and from the proximity of the vortex core which had smaller axial velocities in the free jet region. Beyond the shear layer ($r > 0.6R$), a general observation was that axial velocities decreased rapidly for an increasing radial distance such that, along the x-axis, they had magnitudes varying between $0.2 U_o$ and $0.35 U_o$ at $r = 1.25R$. The spreading the flow was more significant along the y-axis, where axial velocities were maximum at the downstream edge of the hole with magnitudes of approximately $0.85 U_o$ at $y = 1.0R$. The measured axial velocities along the x-axis are slightly overestimated by equation 3-4 while axial velocities along the y-axis are underestimated by the equation.

One x-y plot of the axial and horizontal velocities was made for Run no. 195b at $z/d = 1.58$ and is presented in Figure 3-33. Only 15 data points were collected such that this plot only represents a rough estimate of the velocity distribution. Along the y-axis, maximum axial velocities with magnitudes of $0.9 U_o$ were observed along the downstream edge of the hole between y-distance of $0.5R$ and $1.0R$. Along the x-axis, axial velocities varied between $0.4 U_o$ and $0.7 U_o$ within the hole boundaries. No distinct vortex core was observed, as was observed for the free jet region, but the irrotational flow was clearly seen to be rotating in a counter-clockwise direction. From the horizontal velocity profiles presented in Appendix D, the horizontal velocities inside the hole boundaries had maximum magnitudes varying between $0.15 U_o$ (Run no. 267) and

$0.30 U_o$ (Run no. 266). No conclusions were made with regards to the horizontal velocities outside the hole boundaries due to a lack of collected data.

3.4.2.4 Impingement Region

A number of velocity measurements were performed close to the boundary at a z/d distance of 2.18 ($z'/d = 0.40$) where the empirical equations describing the impingement region of the fully turbulent jet flow should be valid. Equation 3-13 estimates the axial velocities beyond the shear region of the jet and equation 3-8 estimates the centerline velocity of the jet, which is the smallest velocity in the core region of the jet. Equation 3-10 defines the radial velocities in the impingement region.

For $z/d = 2.18$, the axial velocities along the x- and y-axis, presented in Figure 3-34 and Figure 3-35, were observed to be scattered. However, some general trends were observed. First, the majority of the axial velocities were smaller than predicted by equations 3-13 and 3-8. The axial velocities in the core region of the flow were usually smallest at the jet centerline with minimum magnitudes varying between $0.0 U_o$ (Run no. 195b) and $0.4 U_o$ (Run no. 267), ignoring the runs where full profiles were not performed. For Run no. 266, the minimum axial velocity was recorded slightly beside the hole centerline along the x-axis at $x/R = -0.5$. The maximum velocities varied between magnitudes of $0.55 U_o$ (Run no. 260) and $0.75 U_o$ (Run no. 260) at distances of $0.5R$ to $1.1R$ along the x- and y-axis. These axial velocities were obviously affected by the impinging boundary as they were much smaller than for the fully turbulent jet in the free jet region, estimated as $1.0 U_o$ for $r < 0.5R$. Furthermore, the axial velocities were also smaller than estimated by both equation 3-13 and 3-8. These two equations predicted a minimum centerline axial velocity of $0.6 U_o$ with a maximum of $0.7 U_o$ at a distance of $0.8R$ from the hole centerline. As a result, these equations do not well describe the free-surface vortex axial velocities in the impingement region.

The radial velocities, presented in Figure 3-36 and Figure 3-37 are observed to be very well represented by equation 3-10 with a correlation coefficient (R) of 0.81 along the x-axis and 97 % along the y-axis, for a combined correlation coefficient (R) of 0.85. As seen from Figure 3-36, a difference of $0.13 U_o$ between the radial velocity of run no. 195b at $x = -0.5R$ and the theoretical equation was observed, probably due to

measurement errors. At the jet centerline, the radial velocities varied between $0.0 U_o$ and $0.1 U_o$. Along the x-axis, the radial velocities were continuously increasing for increasing radial distance up to $x = 1.25R$, with a maximum of $0.3 U_o$. Velocities were not measured beyond this x-distance. Along the y-axis, the radial velocities had a maximum of approximately $0.25 U_o$ at $y = 1.0R$. Beyond this distance, the radial velocities seemed to be slightly decreasing but were mostly constant.

The tangential velocities presented in Figure 3-38 and Figure 3-39 were smaller than for the free jet region but were still observed to rotate in a counter-clockwise direction. The maximum tangential velocities varied between $0.05 U_o$ and $0.2 U_o$ at an approximate distance of $1.25R$ from the jet centerline. The minimum velocities were recorded at the jet centerline with magnitudes of $0.0 U_o$ to $0.1 U_o$. The rotation induced by the free-surface vortex flow is also observed from the x-y plot of Figure 3-40. However, the arrows are mostly pointing in the radial direction as radial velocities surpassed the tangential velocities. The formation of a stagnation point in the axial direction is also observed at the jet centerline.

3.4.2.5 Summary

The irrotational jet flow induced by a free-surface vortex and by hydraulic head difference principles, with a significant upstream to downstream flow direction, was found to have similarities but also significant differences with the fully turbulent jet flow in the free jet region, the transition region and the impingement region.

The following states the three key findings of the free-surface vortex flow in the free jet region. First, axial velocities at the core of the vortex were measured to be significantly smaller than the surrounding velocities. Second, the horizontal velocities were usually largest at the proximity of the vortex core where a strong rotation was observed. Third, the spread of the flow was observed to be larger in the longitudinal direction, especially along the downstream edge of the hole where a skew was observed, and it was smaller along the lateral axis. As a result, the axial velocities estimated from the empirical equation 3-4 were underestimated in the longitudinal (y) direction and overestimated in the lateral (x) direction. To summarize, the flow profile of the free-surface vortex jet in the free jet region was similar to the fully turbulent jet, with the addition of a significant

rotation throughout the entire cross-section of the jet and smaller velocities at the vortex core.

In the transition and impingement region, the following main observations were made. First, the axial flow was observed to be smaller than estimated by the fully turbulent jet equation 3-4 for the free jet region and by equations 3-8 and 3-13 for the impingement region. Furthermore, a stagnation point seemed to form along the jet centerline. Even though the irrotational jet followed the same velocity pattern as predicted by equation 3-8 and 3-13, that is having minimum axial velocities at the jet centerline and maximum axial velocities near the hole boundary, the equations did not accurately represent the jet velocity distribution in the axial direction as there was too much scatter. However, the radial velocities were well characterized by the empirical equation 3-10 with a correlation coefficient (R) of 0.85. Furthermore, small tangential velocities were still observed but the radial component of the flow was more significant.

3.4.3 Relation between the Hydraulic Parameters of the Free-Surface Vortex Flow

In an attempt to find relationships between the six non-dimensional II parameters (C_d , Re , $\frac{t}{d}$, $\frac{H_d}{d}$, $\frac{h_o}{d}$, $\frac{H}{d}$), the parameters were plotted versus one another for a total of 15 graphs. Most plots did not show any relation or too few data were collected to obtain a relation. However, two graphs were of interest and they are discussed below. These two graphs are the plots of the discharge coefficient versus the Reynolds Number and of the discharge coefficient versus the overflow depth / hole diameter ratio.

The discharge coefficients (C_d) are plotted versus the Reynolds Numbers (Re) in Figure 3-41. (The complete dataset of C_d and Re is presented in Appendix A). There is a lot of scatter in the data but one obvious trend is observed. As Re increases, C_d approaches a value of 0.6 to 0.8 for each t/d value. For $t/d = 2.98$ and $Re > 20,000$, C_d is approximately constant and equal to 0.66-0.80. For $t/d = 7.6$, $C_d = 0.77$ for $Re > 15,000$. For $t/d = 1.95$ there is a lot of scatter but the trend is that $C_d = 0.56-0.74$ for $Re > 40,000$. Johnson (1985) stated that the discharge coefficient increases with an increase in the Reynolds Number up to a critical value of 25,000 where the discharge coefficient becomes constant. The relations made by Johnson (1985) were not observed from the

collected data but a constant discharge coefficient for larger Reynolds numbers was in fact observed. It should be noted that the accuracy of Johnson's (1985) data collection is uncertain because the author calculated discharge coefficient values larger than 1.0 which is theoretically not possible.

The best relation between the non-dimensional variables was between the discharge coefficient (C_d) and the overflow depth / hole diameter (h_o/d) ratio, presented in Figure 3-42 (The complete dataset of C_d and h_o/d is presented in Appendix A). The graph in Figure 3-42 shows that the discharge coefficient varies as a function of the overflow depth / hole diameter ratio. At small h_o/d ratios, $h_o/d < 0.5$, the C_d increases very rapidly. For $0.5 < h_o/d < 0.8$, C_d continues to increase but at a slower rate and for large h_o/d ratios, $h_o/d > 0.8$, C_d approaches a constant maximum value of 0.74. There is some scatter in the C_d data and the standard deviation of the data in this range ($h_o/d > 0.8$) is 0.07. It should be noted that this constant maximum value of C_d may only be applicable to this experimental set-up. It is quite possible that it will be different for strudel in the field or even for different laboratory set-ups. Additional research is required to investigate this issue.

The following empirical equation was fitted to the data in Figure 3-42,

$$C_d = 0.74 - \exp(-8 \cdot (h_o/d)^{1.3}) \quad \text{valid for } (h_o/d) > 0.1 \quad [3-20]$$

with a correlation coefficient (R) of 0.89. The largest scatter was observed for small hydraulic head difference / hole diameter (H_d/d) ratios, likely due to the occurrence of larger errors when measuring H_d values. For the larger H_d/d values, the scatter mostly results from other environmental factors such as the presence of large free-surface vortex dips and air entrainment which reduced the flow capacity of the hole. Combining equation 3-20 with this equation, $C_d = U_o/\sqrt{2gH_d}$, gives the following equation,

$$U_o = [0.74 - \exp(-8 \cdot (h_o/d)^{1.3})] \cdot \sqrt{2gH_d} \quad \text{valid for } (h_o/d) > 0.1 \quad [3-21]$$

which can be used to estimate the average velocity in a circular strudel hole as a function of the hydraulic head difference, overflow depth and hole diameter.

As sketched in Figure 3-43, a critical h_o/d ratio of approximately 0.8 exists above which the entire cross-sectional area of the circular hole cross-sectional area is being used to

convey the flow and as a result C_d is constant and at its maximum value. Below a critical h_o/d value of 0.5, sketched in Figure 3-44, C_d was observed to decrease suggesting that the overflow depth was so shallow that the flow into the strudel hole was constricted. Therefore, it is hypothesized the hole was not used at its full capacity such that a stagnant or weak vertical flow was present at the centerline of the hole at the hole entrance. Only one velocity profile plot (Run no. 261) shown in Figure 3-29 shows the axial velocities below the ice cover for a small h_o/d ratio at which a slight velocity deficit at the centerline is observed ($0.8 U_o$) compared to the maximum axial velocities near the edges of the hole ($0.9 U_o$). However, this deficit might be caused by the presence of a vortex which was observed to significantly reduce the axial velocities at its core. Consequently, a lack of ADV velocity measurements below the ice cover for small h_o/d ratios meant that this hypothesis could not be validated. Furthermore, ADV measurements could not be performed above the hole due to the small overflow depth constraint, or inside the hole as the circular holes were too small to perform adequate ADV measurements.

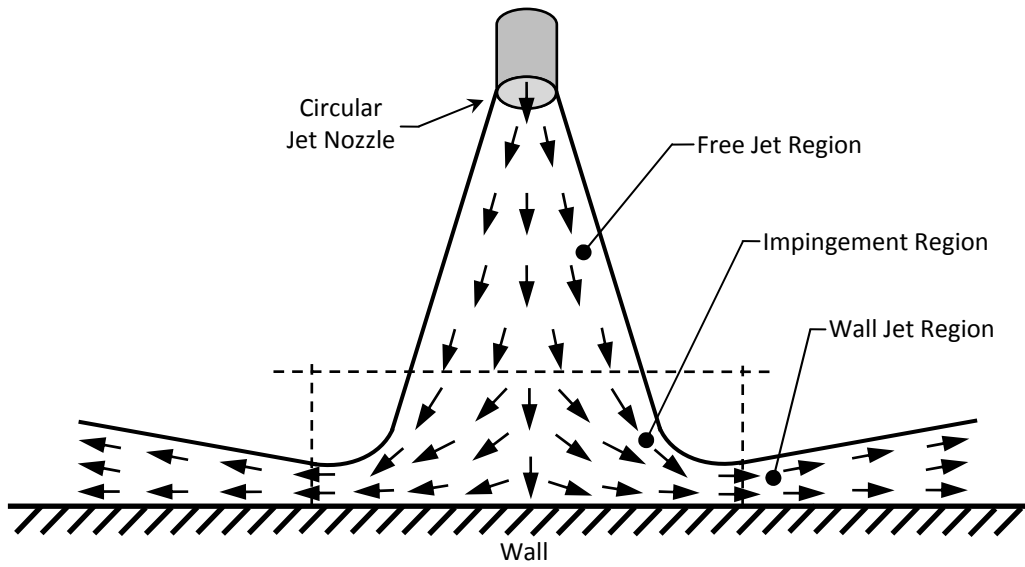


Figure 3-1 Flow regions of a jet impinging on a perpendicular wall (adapted from Beltaos & Rajaratnam, 1977).

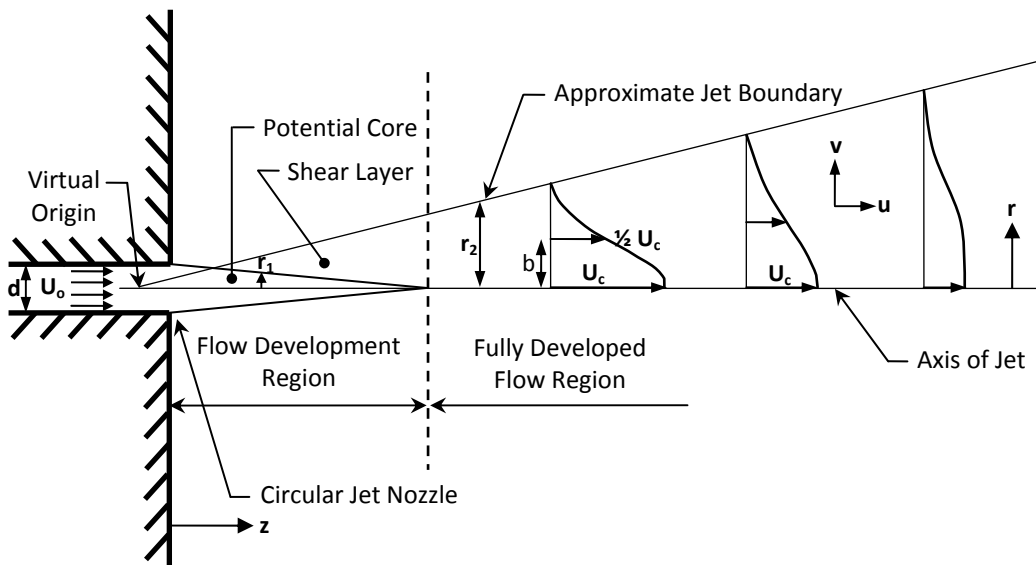


Figure 3-2 Free jet region of a circular turbulent jet (adapted from Rajaratnam, 1987).

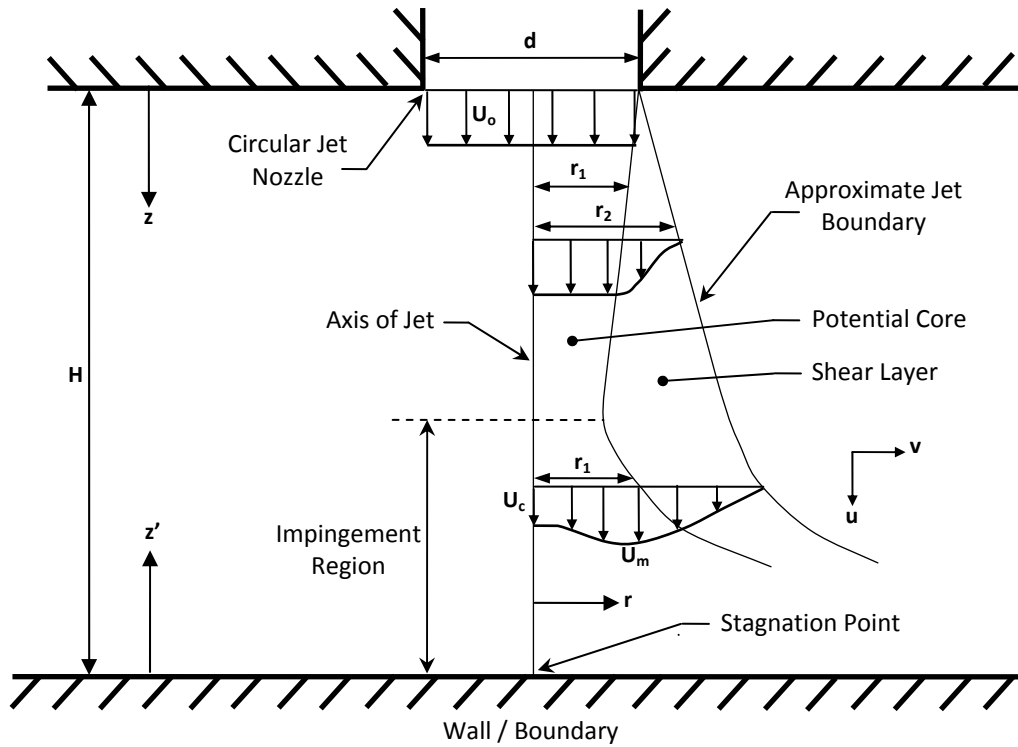


Figure 3-3 Impingement region of a jet hitting a perpendicular wall at a small impingement height (adapted from Beltaos & Rajaratnam, 1977).

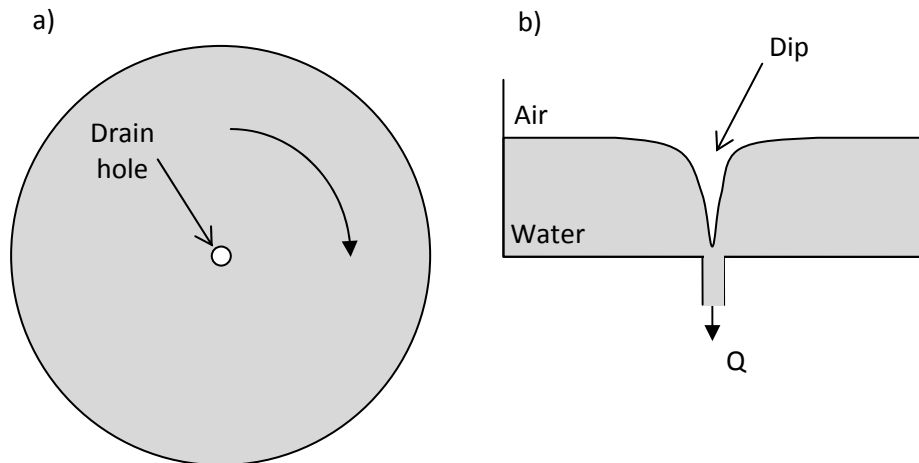


Figure 3-4 a) Top view and b) side view of a typical bathtub vortex experimental setup (adapted from Lubin and Springer, 1967).

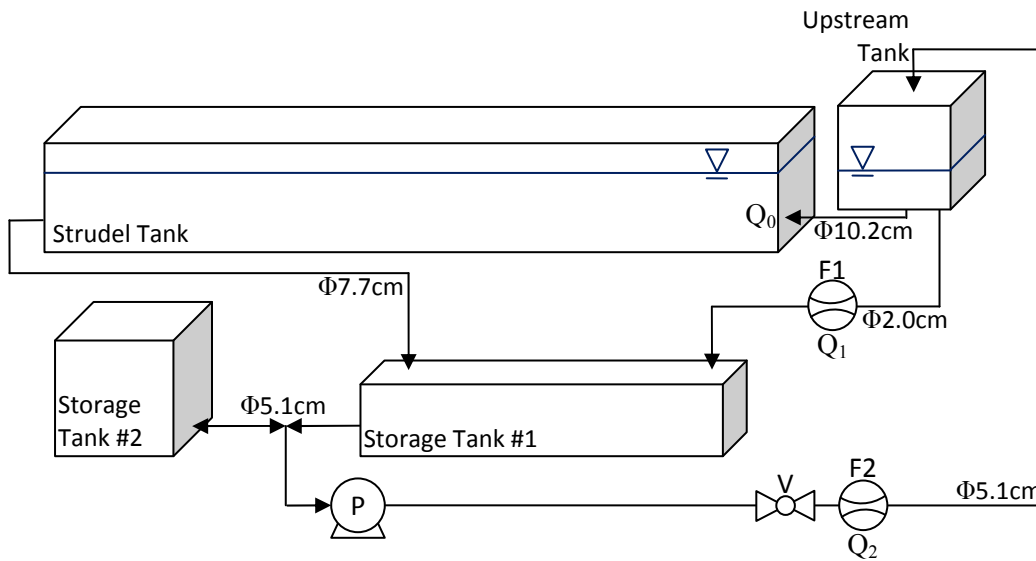


Figure 3-5 Sketch of the physical experiment setup with the corresponding pipe diameters (Φ). The arrows indicate the flow direction. P is the pump, V is the valve, F1 is the flow meter measuring Q_1 , F2 is the flow meter measuring Q_2 .

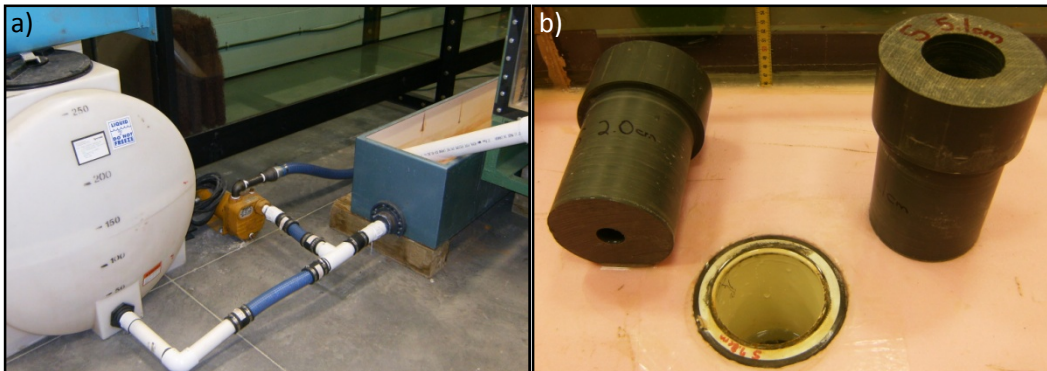


Figure 3-6 a) *Storage Tank #2* (left), *Storage Tank #1* (right) and pump (center). b) Strudel hole diameter inserts of diameter 2.0 cm, 7.8 cm and 5.1 cm (from left to right).



Figure 3-7 Picture of the *Upstream Tank* and of the *Strudel Tank*. The flow direction is from right to left.

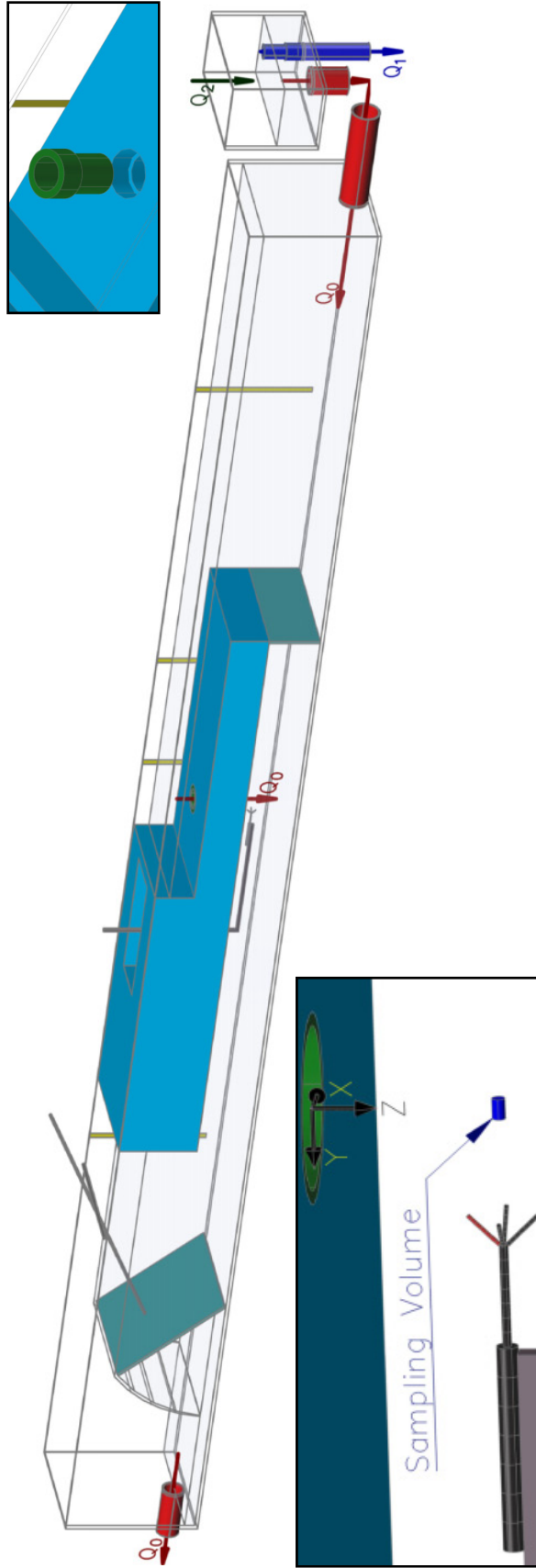


Figure 3-8 Three-Dimensional view of the *Upstream Tank* (right) and of the *Strudel Tank* model. Bottom-left Inset: ADV probe setup under the circular strudel hole. Top-right Inset: Circular strudel hole insert.

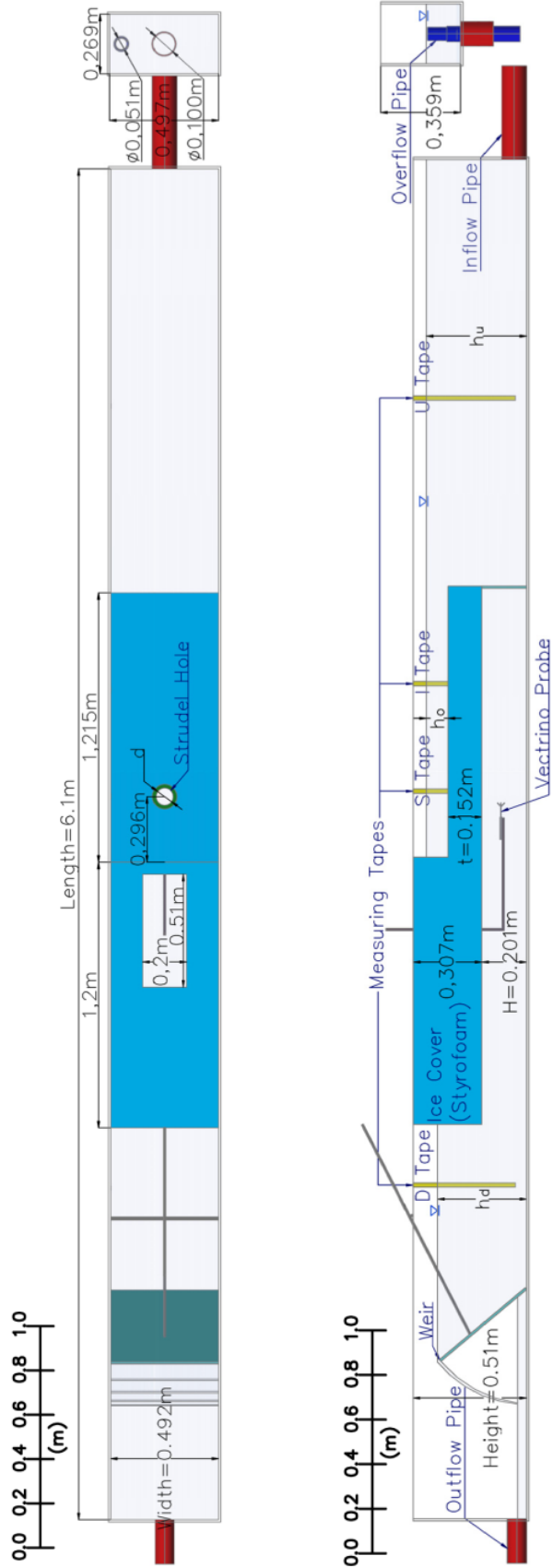


Figure 3-9 Top view and side view of the *Upstream Tank* (right) and of the *Strudel Tank*.

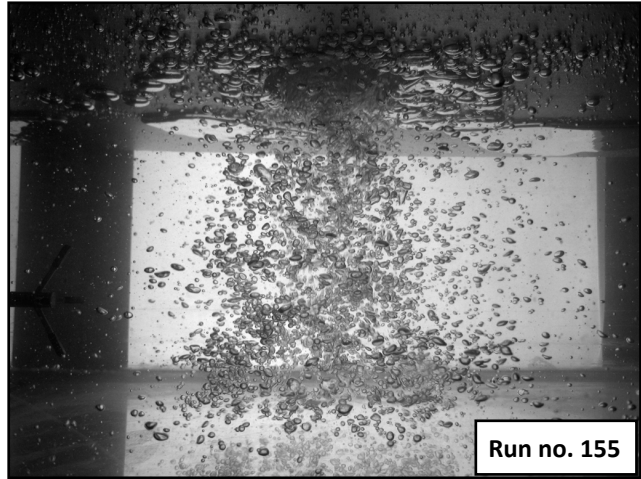


Figure 3-10 Air entrainment below the ice cover.

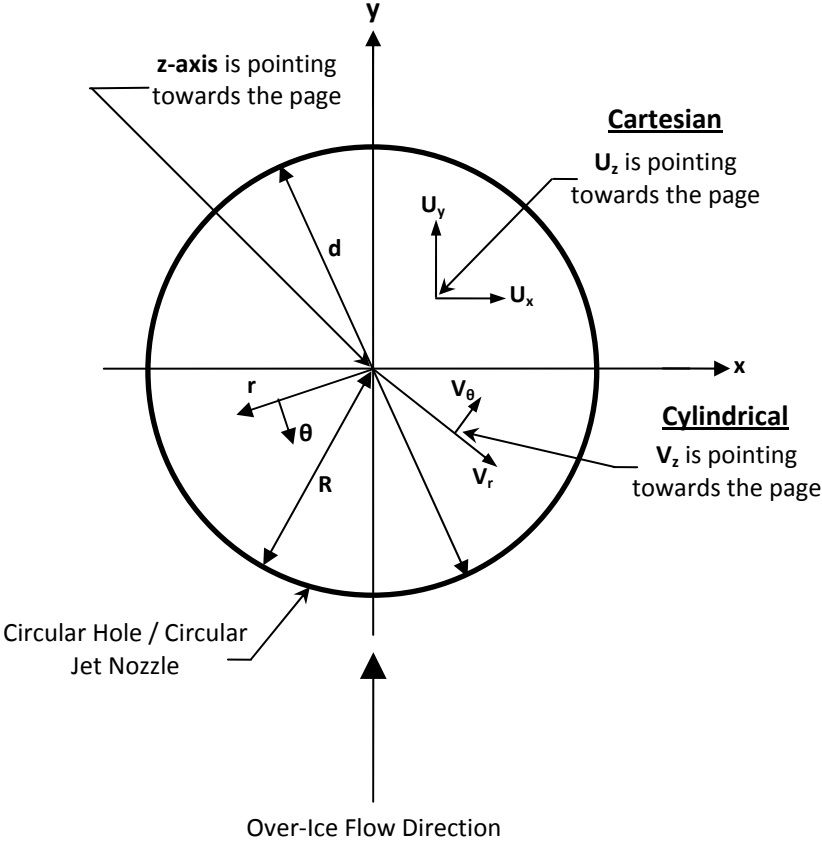


Figure 3-11 Top view of the circular hole and definition of the length and velocity variables in the Cartesian and the Cylindrical's global coordinate systems.

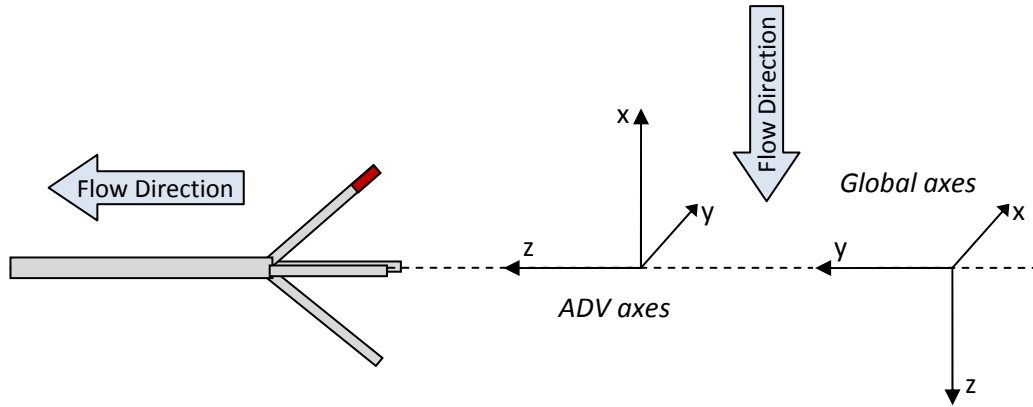


Figure 3-12 Vectrino ADV probe alignment below the ice surface and conversion of local (ADV) coordinate system to global coordinate system.

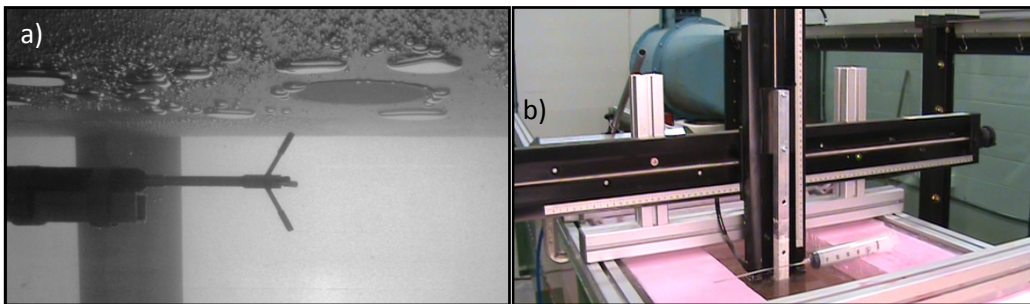


Figure 3-13 a) ADV probe below the ice cover. b) System of traverse used to position the ADV below the ice cover.

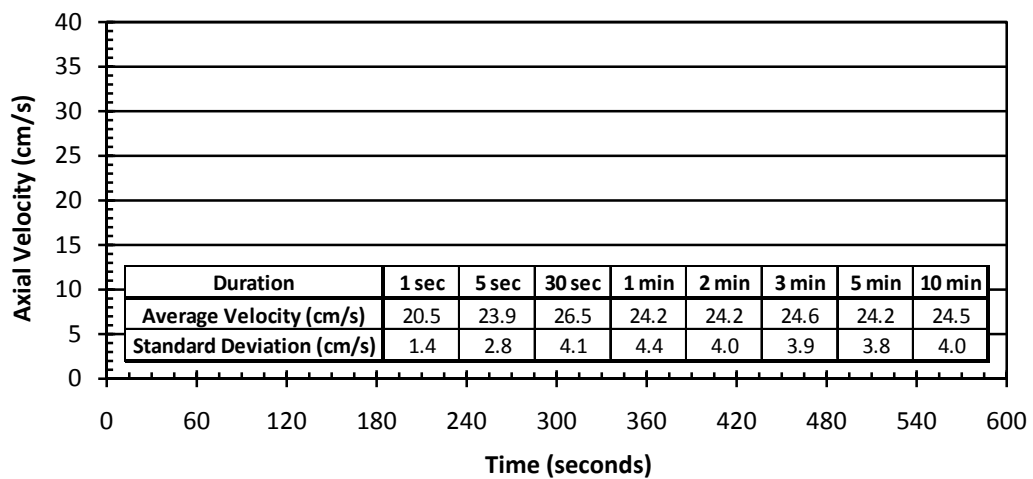


Figure 3-14 Axial velocity data (1-second average) collected from the ADV for Run #195b at $(x, y, z) = (0, 4, 3.3)$ and calculation of average velocities and standard deviations for various duration.

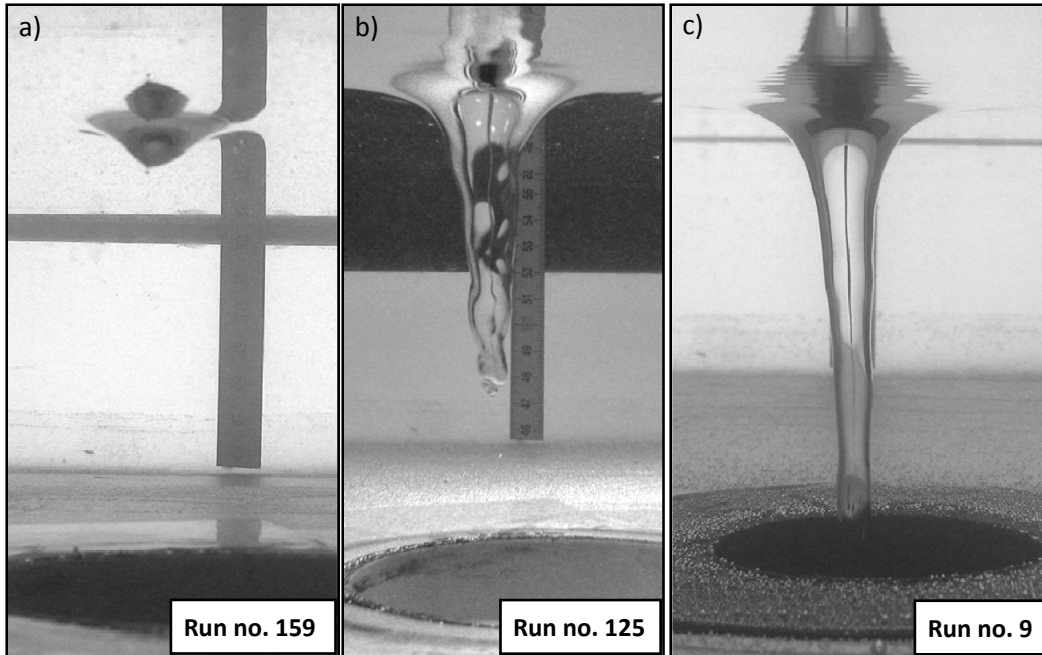


Figure 3-15 Side view of a) shallow air dip, b) deep air dip above the hole entrance, and c) deep air dip penetrating inside the hole. The overflow direction is from right to left and the vortices are rotating counter-clockwise.

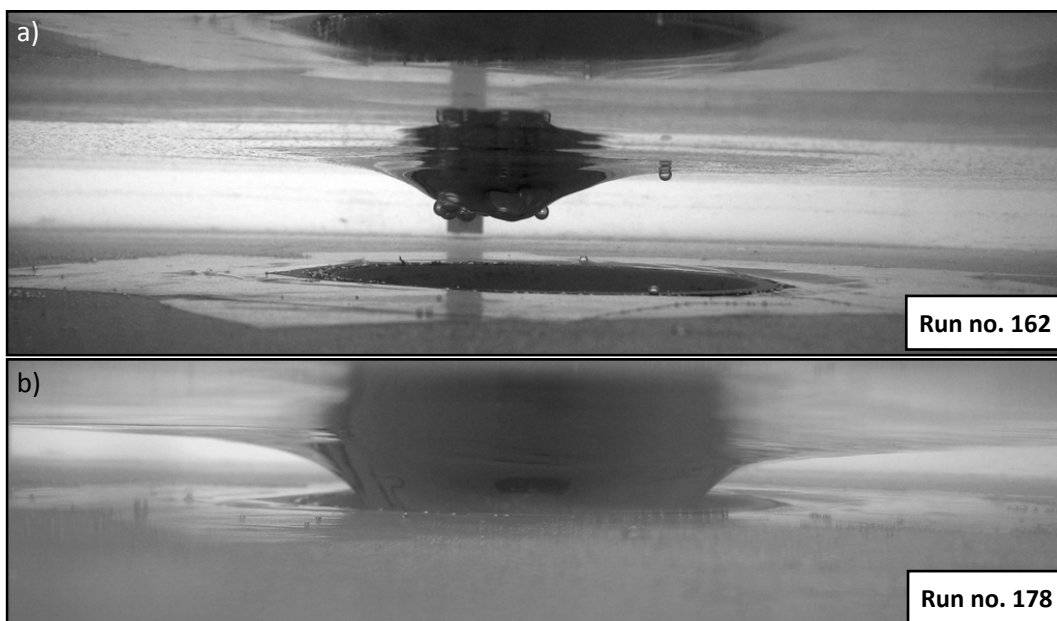


Figure 3-16 Side view of the vortex dip for small overflow depths a) above the hole entrance, and b) penetrating inside the hole. The overflow direction is from right to left and the vortices are rotating clockwise.

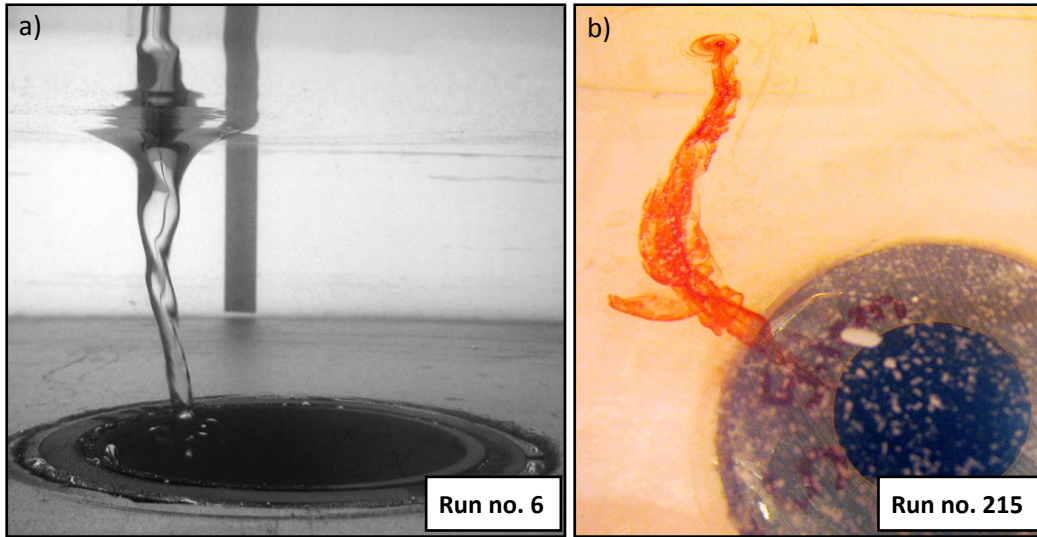


Figure 3-17 a) Side view of a vortex dip located on the downstream side of the hole. b) Top (angled) view of the curved vortex flow streamlines using dye. The overflow direction is from right to left and the vortices are rotating counter-clockwise.

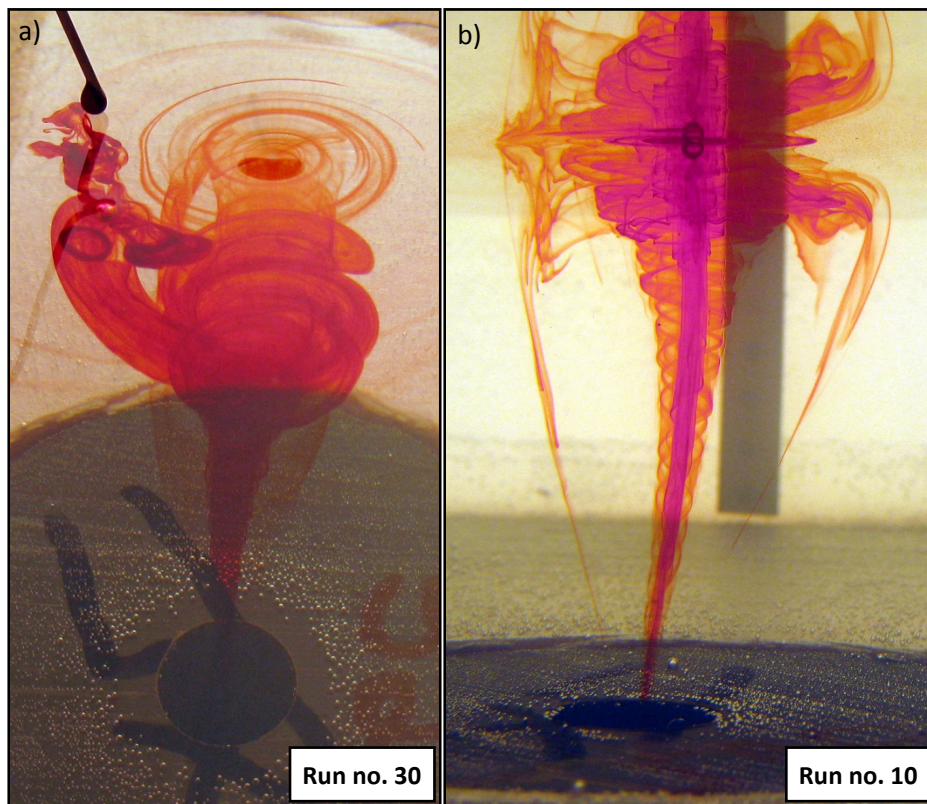


Figure 3-18 a) Top (angled) view, and b) side view of the strudel vortex streamlines into a circular hole using dye. The overflow direction is from right to left and the vortices are rotating counter-clockwise.

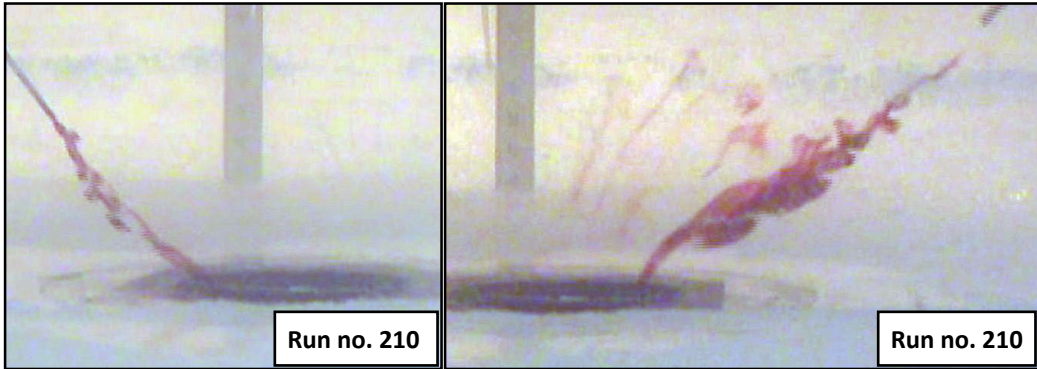


Figure 3-19 Side view of the vortex flow streamlines into a circular hole using dye. The overflow direction is from right to left and the vortices are rotating counter-clockwise.

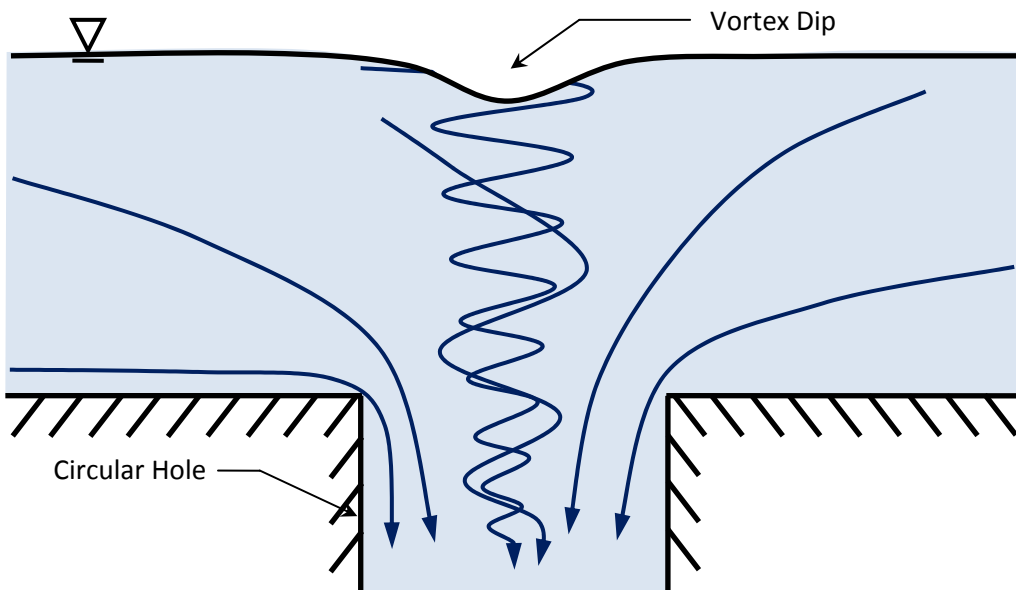


Figure 3-20 Sketch of the side view of the dye streaks flowing into the circular hole.

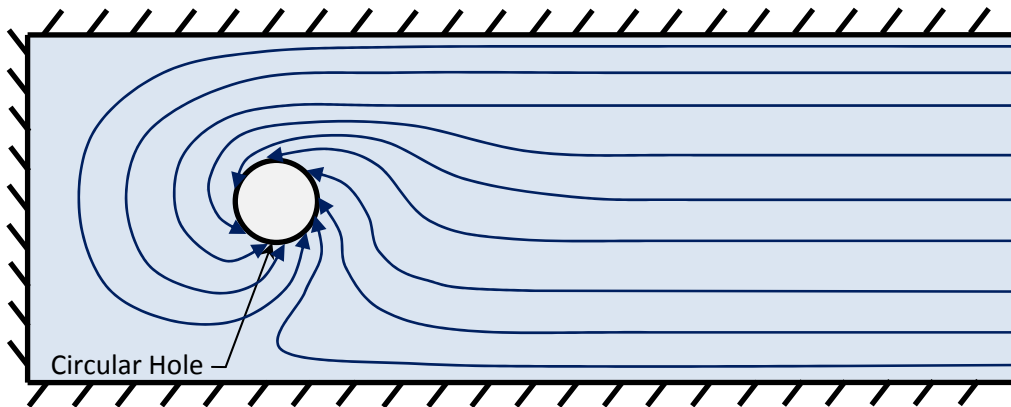


Figure 3-21 Sketch of the top view of the dye streaks inserted at the upstream water surface flowing towards the counter-clockwise free-surface vortex flow. The flow direction is from right to left.

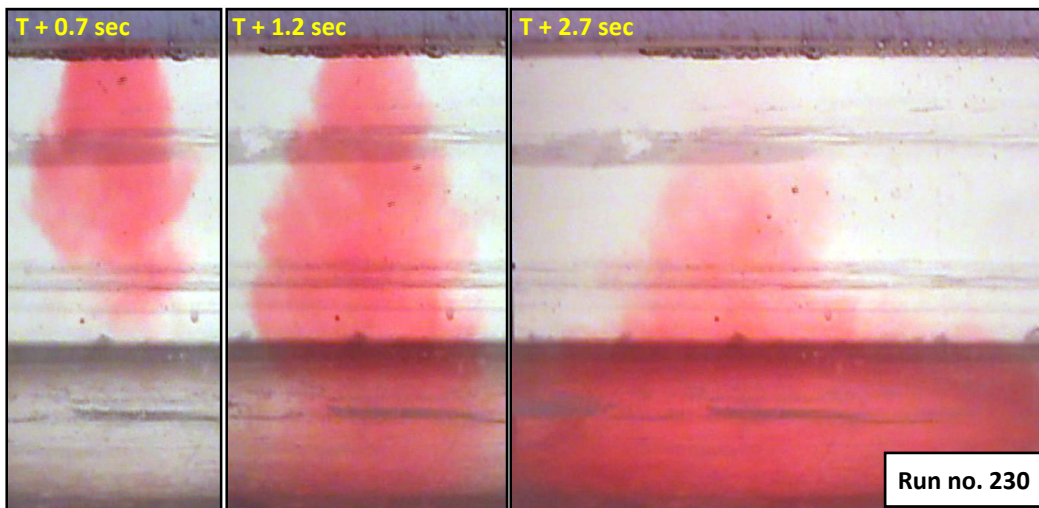


Figure 3-22 Side view images of the free-surface vortex flow under the ice cover impinging on a perpendicular boundary. The time T is referenced to the instant the dye started to flow out of the hole. The under-ice flow is from right to left.

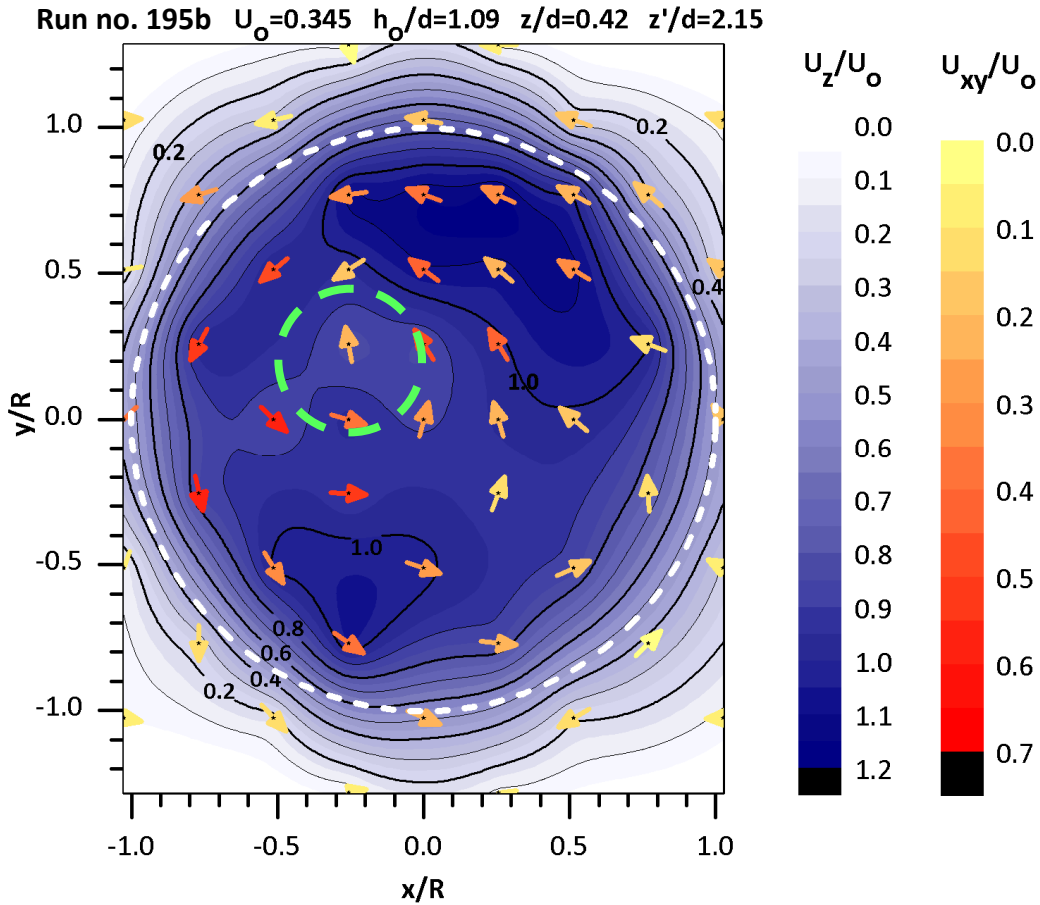


Figure 3-23 Dimensionless axial (U_z/U_o) and horizontal (U_{xy}/U_o) velocities in the x - y plane for run number 195b at $z/d = 0.42$. The arrows indicate the location of the ADV measurements. Each arrow shows the magnitude (colour coded) and direction of the dimensionless horizontal velocity vector, U_{xy}/U_o . The magnitude (colour coded) of the dimensionless axial velocities were linearly interpolated / extrapolated for the entire cross-section. The hole boundary is marked by a white circle and the vortex core's location is marked by a green circle. The overflow and under-ice flow direction is towards the positive y/R direction.

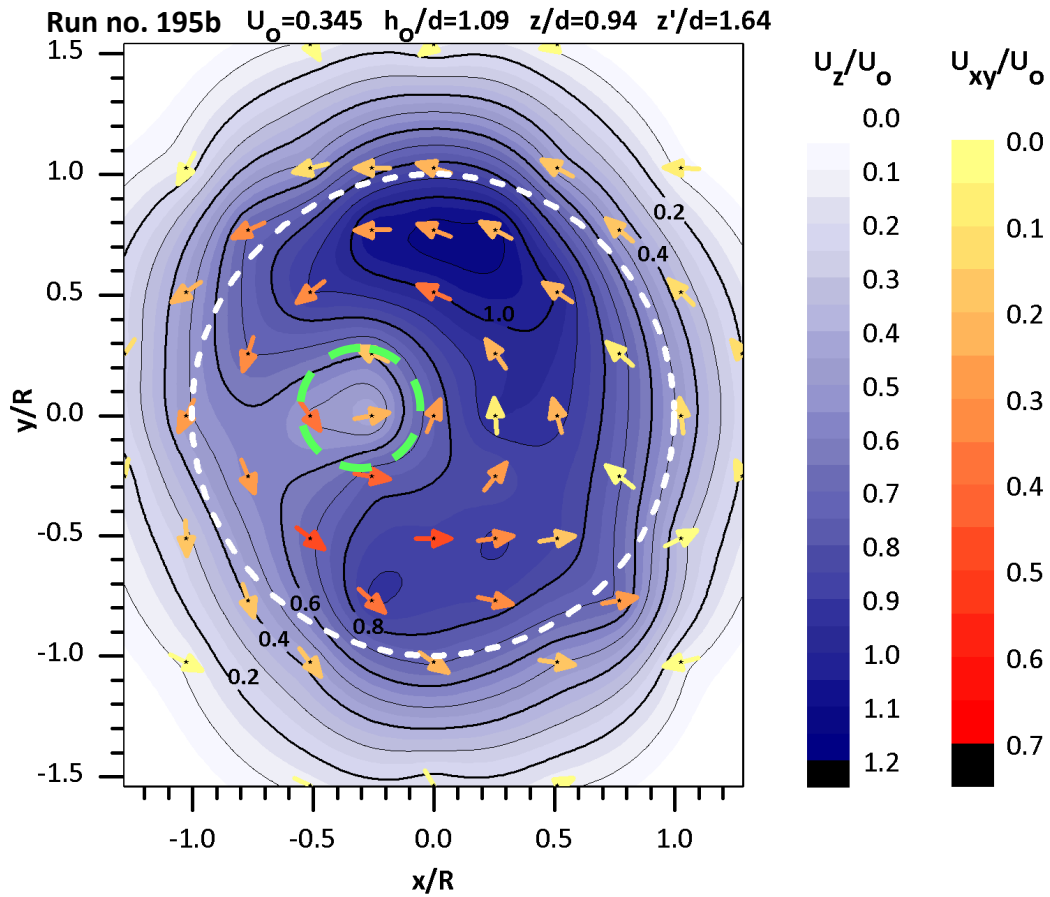


Figure 3-24 Dimensionless axial (U_z/U_o) and horizontal (U_{xy}/U_o) velocities in the x - y plane for run number 195b at $z/d = 0.94$. The arrows indicate the location of the ADV measurements. Each arrow shows the magnitude (colour coded) and direction of the dimensionless horizontal velocity vector, U_{xy}/U_o . The magnitude (colour coded) of the dimensionless axial velocities were linearly interpolated / extrapolated for the entire cross-section. The hole boundary is marked by a white circle and the vortex core's location is marked by a green circle. The overflow and under-ice flow direction is towards the positive y/R direction.

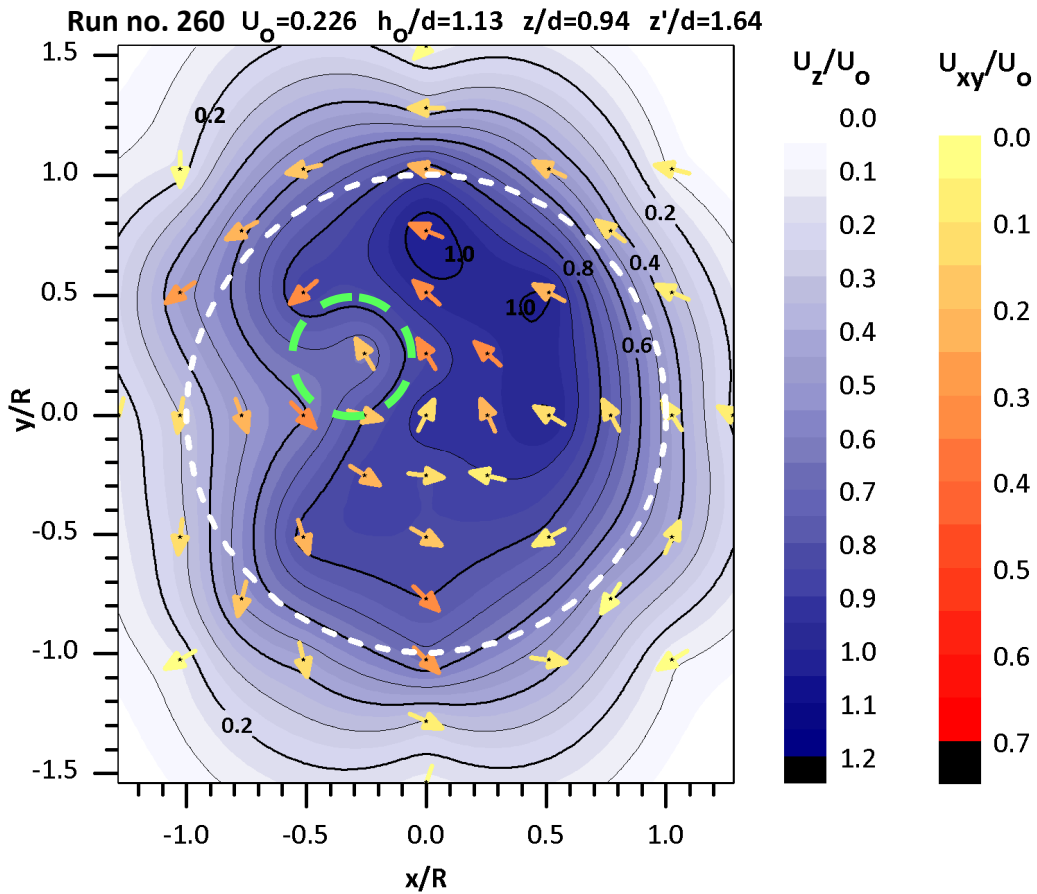


Figure 3-25 Dimensionless axial (U_z/U_o) and horizontal (U_{xy}/U_o) velocities in the x - y plane for run number 260 at $z/d = 0.94$. The arrows indicate the location of the ADV measurements. Each arrow shows the magnitude (colour coded) and direction of the dimensionless horizontal velocity vector, U_{xy}/U_o . The magnitude (colour coded) of the dimensionless axial velocities were linearly interpolated / extrapolated for the entire cross-section. The hole boundary is marked by a white circle and the vortex core's location is marked by a green circle. The overflow and under-ice flow direction is towards the positive y/R direction.

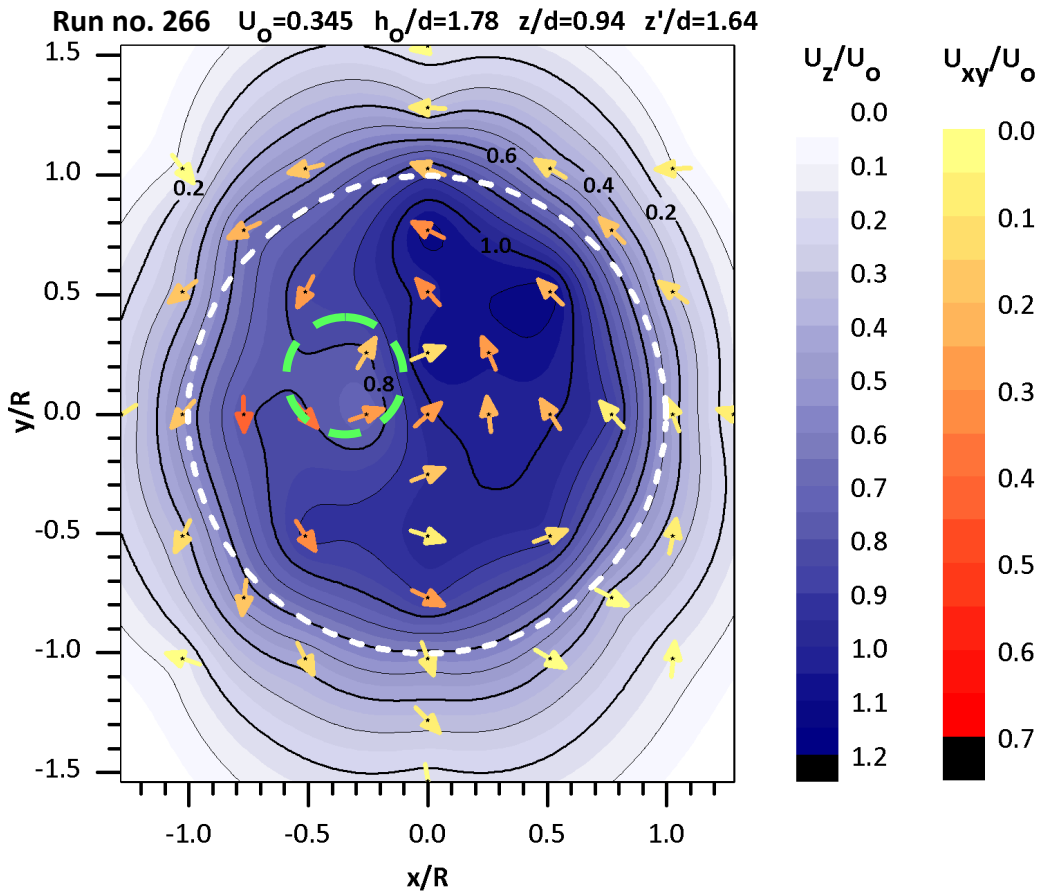


Figure 3-26 Dimensionless axial (U_z/U_o) and horizontal (U_{xy}/U_o) velocities in the x - y plane for run number 266 at $z/d = 0.94$. The arrows indicate the location of the ADV measurements. Each arrow shows the magnitude (colour coded) and direction of the dimensionless horizontal velocity vector, U_{xy}/U_o . The magnitude (colour coded) of the dimensionless axial velocities were linearly interpolated / extrapolated for the entire cross-section. The hole boundary is marked by a white circle and the vortex core's location is marked by a green circle. The overflow and under-ice flow direction is towards the positive y/R direction.

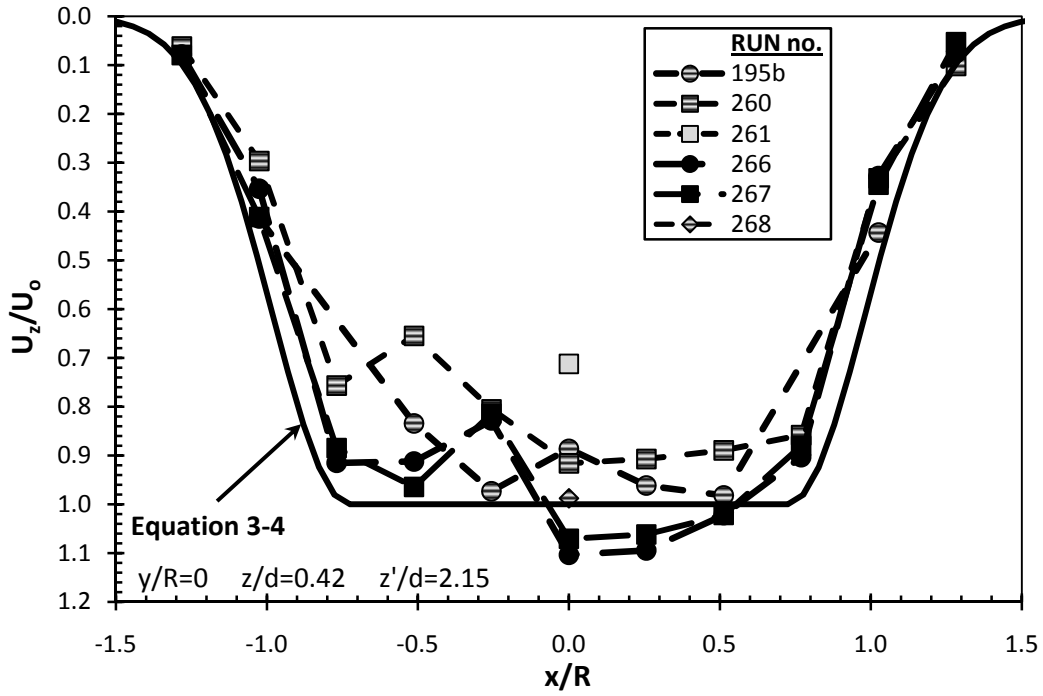


Figure 3-27 Dimensionless axial (U_z/U_0) velocities along the x-axis for $z/d = 0.42$.

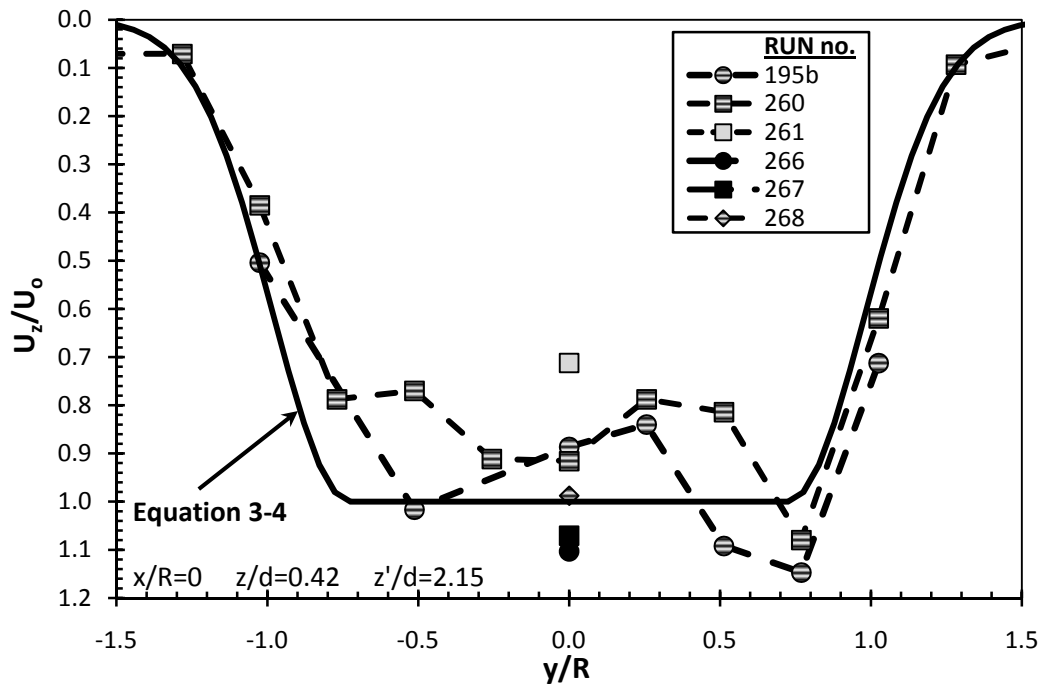


Figure 3-28 Dimensionless axial (U_z/U_0) velocities along the y-axis for $z/d = 0.42$.

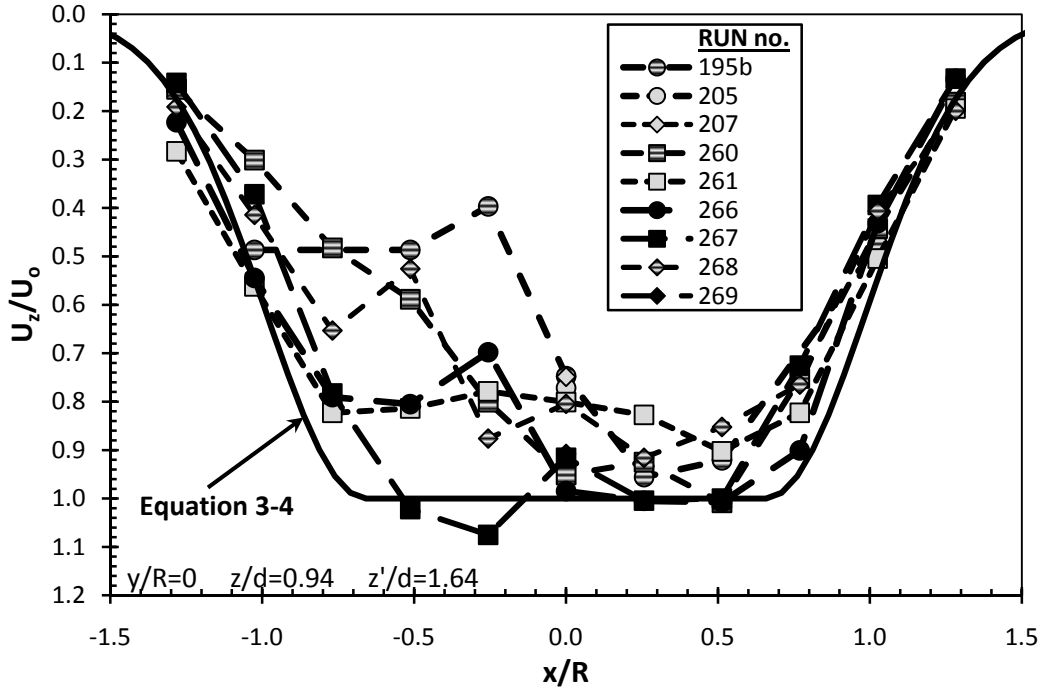


Figure 3-29 Dimensionless axial (U_z/U_o) velocities along the x-axis for $z/d = 0.94$.

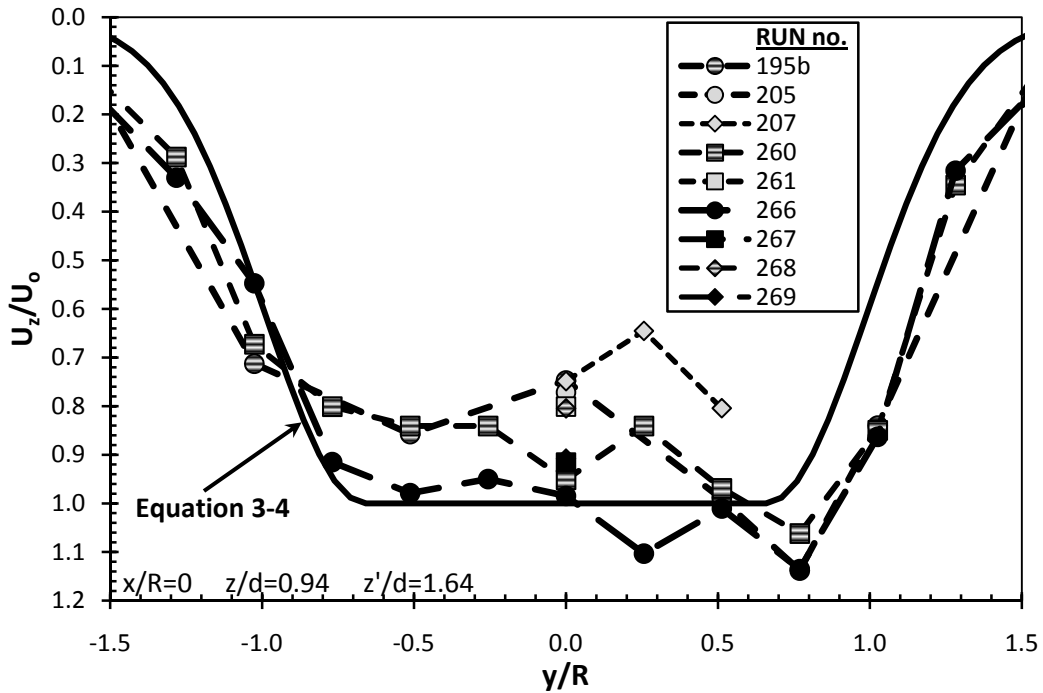


Figure 3-30 Dimensionless axial (U_z/U_o) velocities along the y-axis for $z/d = 0.94$.

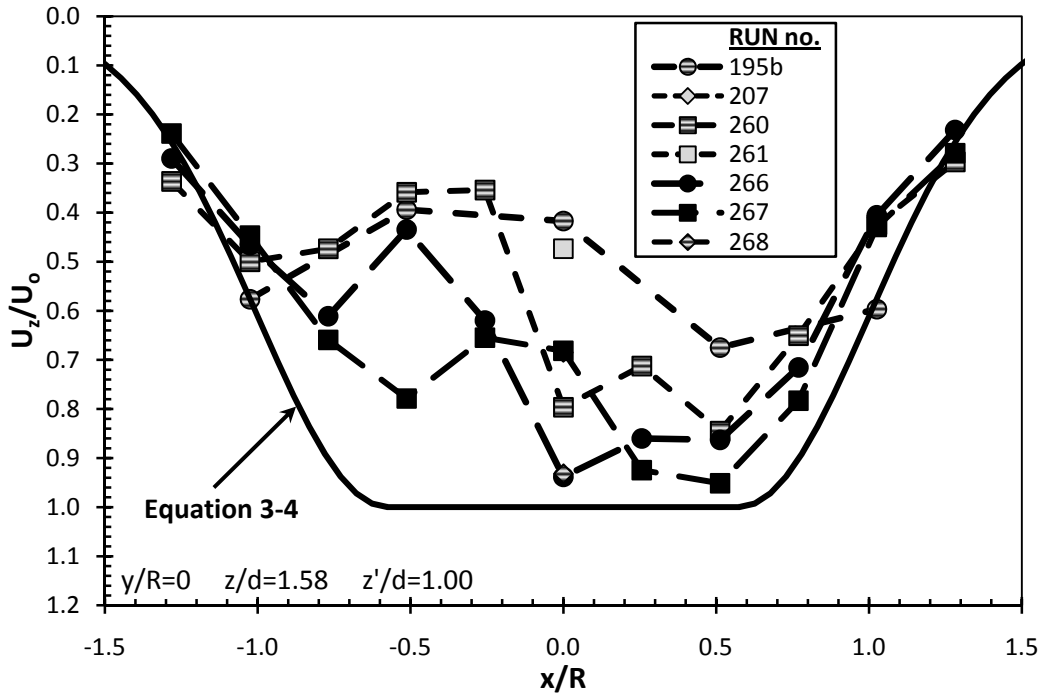


Figure 3-31 Dimensionless axial (U_z/U_0) velocities along the x-axis for $z/d = 1.58$.

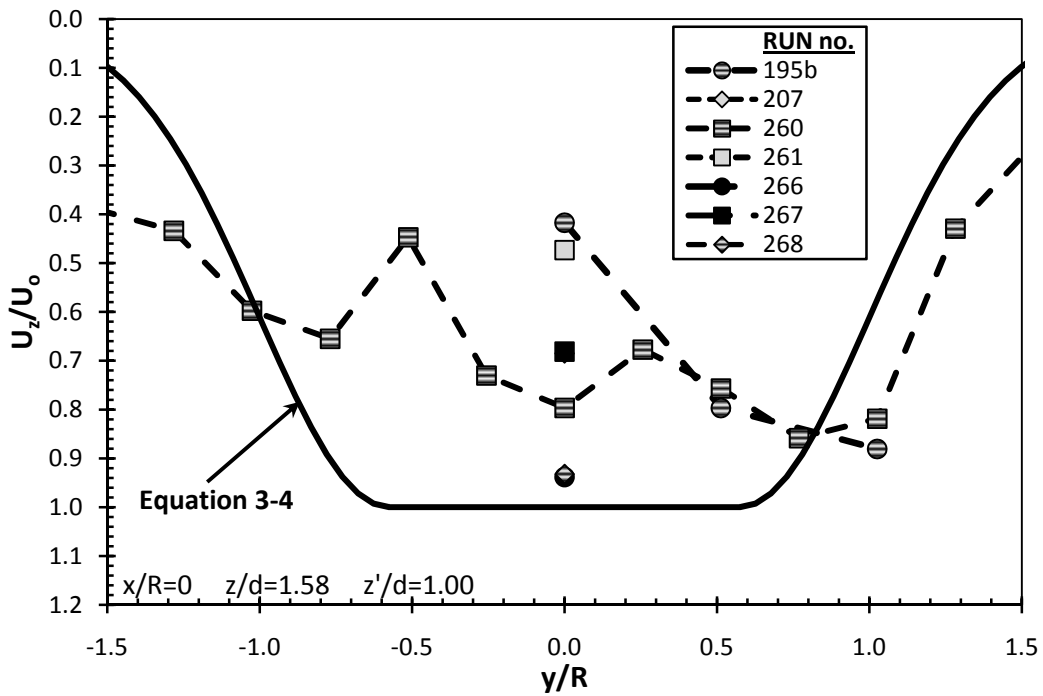


Figure 3-32 Dimensionless axial (U_z/U_0) velocities along the y-axis for $z/d = 1.58$.

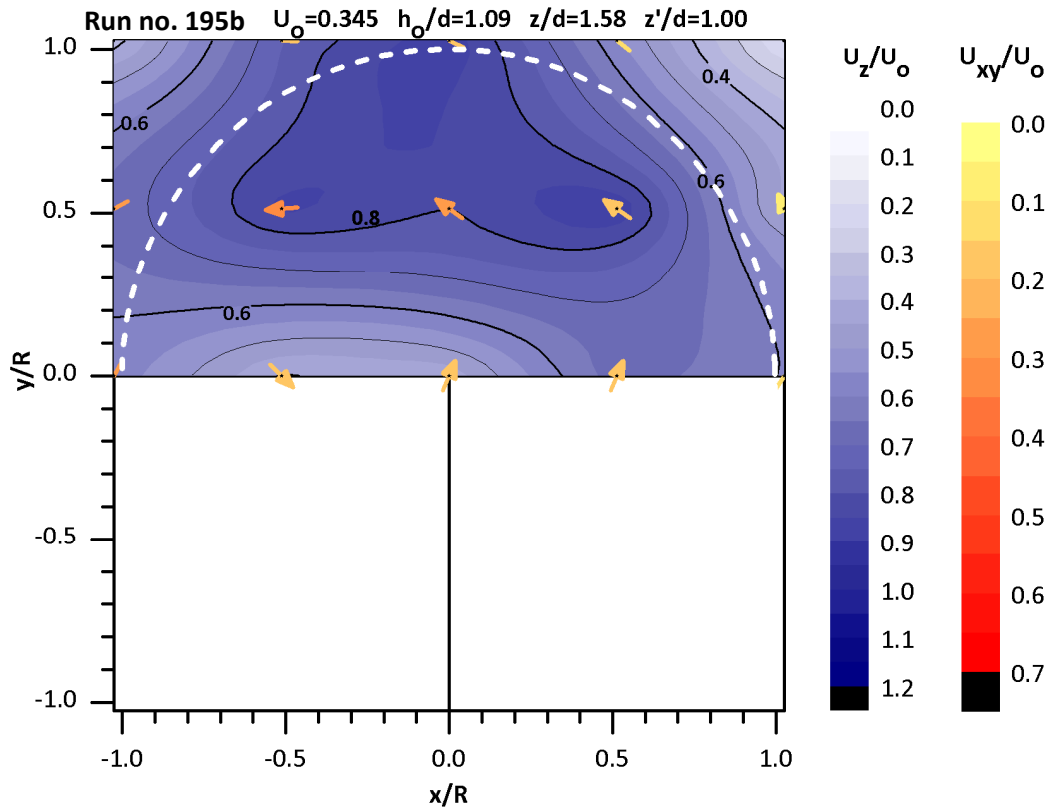


Figure 3-33 Dimensionless axial (U_z/U_o) and horizontal (U_{xy}/U_o) velocities in the x - y plane for run number 195b at $z/d = 1.58$. The arrows indicate the location of the ADV measurements. Each arrow shows the magnitude (colour coded) and direction of the dimensionless horizontal velocity vector, U_{xy}/U_o . The magnitude (colour coded) of the dimensionless axial velocities were linearly interpolated / extrapolated for half of the cross-section. The hole boundary is marked by a white circle. The overflow and under-ice flow direction is towards the positive y/R direction.

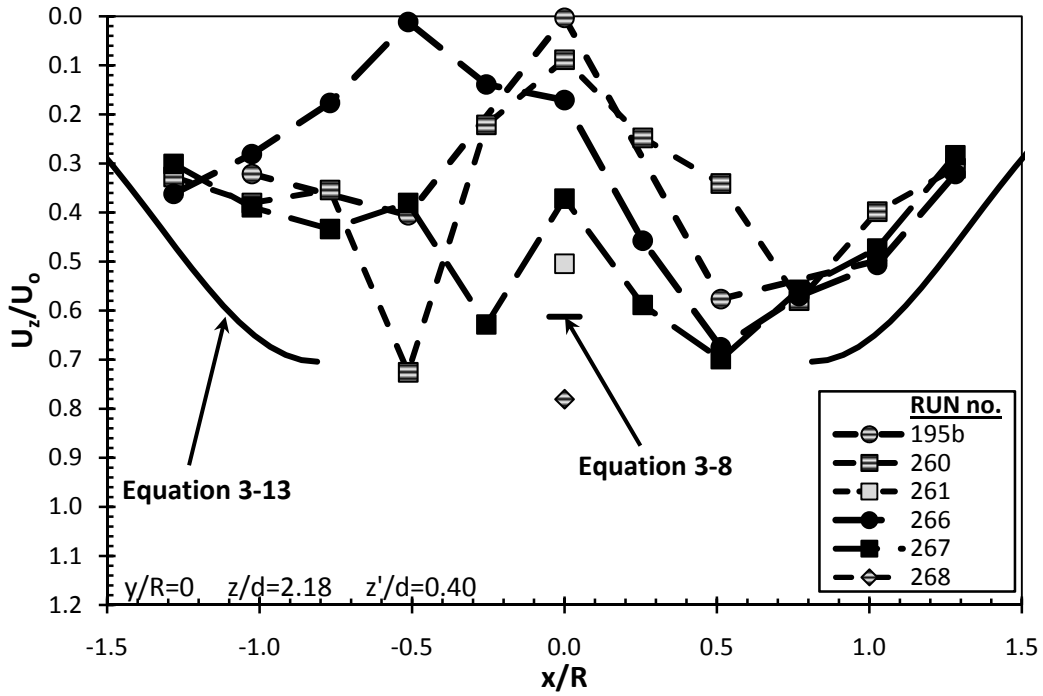


Figure 3-34 Dimensionless axial (U_z/U_0) velocities along the x-axis for $z/d = 2.18$.

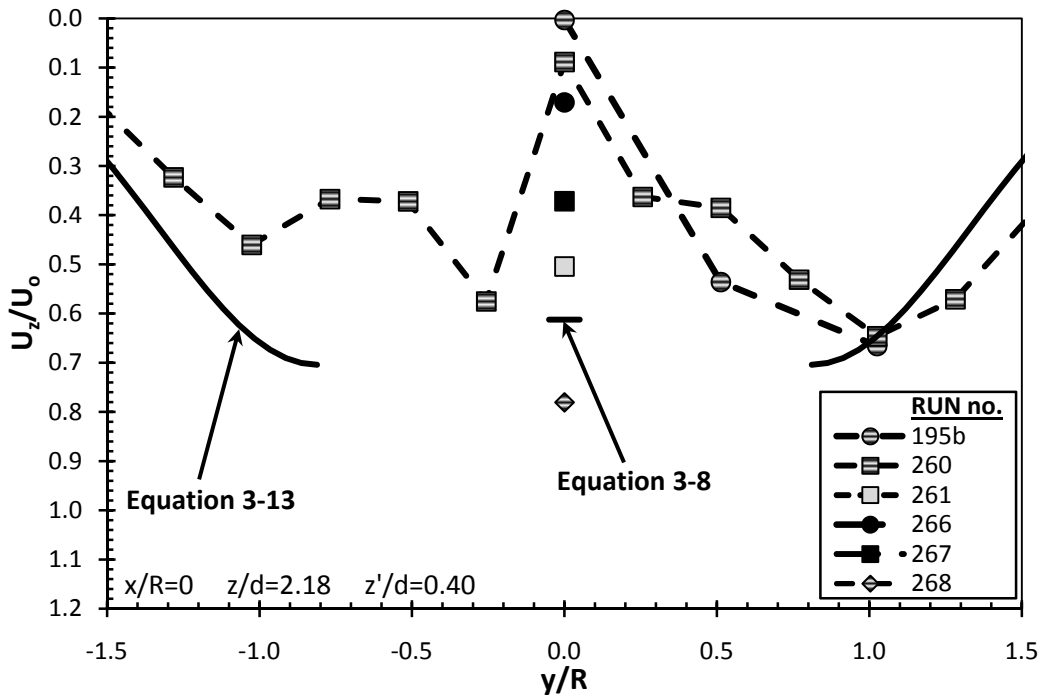


Figure 3-35 Dimensionless axial (U_z/U_0) velocities along the y-axis for $z/d = 2.18$.

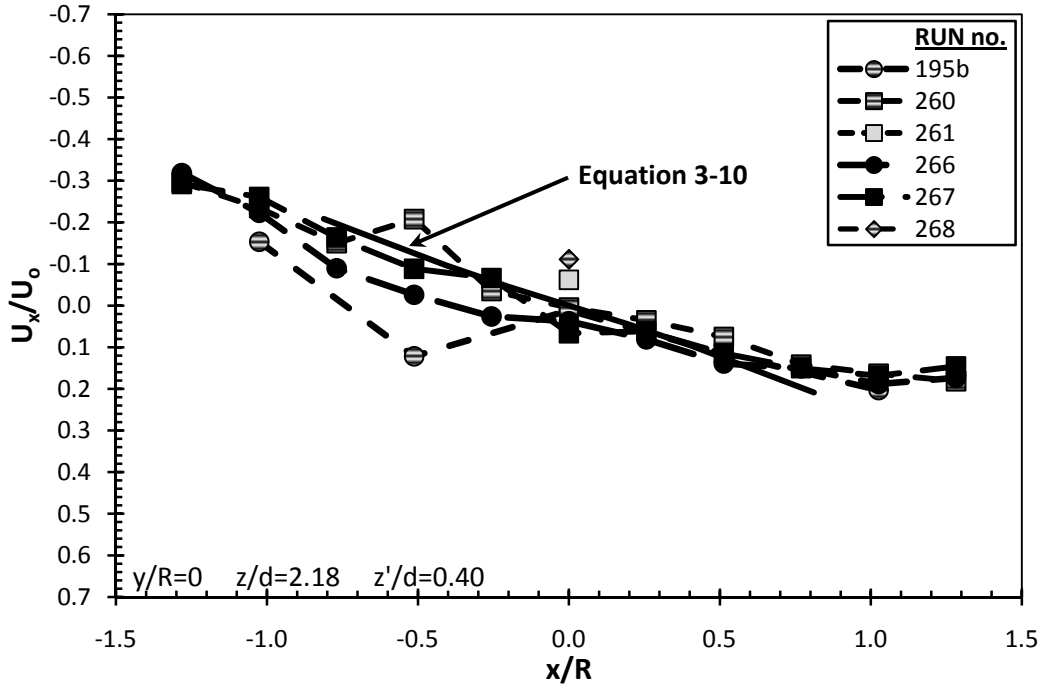


Figure 3-36 Dimensionless lateral (U_x/U_o) / radial velocities along the x-axis for $z/d = 2.18$.

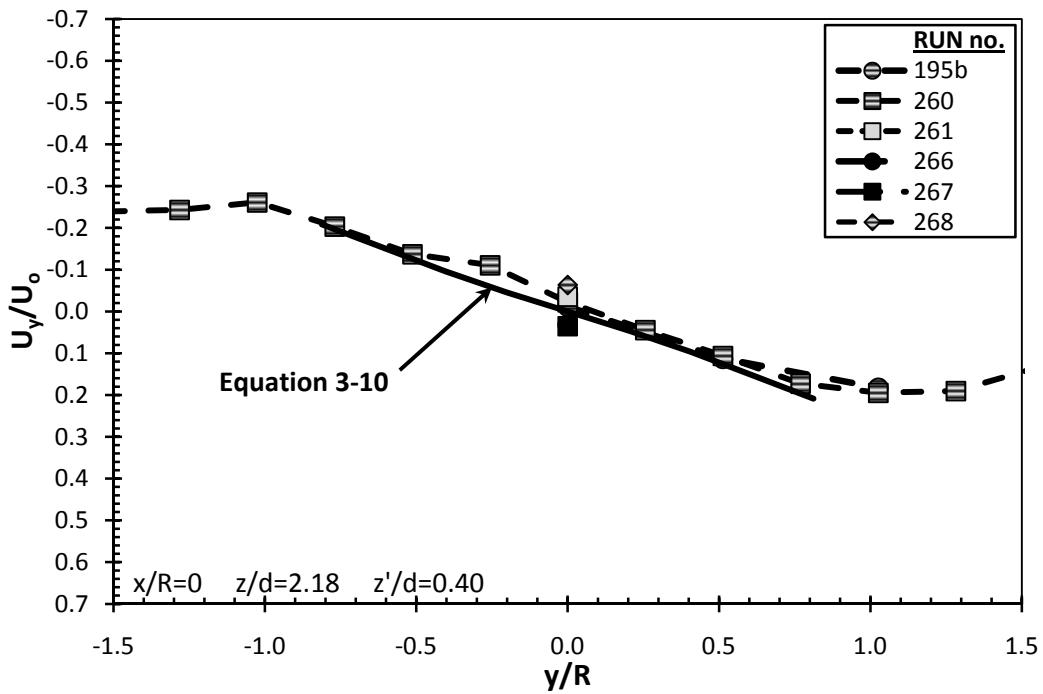


Figure 3-37 Dimensionless longitudinal (U_y/U_o) / radial velocities along the y-axis for $z/d = 2.18$.

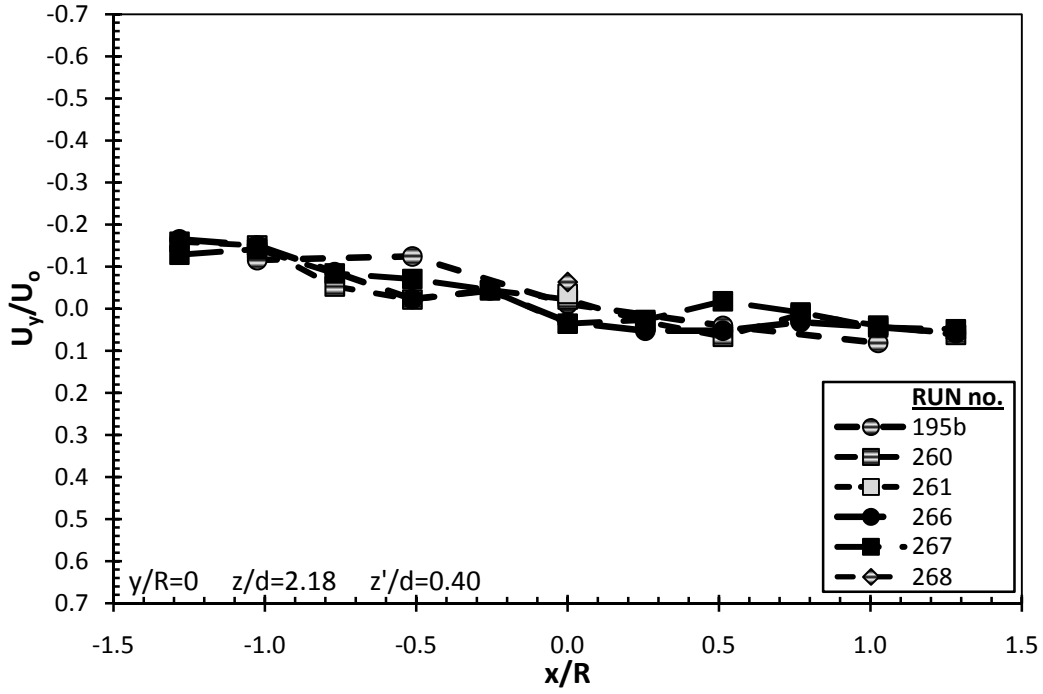


Figure 3-38 Dimensionless longitudinal (U_y/U_o) / tangential velocities along the x-axis for $z/d = 2.18$.

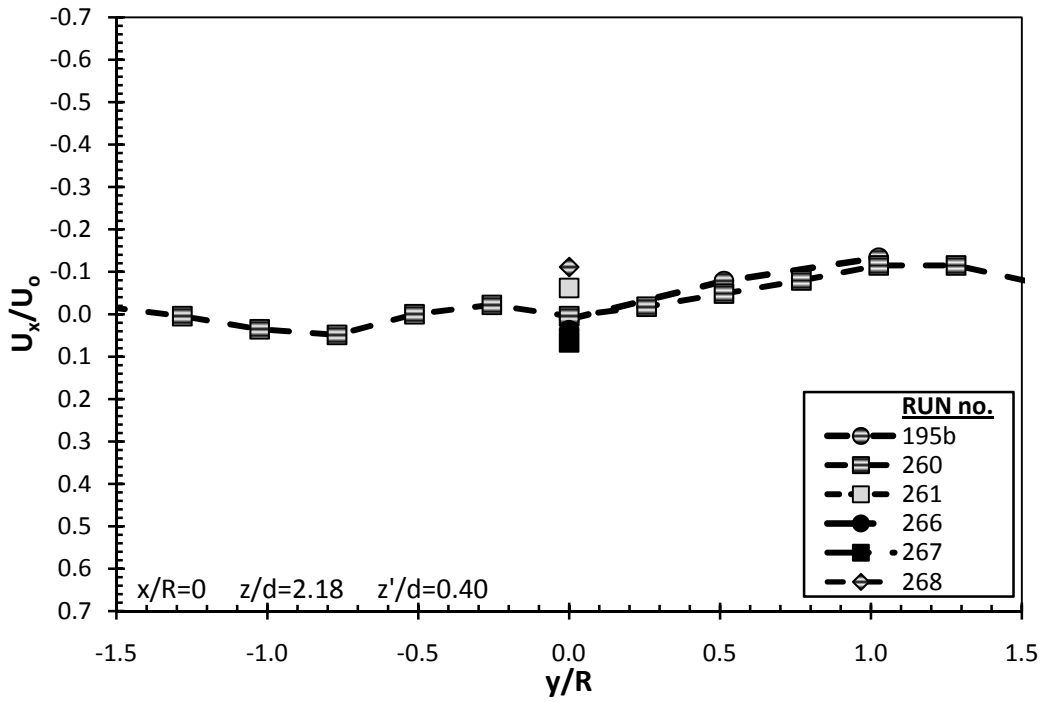


Figure 3-39 Dimensionless lateral (U_x/U_o) / tangential velocities along the y-axis for $z/d = 2.18$.

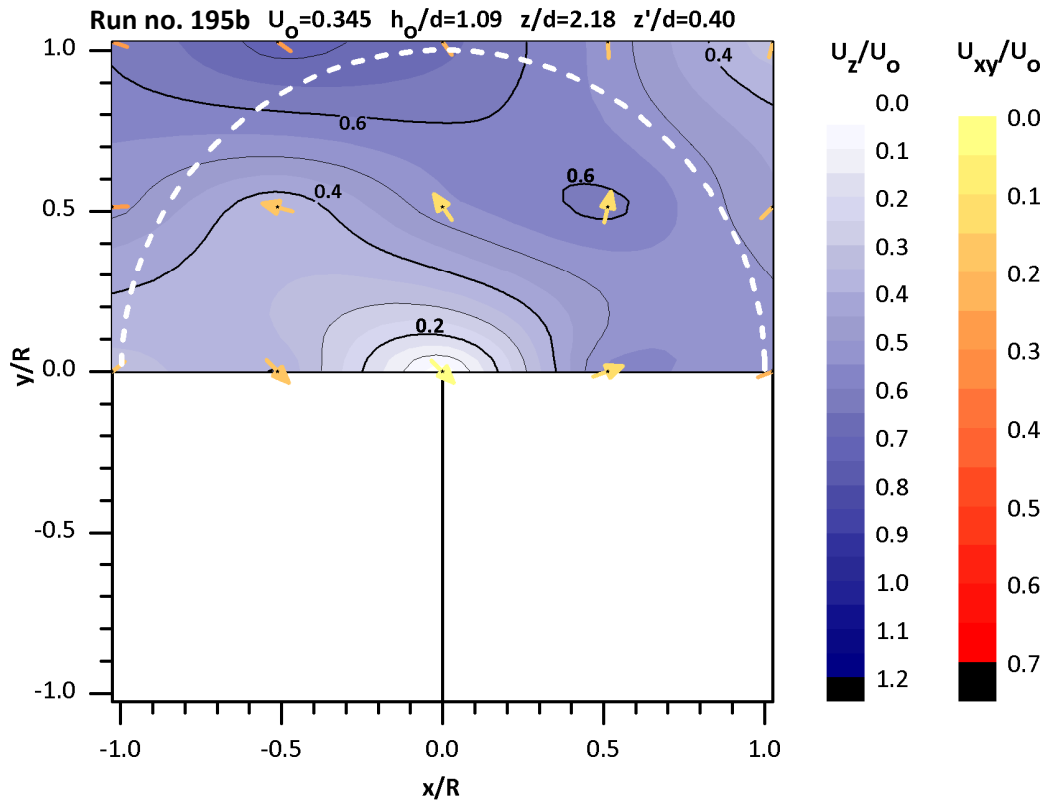


Figure 3-40 Dimensionless axial (U_z/U_o) and horizontal (U_{xy}/U_o) velocities in the x-y plane for run number 195b at $z/d = 2.18$. The arrows indicate the location of the ADV measurements. Each arrow shows the magnitude (colour coded) and direction of the dimensionless horizontal velocity vector, U_{xy}/U_o . The magnitude (colour coded) of the dimensionless axial velocities were linearly interpolated / extrapolated for half of the cross-section. The hole boundary is marked by a white circle. The overflow and under-ice flow direction is towards the positive y/R direction.

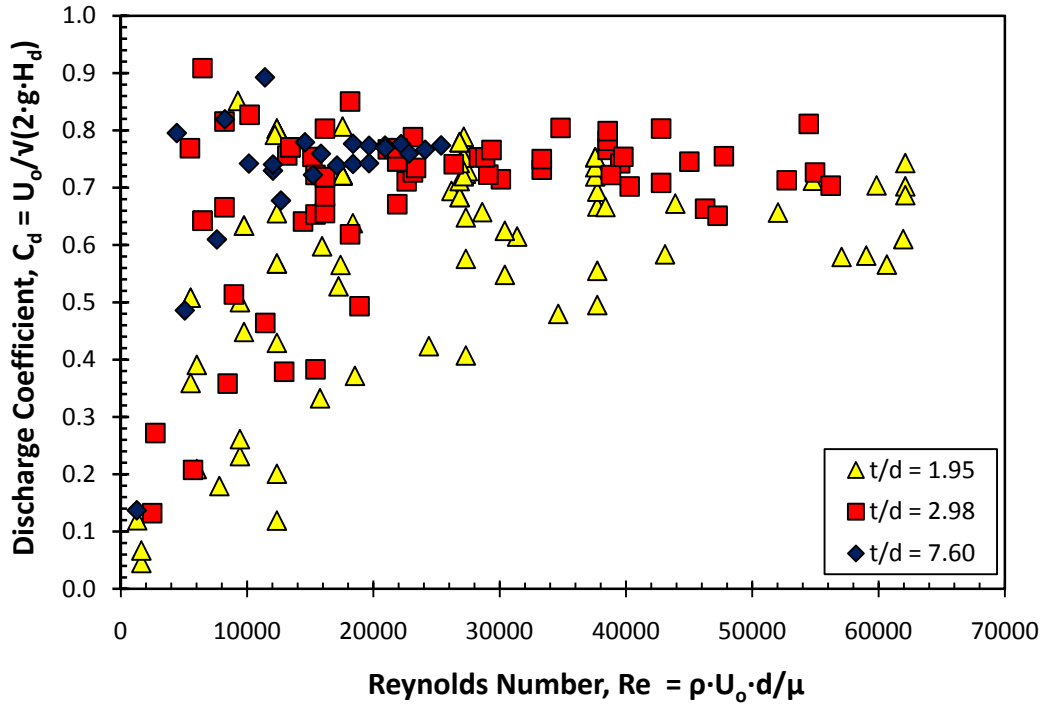


Figure 3-41 Graph of the Discharge Coefficient (C_d) vs. the Reynolds Number (Re). t/d is the ice thickness / hole diameter ratio.

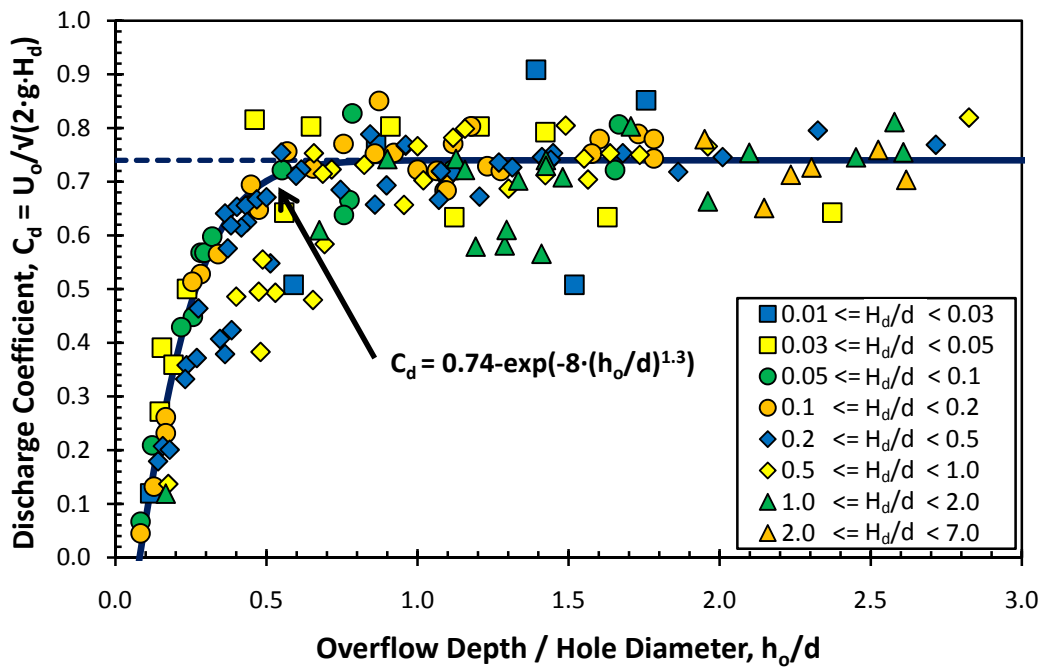


Figure 3-42 Graph of the discharge coefficient (C_d) versus the overflow depth / hole diameter (h_o/d) ratio. H_d/d is the hydraulic head difference / hole diameter ratio.

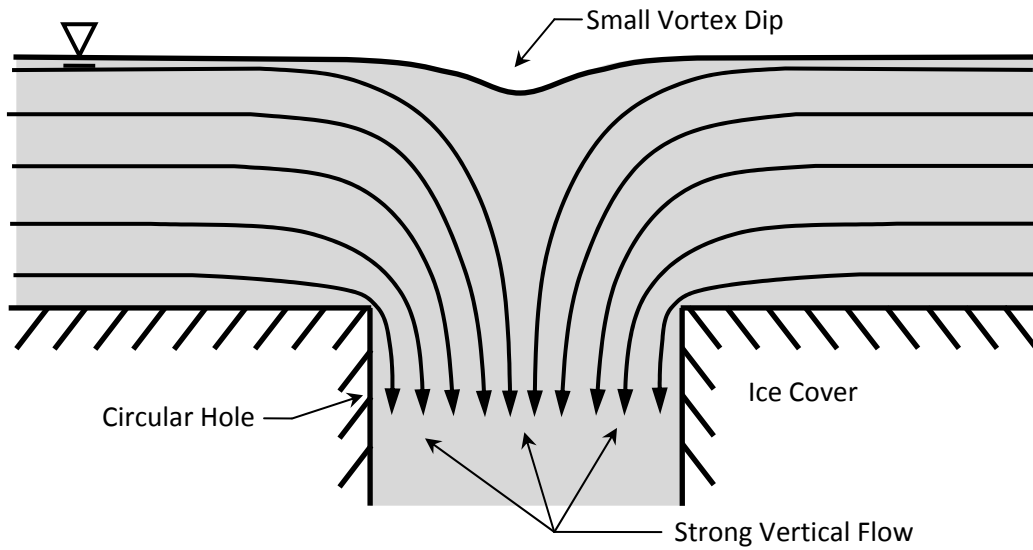


Figure 3-43 Sketch of the profile view of the flow streamline inside the circular hole for large overflow depths, neglecting rotation of the flow.

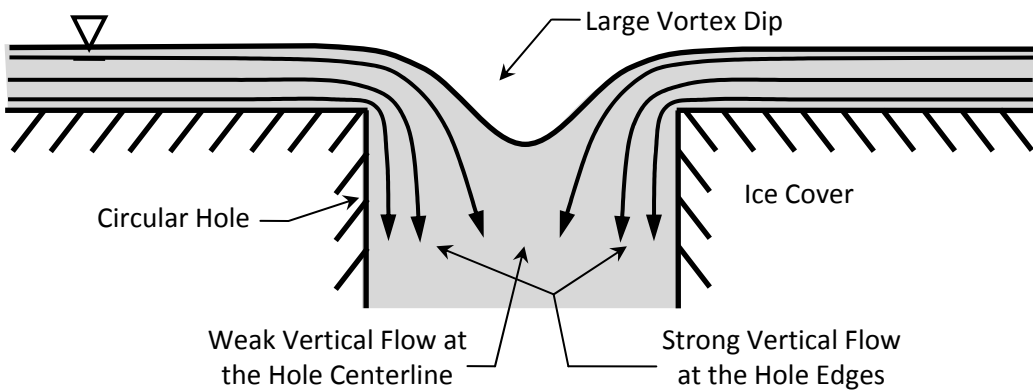


Figure 3-44 Sketch of the profile view of the flow streamline inside the circular hole for small overflow depths, neglecting rotation of the flow.

4.0 Estimation of the Strudel Scour Depths in the Mackenzie Outer Delta

4.1 Overview

Until now, estimates of the maximum scour depth were mostly based on statistical analysis of measured strudel scour in the field. An accurate theoretical estimation of the maximum strudel scour depth in the Mackenzie Outer Delta has yet to be provided. One early attempt at predicting this depth using theoretical experiments was made over twenty years ago by Arctec Newfoundland Limited (1987). The authors estimated the scour depth using an equation developed from Rajaratnam's experiments on jets impinging on cohesionless sediments with no tailwater, and concluded that the general agreement between the predicted strudel scour depths and the strudel scours measured in the field was encouraging.

Numerous experimental studies related to scouring of cohesive and cohesionless material have been performed since the 1990's, and as a result more is now known about the physical and hydraulic characteristics of strudel flows. Using this more recent research, another attempt at estimating the maximum strudel scour depth that might occur in the Mackenzie Outer Delta due to a strudel flow through a circular hole is presented in this Chapter. The following sections also present an analysis comparing the importance of the various hydraulic and physical parameters controlling the maximum strudel scour depth.

4.2 Theoretical Background

4.2.1 Scouring by Vertically Impinging Jets

Many vertical impinging jet experiments have been performed on cohesive and cohesionless soils for small to large impingement heights. A summary of the results and conclusions from these experiments is presented below. This section is introduced by an overview of the scouring development and of scour profile and is followed by theoretical scour results for the cohesionless soils and for cohesive soils. There are similarities but also considerable differences in the depth and radial extent of the scour hole between air and water jet systems (Rajaratnam, 1982), for example, the different mode of transport of the eroded bed material out of the scour (Rajaratnam, 1981a). Therefore, only the results developed from water jet experiments are presented below.

The variables used to measure and define the erosion parameters of the bed by vertically impinging circular turbulent jets are presented in the illustration of Figure 4-1.

There are two reasons to treat scouring in cohesive and cohesionless sediments separately. First, a cohesive soil may show a number of different modes of erosion: *flake erosion* where only very thin flakes are removed from the soil surface; *mass erosion*, which is the dominant erosion mechanism and usually happens in the first four hours of jet impact, where lumps or chunks of soil are intermittently ripped or torn from the soil body through failure of the bed under the soil surface; and *rapid surface erosion*, which occurs at higher stresses (greater than about 200 Pa) and forms a very smooth symmetrical scour hole (Mazurek *et al.*, 2001; Rajaratnam & Mazurek, 2003; Mehta, 1991, as cited in Mazurek & Hossain, 2007). Conversely, a cohesionless soil erodes by the removal of individual particles. Second, the erosion resistance of a cohesive soil is difficult to predict based on simple descriptors of the soil characteristics. The critical shear stress of a cohesive material depends on a number of physical and electrochemical properties of the material and the chemistry and temperature of the eroding fluid (Paaswell, 1973, as cited in Mazurek & Hossain, 2007), whereas the erosion resistance of a cohesionless material depends primarily on the particle buoyant weight, shape, and packing (Raudkivi, 1998, as cited in Mazurek & Hossain, 2007).

From past studies, the parameters governing the maximum depth of erosion (ε_m), radial extent of scour hole (r_o), and height of ridge ($\Delta\varepsilon$) were found. For small impingement heights, these three parameters are mainly a function of the dimensionless F_o parameter (Rajaratnam & Beltaos, 1977), defined as

$$F_o = \frac{U_o}{\sqrt{gD_{50}(\Delta\rho/\rho)}} \quad [4-1]$$

where:

F_o = a parameter defining the scour potential;

U_o = the average axial velocity at the jet nozzle;

g = the gravity constant;

D_{50} = the median size of the sand particles;

$\Delta\rho$ = the difference between the densities of sand and of the eroding fluid; and

ρ = the mass density of the eroding fluid.

For large impingement heights, these three parameters are mostly a function of the dimensionless erosion parameter (Rajaratnam, 1981b; Rajaratnam, 1982; Aderibigbe and Rajaratnam, 1996), defined as

$$E_c = \frac{F_o}{H/d} \quad [4-2]$$

where:

- E_c = the erosion parameter;
- H = the impingement distance; and
- d = the jet nozzle diameter.

4.2.2 Scouring Development and Scour Profile

When a vertical jet impinges on an erodible material, the depth of erosion varies linearly with the logarithm of time for both cohesive (Moore & Masch, 1962; Mazurek *et al.*, 2001) and cohesionless (Rajaratnam & Beltaos, 1977; Rajaratnam, 1981b; Rajaratnam & Mazurek, 2003) soils, until it reaches an asymptotic state of equilibrium scour after 6 to 50 hours (Aderibigbe & Rajaratnam, 1996) for cohesionless soils and 80 to 100 hours for cohesive soils (Mazurek *et al.*, 2001). However, for the cohesive soil, some discontinuities are seen in this linearity as a result of large pieces of sediment breaking out of the sample and being carried away by the jet (Moore & Masch, 1962; Mazurek *et al.*, 2001). For small time values (less than 30 seconds), the maximum scour depth occurs some distance away from the jet centerline at the location of the maximum erosive stresses which is not at the centerline. With time, the maximum depth of erosion occurs at the centerline of the impingement region (Rajaratnam & Beltaos, 1977; Rajaratnam, 1981b) but some exceptions were observed for cohesive soils (Mazurek *et al.*, 2001). In the first 30 minutes of the experiments, more than 70% of the bed depth is already scoured (Rajaratnam, 1982; Ansari, Kothiyari, & Raju, 2003).

There are significant differences between the scour profiles of cohesive and cohesionless soils. First, a ridge is present around the scour hole of cohesionless soils (Rajaratnam, 1981b) while no ridge forms for the cohesive soils (Mazurek *et al.*, 2001). The sides of the scour holes for non-plastic sediments, having a clay content ranging between 10 and 20 %, were found to have a slope nearly equal to 90° during the initial stages of scouring (Ansari *et al.*, 2003). However, the geometry of the scour holes at

equilibrium for such sediments was similar to that of the cohesionless sediments (Ansari *et al.*, 2003). For sediments with a clay content larger than 20% and plasticity index larger than 0, the slope of the scour hole sides was observed to be about 90° during the entire scouring activity (Ansari *et al.*, 2003).

The equations defining the scour hole profile are summarized as follows. For large impinging heights ($H/d > 8.3$), the asymptotic profile of the scoured bed up to $r/b = 1.4$ (1.7 in Rajaratnam, 1982) was defined by Rajaratnam and Beltaos (1977) as

$$\frac{\varepsilon}{\varepsilon_m} = \exp \left[-0.693 \left(\frac{r}{b} \right)^2 \right] \quad [4-3]$$

where:

- ε = the static depth of erosion;
- ε_m = the maximum static depth of erosion;
- r = the radial distance from the jet centerline; and
- b = the radial distance of half-scoured depth.

The authors derived this equation from impingement of air jets on cohesionless soils but it has also been shown to be accurate for water jets on cohesionless soils (Rajaratnam, 1981b; Rajaratnam, 1982; Aderibigbe & Rajaratnam, 1996), water jets on cohesive soils (Mazurek & Hossain, 2007), and for plane turbulent water jets on cohesionless soils (Rajaratnam, 1981a). Nonetheless, Mazurek *et al.* (2001) developed a second order equation for the erosion scour profile in cohesive soils defined as

$$\frac{\varepsilon}{\varepsilon_m} = 1.08 \left(\frac{r}{r_o} \right)^2 + 0.03 \left(\frac{r}{r_o} \right) - 1.00 \quad [4-4]$$

where:

- r_o = the radial extent of scour hole at the original bed level.

For an impingement height in the transition region of the jet at $H/d = 6.0$, Yeh, Chang, Henriksen, Edge, Chang, Silver and Vargas (2009) suggested a modification to the scour profile equation for cohesionless materials to represent both the scour hole presented as

$$\frac{\varepsilon}{\varepsilon_m + \Delta\varepsilon} = -1.2 \cdot \exp \left[-0.5 \left(\frac{r/r_1}{0.528} \right)^2 \right] + 0.4 \quad \text{valid for } r \leq r_1 \quad [4-5]$$

where:

$\Delta\varepsilon$ = the height of ridge; and

r_1 = the radial extent of scour hole at the top of ridge.

and the ridge profile, presented as

$$\frac{\varepsilon}{\varepsilon_m + \Delta\varepsilon} = 0.88 \cdot \exp \left[-0.5 \left(\frac{r/r_1}{0.580} \right)^2 \right] \quad \text{valid for } r > r_1 \quad [4-6]$$

4.2.3 Scours in Cohesionless Soils

For cohesionless soils, the scour or erosion observed after the jet is stopped, defined as the static depth of erosion (ε), can be significantly different from the erosion profile that exists with the jet on, defined as the dynamic depth of erosion (ε') (Rajaratnam, 1981b; Rajaratnam, 1982). Aderibigbe and Rajaratnam (1996) state the existence of a critical impingement distance at $E_c = 0.35$ at which the maximum static scour depth takes place and which separates two different flow regimes affecting strudel scour dimensions. The first regime is the *Weakly Deflected Jet Regime* and occurs at values of E_c less than 0.35. For this regime, the jet is weakly deflected travelling along the boundary of the scour hole as far as the crest of the dune, and the static and dynamic profiles are the same. Also, the strudel scour width to depth ratio (r_o/ε_m) rapidly increases with a decrease in the erosion parameter. The second regime is the *Strongly Deflected Jet Regime* and occurs at values of E_c greater than 0.35. The distinctive flow pattern in this regime is the re-circulatory flow and its interaction with the suspended materials. Other significant features are that the time required for the scour to reach an asymptotic state is much less than in the Weakly Deflected Jet Regime, the static depth of scour is smaller than the dynamic depth of scour, and the scour hole side slope is equal to the submerged angle of repose of the material.

The results and equations presented in this paragraph were defined from large impingement height ($H/d < 8.3$) water jet experiments. At incipient motion, thus the point of no scour, E_c is estimated to be 0.12 from Aderibigbe and Rajaratnam (1996) or 0.17 from Ansari *et al.* (2003). The asymptotic maximum static and dynamic scoured depths were respectively defined by Aderibigbe and Rajaratnam (1996) as

$$\frac{\varepsilon_m}{H} = 1.26E_c^{0.11} - 1 \quad [4-7]$$

and

$$\frac{\varepsilon'_m}{H} = 7.32E_c \left(\frac{d}{H}\right)^{1.53E_c^{0.22}-1} - 1 \quad [4-8]$$

where:

ε'_m = the maximum dynamic depth of erosion.

Ansari *et al.* (2003) proposed a modification to the static scoured depth equation by combining the results from several other papers, resulting in

$$\frac{\varepsilon_m}{H} = 1.3E_c^{0.15} - 1.0 \quad [4-9]$$

The asymptotic maximum scoured hole radius and scoured hole radius at half-scoured depth were respectively defined by Aderibigbe and Rajaratnam (1996) for $E_c \leq 0.5$ as

$$\frac{r_o}{H} = 1.46E_c^{0.15} - 1 \quad [4-10]$$

and

$$\frac{b}{H} = 1.2E_c^{0.06} - 1 \quad [4-11]$$

and for $0.5 < E_c < 5$ as

$$\frac{r_o}{H} = 0.22 + 0.2E_c \quad [4-12]$$

and

$$\frac{b}{H} = 0.11 + 0.08E_c \quad [4-13]$$

The asymptotic ridge radius to scour radius ratio was defined as $(r_1/r_o) \cong 1.4$ (Rajaratnam, 1982). The asymptotic ridge height in cohesionless materials was defined by Aderibigbe and Rajaratnam (1996) by the following empirical equation,

$$\frac{\Delta\varepsilon}{H} = C_5 + 0.044E_c \quad -0.02 \leq C_5 \leq 0.077 \quad [4-14]$$

where:

C_5 = the lower / upper limit constant.

It should be noted that experiments performed in small tailwater demonstrated that a sand ridge did not form around the edge of the scour hole in this case (Rajaratnam & Mazurek, 2003).

Scouring properties and dimensions of the scour holes at small impinging heights are different than for large impinging heights. For small impingement heights, the impinging jet is in the flow development region such that it has a top-hat velocity profile as it impinges on the bed. Therefore, the jet exit velocity and momentum are preserved and the cross-jet variations of these two properties are small and insignificant (Yeh *et al.*, 2009). Unfortunately, few experiments were performed for small impingement heights. Yeh *et al.* (2009) performed water jet experiments in cohesionless materials at an impingement height of $H/d = 6$, which is in the transition region of the jet. Their measurements for the maximum static scour depth, scour hole radius and ridge height were all smaller than predicted by Aderibigbe and Rajaratnam's (1996) equations' 4-7, 4-10, and 4-14 such that they suggested modifications to these equations by introducing correction factors of 0.64, 0.78 and 0.52 respectively. However, these proposed corrections might not be accurate because the authors only performed two scour experiments. Experiments of water jets impinging directly on a cohesionless soil ($H/d = 0$) were performed by Niven and Khalili (1998). From their experiments, the maximum static scoured depth was seen to take the form

$$\frac{\varepsilon_m}{d} \Big|_{H=0} = 2.25 F_o^{0.987} \left(\frac{D_{50}}{d} \right)^{0.387} \quad [4-15]$$

valid for $F_o < 12$, $\varepsilon_m/d > 2$ and $D_{50}/d < 2$, while the relationship for the top of ridge radius took the form

$$\frac{r_1}{d} \Big|_{H=0} = 0.64 F_o^{0.625} \left(\frac{D_{50}}{d} \right)^{-0.187} \left(\frac{h_w}{d} \right)^{0.104} \quad [4-16]$$

valid for $F_o < 12$, $\varepsilon_m/d > 2$ and $D_{50}/d < 2$, where:

h_w = the water depth.

4.2.4 Scours in Cohesive Soils

Cohesive soil experiments by Moore and Masch (1962) showed that for $6.0 \leq H/d \leq 10.0$, a maximum amount of scour is obtained at a value of H/d near 8.0. A large amount of data scatter at a H/d ratio of 7.0 indicated a change in the type of scour. Therefore, there exists a critical impingement distance for cohesive soils at $H/d = 7.0$ which divides the two different flow regimes affecting the strudel scour dimensions for cohesive soils. The first regime happens for $H/d \leq 7.0$, where the potential core of the jet is of sufficient length (Baines, 1950, as cited in Moore & Masch, 1962) to strike the surface of the sample, causing an intense and localised scour (narrow and deep). This jet is almost completely reversed and very little scour takes place once the scour hole is developed (Moore & Masch, 1962). Also, the scour rate is low as the energy of the jet is dissipated in a relatively deep narrow hole. The second regime happens for $H/d > 7.0$, where the scour hole is wider and shallower, the potential core does not hit the sample and the jet is of broader extent (Moore & Masch, 1962). Opposite to cohesionless soils, the difference between the dynamic and the static scour depths in cohesive soils is very small (Ansari *et al.*, 2003) or even non-existent (Mazurek *et al.*, 2001) for both regimes.

No scour experiments in cohesive soils for small impingement heights were found from the literature. For a large impingement height, the asymptotic maximum static scoured depth was defined by Mazurek *et al.* (2001) as

$$\frac{\varepsilon_m}{H} = 0.19 \left\{ \frac{X - X_c}{X_c} \right\}^{0.74} \quad \text{valid for } X \geq X_c \quad [4-17]$$

where:

X = the parameter describing the hydraulic properties of the jet; and

X_c = the value of X at which mass erosion first occurs.

The X parameter is defined as

$$X = \rho U_o^2 \left(\frac{d}{H} \right)^2 \quad [4-18]$$

where:

ρ = the mass density of the eroding fluid.

It is important to note that the authors only tested one cohesive soil (40% clay, 53% silt and 7% fine with a critical shear stress of 300 Pa) in order to define this equation. The authors stated that the equation is unlikely to apply to mass erosion in a cohesive soil sample that is fissured, disturbed by sampling, slaking, layered, or relatively inhomogeneous. Fortunately, an experimental study by Ansari *et al.* (2003) defined a complex equation for the maximum scour depth presented as

$$\frac{(\varepsilon_m)_{COHESIVE}}{(\varepsilon_m)_{COHESIONLESS}} = 0.38 \left(\frac{C_*}{\varphi_*}\right)^{0.3} \left(\frac{W}{W_*}\right)^{0.11} \left(\frac{\gamma_d}{\gamma_w}\right)^{2.0} \quad [4-19]$$

where:

- C_* = a variable defining the cohesive soil properties;
- φ_* = a variable defining the cohesive soil properties;
- W = the antecedent moisture content of the cohesive sediments;
- W_* = the moisture content at saturation of the cohesive sediments;
- γ_d = the specific density of dry sediments; and
- γ_w = the specific density of water.

In equation 4-19, the C_* parameter is defined as

$$C_* = \frac{P_c \cdot C_u}{(\gamma_s - \gamma_w) \cdot d_a} \quad [4-20]$$

where:

- P_c = the percentage of clay content;
- C_u = the cohesion strength parameter;
- γ_s = the specific density of sediments; and
- d_a = the arithmetic mean size of cohesive sediment.

and the φ_* parameter is defined as

$$\varphi_* = \frac{P_c \cdot \tan \varphi_c + (1 - P_c) \tan \varphi_s}{\tan \varphi_s} \quad [4-21]$$

where:

- φ_c = the angle of internal friction of the cohesive sediments; and
- φ_s = the angle of repose / internal friction of the sand.

In equation 4-19, $(\varepsilon_m)_{COHESIONLESS}$ can be calculated from Equation 4-7 or from Equation 4-9. Ansari *et al.* (2003) found that the ratio $(\varepsilon_m)_{COHESIVE} / (\varepsilon_m)_{COHESIONLESS}$

is always greater than unity and equal to 1.5 ± 0.3 , meaning that the scour in clay is deeper than the static scour in sand. The only published equation for the asymptotic maximum scoured hole radius for cohesive soils was proposed by Mazurek *et al.* (2001) as

$$\frac{r_o}{H} = 0.44 \left\{ \frac{X-X_c}{X_c} \right\}^{0.37} \quad [4-22]$$

The radius of the scour hole for the cohesive soil experiments was also found to be always greater than that for the cohesionless soils (Mazurek & Hossain, 2007) such that $r_o/b \cong 1.55$ (Mazurek *et al.*, 2001).

4.3 Selection of the Strudel Scour Depth Estimation Equation

A number of equations presented in the Theoretical Background section could be used to estimate the maximum strudel scour depth in the cohesive bed of the Mackenzie Delta. For large impingement heights, the maximum cohesive bed scour depth can be approximated as

$$\frac{\varepsilon_m}{H} = 1.5(1.3E_c^{0.15} - 1.0) \quad [4-23]$$

This equation assumes that the cohesive scour depth is equal to 1.5 times the maximum cohesionless static bed scour predicted by Equation 4-9 as proposed by Ansari *et al.* (2003). Note that this approach was chosen because it does not require in-depth knowledge of cohesive soil properties (e.g. cohesion strength parameter, moisture content and angle of internal friction) required in Equation 4-19, or the hydraulic properties of the jet at which mass erosion first occurs (X_c) required in Equation 4-17, because this data is not available for the Mackenzie Outer Delta.

Unfortunately, the maximum strudel scour depth can only be estimated for large impingement heights ($H/d > 8.3$) as experimental studies for small impingement heights ($H/d < 5.5$) are lacking. Furthermore, the equations developed for jets impinging directly on the sediments ($H/d = 0$) cannot be used to predict the scour depth since they are only valid for $F_o < 12$ (Niven and Khalili, 1998) and values of F_o for strudel flows on the Mackenzie Delta are typically greater than 50. Therefore, Equation

4-23 will be used to estimate maximum scour depths for strudel flows with large impingement heights.

Studies indicate that strudel scour depths in cohesionless and cohesive soils are larger at large impingement heights than for small impingement heights. Yeh *et al.* (2009) observed from the jet experiments with cohesionless soils that for small impingement heights, the maximum static scour depth, scour hole radius and ridge height were all smaller than predicted by the large impingement height equations. Additionally, Moore and Masch (1962) measured the maximum cohesive scour depths to happen at an approximate H/d value of 8.0. Additional physical laboratory experiments of jets impinging on cohesive soils at small impingement heights should be performed in order to verify and confirm these statements.

4.4 Definition of Strudel Scour Depth Estimation Parameters

This section presents the constants and variables used to estimate the strudel scour depths using Equation 4-23. The gravity (g) is 9.81 m/s^2 and the mass density of the eroding fluid (ρ), in this case water, is approximately $1,000 \text{ kg/m}^3$. From the collected sediments in the Mackenzie Delta, presented in Section 2.4.9, the median size of the sand particles (D_{50}) is $75 \text{ }\mu\text{m}$ and the sediment density (ρ_s) averages $2,700 \text{ kg/m}^3$ such that $\Delta\rho$ is equal to $1,700 \text{ kg/m}^3$.

The impingement distance (H) and the hole diameter (d) were obtained from site measurements and previous publications, summarised in Chapter 2. In the Mackenzie Outer Delta in 2008 and 2009, strudel scours were located in water depths between 1.5 and 2.5 m and the average ice thickness of 1.8 m gives a maximum impingement distance of approximately 0.7 m. In the primary strudel zone of the Alaskan Beaufort Sea, strudel scours were measured in water depths up to 6 m (DF Dickins Associates *et al.*, 2009) such that the maximum impingement distance was approximately 4 m. In the Mackenzie Outer Delta, measured strudel drain diameters varied in size up to 3.5 m. However, the diameter could potentially be much larger and was even said to reach values of 15 m in Alaska (Reimnitz & Bruder, 1972).

The axial velocity (U_o) through the strudel hole is the only variable that was not measured in the field, nor found in the literature. Consequently, the theoretical velocity

was estimated from the hydraulic head difference (H_d) which drives the water under the ice cover. Reimnitz (2002) stated that the strudel flow is not only a function of the hydraulic head difference or water depth on top of the ice but it is also driven by buoyancy of initially submerged fast ice driven to rise to the surface. However, for this analysis, the ice buoyancy effect was ignored as the ice cover rises very slowly. Furthermore, strudel were observed at the interface of the bottomfast ice and the floating sea ice where the ice cover was not rising.

Johnson (1985) developed an equation, derived from the buoyancy equation for the sea ice surface, which estimates the hydraulic head difference driving the strudel flow. This equation assumes that the weight of the freshwater on the floating sea ice deflects the ice cover, as illustrated in Figure 4-2. The equation's variables have been renamed and rearranged to

$$H_d = (h_o + t) - \frac{h_o \cdot \gamma_{fw} + t \cdot \gamma_i}{\gamma_{sw}} \quad [4-24]$$

where:

H_d = the hydraulic head difference;

h_o = the overflow depth;

t = the ice thickness;

γ_{fw} = the specific density of fresh water, given as 9,810 N/m³;

γ_i = the specific density of sea ice, given as 9,025 N/m³; and

γ_{sw} = the specific density of sea water, given as 10,061 N/m³.

The above equation assumes a situation where the floating sea ice is acting independently from the surrounding ice and its surrounding environment. However, important factors should be included into this equation such as the bonds with the adjacent floating ice and bottomfast ice covers which could restrict the movement of the floating sea ice by providing excess buoyancy, the physical constraints such as the small distance between the ice cover and the bed, and the fact that the under ice seawater has to be displaced in order for the ice cover to lower. Other factors include the spatial variations in ice thicknesses and in the overflow depths. Since Johnson (1985) did not account for those factors, the equation might underestimate the hydraulic head difference driving the strudel flow. Therefore, it was attempted to find the maximum

hydraulic head difference which could drive the largest axial velocity through a strudel hole.

From the data collected during field investigations in the Mackenzie Delta, it was impossible to determine the hydraulic head difference which controls both the upwelling and strudel processes as the differences between the upstream and downstream water levels were not measured. However, it was possible to estimate this head from the overflow depth (h_o) measured in the field as explained below. As the density of ice and water at 0°C are 916.7 kg/m³ and 999.8 kg/m³ respectively (Lide, D. R., 2005), the buoyancy equation reveals that, the freeboard (f_b) of the ice is 8% of the total ice thickness (Figure 4-3a). In this calculation the weight of the snow on the ice cover was neglected because it was only approximately 10 cm in depth. Therefore, for a 1.8 m ice thickness, the freeboard is 14 cm which correlates with freeboard measurements in the Mackenzie Outer Delta. The overflow covers the floating sea ice very rapidly and reaches a maximum depth within a day. Therefore, to obtain the largest theoretical hydraulic head difference value, the deflection of the ice due to the weight of the overflow was neglected and the downstream water level was assumed to be at the same level as before the overflow occurred, therefore 14 cm below the ice surface (Figure 4-3b). As a result, the maximum hydraulic head difference is equal to the sum of the maximum overflow depth and of the maximum freeboard.

In 2008, the floating ice overflow in the Mackenzie Delta reached a maximum depth of 48 cm. In the Alaskan Beaufort Sea, the depth of overflow is said to vary between 0.5 and 1.5 m (Reimnitz *et al.*, 1974; Reimnitz & Bruder, 1972). As a result, the maximum hydraulic head difference driving the strudel flow is equal to 62 cm for the Mackenzie Delta and 1.6 m for the Alaskan Beaufort Sea. The axial velocity in the strudel hole can be approximated using equation 3-21 developed in Section 3.4.3, defined as

$$U_o = [0.74 - \exp(-8 \cdot (h_o/d)^{1.3})] \cdot \sqrt{2 g H_d} \quad \text{valid for } (h_o/d) > 0.1 \quad [3-21]$$

Therefore, the maximum axial velocity in the strudel drain, for a large overflow depth / hole diameter (h_o/d) ratio is approximated as 2.6 m/s for the Mackenzie Delta and 4.1 m/s for the Alaskan Beaufort Sea.

4.5 Estimation of the Strudel Scour Depth

In order to estimate the strudel scour depth, studies of fully turbulent circular jet vertically impinging on uniform cohesionless and cohesive soils were used. For the moment, the maximum strudel scour depth can only be estimated for large impingement heights ($H/d > 8.3$) as studies at small impingement heights are lacking. Unfortunately, as the maximum impingement distance measured in the delta was approximately 0.7 m, the maximum strudel drain diameter at which the strudel scour depth can be estimated is 8 cm. As most of strudel drains in the Mackenzie Delta are larger than 30 cm in diameter, the strudel scour depth for the majority of the observed strudel cases cannot be estimated. The impingement height is one of the most important factor governing the maximum strudel scour depth. Therefore, impinging jet experiments with small impinging heights should be carried out in the near future so that scour depths under larger strudel drains can be estimated.

Other important factors were also neglected in the scour depth estimation due to the limitation of the published studies and of the data collected in the Mackenzie Outer Delta. These include temporal and spatial variations to the strudel scour hole sizes and shapes and to the under-ice depth (impingement distance), velocity distribution in the strudel hole and bed sediment characteristics. It should be noted that a variation in these physical and hydraulic parameters are likely affecting the strudel scour depth and shape. Unfortunately, the effects of those variations on the strudel scour characteristics are not known as they were not studied. As a result, this study simplifies the real world strudel scour case but still provides useful approximate estimates of strudel scour depths. This study also provides an estimate of the maximum strudel scour depth based on currently known data from the Mackenzie Delta and published scour depth equations.

For a circular strudel drain diameter of 8 cm, an impingement distance of 0.7 m, and an overflow depth of 48 cm, such that the hydraulic head difference is equal to 62 cm, Equation 4-23 reveals that the maximum strudel depth estimated to occur in the cohesive sediments of the Mackenzie Outer Delta is approximately 0.83 m. This theoretical depth is slightly lower than the measured strudel scour depths in the outer

delta which had a maximum of 0.87 m in 2008 and 1.38 m in 2009. However, it should be noted that these measured scours were formed below larger diameter strudel holes.

In the Alaskan Beaufort Sea, it was calculated that for an impingement distance of 4.0 m, a strudel drain diameter of 48 cm (for an impingement height of 8.3), and an overflow depth of 1.5 m, such that the hydraulic head difference equals 1.6 m, the scour in cohesive soils could reach maximum depths of 5.60 m. Maximum strudel scour depths in the Alaskan Beaufort Sea were observed to reach values up to 4.27 m (DF Dickins Associates *et al.*, 2009) and one was even found to measure up to 6.7 m in depth (McClelland Engineering, 1982, reported in Coastal Frontiers, 1997, as cited in DF Dickins Associates *et al.*, 2009).

It is interesting to note that for a strudel hole with a hydraulic head difference of 50 cm, an impingement distance of 1.0 m and a hole diameter of only 5 cm, Equation 4-12 reveals that the scour diameter could measure 1.75 m, which is 35 times larger in diameter and 1,225 times larger in surface area than the strudel hole itself.

The graph of Figure 4-4 presents the estimated strudel depth in the cohesive soil of the Mackenzie Delta, derived from Equation 4-23, for various impingement distances, hole diameter and axial velocities, with the assumption that the overflow depth is sufficient not to affect the velocities. Up to an erosion parameter (E_c) value of 0.35, an increase in the impingement distance increases the scour depth. Further increase of the erosion parameter leads to a decrease in the scour depth. Additionally, increases in both the strudel hole diameter and the axial velocity inside the strudel hole increase the scour depth.

Table 4-1 presents the variation in the strudel scour depth in the Mackenzie Delta if the overflow depth, the impingement distance and the strudel hole diameter are increased. The *Referenced Estimation* row, was calculated as a reference strudel scour estimate for comparison purposes. It is calculated that increasing the hydraulic head difference by a factor of two only increased the maximum scour depth by 14 %. Increasing the hole diameter by a factor of two increased the maximum static scour depth by 31 %. Increasing the impingement distance by a factor of two increased the static scour by 45 %. Finally, increasing both the impingement distance and the hole diameter by a

factor of two, such that the impingement height ratio is kept constant, was observed to also increase the scour depth by a factor of two. Therefore, defining an accurate impingement distance in the field is more important than defining an accurate overflow depth and hydraulic head difference value. It should be noted that depending on the original estimation parameters, the percentage difference values presented above might slightly differ.

Table 4-1 Strudel scour depth estimations for various parameter increase scenarios.

	Hydraulic Head Difference, H_d (m)	Axial Velocity, U_o , (m/s)	Impingement Distance, H (m)	Hole Diameter, d (m)	Impingement Height, H/d	F_o Parameter	Erosion Parameter, E_c	Maximum Cohesive Soil Scour Depth, ε_m (m)	% Difference with Original Estimation
Referenced Estimation	0.5	2.3	1.0	0.05	20	65.5	3.3	0.83	-
Hydraulic Head Difference (+100%)	1.0	3.3	1.0	0.05	20	92.7	4.6	0.95	+14%
Impingement Distance (+100%)	0.5	2.3	2.0	0.05	40	65.5	1.6	1.20	+45%
Hole Diameter (+100%)	0.5	2.3	1.0	0.1	10	65.5	6.6	1.09	+31%
Impingement Distance and Hole Diameter (+100%)	0.5	2.0	2.0	0.1	20	65.5	3.3	1.66	+100%

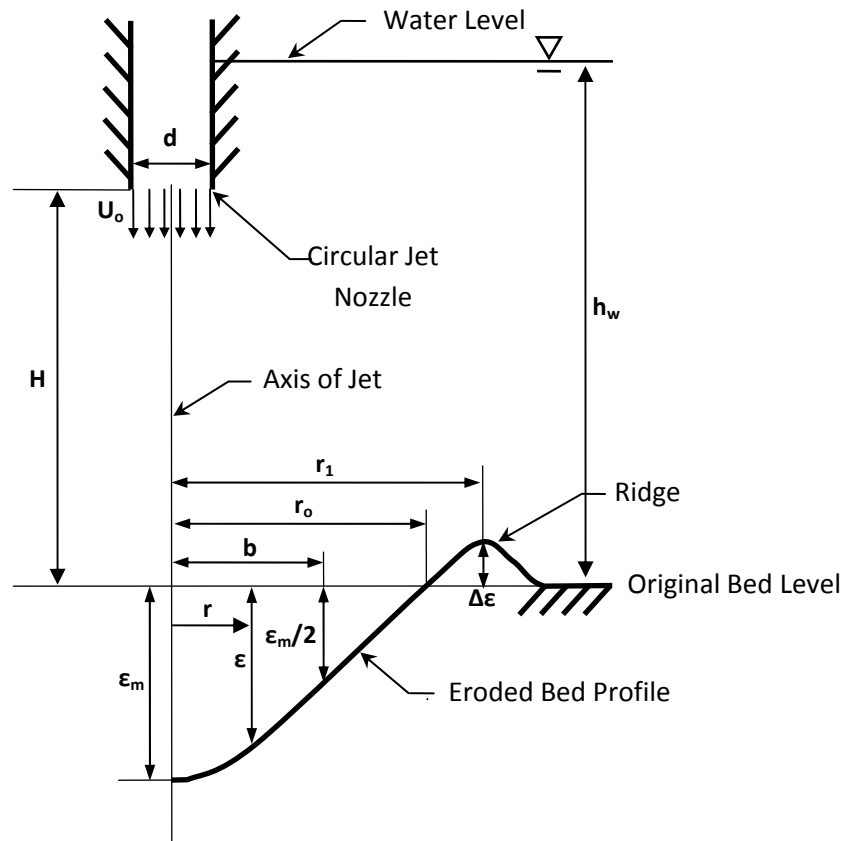


Figure 4-1 Half-sectional view of the eroded bed profile created by a vertical impinging jet (adapted from Rajaratnam, 1982).

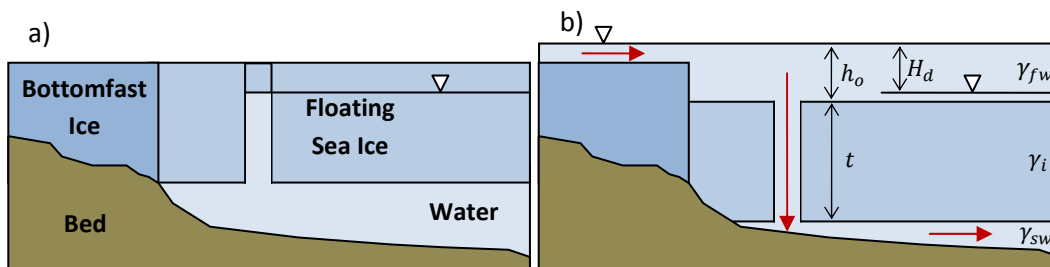


Figure 4-2 Diagrams showing Johnson's (1985) theory on the hydraulic head difference calculation a) before overflow of the sea ice surface, and b) after overflow of the sea ice surface. The arrows indicate the flow direction.

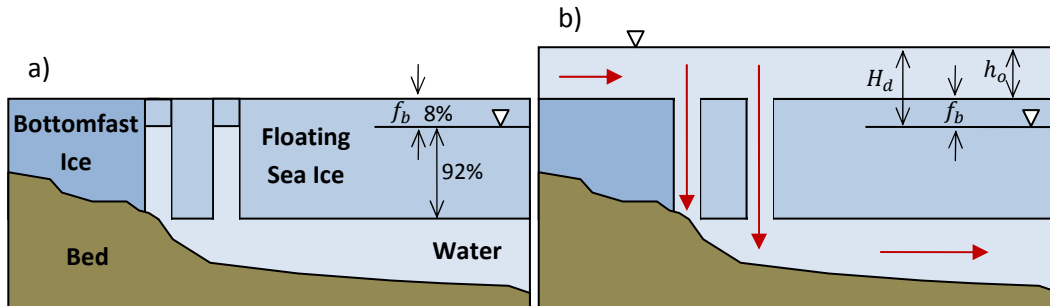


Figure 4-3 Diagrams showing the maximum theoretical hydraulic head difference due to rapid overflow of the ice cover a) before the overflow of the sea ice surface, and b) after overflow of the sea ice surface. The arrows indicate the flow direction.

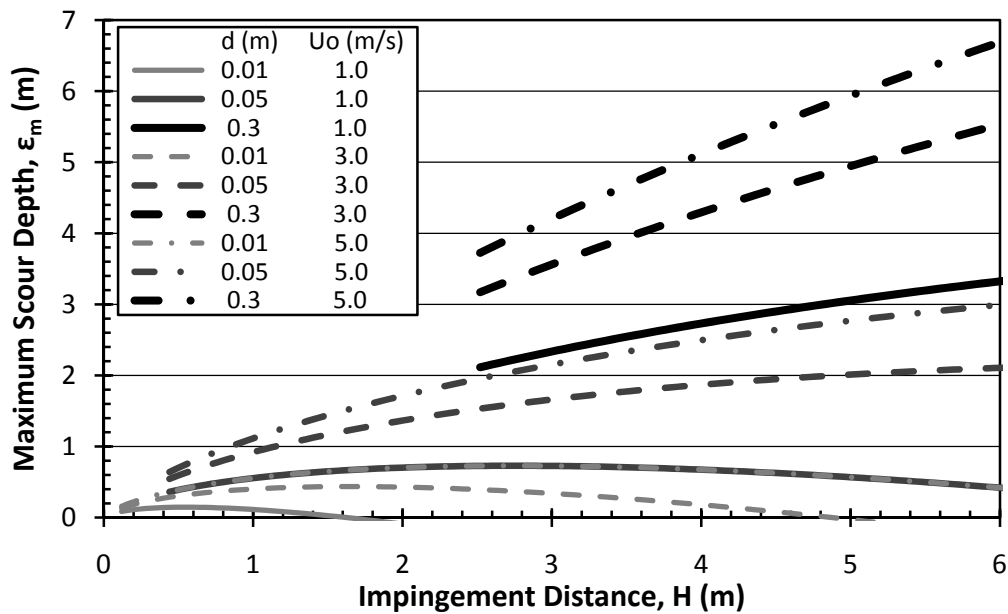


Figure 4-4 Estimation of the maximum strudel scour depth (ϵ_m) in the Mackenzie Delta for various impingement distance (H), hole diameter (d) and axial velocities (U_o) for large impingement heights ($H/d > 8.3$).

5.0 Conclusions and Recommendations

Each spring, the sea ice surface of the Mackenzie Delta floods at distances up to 20 km from the shore due to the increasing freshet flow of the Mackenzie River. Additionally, upwelling and strudel drains, which are integral components of the overflow process, are present in various regions of the outer delta. Vertical flow through strudel drains impinges on the sea bed and produces scour holes that may impose a risk to buried oil and gas pipelines. Unfortunately, the hydraulic behaviour of these upwelling, overflow and strudel events, has not been systematically studied. Most of the previous research focused on field observations and measurements of such events such that their hydraulic properties were usually left undefined. Furthermore, the majority of these studies were conducted in the Alaskan Beaufort Sea and only a few have been conducted in the Mackenzie Delta. As a result, very little is known about the hydraulics of these events. The goal of this research was to increase scientific knowledge regarding the hydraulic processes leading to overflow of the sea ice surface and regarding the hydraulic properties of the upwelling and of the strudel features in the Mackenzie Delta, and possibly at other locations where water on ice overflow occurs such as in the Alaskan Beaufort Sea, at the Lena Delta, and even on lakes.

From the analysis of collected field data, satellite images and other published material, a thorough description of the overflow process that occurs in the Mackenzie Delta was developed and is described in Chapter 2. This description spans from freeze-up in fall to the complete melting of the nearshore sea ice surface in spring. The most important result of the field study is the description of the chronology of the overflow process which is divided into four main stages: the *initial bottomfast ice overflow* where water is first observed to overflow on the bottomfast ice surface; the *initial floating sea ice overflow* where the bottomfast ice overflow has reached the floating ice cover and is flooding its surface; the *maximum floating sea ice overflow* where the overflow covers the largest ice surface area; and the *drained overflow* where the overflow has completely drained from the floating ice surface and covers only the bottomfast ice surface. Between 2006 and 2009, these four stages were respectively reached on average on 13-May, 16-May, 19-May, and 24-May at the South of Garry Island overflow region, and on 09-May, 14-May, 18-May, and 23-May at the overflow region north of

the Olivier Islands. The peak freshet arrives in the outer delta on approximately 01-June in the Shallow Bay and 04-June at the Middle Channel Mouth.

In Chapter 2, the first attempt at forecasting the various overflow stages in the Mackenzie Outer Delta from the water level in the Mackenzie River at Arctic Red River is presented. Forecasting the four main stages of the overflow at the South of Garry Island and north of Olivier Islands regions was found to be accurate, for example, the initial bottomfast ice overflow in these two regions can be predicted 1 to 5 days before their occurrence. Furthermore, this forecasting scheme could be used to predict the timing of the overflow in the upcoming years. However, it was observed that warm temperatures throughout the delta can cause local melting and initiate the overflow process before any significant increase in water level is measured in the Mackenzie River at Arctic Red River. The forecasting of the overflow timing could be useful for the planning of outer delta activities such as ice road closures, but mostly for the planning of field investigations to further study the upwelling, overflow and strudel phenomena.

Field investigations performed in 2008 and 2009, presented in Chapter 2, were useful to describe the upwelling and strudel events that occur in the Mackenzie Outer Delta during the overflow period. Upwellings were found to usually be located along the interface separating the floating channel ice and the bottomfast ice. In the Mackenzie Delta, upwellings are mostly located at the upstream edge of the bottomfast ice, near the mouth of the delta's channels. Circular shaped upwelling flows had diameters up to 3 m. Strudel mostly formed at the interface between the bottomfast ice and the floating sea ice and also through the floating sea ice surface. The greatest strudel density was observed at the north-western edge of the south of Garry Island overflow region and at the Middle Channel mouth. The strudel drains averaged between 0.1 m and 1.0 m in diameter but reached diameters up to 3.5 m with a possibility that larger drains existed. Strong vertical strudel flows were observed to scour the sea bed surface of the Mackenzie Delta to depths of 1.4 m below the bed surface.

The hydraulic model study of strudel flows in a circular hole, presented in Chapter 3, revealed an important relationship between the discharge coefficient (C_d) and the overflow depth / hole diameter ratio (h_o/d). It was observed that above an h_o/d ratio of 0.8, the discharge was unaffected by the depth of overflow, that is, the discharge

coefficient was constant and equal to 0.74 ± 0.07 . At an h_o/d ratio smaller than 0.5, C_d rapidly decreased with decreasing ratios as the overflow depth was insufficient for its flow to be conveyed throughout the entire cross-sectional area of the hole. An empirical equation defining the relationship between the two dimensionless parameters, Equation 3-20, was observed to fit the data reasonably well, especially for small ratios, with a correlation coefficient (R) of 0.89.

Some interesting flow behaviour was observed from the ADV velocity measurements of the free-surface vortex flow below the hole, as presented in Chapter 3. In the free jet region, the velocity profiles were similar to the well-studied non-rotational fully turbulent jet, described by equation 3-4. The main difference was the presence of a rotation along the cross-sectional plane, where horizontal velocity vectors near the vortex centerline reached a maximum of $0.65 U_o$, where U_o is the average axial velocity inside the hole. Additionally, the axial velocities at the vortex centerline were significantly smaller, with a measured minimum of $0.4 U_o$, than the surrounding velocities, having magnitudes of approximately $1.0 U_o$. In the impingement region of the jet, the axial velocities of the vortex flow were not well described by the fully turbulent jet equations 3-8 and 3-13 due to large amount of scatter. However, axial velocities were reduced due to the impinging boundary such that a stagnation point seemed to form at the jet centerline. In this region, the flow was redirected in the radial direction where the radial velocities were well predicted by empirical equation 3-10 with a correlation coefficient (R) of 0.85. Furthermore a rotation induced by the free-surface vortex was observed.

Finally, Chapter 4 presents an attempt at estimating the maximum strudel scour depth to occur in the Mackenzie Delta from the latest published impinging jet experiments. This prediction has only been attempted on one other occasion more than twenty years ago (Arctec Newfoundland Limited, 1987) when most of the studies of vertically impinging jets on sediments were not yet completed. Unfortunately, the majority of these studies were performed in cohesionless soils and at large impingement heights while scour of the sea bed usually occurs in cohesive soil and at small impingement heights. The analysis revealed that, for a strudel hole diameter of 8 cm and an impingement distance of 0.7 m, the estimated maximum strudel scour depth in the

Mackenzie Outer Delta, is approximately 0.83 m. This depth is slightly smaller than the measured strudel scour depths in the field which had a maximum of 0.87 m in 2008 and 1.38 m in 2009. The strudel hole diameter and the impingement distance were the most significant parameters defining the strudel hole geometry. Increasing both these parameters by a factor of two, such that the impingement height ratio remains the same, would also increase the scour depth by a factor of two. However, increasing the hydraulic head difference by a factor of two would only increase this depth by approximately 14 %. As the erosive properties of the soil sediments, such as their cohesive properties, mean particle size and soil density, are likely to affect the maximum strudel scour, future studies of vertically impinging jets on cohesive soils are necessary to account for these factors.

In the hope of improving scientific knowledge of the upwelling phenomenon, the flooding of the sea ice surface, and strudel flow and scouring in the Mackenzie Outer Delta, the following recommendations are made for future studies. First, it is recommended to collect a large amount of information from the Mackenzie Outer Delta, especially during the overflow period, as the amount of collected data is very limited at the moment. This data should include overflow depths on the bottomfast ice and on the floating ice surface at various regions of the outer delta which was done efficiently for this study using depth sensors. Furthermore, manual measurements of the impingement depth (the distance between the underside of the ice surface and the bed elevation), and of strudel drain dimensions should be performed. In addition, studies of the erosive properties of the sea bed sediments are very important. As a result, undisturbed bed soil samples should be collected and analysed for their soil type, particle size, erosive strength, and cohesive properties. The collection of the above mentioned data is important as all these parameters significantly affect the formation of strudel scour in the sea bed. Direct measurements of strudel scour dimensions when the ice surface is still in place, as well as performing sonar and echo sounder boat surveys in spring, remains the most accurate way of determining typical strudel scour depth and dimensions and these types of measurements should be performed every year.

In addition, satellite image and field investigation based observations of the sea ice overflow progression and bottomfast ice locations for the upcoming years should be

compiled. These additional data could improve the precision and accuracy of the forecasting method regarding the timing and duration of the overflow on the sea ice surface, and could help describe the overflow process in more detail. Location of upwelling and strudel drains in the Mackenzie Outer Delta, from field investigations and from satellite images, should also be compiled in order to pinpoint where these hydraulic events are likely to be located.

All of the measurements, observations and analysis performed throughout this thesis should also be performed for other regions where overflow on ice and strudel are observed such as in the Alaskan Beaufort Sea in the United States and at the Lena Delta in Russia. Ideally, the results from these regions would be combined such that a general prediction and explanation of the upwelling, overflow and strudel events could be developed. Another recommendation would be to build a physical or computer model of the overflow process in the Mackenzie Delta. This model could simulate an increasing discharge into the outer delta such that observations of the overflow on the bottomfast ice and on the floating sea ice could be observed. The hydraulics of the flow both under and over the ice surface could also be defined. Other research could include studies of the increase of the strudel drain dimensions with time due to the erosion of the ice by water, as well as studies determining the effect of sea ice buoyancy on the strudel drain flow and drainage of the floating sea ice surface.

Recommendations for future laboratory experimental work are described as follow. First, it is a priority to perform impinging jet experiments on cohesive soils at small impingement heights ($H/d < 5.5$). These studies are required for a better understanding of the effect of the soil type, hole diameter, and of the small impingement distance on the maximum strudel scour dimensions, and to have a better understanding of the interaction between the jet flow and the bed sediments. It would be ideal to make these types of measurements in the field by measuring the physical and hydraulic characteristics of the strudel flow and the resulting scour profile. However, performing strudel scour experiments in a laboratory would be more feasible and cost effective and would still likely provide useful results.

Furthermore, it would be useful to study the velocity profile of the free-surface vortex above and below the ice surface for various overflow depth / hole diameter ratios, but

especially for small ratios ($h_o/d < 0.5$). It was found from ADV velocity measurements that the axial flow at the core of a free-surface vortex is smaller and horizontal velocities at the vortex core are larger than the adjacent flow. As a result, it might be interesting to perform a detailed study defining the effect of a vorticity on the flow properties of the jet flow. Finally, it could be valuable to find relationships between the discharge coefficient and the overflow depth / hole diameter ratio for holes with different shapes, such as a rectangle or an ellipse.

6.0 References

- Abdalla, B., Jukes, P., Eltaher, A., & Duron, B. (2008). The technical challenges of designing oil and gas pipelines in the arctic. *Oceans 2008, Vols 1-4*, 758-768.
- Aderibigbe, O. O., & Rajaratnam, N. (1996). Erosion of loose beds by submerged circular impinging vertical turbulent jets. *Journal of Hydraulic Research*, 34(1), 19-33.
- Alekseenko, S. V., Dulin, V. M., Kozorezov, Y. S., & Markovich, D. M. (2008). Effect of axisymmetric forcing on the structure of a swirling turbulent jet. *International Journal of Heat and Fluid Flow*, 29(6), 1699-1715. doi:10.1016/j.ijheatfluidflow.2008.07.005
- Andersen, A., Bohr, T., Stenum, B., Rasmussen, J. J., & Lautrup, B. (2003). Anatomy of a bathtub vortex. *Physical Review Letters*, 91(10), 104502.
doi:10.1103/PhysRevLett.91.104502
- Andersen, A., Bohr, T., Stenum, B., Rasmussen, J. J., & Lautrup, B. (2006). The bathtub vortex in a rotating container. *Journal of Fluid Mechanics*, 556, 121-146.
doi:10.1017/S0022112006009463
- Ansari, S. A., Kothiyari, U. C., & Raju, K. G. R. (2003). Influence of cohesion on scour under submerged circular vertical jets. *Journal of Hydraulic Engineering-ASCE*, 129(12), 1014-1019. doi:10.1061/(ASCE)0733-9429(2003)129:12(1014)
- Arctec Newfoundland Limited (1987). Effect of sea ice on Beaufort Sea coastal processes. St. Johns, Newfoundland.
- Bélanger, M., Hicks, F., Solomon, S., & Loewen, M. (2009). Influence of Mackenzie Delta breakup on the timing and duration of water overflow on the outer delta sea ice surface. Poster presented at the *CGU HS Committee on River Ice Processes and the Environment - 15th Workshop on River Ice*, St. John's, Newfoundland and Labrador. Retrieved from http://cripe.civil.ualberta.ca/Downloads/15th_Workshop/Poster-Belanger-et-al-2009.pdf
- Beltaos, S., & Rajaratnam, N. (1977). Impingement of axisymmetric developing jets. *Journal of Hydraulic Research*, 15(4), 311-326.

- Beltaos, S., & Rajaratnam, N. (1974). Impinging circular turbulent jets. *Journal of the Hydraulics Division-ASCE*, 100(NHY10), 1313-1328.
- Bergman, B. (2010). *Mackenzie Valley Pipeline*. Retrieved April 2010, from <http://www.thecanadianencyclopedia.com/index.cfm?PgNm=TCE&Params=M1ARTM0012208>
- Bergmann, R., Andersen, A., van der Meer, D., & Bohr, T. (2009). Bubble pinch-off in a rotating flow. *Physical Review Letters*, 102(20), 204501.
doi:10.1103/PhysRevLett.102.204501
- Boguslawski, L., & Popiel, C. O. (1979). Flow structure of the free round turbulent jet in the initial region. *Journal of Fluid Mechanics*, 90(FEB), 531-539.
- Carriveau, R., Kopp, G. A., & Baddour, R. E. (2009). Free-surface stretching-sustained intake vortices. *Journal of Hydraulic Research*, 47(4), 486-491.
doi:10.3826/jhr.2009.3495
- Crow, S. C., & Champagne, F.H. (1971). Orderly structure in jet turbulence. *Journal of Fluid Mechanics*, 48(AUG16), 547-&.
- Dean, K. G., Stringer, W. J., Ahlnas, K., Searcy, C., & Weingartner, T. (1994). The influence of river discharge on the thawing of sea-ice, Mackenzie River Delta - albedo and temperature analyses. *Polar Research*, 13(1), 83-94.
- Dey, B. (1980). Orbital sensing of Mackenzie Bay ice dynamics. *Arctic*, 33(2), 280-291.
- DF Dickins Associates, Coastal Frontiers Corporation, Aero-Metric Inc., & University of Alaska Fairbanks. (2009). *Mapping sea ice overflow using remote sensing: Smith Bay to Camden Bay* (OCS Study MMS 2009-017). Anchorage, Alaska: US Department of the Interior, Minerals Management Service, Alaska OCS Region. Retrieved from http://www.mms.gov/alaska/reports/2009rpts/2009_017.pdf
- Environment Canada. (2010a). *Canada's National Climate Archive - National Climate Data and Information Archive*. Retrieved January 2010, from http://www.climate.weatheroffice.ec.gc.ca/climateData/canada_e.html

- Environment Canada. (2010b). *Water Survey of Canada (WSC) - Real-time hydrometric data*. Retrieved January 2010, from <http://scitech.pyr.ec.gc.ca/waterweb/>
- European Space Agency (ESA). (2010a). *Earth Observation Link (EOLi)*. Retrieved January 2010, from <http://earth.esa.int/EOLi/EOLi.html>
- European Space Agency (ESA). (2010b). *Earthnet Online - Envisat*. Retrieved January 2010, from <http://envisat.esa.int/>
- European Space Agency (ESA). (2010c). *Instruments - AVHRR/3*. Retrieved March 2010, from http://www.esa.int/esaLP/SEM9VEG23IE_LPmetop_0.html
- Fassnacht, S. R., & Conly, F. M. (2000). Persistence of a scour hole on the east channel of the Mackenzie Delta, NWT. *Canadian Journal of Civil Engineering*, 27(4), 798-804.
- Fisheries and Oceans Canada. (2010). *Canadian historical tides and water level data*. Retrieved January 2010, from <http://www.meds-sdmm.dfo-mpo.gc.ca/isdm-gdsi/twl-mne/inventory-inventaire/index-eng.htm>
- Forbes, D. L., & Taylor, R. B. (1994). Ice in the shore zone and the geomorphology of cold coasts. *Progress in Physical Geography*, 18(1), 59-96.
- Great Canadian Rivers. (2007). *Mackenzie River Ecosystem*. Retrieved January 2010, from <http://www.greatcanadianrivers.com/rivers/mack/species-home.html>
- Hill, P. R., Blasco, S. M., Harper, J. R., & Fissel, D. B. (1991). Sedimentation on the Canadian Beaufort shelf. *Continental Shelf Research*, 11(8-10), 821-842.
- Hill, P. R., Lewis, C. P., Desmarais, S., Kauppamuthoo, V., & Rais, H. (2001). The Mackenzie Delta: Sedimentary processes and facies of a high-latitude, fine-grained delta. *Sedimentology*, 48(5), 1047-1078.
- Hirose, T., Kapfer, M., Bennett, J., Cott, P., Manson, G., & Solomon, S. (2008). Bottomfast ice mapping and the measurement of ice thickness on tundra lakes using C-band synthetic aperture radar remote sensing. *Journal of the American Water Resources Association*, 44(2), 285-292. doi:10.1111/j.1752-1688.2007.00161.x ER

Hocking, G. C., Vanden-Broeck, J. M., & Forbes, L. K. (2002). A note on withdrawal from a fluid of finite depth through a point sink. *Anziam Journal*, 44, 181-191.

Johnson, T. L. (1985). Strudel scour: An arctic sea floor scouring process. *American Society of Civil Engineers Arctic '85 Specialty Conference Proceedings*, San Francisco, California. 745-753.

Kelly, D. L., Martin, B. W., & Taylor, E. S. (1964). A further note on the bathtub vortex. *Journal of Fluid Mechanics*, 19(4), 539-542.

King, T., Phillips, R., & Barrett, J. (2009). Evaluating pipeline risk due to strudel scour. *Proceedings of the 20th International Conference on Port and Ocean Engineering Under Arctic Conditions*, Lulea, Sweden.

Kundu, P. K., Cohen, I. M., & Hu, H. H. (2002). *Fluid mechanics* (2nd Edition ed.). San Diego: Academic Press.

Leidersdorf, C.B., Gadd, P.E., & Vaudrey, K.D. (1996). Design Considerations for Coastal Projects in Cold Regions. *Proceedings of the 25th International Conference on Coastal Engineering*, ASCE, 4397-4410.

Leidersdorf, C. B., Hearon, G. E., Vaudrey, K. D., & Swank, G. (September 3-8, 2006). Strudel scour formation off arctic river deltas. Paper presented at the *Coastal Engineering 2006 - Proceedings of the 30th International Conference*, San Diego, California, USA. 5312-5324. doi:10.1142/9789812709554_0445

Lide, D. R. (2005). *CRC handbook of chemistry and physics* (86th Edition ed.). Boca Raton, Florida: CRC Press. doi:ISBN 0-8493-0486-5

Lubin, B. T., & Springer, G. S. (1967). Formation of a dip on surface of a liquid draining from a tank. *Journal of Fluid Mechanics*, 29, 385-&.

Mackenzie Pipeline's Numbers Questioned. (2010, February 8). *CBC News*, Retrieved from <http://www.cbc.ca/canada/north/story/2010/02/08/mackenzie-altnorth.html#ixzzOmGZWBW4V>

Mak, H., & Balabani, S. (2007). Near field characteristics of swirling flow past a sudden expansion. *Chemical Engineering Science*, 62(23), 6726-6746.

doi:10.1016/j.ces.2007.07.009

Mazurek, K. A., & Hossain, T. (2007). Scour by jets in cohesionless and cohesive soils. *Canadian Journal of Civil Engineering*, 34(6), 744-751. doi:10.1139/L07-005

Mazurek, K. A., Rajaratnam, N., & Segoo, D. C. (2001). Scour of cohesive soil by submerged circular turbulent impinging jets. *Journal of Hydraulic Engineering-ASCE*, 127(7), 598-606.

Mackenzie River Basin Board (MRBB). (2001). *Maps of the Mackenzie River Basin*.

Retrieved January 2010, from <http://www.mrbb.ca/maps.asp>

Moore, W. L., & Masch, F. D. (1962). Experiments on scour resistance of cohesive sediments. *Journal of Geophysical Research*, 67(4), 1437-&.

National Aeronautics and Space Administration (NASA). (2005). *Landsat: A Global Land Imaging Project*. Retrieved July 2010, from

http://landsat.usgs.gov/documents/Landsat_Fact_sheet.pdf

National Aeronautics and Space Administration (NASA). (2009). *Landsat 7 science data users handbook*. Retrieved January 2010, from

http://landsathandbook.gsfc.nasa.gov/handbook/handbook_toc.html

National Aeronautics and Space Administration (NASA). (2010a). *Aqua Project Science*.

Retrieved March 2010, from <http://aqua.nasa.gov/about/instruments.php>

National Aeronautics and Space Administration (NASA). (2010b). *MODIS Web*. Retrieved

January 2010, from <http://modis.gsfc.nasa.gov/>

National Oceanic and Atmospheric Administration (NOAA). (2010). *NOAA KLM user's guide - Advanced Very High Resolution Radiometer/3 (AVHRR/3)*. Retrieved January

2010, from <http://www2.ncdc.noaa.gov/docs/klm/html/c3/sec3-1.htm>

Natural Resources Canada (NRCan). (2010). *The Atlas of Canada*. Retrieved January 2010, from <http://atlas.nrcan.gc.ca/site/english/maps/topo/index.html>

Niven, R. K., & Khalili, N. (1998). In situ fluidisation by a single internal vertical jet. *Journal of Hydraulic Research*, 36(2), 199-228.

Örlü, R., & Alfredsson, P. H. (2008). An experimental study of the near-field mixing characteristics of a swirling jet. *Flow Turbulence and Combustion*, 80(3), 323-350.
doi:10.1007/s10494-007-9126-y

Rajaratnam, N. (1981a). Erosion by plane turbulent jets. *Journal of Hydraulic Research*, 19(4), 339-358.

Rajaratnam, N. (1981b). *Erosion of sand beds by submerged impinging circular turbulent water jets* (Technical Report No. WRE 81-1). Edmonton, Canada: Dept. of Civil Engineering, University of Alberta.

Rajaratnam, N. (1982). Erosion by submerged circular jets. *Journal of the Hydraulics Division-Asce*, 108(2), 262-267.

Rajaratnam, N. (1987). *Engineering Fluid Mechanics* (CivE631 Class Notes). Edmonton, Alberta, Canada: Dept. of Civil Engineering, University of Alberta.

Rajaratnam, N., & Beltaos, S. (1977). Erosion by impinging circular turbulent jets. *Journal of the Hydraulics Division-Asce*, 103(10), 1191-1205.

Rajaratnam, N., & Mazurek, K. A. (2003). Erosion of sand by circular impinging water jets with small tailwater. *Journal of Hydraulic Engineering-ASCE*, 129(3), 225-229.
doi:10.1061/(ASCE)0733-9429(2003)129:3(225)

Rajaratnam, N., & Mazurek, K. A. (2005). Impingement of circular turbulent jets on rough boundaries. *Journal of Hydraulic Research*, 43(6), 689-695.

Reimnitz, E. (2002). Interactions of river discharge with sea ice in proximity of arctic deltas: A review. *Polarforschung* 70, 123-134. doi:hdl:10013/epic.29865.d001

Reimnitz, E., & Bruder, K. F. (1972). River discharge into an ice-covered ocean and related sediment dispersal, Beaufort Sea, Coast of Alaska. *Geological Society of America Bulletin*, 83(3), 861-&.

Reimnitz, E., & Kempema, E. W. (1983). High-rates of bedload transport measured from infilling rate of large strudel-scour craters in the Beaufort Sea, Alaska. *Continental Shelf Research*, 1(3), 237-&.

Reimnitz, E., Rodeick, C. A., & Wolf, S. C. (1974). Strudel scour - Unique arctic marine geologic phenomenon. *Journal of Sedimentary Petrology*, 44(2), 409-420.

Sibulkin, M. (1962). A note on the bathtub vortex. *Journal of Fluid Mechanics*, 14(1), 21-24.

Solomon, S. M., Forbes, D. L., Fraser, P., Moorman, B., Stevens, C. W., Whalen, D., & ASME. (2009). Nearshore geohazards in the southern Beaufort Sea, Canada. *IPC2008: Proceedings of the ASME International Pipeline Conference, Vol 4*, 281-289.

Solomon, S., Fraser, P., & Whalen, D. (2007). Tracking changes in coastal and nearshore morphology in the southern Beaufort Sea using synthetic aperture radar. Poster presented at the *American Geophysical Union (Fall Meeting)*, San Francisco, California, USA. doi:2007AGUFM.H41B0509S

Stepanyants, Y. A., & Yeoh, G. H. (2008). Stationary bathtub vortices and a critical regime of liquid discharge. *Journal of Fluid Mechanics*, 604, 77-98.
doi:10.1017/S0022112008001080

Tani, I., & Komatsu, Y. (1964). Impingement of a round jet on a flat surface. *Proceedings of the Eleventh International Congress of Applied Mechanics*, Munich, Germany. 672-676.

The Canadian Encyclopaedia. (2010). *Mackenzie River*. Retrieved January 2010, from <http://www.thecanadianencyclopedia.com/index.cfm?PgNm=TCE&Params=A1ARTA0004954>

- Tyvand, P. A., & Haugen, K. B. (2005). An impulsive bathtub vortex. *Physics of Fluids*, 17(6), 062105. doi:10.1063/1.1938216
- U.S. Geological Survey. (2010). *USGS Global Visualization Viewer (Glovis)*. Retrieved January 2010, from <http://glovis.usgs.gov/>
- University of Alaska. (2010). *Geographic Information Network of Alaska (GINA)*. Retrieved January 2010, from <http://www.gina.alaska.edu>
- Vectrino Velocimeter - User Guide* (2009). Norway: Nortek AS.
- Walker, H. J. (1998). Arctic Deltas. *Journal of Coastal Research*, 14(3), 718-738.
- Whalen, D., Solomon, S., Forbes, D., Beaver, D., Nelson, A., & Travaglini, P. (2007). Frequency and distribution of shallow hazards that affect the Beaufort Sea potential pipeline area. *35th Annual Yellowknife Geoscience Forum Abstracts of Talks and Posters, Yellowknife, NWT, Canada*, 67.
- Yeh, P., Chang, K., Henriksen, J., Edge, B., Chang, P., Silver, A., & Vargas, A. (2009). Large-scale laboratory experiment on erosion of sand beds by moving circular vertical jets. *Ocean Engineering*, 36(3-4), 248-255. doi:10.1016/j.oceaneng.2008.11.006

Appendix A

Details of Hydraulic Data Collection

from Strudel Experiments

Run no.	Collected Data								Non-Dimensional Data					
	d (cm)	Q _o (L/s)	U _o (m/s)	h _o (m)	h _u (m)	h _d (m)	H _d (m)	Air Entrainment	C _d = U _o /√(2gH _d)	t/d	H _d /d	h _o /d	H/d	Re = ρU _o d/μ
3	5.1	0.22	0.108	0.044	0.397	0.396	0.001	NO	0.77	2.98	0.02	0.86	3.94	5472
4	2.0	0.07	0.223	0.047	0.400	0.396	0.004	NO	0.80	7.60	0.20	2.33	10.05	4439
5	2.0	0.13	0.414	0.057	0.409	0.396	0.013	NO	0.82	7.60	0.65	2.83	10.05	8245
6	5.1	0.65	0.318	0.055	0.408	0.398	0.010	YES	0.72	2.98	0.20	1.08	3.94	16166
7	7.8	1.76	0.368	0.067	0.421	0.405	0.016	YES/NO	0.66	1.95	0.21	0.86	2.58	28621
8	7.8	2.36	0.494	0.084	0.437	0.409	0.028	YES	0.67	1.95	0.36	1.07	2.58	38378
9	5.1	0.93	0.455	0.067	0.421	0.401	0.020	YES	0.73	2.98	0.39	1.31	3.94	23130
10	2.0	0.18	0.573	0.064	0.417	0.396	0.021	NO	0.89	7.60	1.05	3.20	10.05	11416
12	7.8	2.70	0.565	0.094	0.446	0.410	0.036	YES	0.67	1.95	0.46	1.21	2.58	43907
15	7.8	3.37	0.705	0.111	0.463	0.413	0.050	YES	0.71	1.95	0.64	1.42	2.58	54802
19	7.8	3.68	0.770	0.122	0.475	0.414	0.061	YES	0.70	1.95	0.78	1.56	2.58	59843
22	7.8	3.82	0.799	0.121	0.474	0.415	0.059	YES	0.74	1.95	0.76	1.55	2.58	62120
23	5.1	1.06	0.519	0.074	0.427	0.402	0.025	YES	0.74	2.98	0.49	1.44	3.94	26363
24	5.1	1.34	0.656	0.089	0.442	0.403	0.039	YES	0.75	2.98	0.76	1.74	3.94	33327
25	5.1	1.60	0.783	0.107	0.460	0.405	0.055	YES	0.75	2.98	1.08	2.10	3.94	39793
26	5.1	1.81	0.886	0.125	0.478	0.406	0.072	YES	0.75	2.98	1.41	2.45	3.94	45016
27	5.1	1.92	0.940	0.133	0.486	0.407	0.079	YES	0.75	2.98	1.55	2.61	3.94	47752
28	2.0	0.20	0.637	0.088	0.441	0.396	0.045	YES/NO	0.68	7.60	2.25	4.38	10.05	12684
29	2.0	0.24	0.764	0.101	0.454	0.397	0.057	NO	0.72	7.60	2.85	5.05	10.05	15221
30	2.0	0.27	0.859	0.113	0.466	0.397	0.069	NO	0.74	7.60	3.45	5.65	10.05	17124
31	2.0	0.29	0.923	0.123	0.476	0.397	0.079	NO	0.74	7.60	3.95	6.15	10.05	18392
32	2.0	0.31	0.987	0.135	0.487	0.397	0.090	NO	0.74	7.60	4.50	6.73	10.05	19660
33	2.0	0.33	1.050	0.139	0.492	0.397	0.095	NO	0.77	7.60	4.75	6.93	10.05	20929
78	2.0	0.02	0.064	0.003	0.359	0.348	0.011	NO	0.14	7.60	0.55	0.17	10.05	1268
79	2.0	0.08	0.255	0.008	0.362	0.348	0.014	NO	0.49	7.60	0.70	0.40	10.05	5074
80	2.0	0.12	0.382	0.014	0.368	0.348	0.020	NO	0.61	7.60	1.00	0.67	10.05	7610
81	2.0	0.16	0.509	0.018	0.372	0.348	0.024	NO	0.74	7.60	1.20	0.90	10.05	10147
82	2.0	0.19	0.605	0.029	0.383	0.348	0.035	NO	0.73	7.60	1.75	1.43	10.05	12050
83	2.0	0.19	0.605	0.029	0.382	0.348	0.034	NO	0.74	7.60	1.70	1.43	10.05	12050
84	2.0	0.23	0.732	0.039	0.393	0.348	0.045	YES/NO	0.78	7.60	2.25	1.95	10.05	14587
85	2.0	0.25	0.796	0.051	0.404	0.348	0.056	YES/NO	0.76	7.60	2.80	2.53	10.05	15855
86	2.0	0.29	0.923	0.067	0.421	0.349	0.072	YES/NO	0.78	7.60	3.60	3.35	10.05	18392
87	2.0	0.31	0.987	0.079	0.432	0.349	0.083	YES/NO	0.77	7.60	4.15	3.93	10.05	19660
88	2.0	0.33	1.050	0.090	0.443	0.349	0.094	NO	0.77	7.60	4.70	4.50	10.05	20929
89	2.0	0.35	1.114	0.101	0.454	0.349	0.105	NO	0.78	7.60	5.25	5.05	10.05	22197
90	2.0	0.36	1.146	0.112	0.465	0.349	0.116	NO	0.76	7.60	5.80	5.60	10.05	22831
91	2.0	0.38	1.210	0.123	0.476	0.349	0.127	NO	0.77	7.60	6.35	6.13	10.05	24100
92	2.0	0.40	1.273	0.134	0.487	0.349	0.138	NO	0.77	7.60	6.90	6.70	10.05	25368
93	5.1	0.23	0.113	0.008	0.363	0.348	0.015	NO	0.21	2.98	0.29	0.16	3.94	5720
94	5.1	0.52	0.255	0.019	0.372	0.349	0.023	YES	0.38	2.98	0.45	0.36	3.94	12933
96	5.1	0.76	0.372	0.027	0.381	0.352	0.029	YES	0.49	2.98	0.57	0.53	3.94	18902
97	5.1	1.21	0.592	0.035	0.389	0.354	0.035	YES	0.71	2.98	0.69	0.69	3.94	30094
98	5.1	1.34	0.656	0.042	0.396	0.355	0.041	YES	0.73	2.98	0.80	0.82	3.94	33327
99	5.1	1.56	0.764	0.059	0.413	0.356	0.057	YES	0.72	2.98	1.12	1.16	3.94	38798
100	5.1	1.62	0.793	0.068	0.422	0.357	0.065	YES	0.70	2.98	1.27	1.33	3.94	40291
101	5.1	1.72	0.842	0.076	0.429	0.357	0.072	YES	0.71	2.98	1.41	1.48	3.94	42778
103	5.1	1.86	0.911	0.100	0.454	0.358	0.096	YES	0.66	2.98	1.88	1.96	3.94	46260
104	5.1	1.90	0.930	0.110	0.463	0.359	0.104	YES	0.65	2.98	2.04	2.15	3.94	47255
106	5.1	2.12	1.038	0.114	0.467	0.359	0.108	YES	0.71	2.98	2.12	2.24	3.94	52726
107	5.1	2.26	1.106	0.134	0.486	0.360	0.126	YES	0.70	2.98	2.47	2.62	3.94	56208
108	7.8	0.48	0.100	0.011	0.365	0.349	0.016	YES	0.18	1.95	0.21	0.14	2.58	7806
109	7.8	1.14	0.239	0.021	0.375	0.354	0.021	YES	0.37	1.95	0.27	0.27	2.58	18538
111	7.8	1.50	0.314	0.030	0.385	0.357	0.028	YES	0.42	1.95	0.36	0.38	2.58	24393
112	7.8	2.13	0.446	0.051	0.404	0.360	0.044	YES	0.48	1.95	0.56	0.65	2.58	34637
114	7.8	2.65	0.555	0.054	0.408	0.362	0.046	YES	0.58	1.95	0.59	0.69	2.58	43093
115	7.8	3.51	0.735	0.093	0.447	0.365	0.082	YES	0.58	1.95	1.05	1.19	2.58	57078
118	7.8	3.63	0.760	0.101	0.454	0.367	0.087	YES	0.58	1.95	1.12	1.29	2.58	59030

Run no.	Collected Data								Non-Dimensional Data					
	d (cm)	Q _o (L/s)	U _o (m/s)	h _o (m)	h _u (m)	h _d (m)	H _d (m)	Air Entrainment	C _d = U _o /√(2gH _d)	t/d	H _d /d	h _o /d	H/d	Re = ρU _o d/μ
119	7.8	3.73	0.781	0.110	0.464	0.367	0.097	YES	0.57	1.95	1.24	1.41	2.58	60656
120	7.8	3.81	0.797	0.101	0.454	0.367	0.087	YES	0.61	1.95	1.12	1.29	2.58	61957
121	7.8	1.67	0.349	0.135	0.488	0.478	0.010	YES/NO	0.79	1.95	0.13	1.73	2.58	27157
123	7.8	1.67	0.349	0.123	0.476	0.465	0.011	YES/NO	0.75	1.95	0.14	1.58	2.58	27157
125	7.8	1.67	0.349	0.099	0.453	0.441	0.012	YES/NO	0.72	1.95	0.15	1.28	2.58	27157
127	7.8	1.67	0.349	0.083	0.436	0.424	0.012	YES/NO	0.72	1.95	0.15	1.06	2.58	27157
129	7.8	1.67	0.349	0.067	0.421	0.410	0.011	YES/NO	0.75	1.95	0.14	0.86	2.58	27157
131	7.8	1.68	0.352	0.051	0.405	0.393	0.012	YES	0.72	1.95	0.15	0.65	2.58	27320
135	7.8	1.68	0.352	0.037	0.392	0.377	0.015	YES	0.65	1.95	0.19	0.47	2.58	27320
136	7.8	1.68	0.352	0.029	0.384	0.365	0.019	YES	0.58	1.95	0.24	0.37	2.58	27320
138	7.8	1.68	0.352	0.027	0.382	0.344	0.038	YES	0.41	1.95	0.49	0.35	2.58	27320
143	7.8	2.31	0.483	0.131	0.484	0.463	0.021	YES	0.75	1.95	0.27	1.68	2.58	37564
144	7.8	2.31	0.483	0.113	0.466	0.445	0.021	YES	0.75	1.95	0.27	1.45	2.58	37564
145	7.8	2.31	0.483	0.099	0.452	0.430	0.022	YES	0.74	1.95	0.28	1.27	2.58	37564
146	7.8	2.31	0.483	0.084	0.437	0.414	0.023	YES	0.72	1.95	0.29	1.08	2.58	37564
149	7.8	2.32	0.486	0.070	0.424	0.399	0.025	YES	0.69	1.95	0.32	0.90	2.58	37727
150	7.8	2.32	0.486	0.048	0.402	0.379	0.023	YES	0.72	1.95	0.29	0.62	2.58	37727
151	7.8	2.32	0.486	0.036	0.391	0.364	0.027	YES	0.67	1.95	0.35	0.47	2.58	37727
152	7.8	2.32	0.486	0.038	0.392	0.353	0.039	YES	0.56	1.95	0.50	0.49	2.58	37727
153	7.8	2.32	0.486	0.037	0.392	0.343	0.049	YES	0.50	1.95	0.63	0.47	2.58	37727
156	7.8	0.57	0.119	0.137	0.490	0.489	0.001	NO	0.85	1.95	0.01	1.76	2.58	9269
157	7.8	0.75	0.157	0.111	0.465	0.463	0.002	NO	0.79	1.95	0.03	1.42	2.58	12196
158	7.8	0.76	0.159	0.094	0.447	0.445	0.002	NO	0.80	1.95	0.03	1.21	2.58	12359
159	7.8	0.76	0.159	0.071	0.424	0.422	0.002	NO	0.80	1.95	0.03	0.91	2.58	12359
160	7.8	0.76	0.159	0.051	0.404	0.402	0.002	NO	0.80	1.95	0.03	0.65	2.58	12359
161	7.8	0.76	0.159	0.037	0.391	0.388	0.003	NO	0.66	1.95	0.04	0.47	2.58	12359
162	7.8	0.76	0.159	0.022	0.376	0.372	0.004	YES/NO	0.57	1.95	0.05	0.28	2.58	12359
164	7.8	0.76	0.159	0.013	0.369	0.278	0.091	YES	0.12	1.95	1.17	0.17	2.58	12359
165	7.8	0.76	0.159	0.014	0.370	0.338	0.032	YES	0.20	1.95	0.41	0.18	2.58	12359
166	7.8	0.76	0.159	0.017	0.371	0.364	0.007	NO	0.43	1.95	0.09	0.22	2.58	12359
167	7.8	0.34	0.071	0.046	0.400	0.399	0.001	NO	0.51	1.95	0.01	0.59	2.58	5529
169	7.8	0.34	0.071	0.119	0.473	0.472	0.001	NO	0.51	1.95	0.01	1.52	2.58	5529
170	7.8	0.34	0.071	0.015	0.369	0.367	0.002	NO	0.36	1.95	0.03	0.19	2.58	5529
172	7.8	0.58	0.121	0.019	0.373	0.370	0.003	NO	0.50	1.95	0.04	0.24	2.58	9432
173	7.8	0.98	0.205	0.025	0.379	0.373	0.006	YES	0.60	1.95	0.08	0.32	2.58	15936
175	7.8	3.82	0.799	0.102	0.456	0.387	0.069	YES	0.69	1.95	0.88	1.30	2.58	62120
176	7.8	3.82	0.799	0.079	0.435	0.369	0.066	YES	0.70	1.95	0.85	1.02	2.58	62120
177	7.8	0.97	0.203	0.018	0.373	0.354	0.019	YES	0.33	1.95	0.24	0.23	2.58	15774
178	7.8	0.58	0.121	0.013	0.367	0.353	0.014	YES	0.23	1.95	0.18	0.17	2.58	9432
179	7.8	0.10	0.021	0.006	0.361	0.350	0.011	NO	0.05	1.95	0.14	0.08	2.58	1626
180	7.8	0.10	0.021	0.006	0.361	0.356	0.005	NO	0.07	1.95	0.06	0.08	2.58	1626
181	7.8	0.37	0.077	0.009	0.365	0.358	0.007	NO	0.21	1.95	0.09	0.12	2.58	6017
182	7.8	0.37	0.077	0.012	0.366	0.364	0.002	NO	0.39	1.95	0.03	0.15	2.58	6017
183	7.8	0.08	0.017	0.009	0.363	0.362	0.001	NO	0.12	1.95	0.01	0.12	2.58	1301
184	7.8	1.06	0.222	0.022	0.377	0.368	0.009	YES	0.53	1.95	0.12	0.28	2.58	17237
185	7.8	3.20	0.670	0.075	0.427	0.374	0.053	YES	0.66	1.95	0.68	0.96	2.58	52037
186	7.8	1.87	0.391	0.034	0.388	0.368	0.020	YES	0.62	1.95	0.26	0.44	2.58	30409
187	7.8	1.87	0.391	0.040	0.394	0.368	0.026	YES	0.55	1.95	0.33	0.51	2.58	30409
190	7.8	1.13	0.236	0.059	0.413	0.406	0.007	YES/NO	0.64	1.95	0.09	0.76	2.58	18376
191	7.8	0.76	0.159	0.023	0.377	0.373	0.004	NO	0.57	1.95	0.05	0.29	2.58	12359
193	7.8	1.69	0.354	0.096	0.450	0.438	0.012	NO	0.73	1.95	0.15	1.23	2.58	27482
194	7.8	1.65	0.345	0.086	0.439	0.426	0.013	YES/NO	0.68	1.95	0.17	1.10	2.58	26832
195	7.8	1.65	0.345	0.086	0.439	0.427	0.012	YES/NO	0.71	1.95	0.15	1.10	2.58	26832
195b	7.8	1.65	0.345	0.085	0.439	0.426	0.013	YES/NO	0.68	1.95	0.17	1.09	2.58	26832
197	5.1	1.18	0.578	0.100	0.453	0.424	0.029	YES	0.77	2.98	0.57	1.96	3.94	29348
198	5.1	0.91	0.445	0.030	0.384	0.364	0.020	YES	0.71	2.98	0.39	0.60	3.94	22632
199	5.1	0.62	0.304	0.021	0.374	0.363	0.011	YES	0.65	2.98	0.22	0.40	3.94	15420

Run no.	Collected Data								Non-Dimensional Data					
	d (cm)	Q _o (L/s)	U _o (m/s)	h _o (m)	h _u (m)	h _d (m)	H _d (m)	Air Entrainment	C _d = U _o /√(2gH _d)	t/d	H _d /d	h _o /d	H/d	Re = ρU _o d/μ
200	5.1	0.62	0.304	0.051	0.404	0.395	0.009	YES/NO	0.72	2.98	0.18	1.00	3.94	15420
201	5.1	0.62	0.304	0.025	0.378	0.346	0.032	YES	0.38	2.98	0.63	0.48	3.94	15420
202	5.1	1.59	0.778	0.058	0.411	0.355	0.056	YES	0.74	2.98	1.10	1.13	3.94	39545
203	5.1	2.21	1.082	0.118	0.472	0.359	0.113	YES	0.73	2.98	2.22	2.30	3.94	54964
205	7.8	1.61	0.337	0.035	0.389	0.377	0.012	YES/NO	0.69	1.95	0.15	0.45	2.58	26181
206	7.8	1.07	0.224	0.027	0.381	0.373	0.008	YES/NO	0.57	1.95	0.10	0.34	2.58	17400
207	7.8	0.60	0.126	0.020	0.374	0.370	0.004	NO	0.45	1.95	0.05	0.26	2.58	9757
208	5.1	1.16	0.568	0.084	0.437	0.408	0.029	YES/NO	0.75	2.98	0.57	1.64	3.94	28850
209	5.1	0.65	0.318	0.057	0.411	0.401	0.010	YES/NO	0.72	2.98	0.20	1.12	3.94	16166
210	5.1	0.65	0.318	0.095	0.449	0.439	0.010	NO	0.72	2.98	0.20	1.86	3.94	16166
211	5.1	0.65	0.318	0.022	0.376	0.364	0.012	YES	0.66	2.98	0.24	0.43	3.94	16166
212	5.1	0.65	0.318	0.038	0.392	0.381	0.011	YES	0.68	2.98	0.22	0.75	3.94	16166
213	5.1	0.26	0.127	0.029	0.383	0.381	0.002	NO	0.64	2.98	0.04	0.56	3.94	6466
214	5.1	0.26	0.127	0.071	0.424	0.423	0.001	NO	0.91	2.98	0.02	1.39	3.94	6466
215	5.1	0.26	0.127	0.121	0.475	0.473	0.002	NO	0.64	2.98	0.04	2.37	3.94	6466
216	5.1	0.88	0.431	0.139	0.492	0.476	0.016	NO	0.77	2.98	0.31	2.72	3.94	21886
217	5.1	0.88	0.431	0.103	0.456	0.439	0.017	YES/NO	0.75	2.98	0.33	2.01	3.94	21886
218	5.1	0.88	0.431	0.072	0.426	0.409	0.017	YES/NO	0.75	2.98	0.33	1.41	3.94	21886
219	5.1	0.88	0.431	0.049	0.402	0.386	0.016	YES	0.77	2.98	0.31	0.96	3.94	21886
220	5.1	0.88	0.431	0.025	0.380	0.359	0.021	YES/NO	0.67	2.98	0.41	0.50	3.94	21886
221	5.1	0.10	0.049	0.006	0.361	0.354	0.007	NO	0.13	2.98	0.14	0.13	3.94	2487
222	5.1	0.34	0.166	0.012	0.366	0.355	0.011	YES	0.36	2.98	0.22	0.24	3.94	8456
223	5.1	0.46	0.225	0.014	0.368	0.356	0.012	YES	0.46	2.98	0.24	0.27	3.94	11441
224	5.1	0.73	0.357	0.020	0.374	0.357	0.017	YES	0.62	2.98	0.33	0.38	3.94	18156
225	5.1	1.14	0.558	0.034	0.388	0.360	0.028	YES	0.75	2.98	0.55	0.66	3.94	28353
226	5.1	1.55	0.759	0.057	0.410	0.362	0.048	YES	0.78	2.98	0.94	1.12	3.94	38550
227	5.1	1.55	0.759	0.051	0.404	0.354	0.050	YES	0.77	2.98	0.98	1.00	3.94	38550
228	5.1	1.55	0.759	0.059	0.412	0.366	0.046	YES	0.80	2.98	0.90	1.16	3.94	38550
229	5.1	0.89	0.436	0.028	0.382	0.365	0.017	YES/NO	0.75	2.98	0.33	0.55	3.94	22135
230	5.1	0.58	0.284	0.019	0.373	0.363	0.010	YES	0.64	2.98	0.20	0.36	3.94	14425
231	5.1	0.36	0.176	0.013	0.367	0.361	0.006	YES	0.51	2.98	0.12	0.25	3.94	8953
232	5.1	0.11	0.054	0.007	0.362	0.360	0.002	NO	0.27	2.98	0.04	0.15	3.94	2736
233	5.1	1.72	0.842	0.087	0.440	0.384	0.056	YES	0.80	2.98	1.10	1.71	3.94	42778
234	5.1	0.93	0.455	0.043	0.396	0.379	0.017	YES	0.79	2.98	0.33	0.84	3.94	23130
235	5.1	0.53	0.259	0.029	0.383	0.377	0.006	YES/NO	0.76	2.98	0.12	0.57	3.94	13182
236	5.1	0.33	0.162	0.024	0.377	0.375	0.002	NO	0.82	2.98	0.04	0.46	3.94	8207
238	5.1	0.29	0.142	0.033	0.386	0.385	0.001	NO	1.01	2.98	0.02	0.65	3.94	7213
239	5.1	0.54	0.264	0.039	0.392	0.386	0.006	YES/NO	0.77	2.98	0.12	0.75	3.94	13430
240	5.1	0.85	0.416	0.049	0.403	0.388	0.015	YES	0.77	2.98	0.29	0.96	3.94	21140
241	5.1	1.40	0.685	0.076	0.429	0.392	0.037	YES	0.80	2.98	0.73	1.49	3.94	34819
242	5.1	2.19	1.072	0.132	0.485	0.396	0.089	YES	0.81	2.98	1.75	2.58	3.94	54467
243	5.1	0.94	0.460	0.073	0.427	0.407	0.020	YES/NO	0.73	2.98	0.39	1.43	3.94	23379
244	5.1	0.54	0.264	0.057	0.411	0.405	0.006	NO	0.77	2.98	0.12	1.12	3.94	13430
245	5.1	0.65	0.318	0.060	0.413	0.405	0.008	NO	0.80	2.98	0.16	1.18	3.94	16166
246	5.1	0.33	0.162	0.040	0.393	0.390	0.003	NO	0.67	2.98	0.06	0.77	3.94	8207
247	5.1	0.61	0.299	0.047	0.400	0.392	0.008	NO	0.75	2.98	0.16	0.92	3.94	15171
248	5.1	0.41	0.201	0.040	0.393	0.390	0.003	NO	0.83	2.98	0.06	0.78	3.94	10197
249	5.1	0.73	0.357	0.045	0.403	0.394	0.009	YES/NO	0.85	2.98	0.18	0.87	3.94	18156
255	5.1	1.17	0.573	0.037	0.391	0.359	0.032	YES	0.72	2.98	0.63	0.72	3.94	29099
256	7.8	0.58	0.121	0.013	0.368	0.357	0.011	NO	0.26	1.95	0.14	0.17	2.58	9432
257	7.8	1.93	0.404	0.033	0.387	0.365	0.022	YES	0.61	1.95	0.28	0.42	2.58	31385
258	7.8	1.08	0.226	0.087	0.440	0.435	0.005	NO	0.72	1.95	0.06	1.12	2.58	17563
260	7.8	1.08	0.226	0.088	0.441	0.436	0.005	NO	0.72	1.95	0.06	1.13	2.58	17563
261	7.8	1.08	0.226	0.043	0.397	0.392	0.005	NO	0.72	1.95	0.06	0.55	2.58	17563
262	7.8	1.65	0.345	0.125	0.478	0.468	0.010	NO	0.78	1.95	0.13	1.60	2.58	26832
263	7.8	1.65	0.345	0.139	0.492	0.482	0.010	NO	0.78	1.95	0.13	1.78	2.58	26832
264	7.8	1.65	0.345	0.139	0.492	0.482	0.010	NO	0.78	1.95	0.13	1.78	2.58	26832

Run no.	Collected Data								Non-Dimensional Data					
	d (cm)	Q _o (L/s)	U _o (m/s)	h _o (m)	h _u (m)	h _d (m)	H _d (m)	Air Entrainment	C _d = U _o /√(2gH _d)	t/d	H _d /d	h _o /d	H/d	Re = ρU _o d/μ
265	7.8	1.08	0.226	0.129	0.483	0.478	0.005	NO	0.72	1.95	0.06	1.65	2.58	17563
266	7.8	1.65	0.345	0.139	0.492	0.481	0.011	NO	0.74	1.95	0.14	1.78	2.58	26832
267	7.8	1.08	0.226	0.130	0.483	0.479	0.004	NO	0.81	1.95	0.05	1.67	2.58	17563
268	7.8	0.60	0.126	0.088	0.441	0.439	0.002	NO	0.63	1.95	0.03	1.12	2.58	9757
269	7.8	0.60	0.126	0.127	0.480	0.478	0.002	NO	0.63	1.95	0.03	1.63	2.58	9757

Appendix B

Details of Hydraulic Data Collection

from Strudel Experiments

Supplemental Collected Data and Analysis

where the Downstream Water Surface

was below the Under-Ice Surface

An attempt to obtain the same relationship between the overflow depth / hole diameter (h_o/d) ratio and the discharge coefficient (C_d), as presented in Section 3.4.3, using the data where the downstream water surface was below the under-ice surface was performed. For the calculations presented in the table below, the hydraulic head difference (H_d) was assumed equal to the overflow depth (h_o). The resulting graph of Figure B-1 shows that for small h_o/d ratios ($h_o/d < 0.5$), most of these data are well defined by the empirical equation 3-20. For larger ratios, the discharge coefficient varies around the previously defined constant of 0.74.

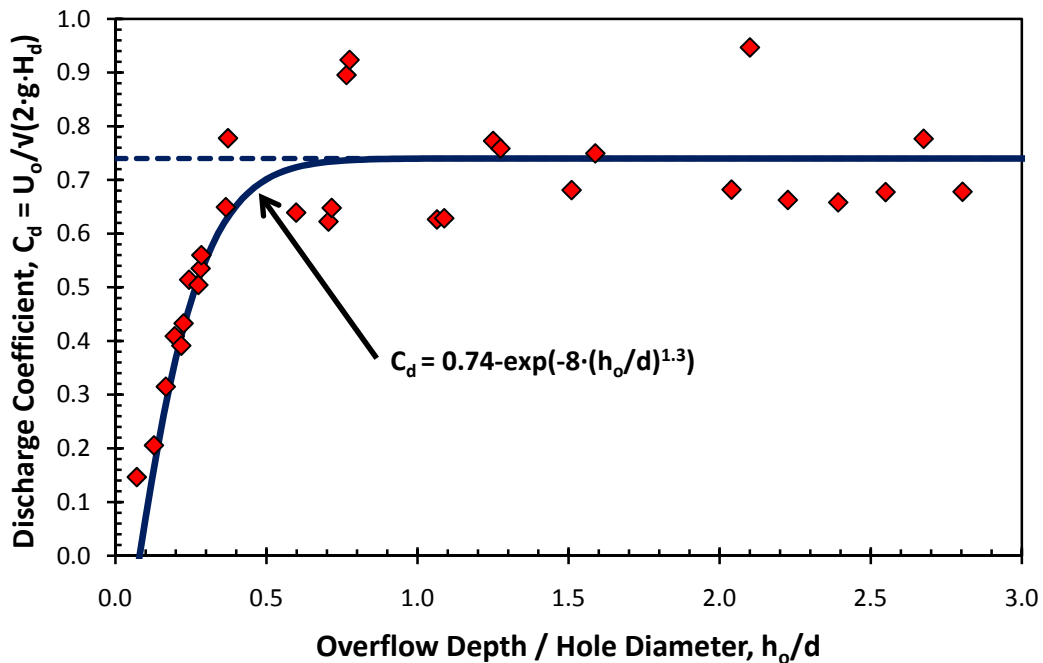


Figure B-1 Graph of the discharge coefficient (C_d) versus the overflow depth / hole diameter (h_o/d) ratio using the collected data where the downstream water level was lower than the ice cover surface and the hydraulic head difference (H_d) was equal to the overflow depth (h_o).

Run no.	Collected Data								Non-Dimensional Data					
	d (cm)	Q _o (L/s)	U _o (m/s)	h _o (m)	h _u (m)	h _d (m)	H _d (m)	Air Entrainment	C _d = U _o /√(2gH _d)	t/d	H _d /d	h _o /d	H/d	Re = ρU _o d/μ
34	7.8	0.23	0.048	0.005	0.363	0.000	0.005	YES	0.15	1.95	0.07	0.07	2.58	3740
35	7.8	1.50	0.314	0.019	0.375	0.000	0.019	YES	0.51	1.95	0.24	0.24	2.58	24393
36	7.8	3.09	0.647	0.055	0.409	0.000	0.055	YES	0.62	1.95	0.71	0.71	2.58	50249
40	7.8	3.82	0.799	0.083	0.436	0.000	0.083	YES	0.63	1.95	1.06	1.06	2.58	62120
41	5.1	0.54	0.264	0.014	0.368	0.000	0.014	YES	0.50	2.98	0.27	0.27	3.94	13430
42	5.1	0.42	0.206	0.012	0.366	0.000	0.012	YES	0.43	2.98	0.23	0.23	3.94	10446
43	5.1	1.01	0.494	0.031	0.384	0.000	0.031	YES/NO	0.64	2.98	0.60	0.60	3.94	25120
44	5.1	1.12	0.548	0.036	0.390	0.000	0.036	YES/NO	0.65	2.98	0.72	0.72	3.94	27855
45	5.1	1.34	0.656	0.056	0.409	0.000	0.056	YES/NO	0.63	2.98	1.09	1.09	3.94	33327
47	5.1	1.75	0.857	0.065	0.419	0.000	0.065	YES	0.76	2.98	1.27	1.27	3.94	43524
49	5.1	1.71	0.837	0.077	0.431	0.000	0.077	YES	0.68	2.98	1.51	1.51	3.94	42529
51	5.1	1.93	0.945	0.081	0.434	0.000	0.081	YES	0.75	2.98	1.59	1.59	3.94	48001
53	5.1	1.99	0.974	0.104	0.457	0.000	0.104	YES	0.68	2.98	2.04	2.04	3.94	49493
55	5.1	2.02	0.989	0.114	0.467	0.000	0.114	YES	0.66	2.98	2.23	2.23	3.94	50239
57	5.1	2.08	1.018	0.122	0.475	0.000	0.122	YES	0.66	2.98	2.39	2.39	3.94	51731
58	5.1	2.21	1.082	0.130	0.482	0.000	0.130	YES	0.68	2.98	2.55	2.55	3.94	54964
60	5.1	2.32	1.136	0.143	0.496	0.000	0.143	YES	0.68	2.98	2.80	2.80	3.94	57700
62	2.0	0.16	0.509	0.016	0.369	0.000	0.016	YES	0.92	7.60	0.77	0.77	10.05	10147
63	2.0	0.17	0.541	0.025	0.379	0.000	0.025	YES	0.77	7.60	1.25	1.25	10.05	10781
67	2.0	0.27	0.859	0.042	0.396	0.000	0.042	YES	0.95	7.60	2.10	2.10	10.05	17124
68	2.0	0.25	0.796	0.054	0.408	0.000	0.054	YES	0.78	7.60	2.68	2.68	10.05	15855
141	7.8	1.68	0.352	0.022	0.378	0.000	0.022	YES	0.54	1.95	0.28	0.28	2.58	27320
155	7.8	2.32	0.486	0.029	0.385	0.000	0.029	YES	0.65	1.95	0.37	0.37	2.58	37727
163	7.8	0.76	0.159	0.013	0.369	0.000	0.013	YES	0.31	1.95	0.17	0.17	2.58	12359
250	5.1	0.97	0.475	0.019	0.374	0.000	0.019	YES	0.78	2.98	0.37	0.37	3.94	24125
251	5.1	0.61	0.299	0.015	0.369	0.000	0.015	YES	0.56	2.98	0.28	0.28	3.94	15171
252	5.1	0.37	0.181	0.010	0.365	0.000	0.010	YES	0.41	2.98	0.20	0.20	3.94	9202
253	5.1	0.15	0.073	0.006	0.362	0.000	0.006	YES	0.21	2.98	0.13	0.13	3.94	3731
254	5.1	1.60	0.783	0.039	0.393	0.000	0.039	YES	0.90	2.98	0.76	0.76	3.94	39793
259	7.8	1.08	0.226	0.017	0.372	0.000	0.017	YES	0.39	1.95	0.22	0.22	2.58	17563

Appendix C

Details of Velocity Data Collection

from ADV Measurements

Run no.	Collected Data						Non-Dimensional Data					
	Distance from Origin (cm)			Average Velocity (cm/s)			Distance from Origin			Average Velocity		
	x	y	z	U _x	U _y	U _z	x/R	y/R	z/d	U _x /U ₀	U _y /U ₀	U _z /U ₀
195b	-1.0	-5.0	3.3	2.3	0.5	1.9	-0.26	-1.28	0.42	0.07	0.01	0.06
195b	1.0	-5.0	3.3	-2.5	-0.3	2.8	0.26	-1.28	0.42	-0.07	-0.01	0.08
195b	-4.0	-4.0	3.3	3.0	-0.6	1.9	-1.03	-1.03	0.42	0.09	-0.02	0.06
195b	-2.0	-4.0	3.3	3.5	-3.8	5.8	-0.51	-1.03	0.42	0.10	-0.11	0.17
195b	0.0	-4.0	3.3	7.0	-2.9	17.4	0.00	-1.03	0.42	0.20	-0.08	0.50
195b	2.0	-4.0	3.3	-3.1	-1.8	7.2	0.51	-1.03	0.42	-0.09	-0.05	0.21
195b	4.0	-4.0	3.3	-2.9	-0.2	2.9	1.03	-1.03	0.42	-0.08	-0.01	0.08
195b	-3.0	-3.0	3.3	0.0	-4.4	8.8	-0.77	-0.77	0.42	0.00	-0.13	0.25
195b	-1.0	-3.0	3.3	11.0	-7.7	36.8	-0.26	-0.77	0.42	0.32	-0.22	1.07
195b	1.0	-3.0	3.3	8.2	-0.8	29.6	0.26	-0.77	0.42	0.24	-0.02	0.86
195b	3.0	-3.0	3.3	0.6	0.6	12.9	0.77	-0.77	0.42	0.02	0.02	0.37
195b	-4.0	-2.0	3.3	-1.0	-3.1	4.1	-1.03	-0.51	0.42	-0.03	-0.09	0.12
195b	-2.0	-2.0	3.3	6.1	-10.0	35.0	-0.51	-0.51	0.42	0.18	-0.29	1.01
195b	0.0	-2.0	3.3	9.6	-3.3	35.1	0.00	-0.51	0.42	0.28	-0.10	1.02
195b	2.0	-2.0	3.3	5.7	2.6	30.1	0.51	-0.51	0.42	0.17	0.08	0.87
195b	4.0	-2.0	3.3	-2.1	1.2	10.0	1.03	-0.51	0.42	-0.06	0.03	0.29
195b	-3.0	-1.0	3.3	4.1	-19.0	29.6	-0.77	-0.26	0.42	0.12	-0.55	0.86
195b	-1.0	-1.0	3.3	18.5	-1.2	31.0	-0.26	-0.26	0.42	0.54	-0.03	0.90
195b	1.0	-1.0	3.3	1.3	3.4	31.3	0.26	-0.26	0.42	0.04	0.10	0.91
195b	3.0	-1.0	3.3	-0.3	4.4	25.8	0.77	-0.26	0.42	-0.01	0.13	0.75
195b	-4.0	0.0	3.3	-8.8	-8.9	14.3	-1.03	0.00	0.42	-0.25	-0.26	0.41
195b	-2.0	0.0	3.3	14.7	-14.0	28.8	-0.51	0.00	0.42	0.43	-0.41	0.83
195b	-1.0	0.0	3.3	11.9	-3.5	33.6	-0.26	0.00	0.42	0.34	-0.10	0.97
195b	0.0	0.0	3.3	2.5	9.3	30.6	0.00	0.00	0.42	0.07	0.27	0.89
195b	1.0	0.0	3.3	-2.2	7.8	33.2	0.26	0.00	0.42	-0.06	0.23	0.96
195b	2.0	0.0	3.3	-4.1	3.4	33.9	0.51	0.00	0.42	-0.12	0.10	0.98
195b	4.0	0.0	3.3	-3.6	4.8	15.3	1.03	0.00	0.42	-0.10	0.14	0.44
195b	-3.0	1.0	3.3	-8.2	-15.6	34.1	-0.77	0.26	0.42	-0.24	-0.45	0.99
195b	-1.0	1.0	3.3	-1.6	8.3	28.3	-0.26	0.26	0.42	-0.05	0.24	0.82
195b	0.0	1.0	3.3	-8.4	13.5	29.0	0.00	0.26	0.42	-0.24	0.39	0.84
195b	1.0	1.0	3.3	-7.2	12.4	33.9	0.26	0.26	0.42	-0.21	0.36	0.98
195b	3.0	1.0	3.3	-4.1	1.6	34.8	0.77	0.26	0.42	-0.12	0.05	1.01
195b	-4.0	2.0	3.3	-2.8	-0.5	5.0	-1.03	0.51	0.42	-0.08	-0.01	0.14
195b	-2.0	2.0	3.3	-12.1	-10.5	34.6	-0.51	0.51	0.42	-0.35	-0.30	1.00
195b	-1.0	2.0	3.3	-4.9	-3.2	32.6	-0.26	0.51	0.42	-0.14	-0.09	0.94
195b	0.0	2.0	3.3	-11.6	8.7	37.7	0.00	0.51	0.42	-0.34	0.25	1.09
195b	1.0	2.0	3.3	-5.4	4.6	36.8	0.26	0.51	0.42	-0.16	0.13	1.07
195b	2.0	2.0	3.3	-9.5	5.8	38.7	0.51	0.51	0.42	-0.28	0.17	1.12
195b	4.0	2.0	3.3	-5.3	3.7	7.5	1.03	0.51	0.42	-0.15	0.11	0.22
195b	-3.0	3.0	3.3	-8.9	-2.7	15.3	-0.77	0.77	0.42	-0.26	-0.08	0.44
195b	-1.0	3.0	3.3	-11.9	-1.7	38.6	-0.26	0.77	0.42	-0.34	-0.05	1.12
195b	0.0	3.0	3.3	-11.7	4.2	39.6	0.00	0.77	0.42	-0.34	0.12	1.15
195b	1.0	3.0	3.3	-10.6	5.0	41.1	0.26	0.77	0.42	-0.31	0.14	1.19
195b	2.0	3.0	3.3	-6.2	3.3	34.4	0.51	0.77	0.42	-0.18	0.10	1.00
195b	3.0	3.0	3.3	-4.7	4.0	13.9	0.77	0.77	0.42	-0.14	0.12	0.40
195b	-4.0	4.0	3.3	3.6	0.2	1.5	-1.03	1.03	0.42	0.10	0.01	0.04
195b	-2.0	4.0	3.3	-3.0	-0.7	10.8	-0.51	1.03	0.42	-0.09	-0.02	0.31
195b	0.0	4.0	3.3	-6.7	1.1	24.6	0.00	1.03	0.42	-0.19	0.03	0.71
195b	2.0	4.0	3.3	-4.9	1.8	8.3	0.51	1.03	0.42	-0.14	0.05	0.24

Run no.	Collected Data						Non-Dimensional Data					
	Distance from Origin (cm)			Average Velocity (cm/s)			Distance from Origin			Average Velocity		
	x	y	z	U _x	U _y	U _z	x/R	y/R	z/d	U _x /U _o	U _y /U _o	U _z /U _o
195b	4.0	4.0	3.3	-3.9	1.4	2.7	1.03	1.03	0.42	-0.11	0.04	0.08
195b	-1.0	5.0	3.3	0.3	-1.0	2.6	-0.26	1.28	0.42	0.01	-0.03	0.08
195b	1.0	5.0	3.3	-3.1	0.0	2.9	0.26	1.28	0.42	-0.09	0.00	0.08
195b	-2.0	-6.0	7.3	0.2	-0.1	4.3	-0.51	-1.54	0.94	0.01	0.00	0.12
195b	0.0	-6.0	7.3	0.4	-0.7	5.1	0.00	-1.54	0.94	0.01	-0.02	0.15
195b	2.0	-6.0	7.3	0.2	0.1	3.8	0.51	-1.54	0.94	0.01	0.00	0.11
195b	-4.0	-4.0	7.3	0.4	-0.2	3.9	-1.03	-1.03	0.94	0.01	-0.01	0.11
195b	-2.0	-4.0	7.3	3.2	-4.2	14.6	-0.51	-1.03	0.94	0.09	-0.12	0.42
195b	0.0	-4.0	7.3	7.0	-4.8	24.6	0.00	-1.03	0.94	0.20	-0.14	0.71
195b	2.0	-4.0	7.3	5.3	-0.8	17.3	0.51	-1.03	0.94	0.15	-0.02	0.50
195b	4.0	-4.0	7.3	-0.4	-0.1	4.3	1.03	-1.03	0.94	-0.01	0.00	0.12
195b	-3.0	-3.0	7.3	2.0	-5.9	14.0	-0.77	-0.77	0.94	0.06	-0.17	0.41
195b	-1.0	-3.0	7.3	9.3	-8.5	31.8	-0.26	-0.77	0.94	0.27	-0.25	0.92
195b	1.0	-3.0	7.3	10.3	-2.2	29.3	0.26	-0.77	0.94	0.30	-0.06	0.85
195b	3.0	-3.0	7.3	9.0	1.7	23.8	0.77	-0.77	0.94	0.26	0.05	0.69
195b	-4.0	-2.0	7.3	0.2	-5.5	9.7	-1.03	-0.51	0.94	0.01	-0.16	0.28
195b	-2.0	-2.0	7.3	12.7	-9.8	23.7	-0.51	-0.51	0.94	0.37	-0.28	0.69
195b	0.0	-2.0	7.3	15.8	-0.2	29.6	0.00	-0.51	0.94	0.46	-0.01	0.86
195b	1.0	-2.0	7.3	10.4	1.5	31.6	0.26	-0.51	0.94	0.30	0.04	0.92
195b	2.0	-2.0	7.3	6.3	1.0	29.5	0.51	-0.51	0.94	0.18	0.03	0.85
195b	4.0	-2.0	7.3	0.2	0.1	11.2	1.03	-0.51	0.94	0.01	0.00	0.32
195b	-5.0	-1.0	7.3	-0.6	-2.8	5.8	-1.28	-0.26	0.94	-0.02	-0.08	0.17
195b	-3.0	-1.0	7.3	3.4	-8.5	19.6	-0.77	-0.26	0.94	0.10	-0.25	0.57
195b	-1.0	-1.0	7.3	13.7	-2.1	26.2	-0.26	-0.26	0.94	0.40	-0.06	0.76
195b	1.0	-1.0	7.3	5.9	7.4	27.4	0.26	-0.26	0.94	0.17	0.21	0.79
195b	3.0	-1.0	7.3	-1.0	0.8	24.6	0.77	-0.26	0.94	-0.03	0.02	0.71
195b	5.0	-1.0	7.3	-0.7	1.6	6.5	1.28	-0.26	0.94	-0.02	0.05	0.19
195b	-4.0	0.0	7.3	-4.0	-8.4	16.8	-1.03	0.00	0.94	-0.12	-0.24	0.49
195b	-2.0	0.0	7.3	7.5	-11.1	16.8	-0.51	0.00	0.94	0.22	-0.32	0.49
195b	-1.0	0.0	7.3	7.9	1.4	13.7	-0.26	0.00	0.94	0.23	0.04	0.40
195b	0.0	0.0	7.3	3.6	8.9	25.8	0.00	0.00	0.94	0.10	0.26	0.75
195b	1.0	0.0	7.3	-0.3	3.3	33.0	0.26	0.00	0.94	-0.01	0.10	0.96
195b	2.0	0.0	7.3	-1.8	6.8	31.8	0.51	0.00	0.94	-0.05	0.20	0.92
195b	4.0	0.0	7.3	-0.4	3.6	16.4	1.03	0.00	0.94	-0.01	0.10	0.47
195b	-5.0	1.0	7.3	-2.8	-4.3	7.9	-1.28	0.26	0.94	-0.08	-0.12	0.23
195b	-3.0	1.0	7.3	-3.3	-10.7	24.2	-0.77	0.26	0.94	-0.10	-0.31	0.70
195b	-1.0	1.0	7.3	-6.1	3.0	20.8	-0.26	0.26	0.94	-0.18	0.09	0.60
195b	1.0	1.0	7.3	-4.8	6.8	32.2	0.26	0.26	0.94	-0.14	0.20	0.93
195b	3.0	1.0	7.3	-2.5	2.2	25.5	0.77	0.26	0.94	-0.07	0.06	0.74
195b	5.0	1.0	7.3	-2.4	3.0	6.8	1.28	0.26	0.94	-0.07	0.09	0.20
195b	-4.0	2.0	7.3	-6.8	-4.8	16.0	-1.03	0.51	0.94	-0.20	-0.14	0.46
195b	-2.0	2.0	7.3	-9.2	-7.2	31.2	-0.51	0.51	0.94	-0.27	-0.21	0.90
195b	0.0	2.0	7.3	-11.6	5.3	34.2	0.00	0.51	0.94	-0.34	0.15	0.99
195b	2.0	2.0	7.3	-7.0	4.7	34.4	0.51	0.51	0.94	-0.20	0.14	1.00
195b	4.0	2.0	7.3	-3.6	3.7	12.1	1.03	0.51	0.94	-0.10	0.11	0.35
195b	-3.0	3.0	7.3	-9.7	-4.7	24.3	-0.77	0.77	0.94	-0.28	-0.14	0.70
195b	-1.0	3.0	7.3	-9.0	-0.2	38.1	-0.26	0.77	0.94	-0.26	-0.01	1.10
195b	0.0	3.0	7.3	-9.5	3.5	39.3	0.00	0.77	0.94	-0.28	0.10	1.14
195b	1.0	3.0	7.3	-6.8	3.7	39.2	0.26	0.77	0.94	-0.20	0.11	1.14

Run no.	Collected Data						Non-Dimensional Data					
	Distance from Origin (cm)			Average Velocity (cm/s)			Distance from Origin			Average Velocity		
	x	y	z	U_x	U_y	U_z	x/R	y/R	z/d	U_x/U_o	U_y/U_o	U_z/U_o
195b	3.0	3.0	7.3	-4.2	3.5	16.0	0.77	0.77	0.94	-0.12	0.10	0.46
195b	-4.0	4.0	7.3	-0.8	-1.5	5.3	-1.03	1.03	0.94	-0.02	-0.04	0.15
195b	-2.0	4.0	7.3	-4.1	-1.0	18.0	-0.51	1.03	0.94	-0.12	-0.03	0.52
195b	-1.0	4.0	7.3	-6.7	0.0	25.9	-0.26	1.03	0.94	-0.19	0.00	0.75
195b	0.0	4.0	7.3	-6.7	1.9	29.0	0.00	1.03	0.94	-0.19	0.06	0.84
195b	2.0	4.0	7.3	-4.7	2.5	16.1	0.51	1.03	0.94	-0.14	0.07	0.47
195b	4.0	4.0	7.3	-2.4	0.1	2.6	1.03	1.03	0.94	-0.07	0.00	0.08
195b	-2.0	6.0	7.3	0.6	-1.0	3.8	-0.51	1.54	0.94	0.02	-0.03	0.11
195b	0.0	6.0	7.3	-0.7	-0.5	4.5	0.00	1.54	0.94	-0.02	-0.01	0.13
195b	2.0	6.0	7.3	-1.6	-0.4	2.7	0.51	1.54	0.94	-0.05	-0.01	0.08
195b	-4.0	0.0	12.3	-4.5	-7.8	19.9	-1.03	0.00	1.58	-0.13	-0.23	0.58
195b	-2.0	0.0	12.3	4.2	-4.1	13.6	-0.51	0.00	1.58	0.12	-0.12	0.39
195b	0.0	0.0	12.3	2.2	5.0	14.4	0.00	0.00	1.58	0.06	0.14	0.42
195b	2.0	0.0	12.3	2.2	5.2	23.3	0.51	0.00	1.58	0.06	0.15	0.67
195b	4.0	0.0	12.3	2.2	3.2	20.6	1.03	0.00	1.58	0.06	0.09	0.60
195b	-4.0	2.0	12.3	-8.3	-4.5	23.0	-1.03	0.51	1.58	-0.24	-0.13	0.67
195b	-2.0	2.0	12.3	-10.4	-0.9	29.8	-0.51	0.51	1.58	-0.30	-0.03	0.86
195b	0.0	2.0	12.3	-8.1	5.8	27.5	0.00	0.51	1.58	-0.23	0.17	0.80
195b	2.0	2.0	12.3	-4.5	3.1	31.0	0.51	0.51	1.58	-0.13	0.09	0.90
195b	4.0	2.0	12.3	-1.4	3.0	14.9	1.03	0.51	1.58	-0.04	0.09	0.43
195b	-4.0	4.0	12.3	-4.0	-1.3	12.9	-1.03	1.03	1.58	-0.12	-0.04	0.37
195b	-2.0	4.0	12.3	-6.7	0.2	25.9	-0.51	1.03	1.58	-0.19	0.01	0.75
195b	0.0	4.0	12.3	-5.9	2.9	30.4	0.00	1.03	1.58	-0.17	0.08	0.88
195b	2.0	4.0	12.3	-3.6	2.8	19.3	0.51	1.03	1.58	-0.10	0.08	0.56
195b	4.0	4.0	12.3	-2.3	1.2	6.8	1.03	1.03	1.58	-0.07	0.03	0.20
195b	-4.0	0.0	17.0	-5.3	-4.0	11.1	-1.03	0.00	2.18	-0.15	-0.12	0.32
195b	-2.0	0.0	17.0	4.2	-4.3	14.0	-0.51	0.00	2.18	0.12	-0.12	0.41
195b	0.0	0.0	17.0	0.4	-0.4	0.1	0.00	0.00	2.18	0.01	-0.01	0.00
195b	2.0	0.0	17.0	4.0	1.4	19.9	0.51	0.00	2.18	0.12	0.04	0.58
195b	4.0	0.0	17.0	7.0	2.8	17.2	1.03	0.00	2.18	0.20	0.08	0.50
195b	-4.0	2.0	17.0	-10.0	-0.6	18.0	-1.03	0.51	2.18	-0.29	-0.02	0.52
195b	-2.0	2.0	17.0	-5.2	1.4	12.0	-0.51	0.51	2.18	-0.15	0.04	0.35
195b	0.0	2.0	17.0	-2.7	3.9	18.5	0.00	0.51	2.18	-0.08	0.11	0.54
195b	2.0	2.0	17.0	1.1	5.0	21.5	0.51	0.51	2.18	0.03	0.14	0.62
195b	4.0	2.0	17.0	4.0	3.7	15.6	1.03	0.51	2.18	0.12	0.11	0.45
195b	-4.0	4.0	17.0	-9.3	3.0	20.8	-1.03	1.03	2.18	-0.27	0.09	0.60
195b	-2.0	4.0	17.0	-7.9	5.6	25.2	-0.51	1.03	2.18	-0.23	0.16	0.73
195b	0.0	4.0	17.0	-4.6	6.3	23.0	0.00	1.03	2.18	-0.13	0.18	0.67
195b	2.0	4.0	17.0	-0.3	6.7	18.3	0.51	1.03	2.18	-0.01	0.19	0.53
195b	4.0	4.0	17.0	1.4	5.1	10.8	1.03	1.03	2.18	0.04	0.15	0.31
205	0.0	0.0	7.3	0.1	2.2	26.0	0.00	0.00	0.94	0.00	0.07	0.77
207	0.0	0.0	7.3	-1.7	-0.8	9.4	0.00	0.00	0.94	-0.14	-0.06	0.75
207	0.0	1.0	7.3	-0.5	-0.3	8.1	0.00	0.26	0.94	-0.04	-0.02	0.65
207	0.0	2.0	7.3	0.0	-0.6	10.1	0.00	0.51	0.94	0.00	-0.05	0.80
207	0.0	0.0	12.3	-1.0	-0.8	8.6	0.00	0.00	1.58	-0.08	-0.06	0.68
260	0.0	-6.0	3.3	-2.3	0.6	1.6	0.00	-1.54	0.42	-0.10	0.03	0.07

Run no.	Collected Data						Non-Dimensional Data					
	Distance from Origin (cm)			Average Velocity (cm/s)			Distance from Origin			Average Velocity		
	x	y	z	U _x	U _y	U _z	x/R	y/R	z/d	U _x /U ₀	U _y /U ₀	U _z /U ₀
260	0.0	-5.0	3.3	0.2	0.1	1.6	0.00	-1.28	0.42	0.01	0.00	0.07
260	0.0	-4.0	3.3	3.1	-1.4	8.7	0.00	-1.03	0.42	0.14	-0.06	0.38
260	0.0	-3.0	3.3	4.1	-3.3	17.8	0.00	-0.77	0.42	0.18	-0.15	0.79
260	0.0	-2.0	3.3	0.4	-1.4	17.4	0.00	-0.51	0.42	0.02	-0.06	0.77
260	0.0	-1.0	3.3	1.2	0.0	20.6	0.00	-0.26	0.42	0.05	0.00	0.91
260	-5.0	0.0	3.3	1.2	0.0	1.4	-1.28	0.00	0.42	0.05	0.00	0.06
260	-4.0	0.0	3.3	-4.6	-3.8	6.7	-1.03	0.00	0.42	-0.20	-0.17	0.30
260	-3.0	0.0	3.3	-2.1	-14.5	17.1	-0.77	0.00	0.42	-0.09	-0.64	0.76
260	-2.0	0.0	3.3	8.6	-8.8	14.8	-0.51	0.00	0.42	0.38	-0.39	0.65
260	-1.0	0.0	3.3	6.6	-2.1	18.2	-0.26	0.00	0.42	0.29	-0.09	0.81
260	0.0	0.0	3.3	0.5	5.1	20.7	0.00	0.00	0.42	0.02	0.23	0.92
260	1.0	0.0	3.3	-1.8	4.2	20.5	0.26	0.00	0.42	-0.08	0.19	0.91
260	2.0	0.0	3.3	-3.4	2.4	20.1	0.51	0.00	0.42	-0.15	0.11	0.89
260	3.0	0.0	3.3	-3.0	-0.1	19.4	0.77	0.00	0.42	-0.13	0.00	0.86
260	4.0	0.0	3.3	-1.4	1.3	7.5	1.03	0.00	0.42	-0.06	0.06	0.33
260	5.0	0.0	3.3	-1.9	0.6	2.3	1.28	0.00	0.42	-0.08	0.03	0.10
260	0.0	1.0	3.3	-0.3	7.8	17.8	0.00	0.26	0.42	-0.01	0.35	0.79
260	0.0	2.0	3.3	-1.8	3.8	18.4	0.00	0.51	0.42	-0.08	0.17	0.81
260	0.0	3.0	3.3	-8.8	2.1	24.4	0.00	0.77	0.42	-0.39	0.09	1.08
260	0.0	4.0	3.3	-3.3	-0.2	14.0	0.00	1.03	0.42	-0.15	-0.01	0.62
260	0.0	5.0	3.3	-0.7	-0.7	2.1	0.00	1.28	0.42	-0.03	-0.03	0.09
260	0.0	6.0	3.3	0.1	-0.5	1.2	0.00	1.54	0.42	0.00	-0.02	0.05
260	0.0	-6.0	7.3	-0.1	-0.3	2.9	0.00	-1.54	0.94	0.00	-0.01	0.13
260	0.0	-5.0	7.3	1.8	-0.8	6.5	0.00	-1.28	0.94	0.08	-0.04	0.29
260	-4.0	-4.0	7.3	-0.5	-0.3	3.4	-1.03	-1.03	0.94	-0.02	-0.01	0.15
260	-2.0	-4.0	7.3	0.5	-2.3	9.8	-0.51	-1.03	0.94	0.02	-0.10	0.43
260	0.0	-4.0	7.3	4.4	-4.5	15.2	0.00	-1.03	0.94	0.19	-0.20	0.67
260	2.0	-4.0	7.3	2.1	-0.3	10.0	0.51	-1.03	0.94	0.09	-0.01	0.44
260	4.0	-4.0	7.3	-0.8	-0.5	2.5	1.03	-1.03	0.94	-0.04	-0.02	0.11
260	-3.0	-3.0	7.3	-0.9	-3.6	11.7	-0.77	-0.77	0.94	-0.04	-0.16	0.52
260	0.0	-3.0	7.3	5.5	-5.1	18.1	0.00	-0.77	0.94	0.24	-0.23	0.80
260	3.0	-3.0	7.3	-0.5	-0.8	9.2	0.77	-0.77	0.94	-0.02	-0.04	0.41
260	-4.0	-2.0	7.3	-0.3	-2.5	6.1	-1.03	-0.51	0.94	-0.01	-0.11	0.27
260	-2.0	-2.0	7.3	1.4	-4.5	18.9	-0.51	-0.51	0.94	0.06	-0.20	0.84
260	0.0	-2.0	7.3	3.3	-1.9	19.0	0.00	-0.51	0.94	0.15	-0.08	0.84
260	2.0	-2.0	7.3	-1.3	-0.7	17.5	0.51	-0.51	0.94	-0.06	-0.03	0.77
260	4.0	-2.0	7.3	0.6	1.3	9.3	1.03	-0.51	0.94	0.03	0.06	0.41
260	-1.0	-1.0	7.3	4.0	-2.6	19.7	-0.26	-0.26	0.94	0.18	-0.12	0.87
260	0.0	-1.0	7.3	2.4	-0.3	19.0	0.00	-0.26	0.94	0.11	-0.01	0.84
260	1.0	-1.0	7.3	-1.3	0.3	20.3	0.26	-0.26	0.94	-0.06	0.01	0.90
260	-5.0	0.0	7.3	-0.4	-1.5	3.5	-1.28	0.00	0.94	-0.02	-0.07	0.15
260	-4.0	0.0	7.3	-0.5	-3.0	6.8	-1.03	0.00	0.94	-0.02	-0.13	0.30
260	-3.0	0.0	7.3	1.8	-5.2	10.9	-0.77	0.00	0.94	0.08	-0.23	0.48
260	-2.0	0.0	7.3	5.4	-5.6	13.3	-0.51	0.00	0.94	0.24	-0.25	0.59
260	-1.0	0.0	7.3	3.8	-1.0	18.1	-0.26	0.00	0.94	0.17	-0.04	0.80
260	0.0	0.0	7.3	1.4	2.7	21.5	0.00	0.00	0.94	0.06	0.12	0.95
260	1.0	0.0	7.3	-2.1	4.7	20.9	0.26	0.00	0.94	-0.09	0.21	0.92
260	2.0	0.0	7.3	-2.9	1.7	22.8	0.51	0.00	0.94	-0.13	0.08	1.01
260	3.0	0.0	7.3	-1.4	2.6	17.0	0.77	0.00	0.94	-0.06	0.12	0.75

Run no.	Collected Data						Non-Dimensional Data					
	Distance from Origin (cm)			Average Velocity (cm/s)			Distance from Origin			Average Velocity		
	x	y	z	U _x	U _y	U _z	x/R	y/R	z/d	U _x /U _o	U _y /U _o	U _z /U _o
260	4.0	0.0	7.3	-1.1	1.7	10.0	1.03	0.00	0.94	-0.05	0.08	0.44
260	5.0	0.0	7.3	-1.6	0.9	4.1	1.28	0.00	0.94	-0.07	0.04	0.18
260	-1.0	1.0	7.3	-1.8	3.1	14.1	-0.26	0.26	0.94	-0.08	0.14	0.62
260	0.0	1.0	7.3	-3.9	6.6	19.0	0.00	0.26	0.94	-0.17	0.29	0.84
260	1.0	1.0	7.3	-5.8	5.2	20.7	0.26	0.26	0.94	-0.26	0.23	0.92
260	-4.0	2.0	7.3	-4.6	-3.3	10.6	-1.03	0.51	0.94	-0.20	-0.15	0.47
260	-2.0	2.0	7.3	-5.6	-4.7	20.0	-0.51	0.51	0.94	-0.25	-0.21	0.88
260	0.0	2.0	7.3	-5.6	4.9	21.9	0.00	0.51	0.94	-0.25	0.22	0.97
260	2.0	2.0	7.3	-4.8	2.6	22.8	0.51	0.51	0.94	-0.21	0.12	1.01
260	4.0	2.0	7.3	-1.8	0.8	7.6	1.03	0.51	0.94	-0.08	0.04	0.34
260	-3.0	3.0	7.3	-4.7	-2.6	13.1	-0.77	0.77	0.94	-0.21	-0.12	0.58
260	0.0	3.0	7.3	-6.8	2.8	24.0	0.00	0.77	0.94	-0.30	0.12	1.06
260	3.0	3.0	7.3	-2.6	1.9	10.0	0.77	0.77	0.94	-0.12	0.08	0.44
260	-4.0	4.0	7.3	0.0	-0.3	3.7	-1.03	1.03	0.94	0.00	-0.01	0.16
260	-2.0	4.0	7.3	-3.8	-0.9	13.2	-0.51	1.03	0.94	-0.17	-0.04	0.58
260	0.0	4.0	7.3	-4.5	1.1	19.2	0.00	1.03	0.94	-0.20	0.05	0.85
260	2.0	4.0	7.3	-3.1	1.5	11.1	0.51	1.03	0.94	-0.14	0.07	0.49
260	4.0	4.0	7.3	-1.7	0.4	1.9	1.03	1.03	0.94	-0.08	0.02	0.08
260	0.0	5.0	7.3	-2.6	0.0	7.8	0.00	1.28	0.94	-0.12	0.00	0.35
260	0.0	6.0	7.3	-0.5	-0.5	2.8	0.00	1.54	0.94	-0.02	-0.02	0.12
260	0.0	-7.0	12.3	0.5	-1.2	4.4	0.00	-1.79	1.58	0.02	-0.05	0.19
260	0.0	-6.0	12.3	1.7	-3.5	8.8	0.00	-1.54	1.58	0.08	-0.15	0.39
260	0.0	-5.0	12.3	1.9	-2.1	9.8	0.00	-1.28	1.58	0.08	-0.09	0.43
260	0.0	-4.0	12.3	1.4	-4.2	13.5	0.00	-1.03	1.58	0.06	-0.19	0.60
260	0.0	-3.0	12.3	1.4	-3.2	14.8	0.00	-0.77	1.58	0.06	-0.14	0.65
260	0.0	-2.0	12.3	4.3	-0.8	10.1	0.00	-0.51	1.58	0.19	-0.04	0.45
260	0.0	-1.0	12.3	0.4	-1.1	16.5	0.00	-0.26	1.58	0.02	-0.05	0.73
260	-5.0	0.0	12.3	-2.4	-2.9	7.6	-1.28	0.00	1.58	-0.11	-0.13	0.34
260	-4.0	0.0	12.3	-2.8	-5.4	11.3	-1.03	0.00	1.58	-0.12	-0.24	0.50
260	-3.0	0.0	12.3	-0.4	-4.7	10.7	-0.77	0.00	1.58	-0.02	-0.21	0.47
260	-2.0	0.0	12.3	1.7	-3.4	8.1	-0.51	0.00	1.58	0.08	-0.15	0.36
260	-1.0	0.0	12.3	1.9	-0.1	8.0	-0.26	0.00	1.58	0.08	0.00	0.35
260	0.0	0.0	12.3	-0.4	-0.5	18.0	0.00	0.00	1.58	-0.02	-0.02	0.80
260	1.0	0.0	12.3	-0.7	2.0	16.1	0.26	0.00	1.58	-0.03	0.09	0.71
260	2.0	0.0	12.3	-1.9	-0.3	19.1	0.51	0.00	1.58	-0.08	-0.01	0.85
260	3.0	0.0	12.3	-0.7	0.4	14.7	0.77	0.00	1.58	-0.03	0.02	0.65
260	4.0	0.0	12.3	-0.4	-0.1	9.6	1.03	0.00	1.58	-0.02	0.00	0.42
260	5.0	0.0	12.3	-0.1	1.1	6.7	1.28	0.00	1.58	0.00	0.05	0.30
260	0.0	1.0	12.3	-0.9	2.3	15.3	0.00	0.26	1.58	-0.04	0.10	0.68
260	0.0	2.0	12.3	-3.2	0.9	17.1	0.00	0.51	1.58	-0.14	0.04	0.76
260	0.0	3.0	12.3	-5.1	1.7	19.4	0.00	0.77	1.58	-0.23	0.08	0.86
260	0.0	4.0	12.3	-4.7	1.6	18.5	0.00	1.03	1.58	-0.21	0.07	0.82
260	0.0	5.0	12.3	-2.6	0.1	9.7	0.00	1.28	1.58	-0.12	0.00	0.43
260	0.0	6.0	12.3	-1.7	0.1	5.8	0.00	1.54	1.58	-0.08	0.00	0.26
260	0.0	7.0	12.3	-0.1	-0.5	3.1	0.00	1.79	1.58	0.00	-0.02	0.14
260	0.0	-7.0	17.0	0.8	-5.4	4.7	0.00	-1.79	2.18	0.04	-0.24	0.21
260	0.0	-6.0	17.0	-0.4	-5.4	3.8	0.00	-1.54	2.18	-0.02	-0.24	0.17
260	0.0	-5.0	17.0	0.1	-5.5	7.3	0.00	-1.28	2.18	0.00	-0.24	0.32
260	0.0	-4.0	17.0	0.8	-5.9	10.4	0.00	-1.03	2.18	0.04	-0.26	0.46

Run no.	Collected Data						Non-Dimensional Data					
	Distance from Origin (cm)			Average Velocity (cm/s)			Distance from Origin			Average Velocity		
	x	y	z	U _x	U _y	U _z	x/R	y/R	z/d	U _x /U ₀	U _y /U ₀	U _z /U ₀
260	0.0	-3.0	17.0	1.1	-4.6	8.3	0.00	-0.77	2.18	0.05	-0.20	0.37
260	0.0	-2.0	17.0	0.0	-3.1	8.4	0.00	-0.51	2.18	0.00	-0.14	0.37
260	0.0	-1.0	17.0	-0.5	-2.5	13.0	0.00	-0.26	2.18	-0.02	-0.11	0.58
260	-5.0	0.0	17.0	-6.7	-3.6	7.4	-1.28	0.00	2.18	-0.30	-0.16	0.33
260	-4.0	0.0	17.0	-5.3	-3.4	8.6	-1.03	0.00	2.18	-0.23	-0.15	0.38
260	-3.0	0.0	17.0	-3.4	-1.2	8.0	-0.77	0.00	2.18	-0.15	-0.05	0.35
260	-2.0	0.0	17.0	-4.7	-0.5	16.4	-0.51	0.00	2.18	-0.21	-0.02	0.73
260	-1.0	0.0	17.0	-0.8	-1.0	5.0	-0.26	0.00	2.18	-0.04	-0.04	0.22
260	0.0	0.0	17.0	0.1	-0.5	2.0	0.00	0.00	2.18	0.00	-0.02	0.09
260	1.0	0.0	17.0	0.8	0.7	5.6	0.26	0.00	2.18	0.04	0.03	0.25
260	2.0	0.0	17.0	1.7	1.5	7.7	0.51	0.00	2.18	0.08	0.07	0.34
260	3.0	0.0	17.0	3.2	0.3	13.1	0.77	0.00	2.18	0.14	0.01	0.58
260	4.0	0.0	17.0	3.7	0.9	9.0	1.03	0.00	2.18	0.16	0.04	0.40
260	5.0	0.0	17.0	4.1	1.4	7.0	1.28	0.00	2.18	0.18	0.06	0.31
260	0.0	1.0	17.0	-0.4	1.0	8.2	0.00	0.26	2.18	-0.02	0.04	0.36
260	0.0	2.0	17.0	-1.1	2.4	8.7	0.00	0.51	2.18	-0.05	0.11	0.38
260	0.0	3.0	17.0	-1.8	3.9	12.0	0.00	0.77	2.18	-0.08	0.17	0.53
260	0.0	4.0	17.0	-2.6	4.4	14.6	0.00	1.03	2.18	-0.12	0.19	0.65
260	0.0	5.0	17.0	-2.6	4.3	12.9	0.00	1.28	2.18	-0.12	0.19	0.57
260	0.0	6.0	17.0	-1.7	3.1	8.9	0.00	1.54	2.18	-0.08	0.14	0.39
260	0.0	7.0	17.0	-1.1	2.1	5.4	0.00	1.79	2.18	-0.05	0.09	0.24
261	0.0	0.0	3.3	-2.0	4.3	16.1	0.00	0.00	0.42	-0.09	0.19	0.71
261	-5.0	0.0	7.3	-0.4	0.8	6.4	-1.28	0.00	0.94	-0.02	0.04	0.28
261	-4.0	0.0	7.3	-2.7	-2.9	12.7	-1.03	0.00	0.94	-0.12	-0.13	0.56
261	-3.0	0.0	7.3	-1.3	-2.0	18.6	-0.77	0.00	0.94	-0.06	-0.09	0.82
261	-2.0	0.0	7.3	-0.5	-2.0	18.4	-0.51	0.00	0.94	-0.02	-0.09	0.81
261	-1.0	0.0	7.3	0.3	-1.9	17.6	-0.26	0.00	0.94	0.01	-0.08	0.78
261	0.0	0.0	7.3	-1.9	0.1	18.1	0.00	0.00	0.94	-0.08	0.00	0.80
261	1.0	0.0	7.3	-3.3	-2.0	18.7	0.26	0.00	0.94	-0.15	-0.09	0.83
261	2.0	0.0	7.3	-2.4	-1.6	20.4	0.51	0.00	0.94	-0.11	-0.07	0.90
261	3.0	0.0	7.3	-1.6	-4.0	18.6	0.77	0.00	0.94	-0.07	-0.18	0.82
261	4.0	0.0	7.3	-0.7	-1.4	11.4	1.03	0.00	0.94	-0.03	-0.06	0.50
261	5.0	0.0	7.3	-0.9	0.1	4.4	1.28	0.00	0.94	-0.04	0.00	0.19
261	0.0	0.0	12.3	-0.3	0.6	10.7	0.00	0.00	1.58	-0.01	0.03	0.47
261	0.0	0.0	17.0	-1.4	-0.8	11.4	0.00	0.00	2.18	-0.06	-0.04	0.50
266	-5.0	0.0	3.3	0.9	-0.4	2.7	-1.28	0.00	0.42	0.03	-0.01	0.08
266	-4.0	0.0	3.3	-7.0	-5.4	12.2	-1.03	0.00	0.42	-0.20	-0.16	0.35
266	-3.0	0.0	3.3	-0.6	-11.9	31.6	-0.77	0.00	0.42	-0.02	-0.34	0.92
266	-2.0	0.0	3.3	13.0	-13.5	31.5	-0.51	0.00	0.42	0.38	-0.39	0.91
266	-1.0	0.0	3.3	22.3	1.5	28.6	-0.26	0.00	0.42	0.65	0.04	0.83
266	0.0	0.0	3.3	6.5	7.0	38.1	0.00	0.00	0.42	0.19	0.20	1.10
266	1.0	0.0	3.3	3.3	7.4	37.8	0.26	0.00	0.42	0.10	0.21	1.09
266	2.0	0.0	3.3	-2.4	3.5	35.3	0.51	0.00	0.42	-0.07	0.10	1.02
266	3.0	0.0	3.3	-1.6	1.7	31.2	0.77	0.00	0.42	-0.05	0.05	0.90
266	4.0	0.0	3.3	-2.3	1.3	11.3	1.03	0.00	0.42	-0.07	0.04	0.33
266	5.0	0.0	3.3	-2.6	0.2	2.6	1.28	0.00	0.42	-0.08	0.01	0.08
266	0.0	-6.0	7.3	0.1	-0.6	5.7	0.00	-1.54	0.94	0.00	-0.02	0.17

Run no.	Collected Data						Non-Dimensional Data					
	Distance from Origin (cm)			Average Velocity (cm/s)			Distance from Origin			Average Velocity		
	x	y	z	U _x	U _y	U _z	x/R	y/R	z/d	U _x /U _o	U _y /U _o	U _z /U _o
266	0.0	-5.0	7.3	1.6	-1.7	11.4	0.00	-1.28	0.94	0.05	-0.05	0.33
266	-4.0	-4.0	7.3	-0.3	0.1	4.6	-1.03	-1.03	0.94	-0.01	0.00	0.13
266	-2.0	-4.0	7.3	1.6	-3.2	14.9	-0.51	-1.03	0.94	0.05	-0.09	0.43
266	0.0	-4.0	7.3	0.6	-1.7	18.9	0.00	-1.03	0.94	0.02	-0.05	0.55
266	2.0	-4.0	7.3	1.0	-0.6	14.3	0.51	-1.03	0.94	0.03	-0.02	0.41
266	4.0	-4.0	7.3	0.1	1.0	5.0	1.03	-1.03	0.94	0.00	0.03	0.14
266	-3.0	-3.0	7.3	-0.8	-6.2	19.0	-0.77	-0.77	0.94	-0.02	-0.18	0.55
266	0.0	-3.0	7.3	8.5	-4.0	31.6	0.00	-0.77	0.94	0.25	-0.12	0.92
266	3.0	-3.0	7.3	0.4	-0.2	12.5	0.77	-0.77	0.94	0.01	-0.01	0.36
266	-4.0	-2.0	7.3	-1.7	-3.6	12.8	-1.03	-0.51	0.94	-0.05	-0.10	0.37
266	-2.0	-2.0	7.3	5.9	-8.9	31.9	-0.51	-0.51	0.94	0.17	-0.26	0.92
266	0.0	-2.0	7.3	3.3	-1.0	33.8	0.00	-0.51	0.94	0.10	-0.03	0.98
266	2.0	-2.0	7.3	3.9	1.4	32.0	0.51	-0.51	0.94	0.11	0.04	0.93
266	4.0	-2.0	7.3	0.4	1.9	12.2	1.03	-0.51	0.94	0.01	0.06	0.35
266	0.0	-1.0	7.3	5.9	2.2	32.8	0.00	-0.26	0.94	0.17	0.06	0.95
266	-5.0	0.0	7.3	-1.8	-1.2	7.7	-1.28	0.00	0.94	-0.05	-0.03	0.22
266	-4.0	0.0	7.3	-3.4	-4.1	18.8	-1.03	0.00	0.94	-0.10	-0.12	0.54
266	-3.0	0.0	7.3	0.4	-14.1	27.3	-0.77	0.00	0.94	0.01	-0.41	0.79
266	-2.0	0.0	7.3	8.6	-9.6	27.8	-0.51	0.00	0.94	0.25	-0.28	0.81
266	-1.0	0.0	7.3	9.6	3.1	24.1	-0.26	0.00	0.94	0.28	0.09	0.70
266	0.0	0.0	7.3	6.8	6.0	34.0	0.00	0.00	0.94	0.20	0.17	0.98
266	1.0	0.0	7.3	-1.1	8.4	34.7	0.26	0.00	0.94	-0.03	0.24	1.00
266	2.0	0.0	7.3	-4.3	6.6	34.8	0.51	0.00	0.94	-0.12	0.19	1.01
266	3.0	0.0	7.3	-1.6	1.8	31.1	0.77	0.00	0.94	-0.05	0.05	0.90
266	4.0	0.0	7.3	-1.2	3.2	14.9	1.03	0.00	0.94	-0.03	0.09	0.43
266	5.0	0.0	7.3	-2.0	0.6	4.6	1.28	0.00	0.94	-0.06	0.02	0.13
266	-1.0	1.0	7.3	2.8	4.8	27.0	-0.26	0.26	0.94	0.08	0.14	0.78
266	0.0	1.0	7.3	3.5	1.4	38.1	0.00	0.26	0.94	0.10	0.04	1.10
266	1.0	1.0	7.3	-3.5	8.3	36.4	0.26	0.26	0.94	-0.10	0.24	1.05
266	-4.0	2.0	7.3	-4.1	-3.2	11.8	-1.03	0.51	0.94	-0.12	-0.09	0.34
266	-2.0	2.0	7.3	-4.2	-8.1	29.4	-0.51	0.51	0.94	-0.12	-0.23	0.85
266	0.0	2.0	7.3	-7.0	7.8	34.9	0.00	0.51	0.94	-0.20	0.23	1.01
266	2.0	2.0	7.3	-5.2	5.3	39.3	0.51	0.51	0.94	-0.15	0.15	1.14
266	4.0	2.0	7.3	-3.3	2.4	10.9	1.03	0.51	0.94	-0.10	0.07	0.32
266	-3.0	3.0	7.3	-7.3	-3.6	21.9	-0.77	0.77	0.94	-0.21	-0.10	0.63
266	0.0	3.0	7.3	-9.3	4.6	39.2	0.00	0.77	0.94	-0.27	0.13	1.14
266	3.0	3.0	7.3	-3.8	3.8	16.9	0.77	0.77	0.94	-0.11	0.11	0.49
266	-4.0	4.0	7.3	0.3	-0.4	4.1	-1.03	1.03	0.94	0.01	-0.01	0.12
266	-2.0	4.0	7.3	-5.1	-1.3	18.8	-0.51	1.03	0.94	-0.15	-0.04	0.54
266	0.0	4.0	7.3	-5.8	2.1	29.8	0.00	1.03	0.94	-0.17	0.06	0.86
266	2.0	4.0	7.3	-3.7	2.2	16.3	0.51	1.03	0.94	-0.11	0.06	0.47
266	4.0	4.0	7.3	-1.9	-0.1	3.5	1.03	1.03	0.94	-0.06	0.00	0.10
266	0.0	5.0	7.3	-2.4	0.1	10.9	0.00	1.28	0.94	-0.07	0.00	0.32
266	0.0	6.0	7.3	-1.1	-0.2	5.3	0.00	1.54	0.94	-0.03	-0.01	0.15
266	-5.0	0.0	12.3	-2.5	-3.6	10.0	-1.28	0.00	1.58	-0.07	-0.10	0.29
266	-4.0	0.0	12.3	-2.6	-5.7	16.1	-1.03	0.00	1.58	-0.08	-0.17	0.47
266	-3.0	0.0	12.3	-1.0	-8.3	21.1	-0.77	0.00	1.58	-0.03	-0.24	0.61
266	-2.0	0.0	12.3	5.0	-5.9	15.0	-0.51	0.00	1.58	0.14	-0.17	0.43
266	-1.0	0.0	12.3	10.3	-0.7	21.4	-0.26	0.00	1.58	0.30	-0.02	0.62

Run no.	Collected Data						Non-Dimensional Data					
	Distance from Origin (cm)			Average Velocity (cm/s)			Distance from Origin			Average Velocity		
	x	y	z	U _x	U _y	U _z	x/R	y/R	z/d	U _x /U ₀	U _y /U ₀	U _z /U ₀
266	0.0	0.0	12.3	2.6	2.5	32.4	0.00	0.00	1.58	0.08	0.07	0.94
266	1.0	0.0	12.3	1.3	5.3	29.7	0.26	0.00	1.58	0.04	0.15	0.86
266	2.0	0.0	12.3	-0.5	3.4	29.8	0.51	0.00	1.58	-0.01	0.10	0.86
266	3.0	0.0	12.3	-0.1	1.5	24.7	0.77	0.00	1.58	0.00	0.04	0.72
266	4.0	0.0	12.3	-0.5	1.1	14.0	1.03	0.00	1.58	-0.01	0.03	0.41
266	5.0	0.0	12.3	-0.1	1.5	8.0	1.28	0.00	1.58	0.00	0.04	0.23
266	-5.0	0.0	17.0	-11.0	-5.7	12.5	-1.28	0.00	2.18	-0.32	-0.17	0.36
266	-4.0	0.0	17.0	-7.7	-5.2	9.7	-1.03	0.00	2.18	-0.22	-0.15	0.28
266	-3.0	0.0	17.0	-3.1	-3.0	6.1	-0.77	0.00	2.18	-0.09	-0.09	0.18
266	-2.0	0.0	17.0	-0.9	-0.8	0.4	-0.51	0.00	2.18	-0.03	-0.02	0.01
266	-1.0	0.0	17.0	0.9	-1.5	4.8	-0.26	0.00	2.18	0.03	-0.04	0.14
266	0.0	0.0	17.0	1.3	1.1	5.9	0.00	0.00	2.18	0.04	0.03	0.17
266	1.0	0.0	17.0	2.8	1.8	15.8	0.26	0.00	2.18	0.08	0.05	0.46
266	2.0	0.0	17.0	4.8	1.8	23.3	0.51	0.00	2.18	0.14	0.05	0.67
266	3.0	0.0	17.0	5.2	1.1	19.7	0.77	0.00	2.18	0.15	0.03	0.57
266	4.0	0.0	17.0	6.5	1.5	17.5	1.03	0.00	2.18	0.19	0.04	0.51
266	5.0	0.0	17.0	6.0	2.0	11.1	1.28	0.00	2.18	0.17	0.06	0.32
267	-5.0	0.0	3.3	0.2	-0.1	1.8	-1.28	0.00	0.42	0.01	0.00	0.08
267	-4.0	0.0	3.3	-3.6	-2.9	9.3	-1.03	0.00	0.42	-0.16	-0.13	0.41
267	-3.0	0.0	3.3	0.1	-6.1	20.0	-0.77	0.00	0.42	0.00	-0.27	0.88
267	-2.0	0.0	3.3	1.6	-4.6	21.8	-0.51	0.00	0.42	0.07	-0.20	0.96
267	-1.0	0.0	3.3	9.8	4.4	18.4	-0.26	0.00	0.42	0.43	0.19	0.81
267	0.0	0.0	3.3	2.8	2.2	24.2	0.00	0.00	0.42	0.12	0.10	1.07
267	1.0	0.0	3.3	0.4	-1.5	24.0	0.26	0.00	0.42	0.02	-0.07	1.06
267	2.0	0.0	3.3	-2.5	1.0	23.1	0.51	0.00	0.42	-0.11	0.04	1.02
267	3.0	0.0	3.3	-1.3	1.0	19.9	0.77	0.00	0.42	-0.06	0.04	0.88
267	4.0	0.0	3.3	-2.0	1.5	7.8	1.03	0.00	0.42	-0.09	0.07	0.35
267	5.0	0.0	3.3	-1.8	0.1	1.2	1.28	0.00	0.42	-0.08	0.00	0.05
267	-5.0	0.0	7.3	-0.5	-0.9	3.2	-1.28	0.00	0.94	-0.02	-0.04	0.14
267	-4.0	0.0	7.3	-1.2	-3.0	8.4	-1.03	0.00	0.94	-0.05	-0.13	0.37
267	-3.0	0.0	7.3	-0.8	-3.5	17.7	-0.77	0.00	0.94	-0.04	-0.15	0.78
267	-2.0	0.0	7.3	-0.2	-2.1	23.1	-0.51	0.00	0.94	-0.01	-0.09	1.02
267	-1.0	0.0	7.3	1.9	-1.3	24.3	-0.26	0.00	0.94	0.08	-0.06	1.08
267	0.0	0.0	7.3	1.9	3.8	20.7	0.00	0.00	0.94	0.08	0.17	0.92
267	1.0	0.0	7.3	-2.3	-2.9	22.7	0.26	0.00	0.94	-0.10	-0.13	1.00
267	2.0	0.0	7.3	-3.2	1.7	22.6	0.51	0.00	0.94	-0.14	0.08	1.00
267	3.0	0.0	7.3	-1.9	0.9	16.4	0.77	0.00	0.94	-0.08	0.04	0.73
267	4.0	0.0	7.3	-0.7	0.5	8.9	1.03	0.00	0.94	-0.03	0.02	0.39
267	5.0	0.0	7.3	-0.9	0.0	3.0	1.28	0.00	0.94	-0.04	0.00	0.13
267	-5.0	0.0	12.3	-1.1	-1.6	5.4	-1.28	0.00	1.58	-0.05	-0.07	0.24
267	-4.0	0.0	12.3	-1.4	-3.8	10.1	-1.03	0.00	1.58	-0.06	-0.17	0.45
267	-3.0	0.0	12.3	-0.9	-2.7	14.9	-0.77	0.00	1.58	-0.04	-0.12	0.66
267	-2.0	0.0	12.3	1.3	-3.4	17.6	-0.51	0.00	1.58	0.06	-0.15	0.78
267	-1.0	0.0	12.3	3.4	-1.7	14.8	-0.26	0.00	1.58	0.15	-0.08	0.65
267	0.0	0.0	12.3	0.5	2.6	15.4	0.00	0.00	1.58	0.02	0.12	0.68
267	1.0	0.0	12.3	-0.9	1.8	20.9	0.26	0.00	1.58	-0.04	0.08	0.92
267	2.0	0.0	12.3	-1.1	0.4	21.5	0.51	0.00	1.58	-0.05	0.02	0.95
267	3.0	0.0	12.3	-0.4	-0.2	17.7	0.77	0.00	1.58	-0.02	-0.01	0.78

Run no.	Collected Data						Non-Dimensional Data					
	Distance from Origin (cm)			Average Velocity (cm/s)			Distance from Origin			Average Velocity		
	x	y	z	U _x	U _y	U _z	x/R	y/R	z/d	U _x /U _o	U _y /U _o	U _z /U _o
267	4.0	0.0	12.3	-0.1	0.3	9.7	1.03	0.00	1.58	0.00	0.01	0.43
267	5.0	0.0	12.3	0.1	1.4	6.3	1.28	0.00	1.58	0.00	0.06	0.28
267	-5.0	0.0	17.0	-6.6	-2.9	6.8	-1.28	0.00	2.18	-0.29	-0.13	0.30
267	-4.0	0.0	17.0	-5.9	-3.2	8.8	-1.03	0.00	2.18	-0.26	-0.14	0.39
267	-3.0	0.0	17.0	-3.7	-1.9	9.8	-0.77	0.00	2.18	-0.16	-0.08	0.43
267	-2.0	0.0	17.0	-2.0	-1.6	8.6	-0.51	0.00	2.18	-0.09	-0.07	0.38
267	-1.0	0.0	17.0	-1.5	-1.0	14.2	-0.26	0.00	2.18	-0.07	-0.04	0.63
267	0.0	0.0	17.0	1.5	0.8	8.4	0.00	0.00	2.18	0.07	0.04	0.37
267	1.0	0.0	17.0	1.4	0.6	13.3	0.26	0.00	2.18	0.06	0.03	0.59
267	2.0	0.0	17.0	2.6	-0.4	15.8	0.51	0.00	2.18	0.12	-0.02	0.70
267	3.0	0.0	17.0	3.4	0.2	12.6	0.77	0.00	2.18	0.15	0.01	0.56
267	4.0	0.0	17.0	3.8	1.0	10.7	1.03	0.00	2.18	0.17	0.04	0.47
267	5.0	0.0	17.0	3.3	1.1	6.4	1.28	0.00	2.18	0.15	0.05	0.28
268	0.0	0.0	3.3	0.4	-0.3	12.4	0.00	0.00	0.42	0.03	-0.02	0.99
268	-5.0	0.0	7.3	-0.4	-0.8	2.4	-1.28	0.00	0.94	-0.03	-0.06	0.19
268	-4.0	0.0	7.3	-0.8	-1.5	5.2	-1.03	0.00	0.94	-0.06	-0.12	0.41
268	-3.0	0.0	7.3	-0.7	-3.8	8.2	-0.77	0.00	0.94	-0.06	-0.30	0.65
268	-2.0	0.0	7.3	4.4	-2.9	6.6	-0.51	0.00	0.94	0.35	-0.23	0.53
268	-1.0	0.0	7.3	1.4	-1.5	11.0	-0.26	0.00	0.94	0.11	-0.12	0.88
268	0.0	0.0	7.3	0.8	2.4	10.1	0.00	0.00	0.94	0.06	0.19	0.80
268	1.0	0.0	7.3	-0.7	-0.1	11.5	0.26	0.00	0.94	-0.06	-0.01	0.92
268	2.0	0.0	7.3	-1.8	0.4	10.7	0.51	0.00	0.94	-0.14	0.03	0.85
268	3.0	0.0	7.3	-0.9	-0.3	9.6	0.77	0.00	0.94	-0.07	-0.02	0.76
268	4.0	0.0	7.3	-0.4	1.1	5.1	1.03	0.00	0.94	-0.03	0.09	0.41
268	5.0	0.0	7.3	-0.8	0.8	2.5	1.28	0.00	0.94	-0.06	0.06	0.20
268	0.0	0.0	12.3	-0.1	-0.8	11.7	0.00	0.00	1.58	-0.01	-0.06	0.93
268	0.0	0.0	17.0	-1.4	-0.8	9.8	0.00	0.00	2.18	-0.11	-0.06	0.78
269	0.0	0.0	7.3	0.3	2.1	11.4	0.00	0.00	0.94	0.02	0.17	0.91

Appendix D

Complete Velocity Profiles and x-y Plane Plots

from ADV Measurements

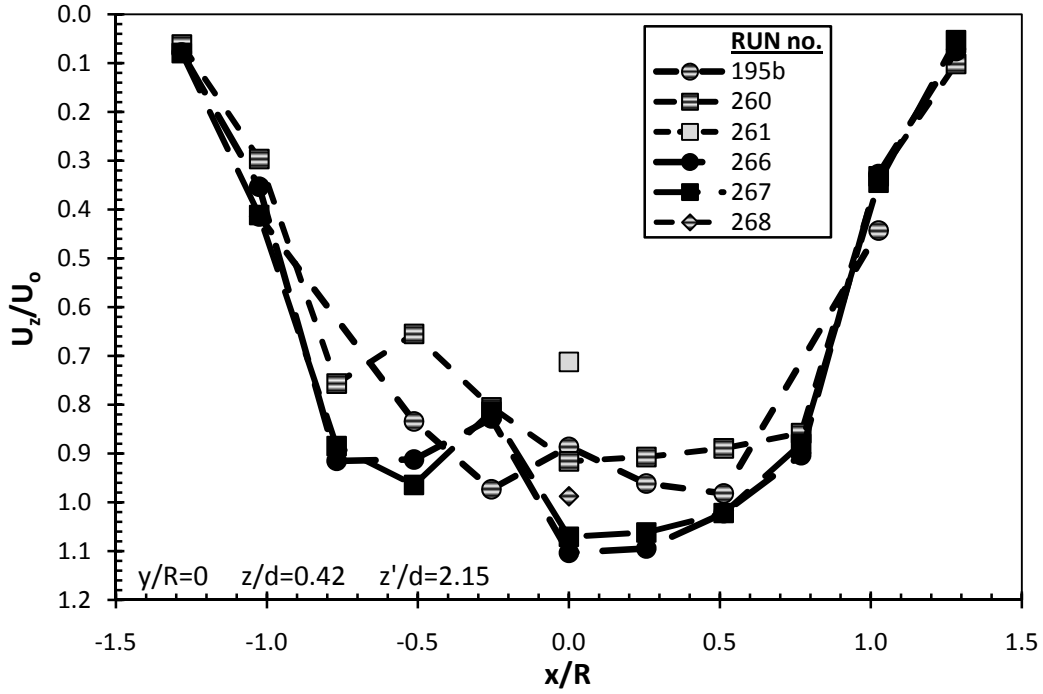


Figure D-1 Dimensionless axial (U_z/U_0) velocities along the x-axis for $z/d = 0.42$.

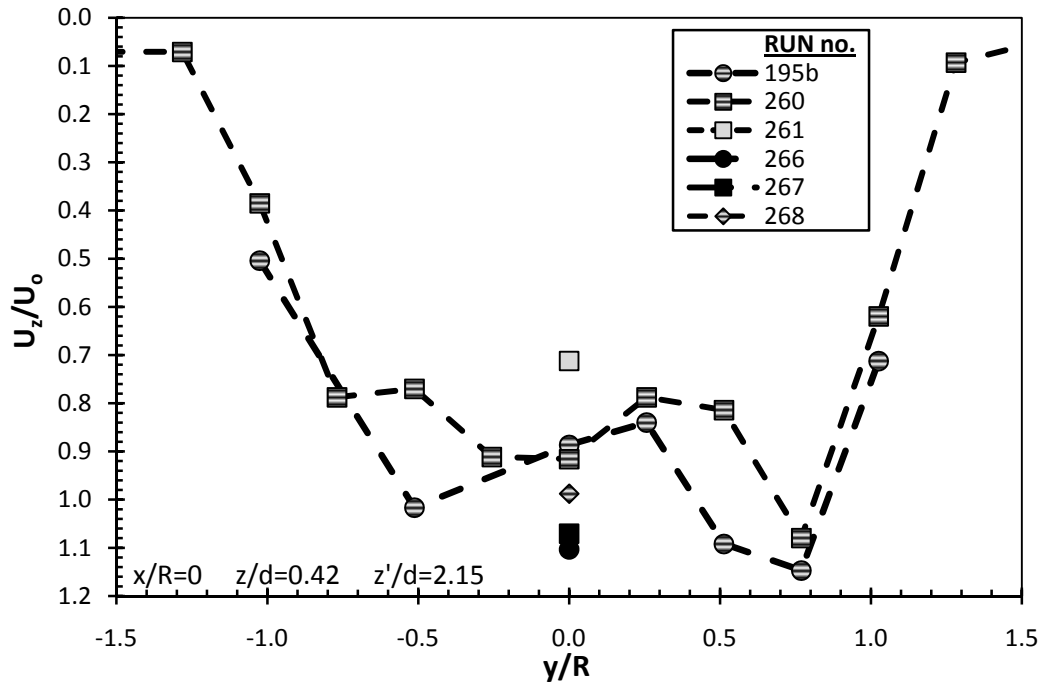


Figure D-2 Dimensionless axial (U_z/U_0) velocities along the y-axis for $z/d = 0.42$.

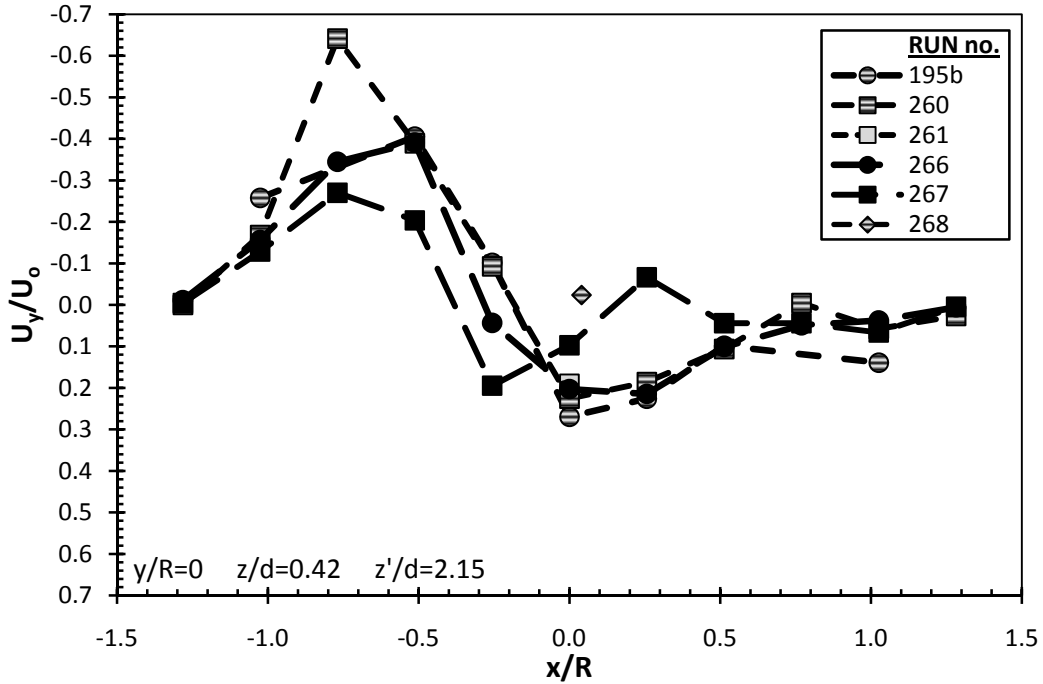


Figure D-3 Dimensionless longitudinal (U_y/U_o) / tangential velocities along the x-axis for $z/d = 0.42$.

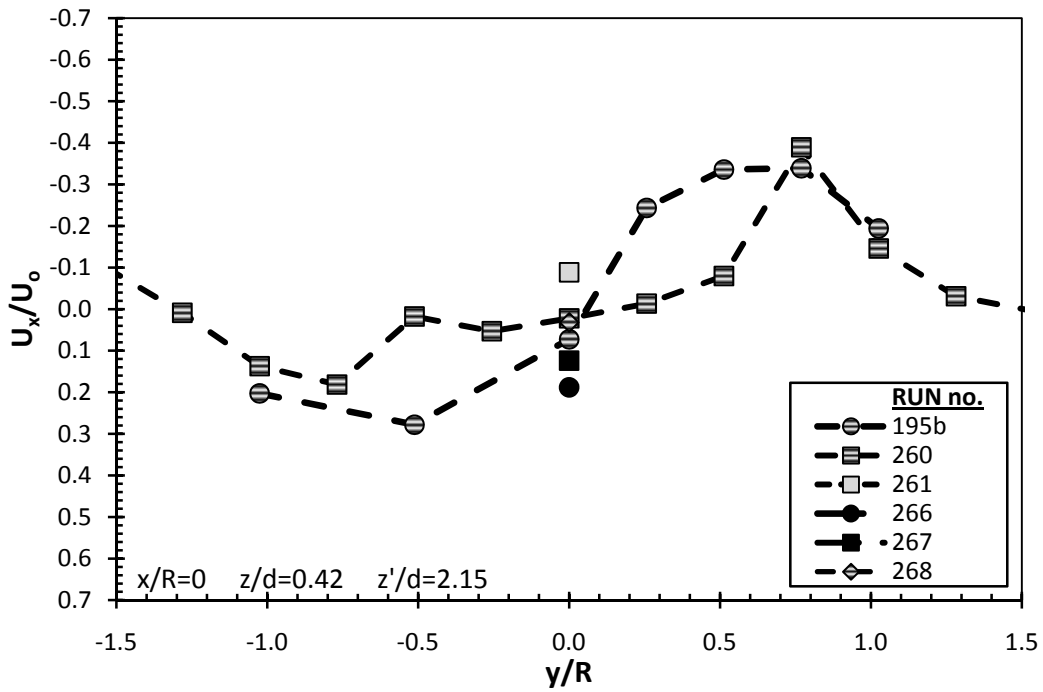


Figure D-4 Dimensionless lateral (U_x/U_o) / tangential velocities along the y-axis for $z/d = 0.42$.

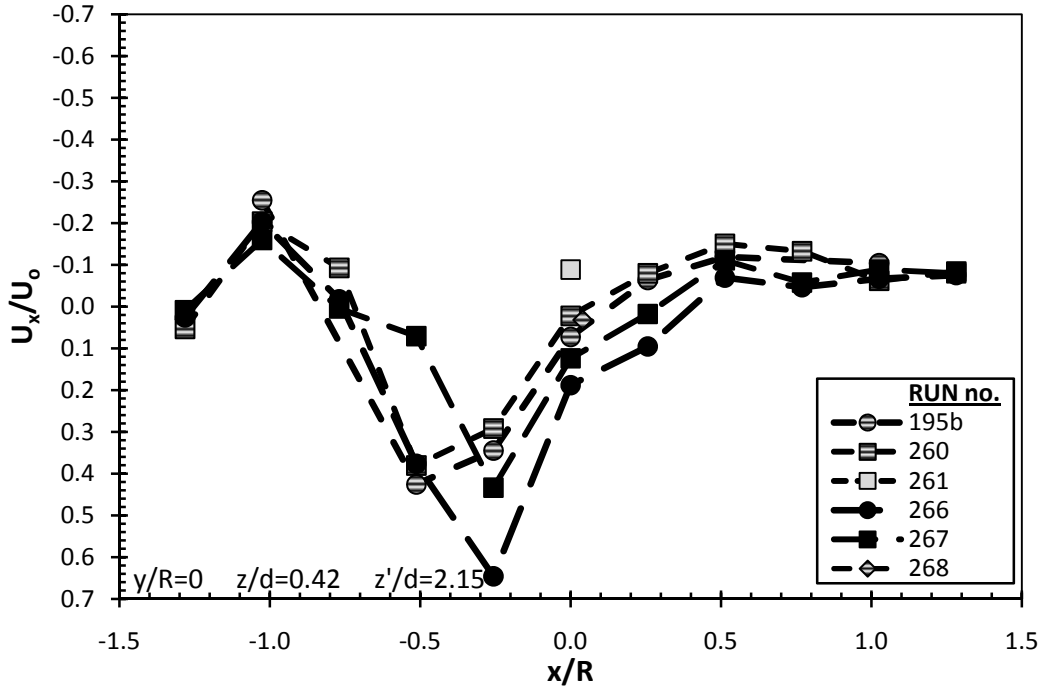


Figure D-5 Dimensionless lateral (U_x/U_o) / radial velocities along the x-axis for $z/d = 0.42$.

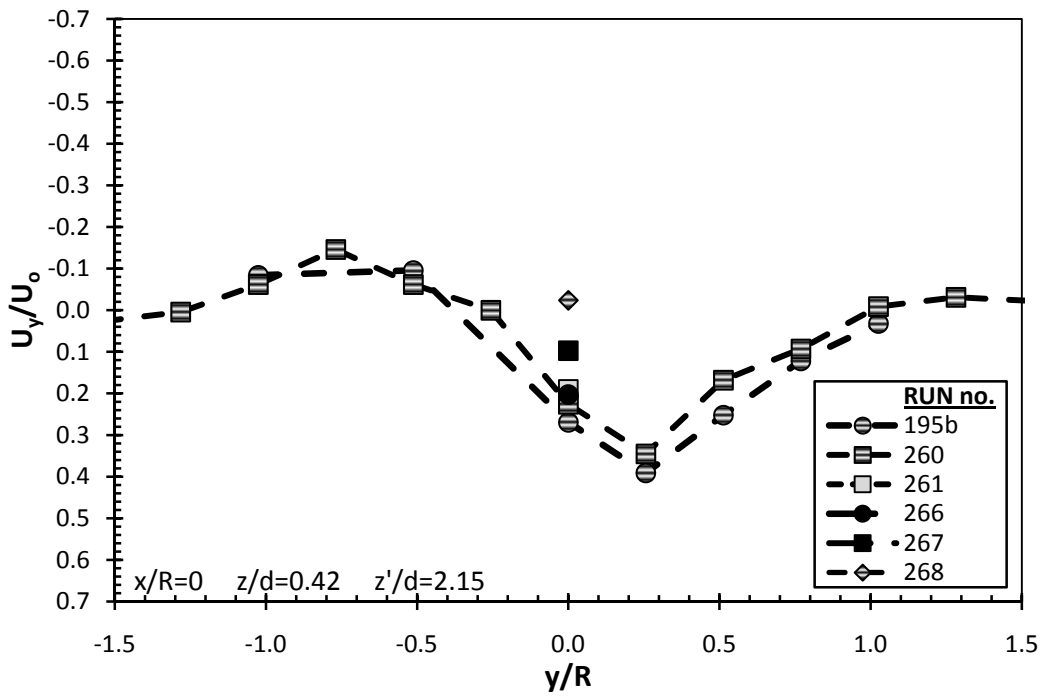


Figure D-6 Dimensionless longitudinal (U_y/U_o) / radial velocities along the y-axis for $z/d = 0.42$.

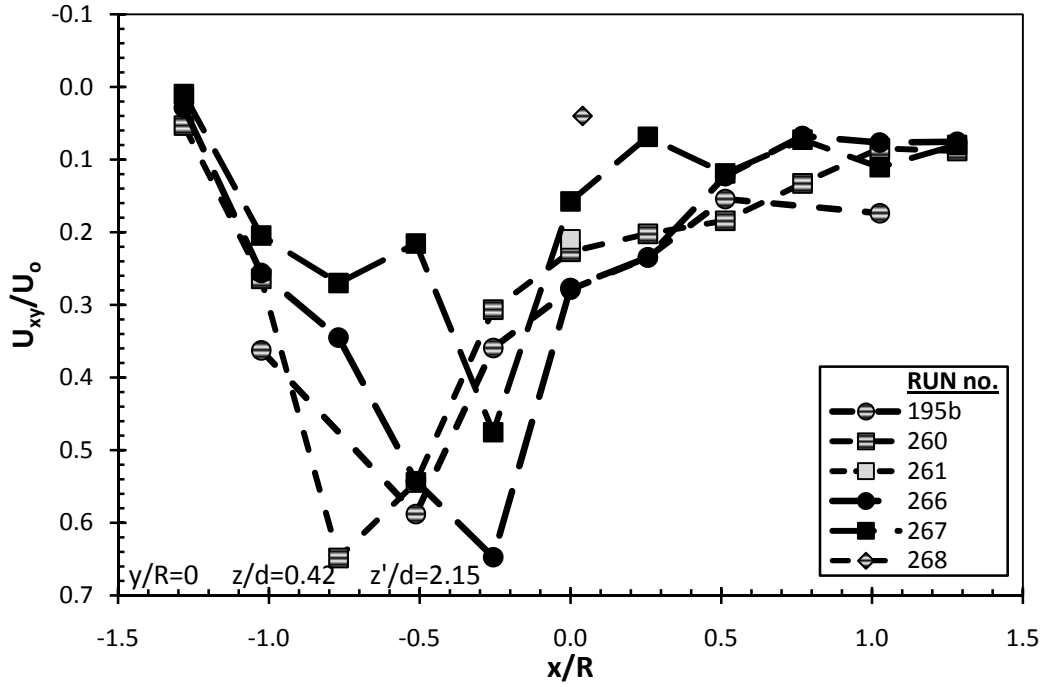


Figure D-7 Dimensionless horizontal (U_{xy}/U_o) velocities along the x-axis for $z/d = 0.42$.

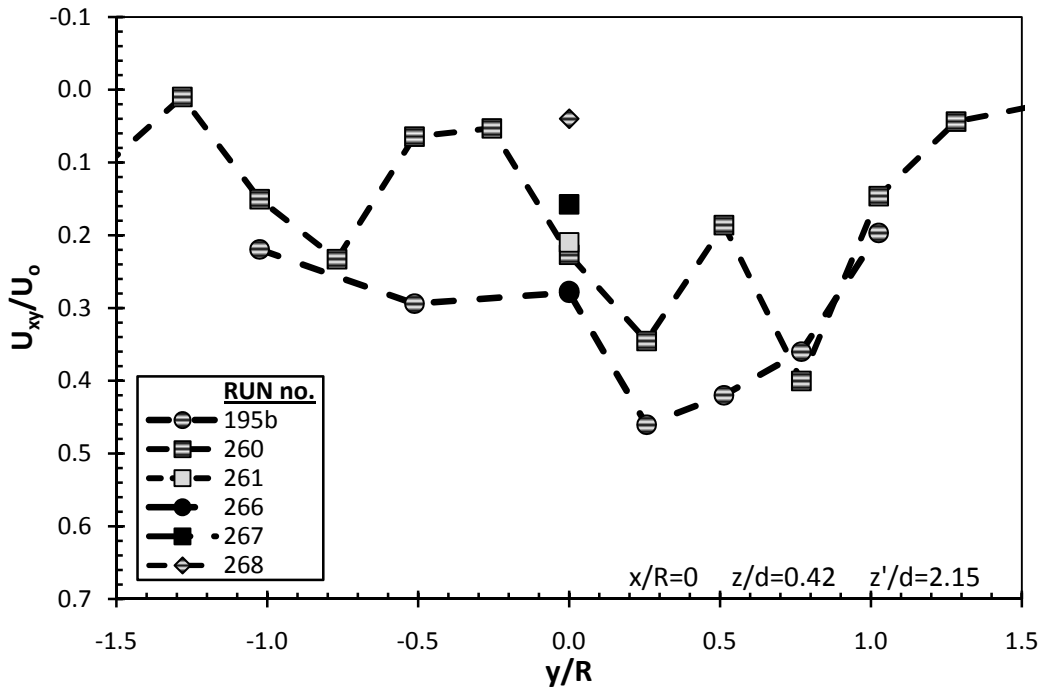


Figure D-8 Dimensionless horizontal (U_{xy}/U_o) velocities along the y-axis for $z/d = 0.42$.

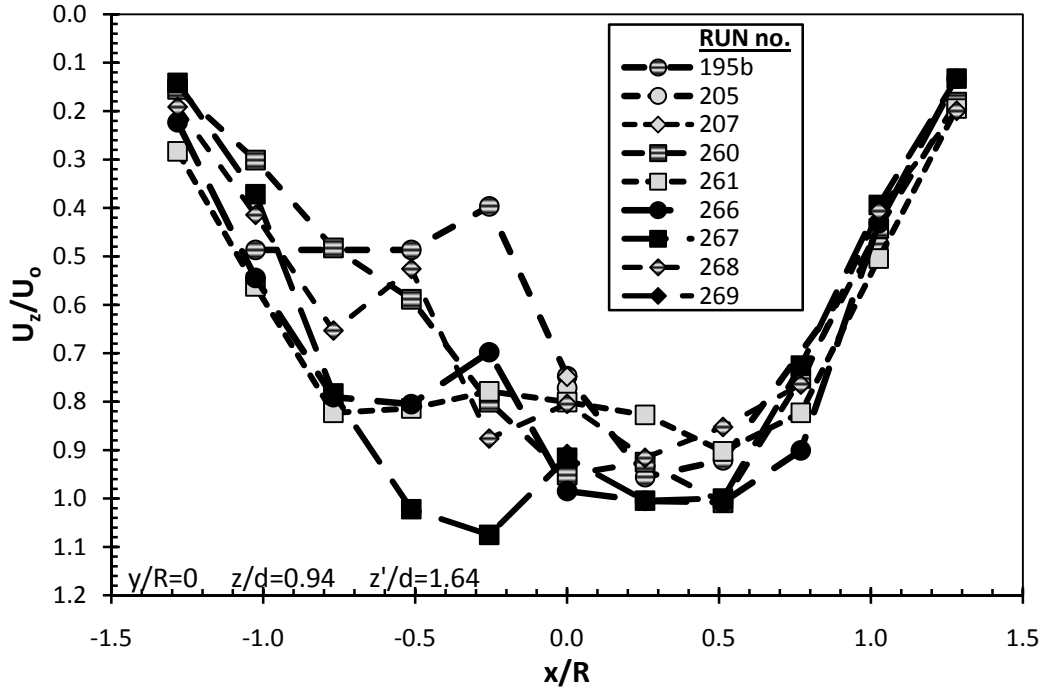


Figure D-9 Dimensionless axial (U_z/U_0) velocities along the x-axis for $z/d = 0.94$.

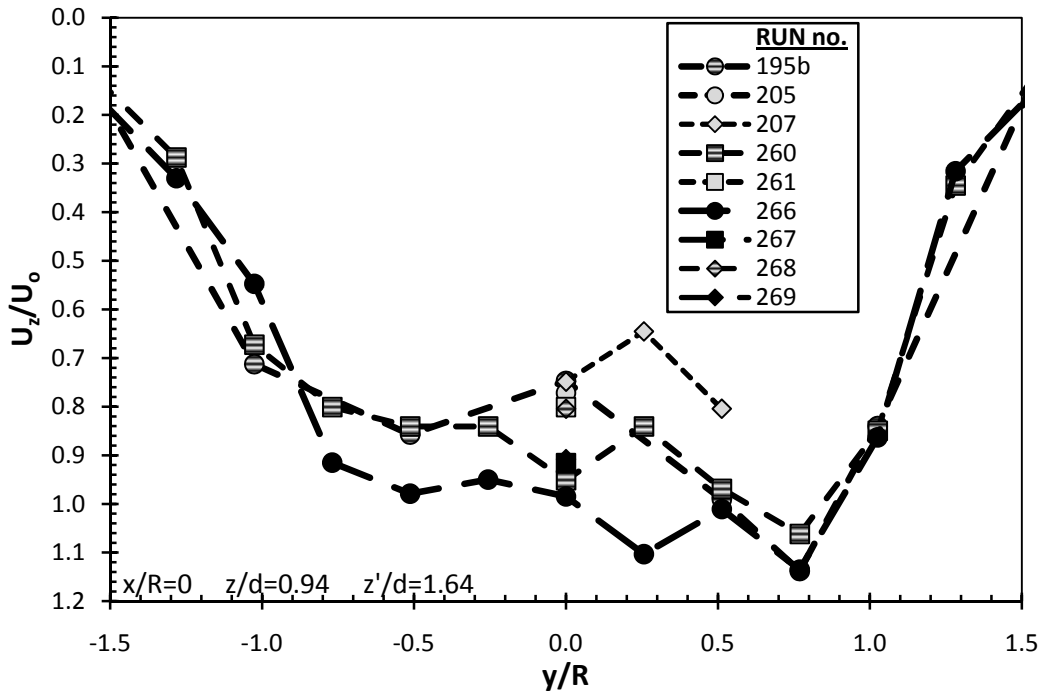


Figure D-10 Dimensionless axial (U_z/U_0) velocities along the y-axis for $z/d = 0.94$.

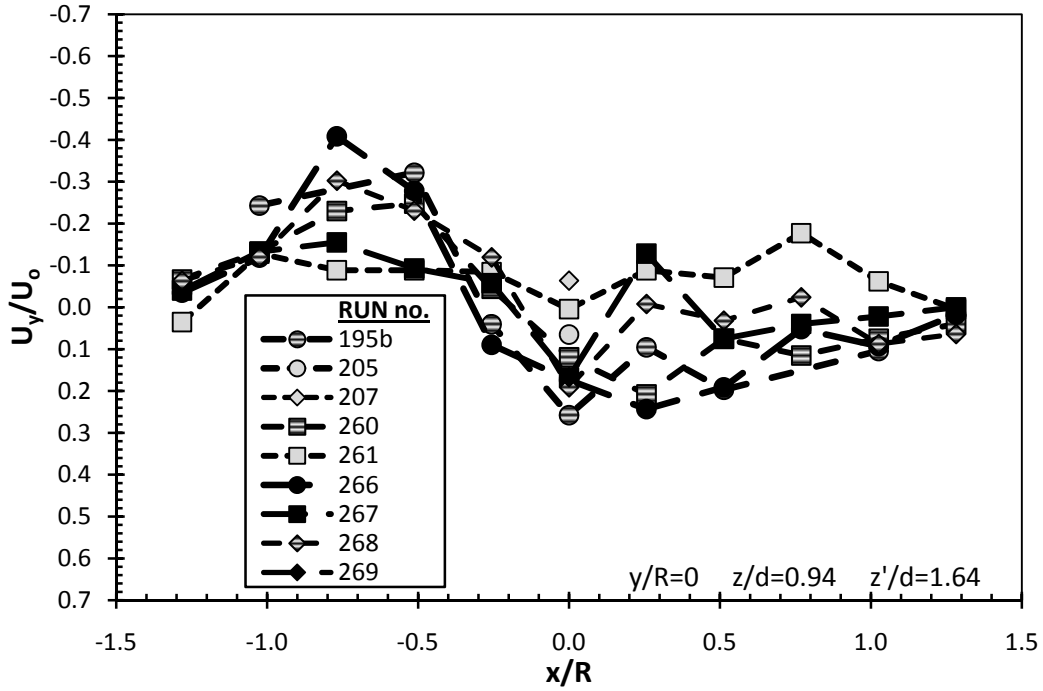


Figure D-11 Dimensionless longitudinal (U_y/U_0) / tangential velocities along the x-axis for $z/d = 0.94$.

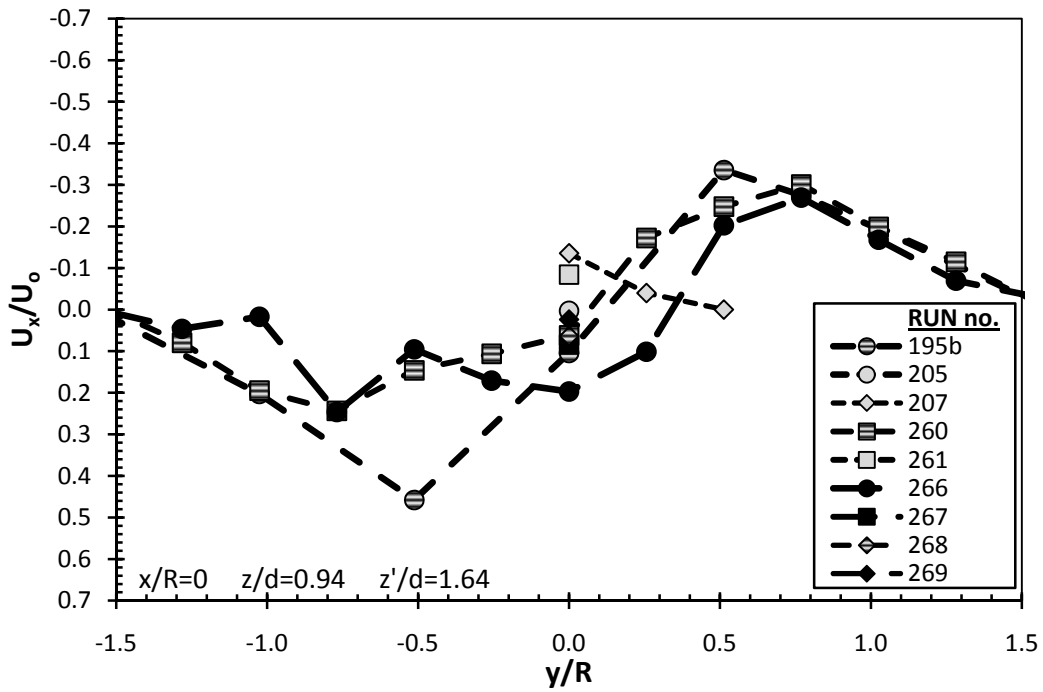


Figure D-12 Dimensionless lateral (U_x/U_0) / tangential velocities along the y-axis for $z/d = 0.94$.

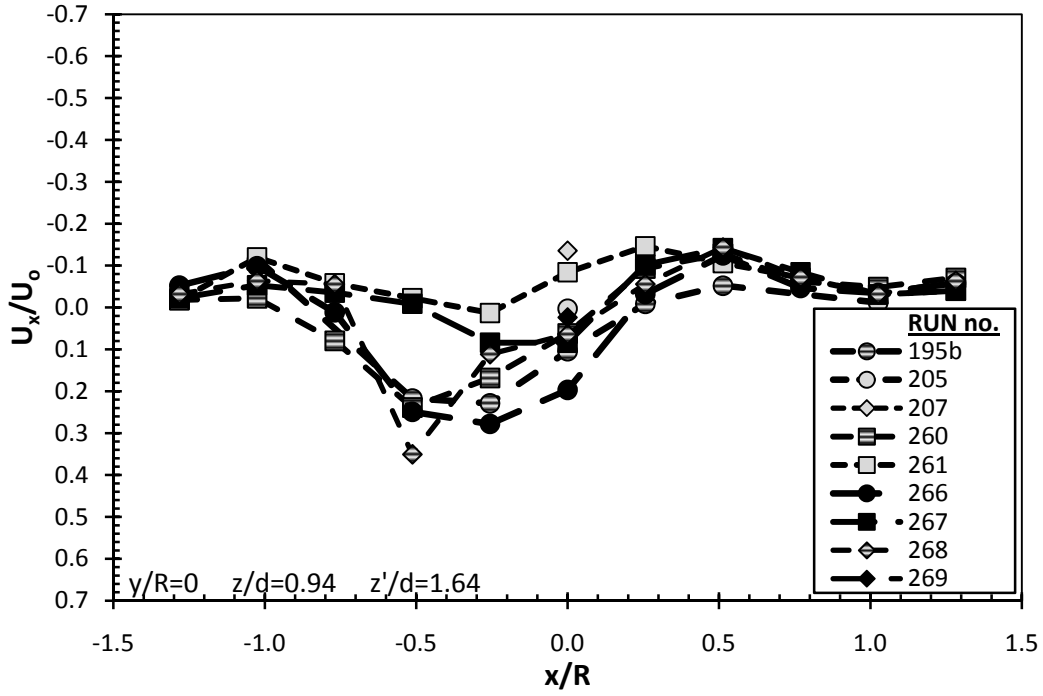


Figure D-13 Dimensionless lateral (U_x/U_o) / radial velocities along the x-axis for $z/d = 0.94$.

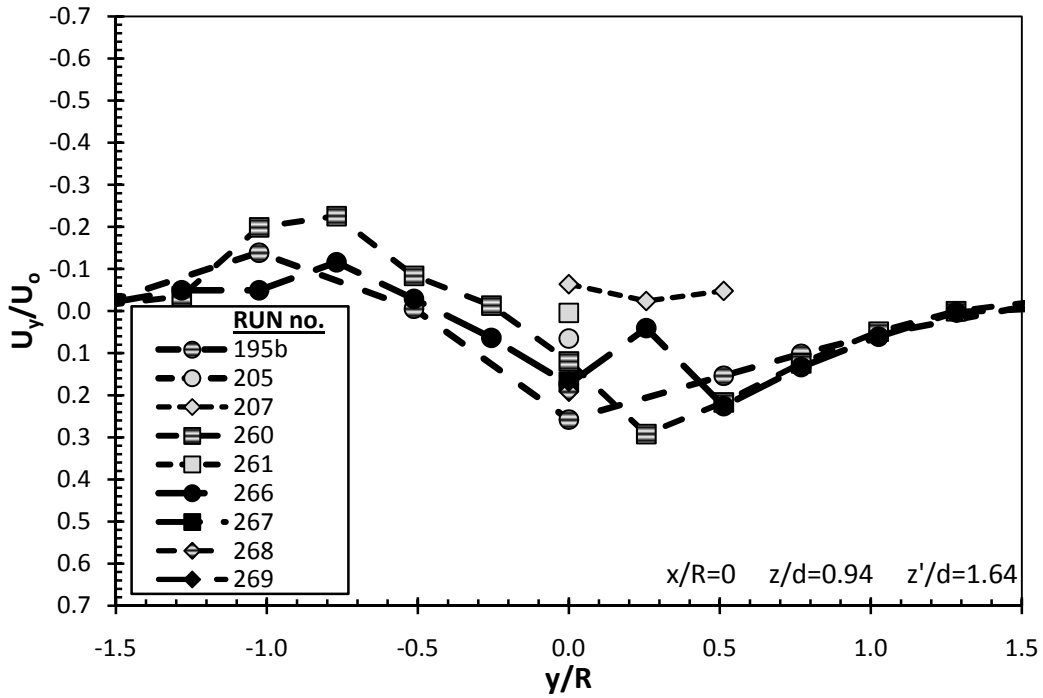


Figure D-14 Dimensionless longitudinal (U_y/U_o) / radial velocities along the y-axis for $z/d = 0.94$.

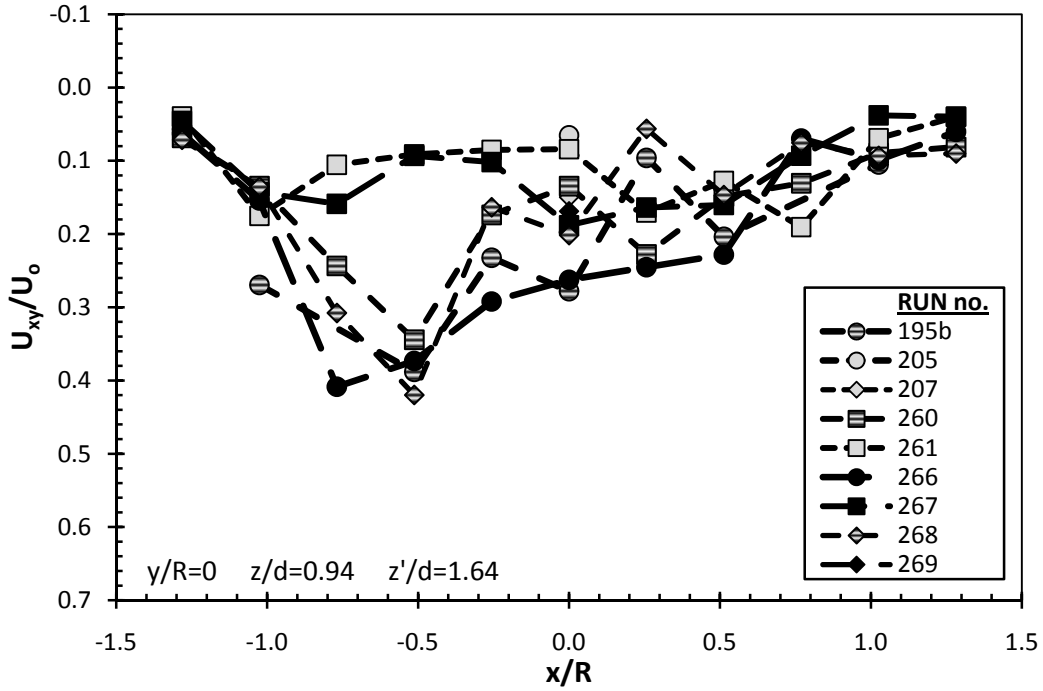


Figure D-15 Dimensionless horizontal (U_{xy}/U_o) velocities along the x-axis for $z/d = 0.94$.

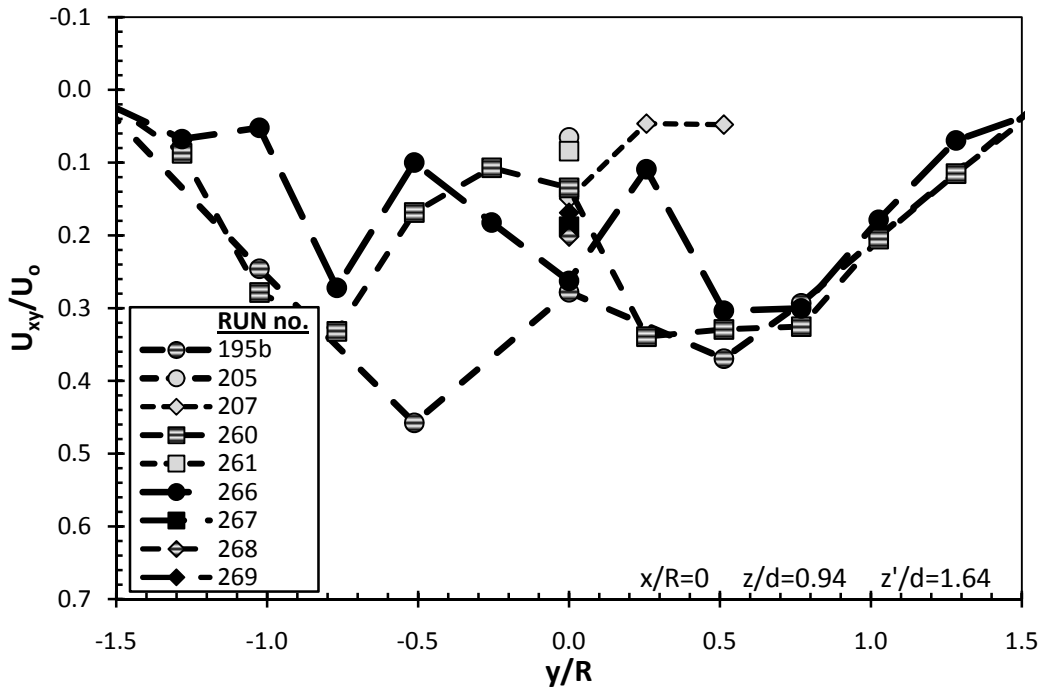


Figure D-16 Dimensionless horizontal (U_{xy}/U_o) velocities along the y-axis for $z/d = 0.94$.

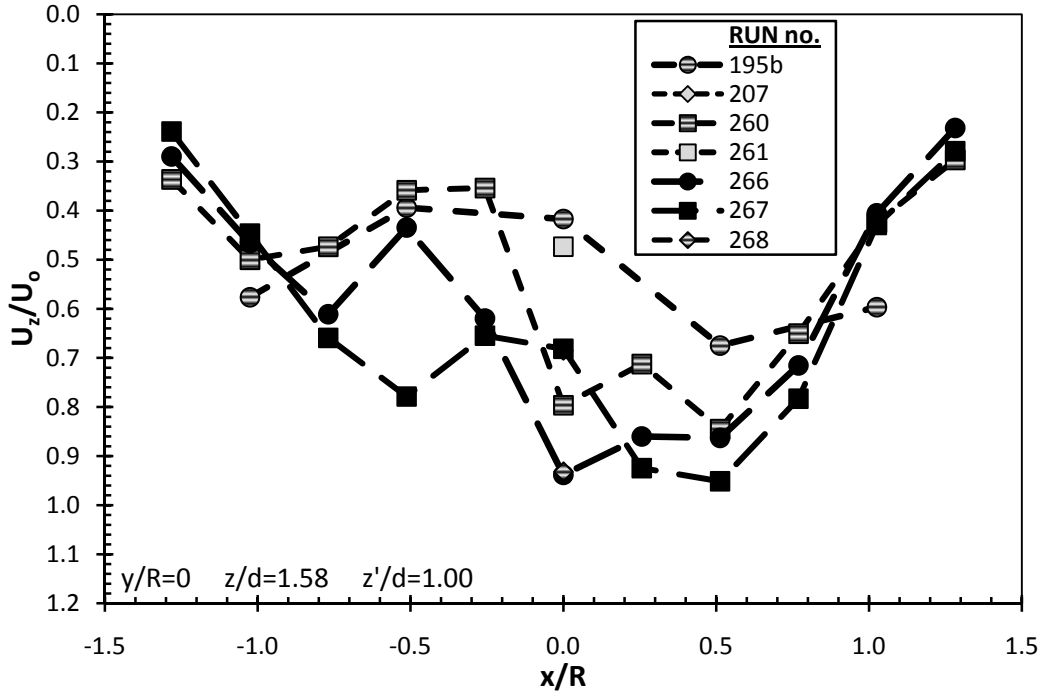


Figure D-17 Dimensionless axial (U_z/U_0) velocities along the x-axis for $z/d = 1.58$.

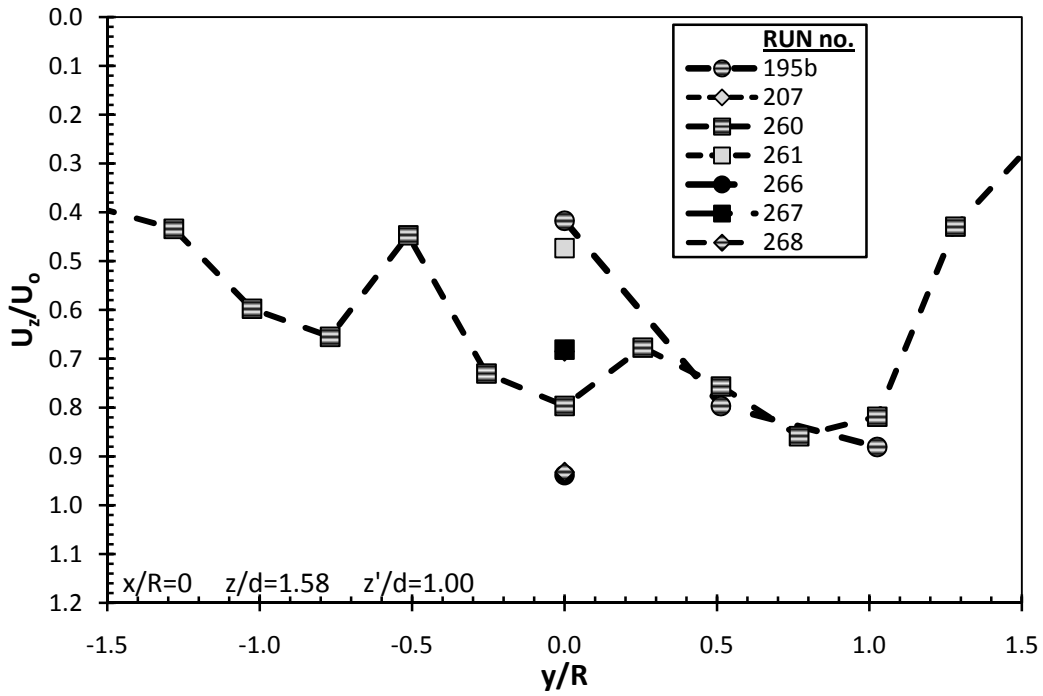


Figure D-18 Dimensionless axial (U_z/U_0) velocities along the y-axis for $z/d = 1.58$.

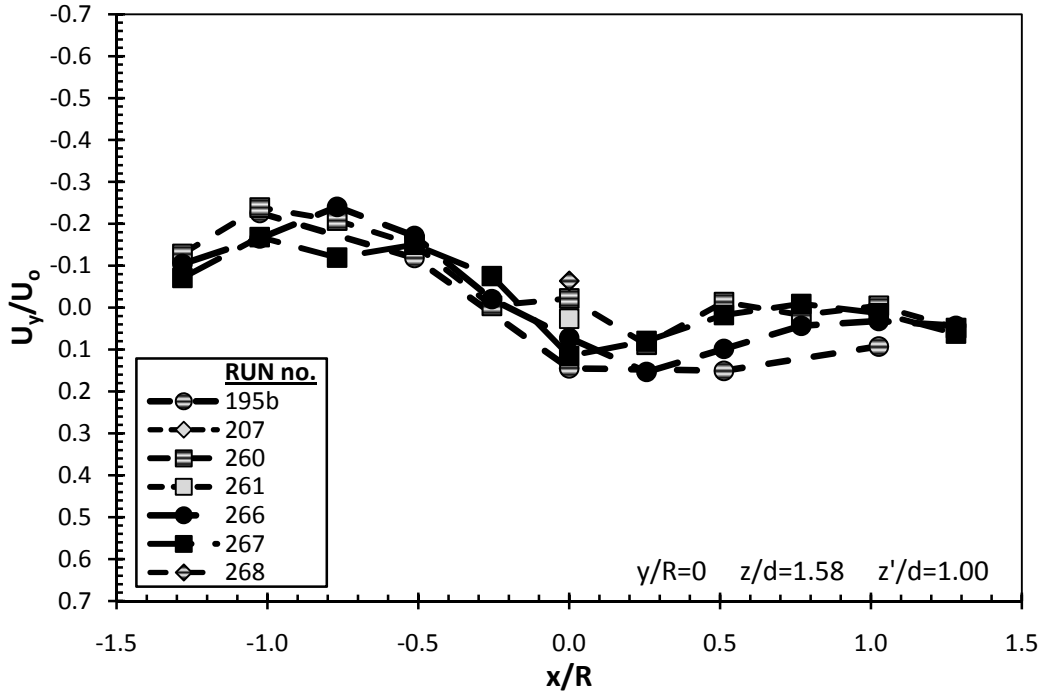


Figure D-19 Dimensionless longitudinal (U_y/U_0) / tangential velocities along the x-axis for $z/d = 1.58$.

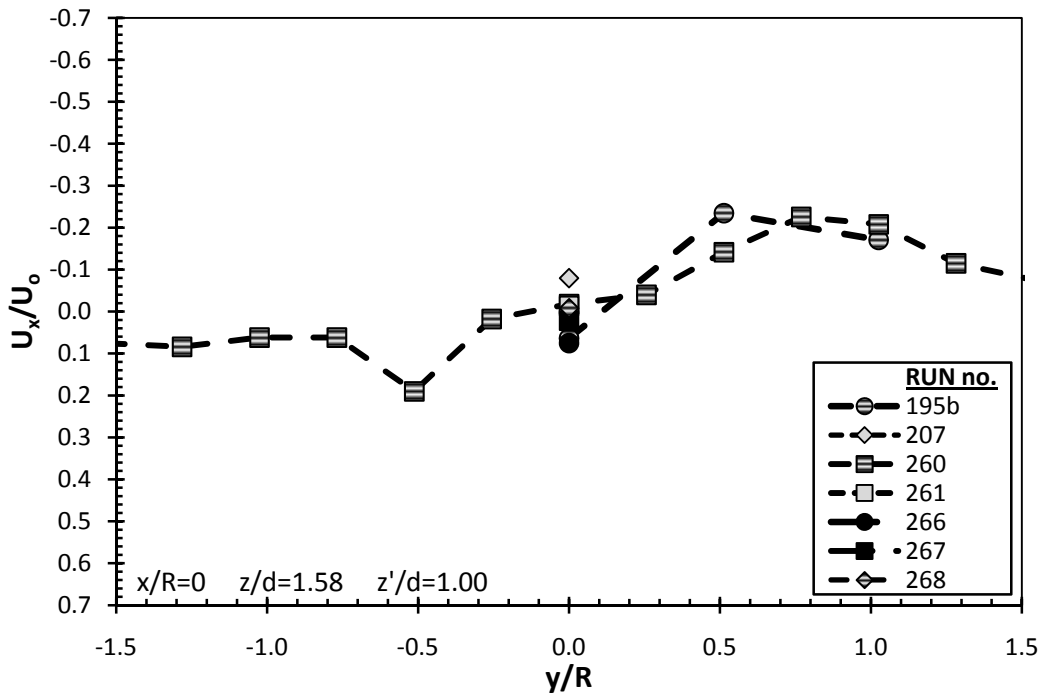


Figure D-20 Dimensionless lateral (U_x/U_0) / tangential velocities along the y-axis for $z/d = 1.58$.

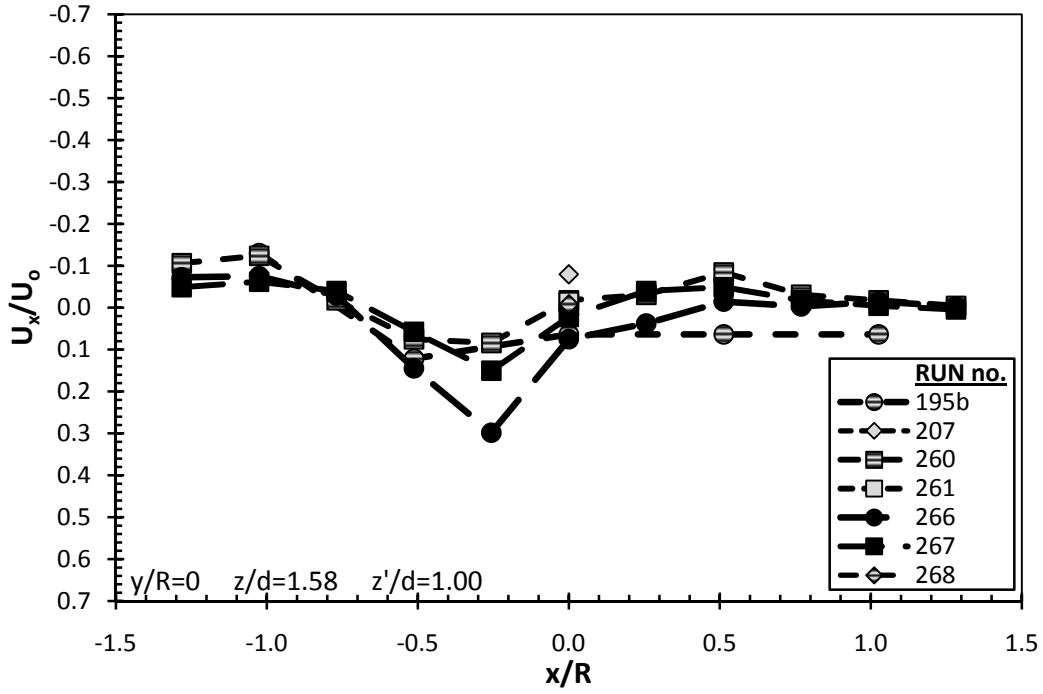


Figure D-21 Dimensionless lateral (U_x/U_o) / radial velocities along the x-axis for $z/d = 1.58$.

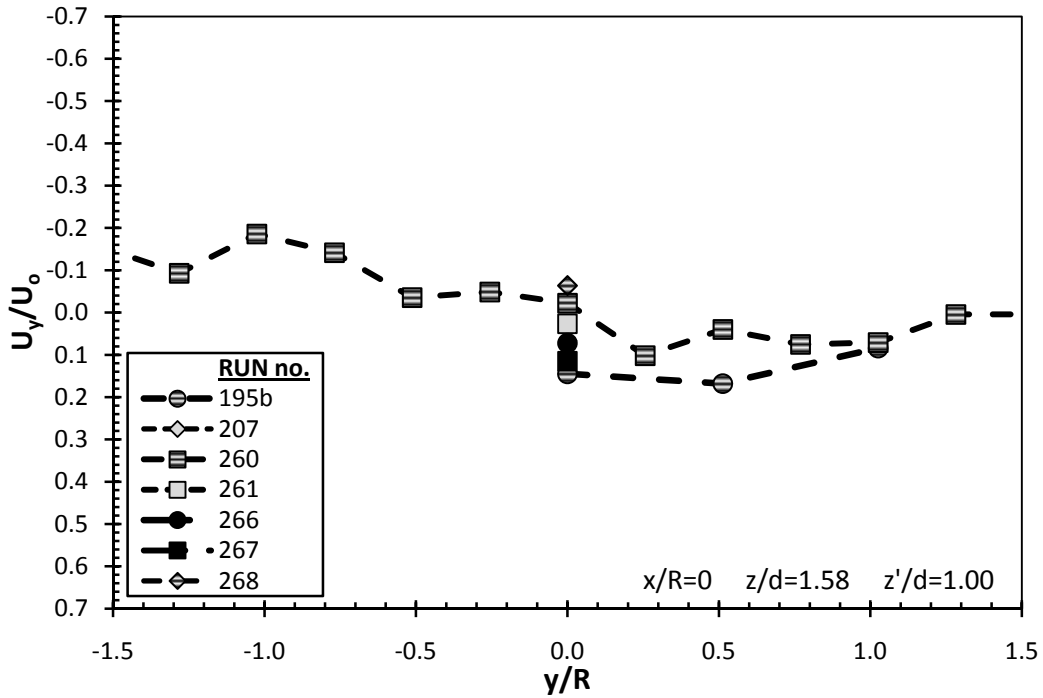


Figure D-22 Dimensionless longitudinal (U_y/U_o) / radial velocities along the y-axis for $z/d = 1.58$.

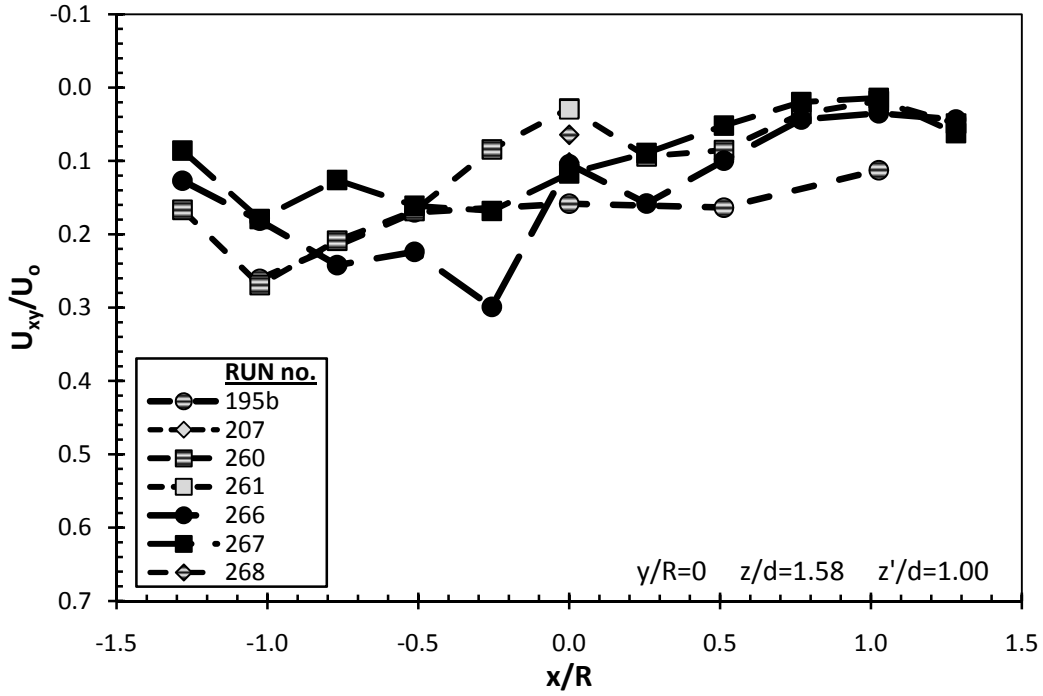


Figure D-23 Dimensionless horizontal (U_{xy}/U_o) velocities along the x-axis for $z/d = 1.58$.

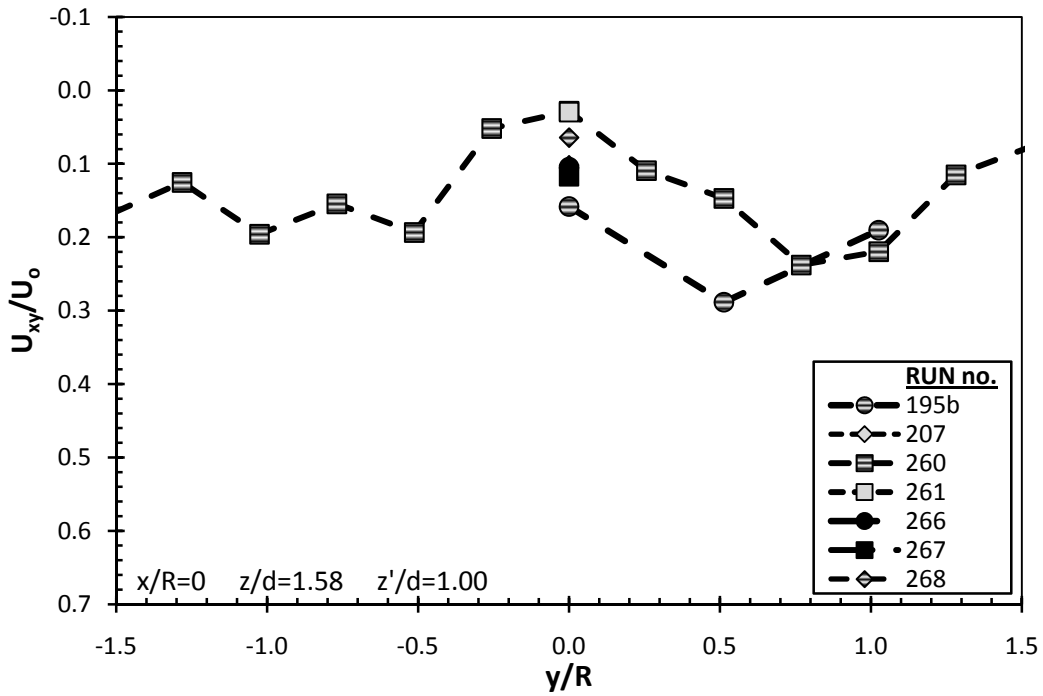


Figure D-24 Dimensionless horizontal (U_{xy}/U_o) velocities along the y-axis for $z/d = 1.58$.

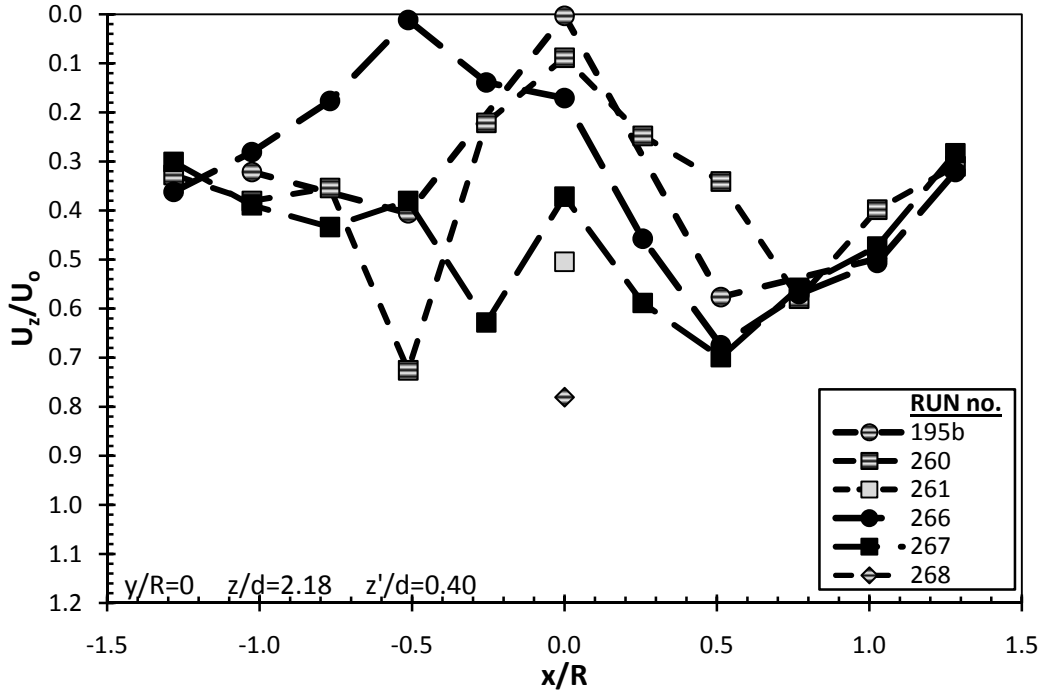


Figure D-25 Dimensionless axial (U_z/U_o) velocities along the x-axis for $z/d = 2.18$.

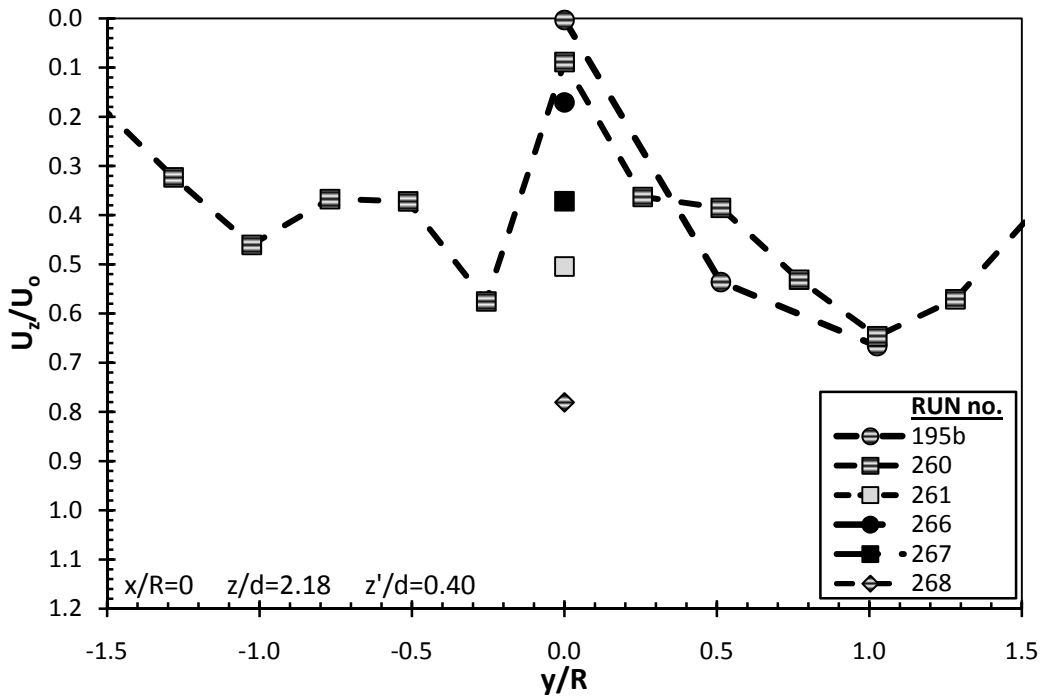


Figure D-26 Dimensionless axial (U_z/U_o) velocities along the y-axis for $z/d = 2.18$.

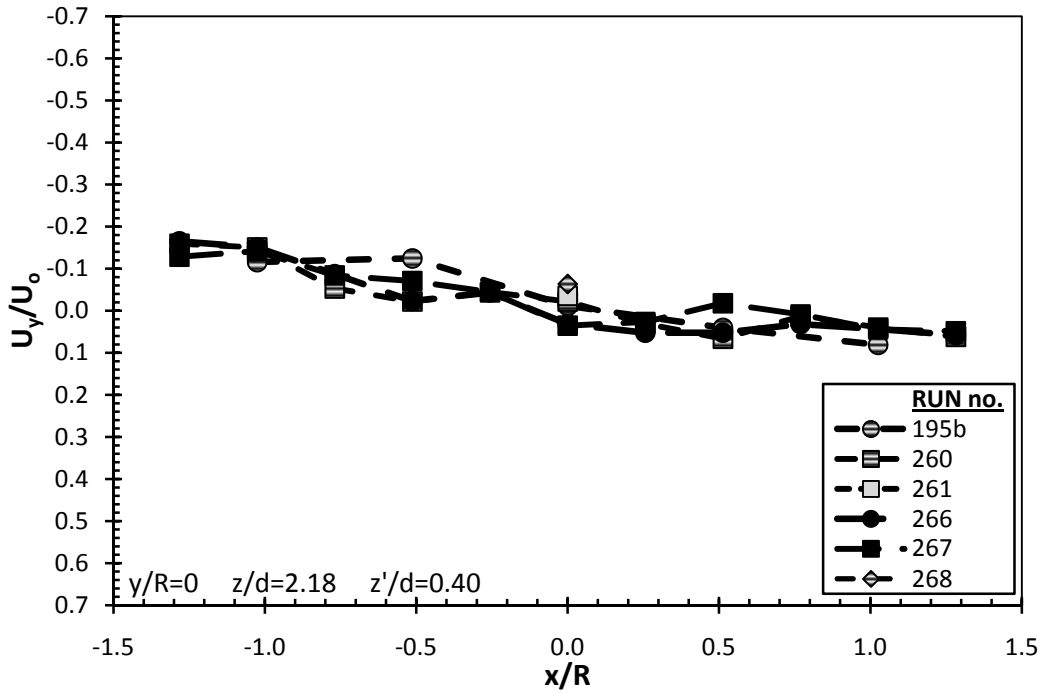


Figure D-27 Dimensionless longitudinal (U_y/U_o) / tangential velocities along the x-axis for $z/d = 2.18$.

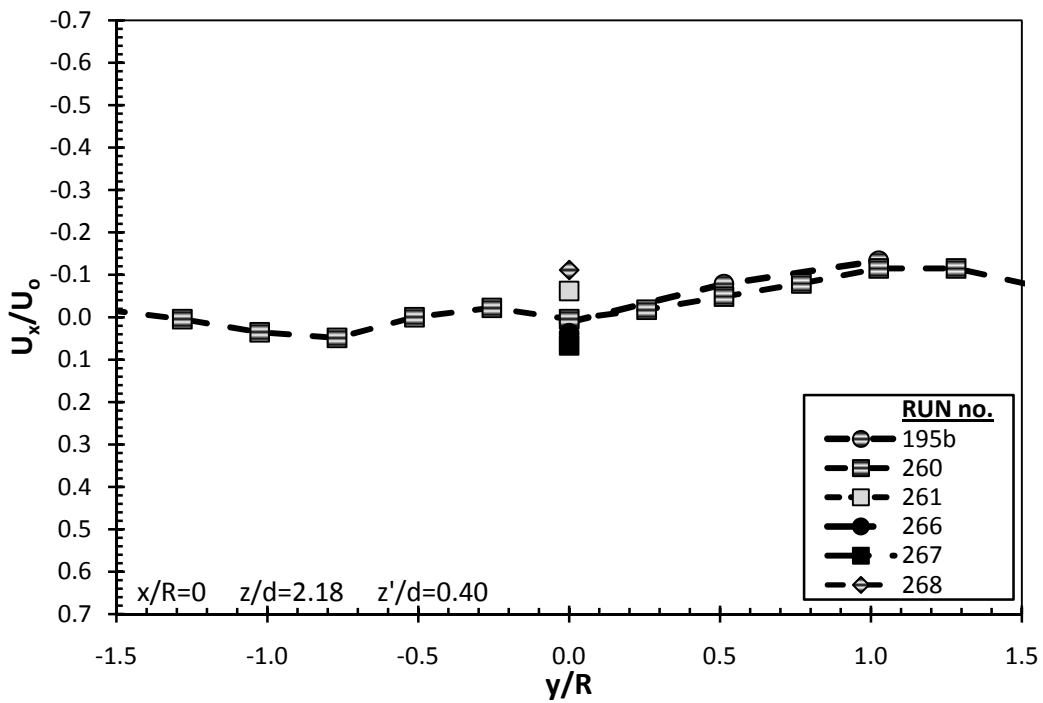


Figure D-28 Dimensionless lateral (U_x/U_o) / tangential velocities along the y-axis for $z/d = 2.18$.

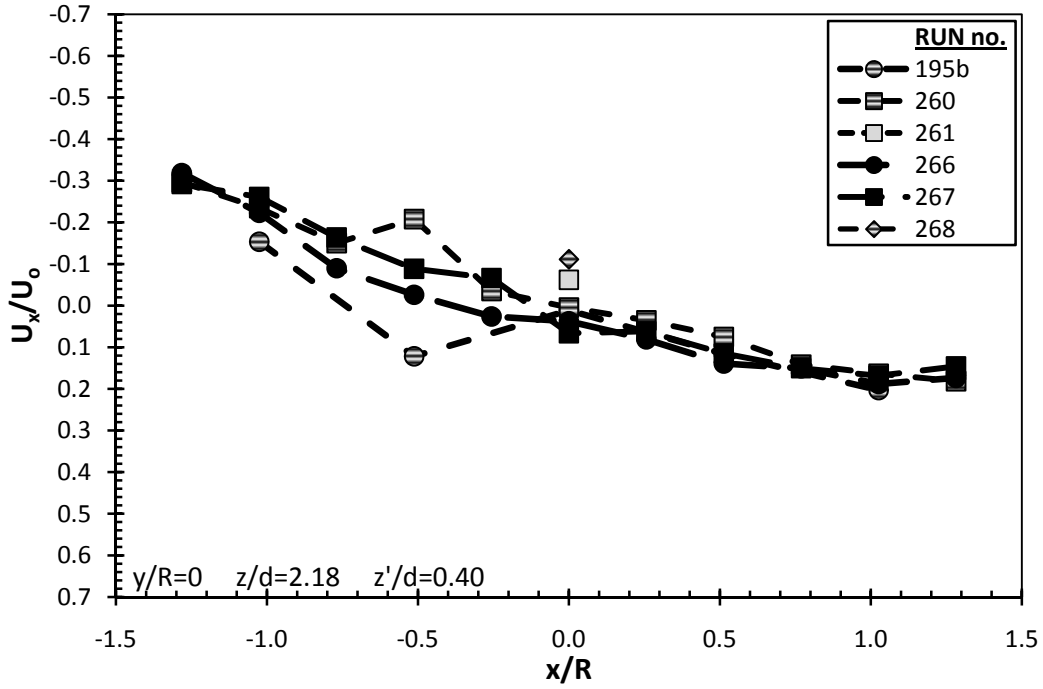


Figure D-29 Dimensionless lateral (U_x/U_o) / radial velocities along the x-axis for $z/d = 2.18$.

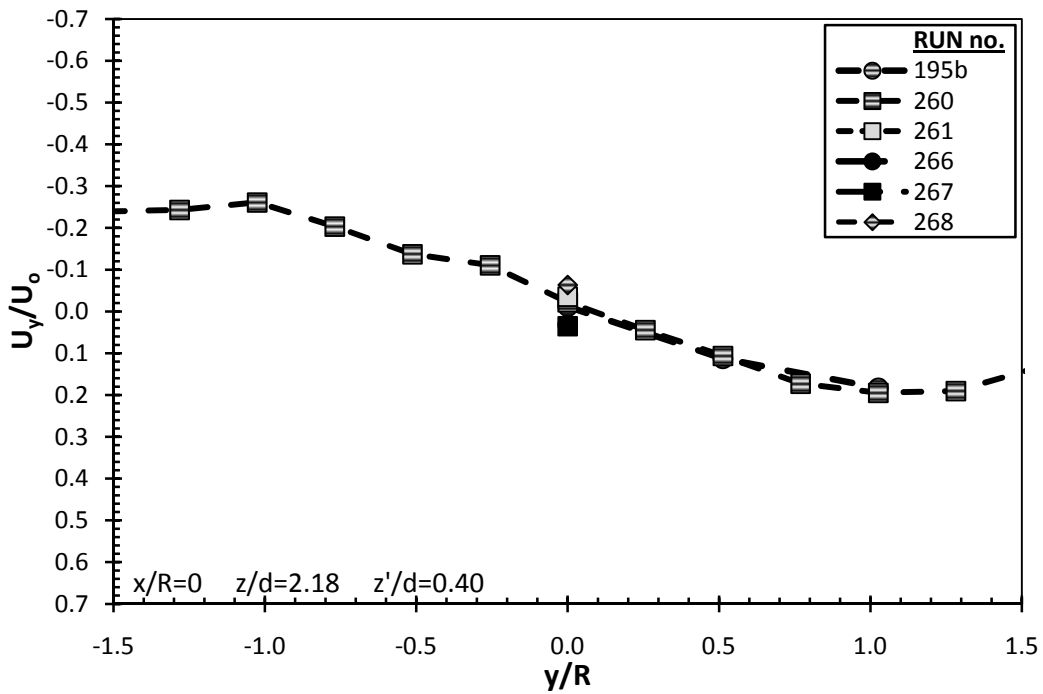


Figure D-30 Dimensionless lateral (U_y/U_o) / radial velocities along the y-axis for $z/d = 2.18$.

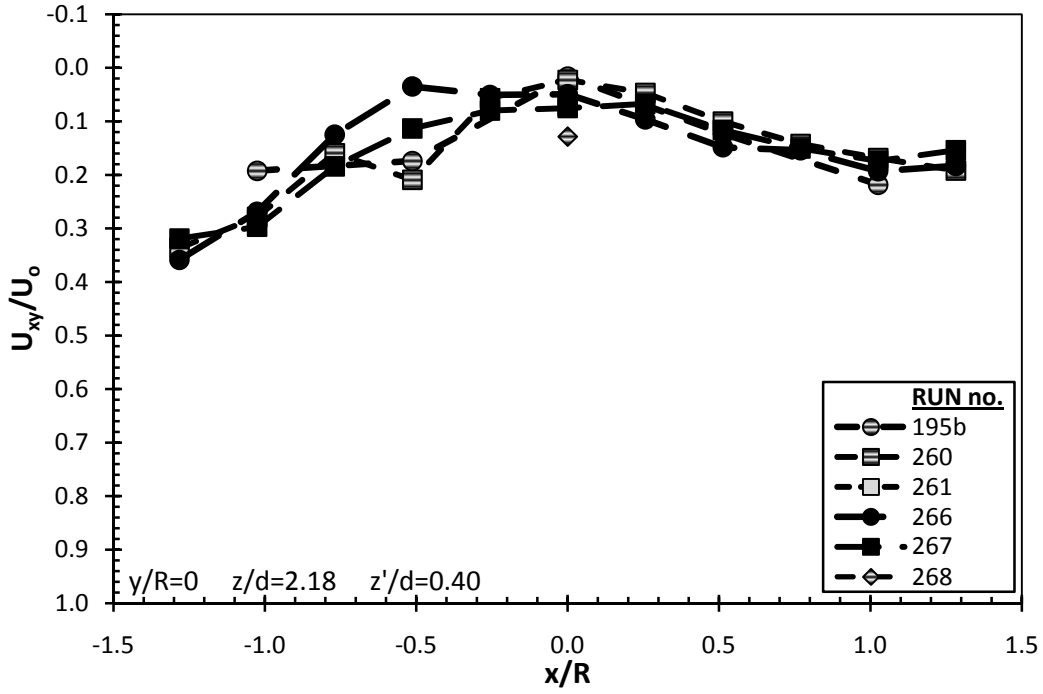


Figure D-31 Dimensionless horizontal (U_x/U_o) velocities along the x-axis for $z/d = 2.18$.

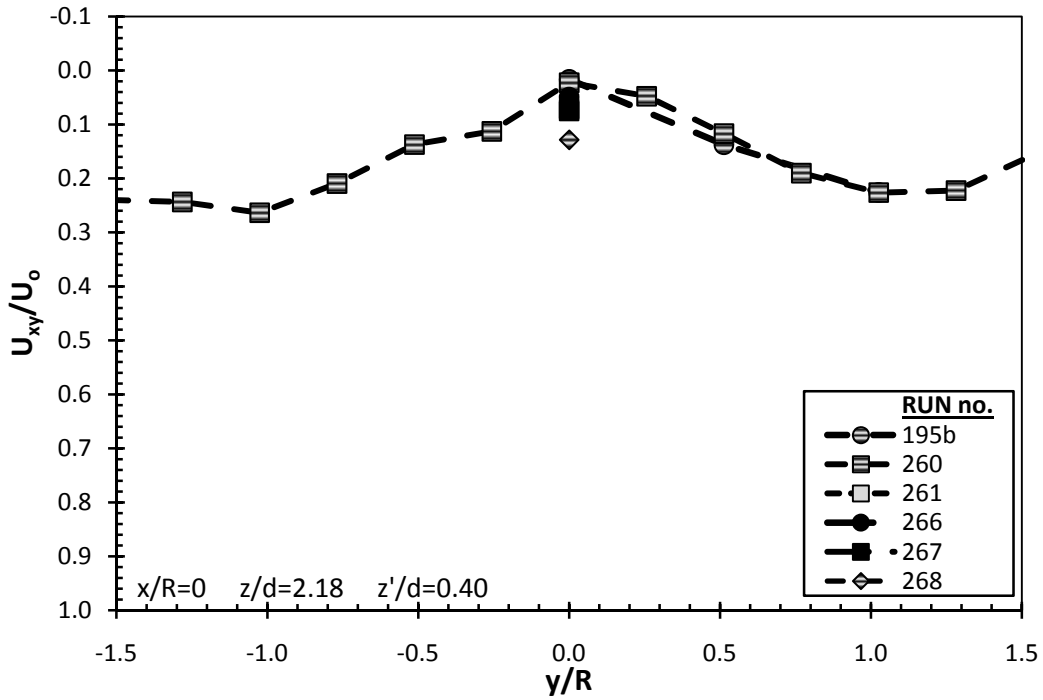


Figure D-32 Dimensionless horizontal (U_y/U_o) velocities along the y-axis for $z/d = 2.18$.

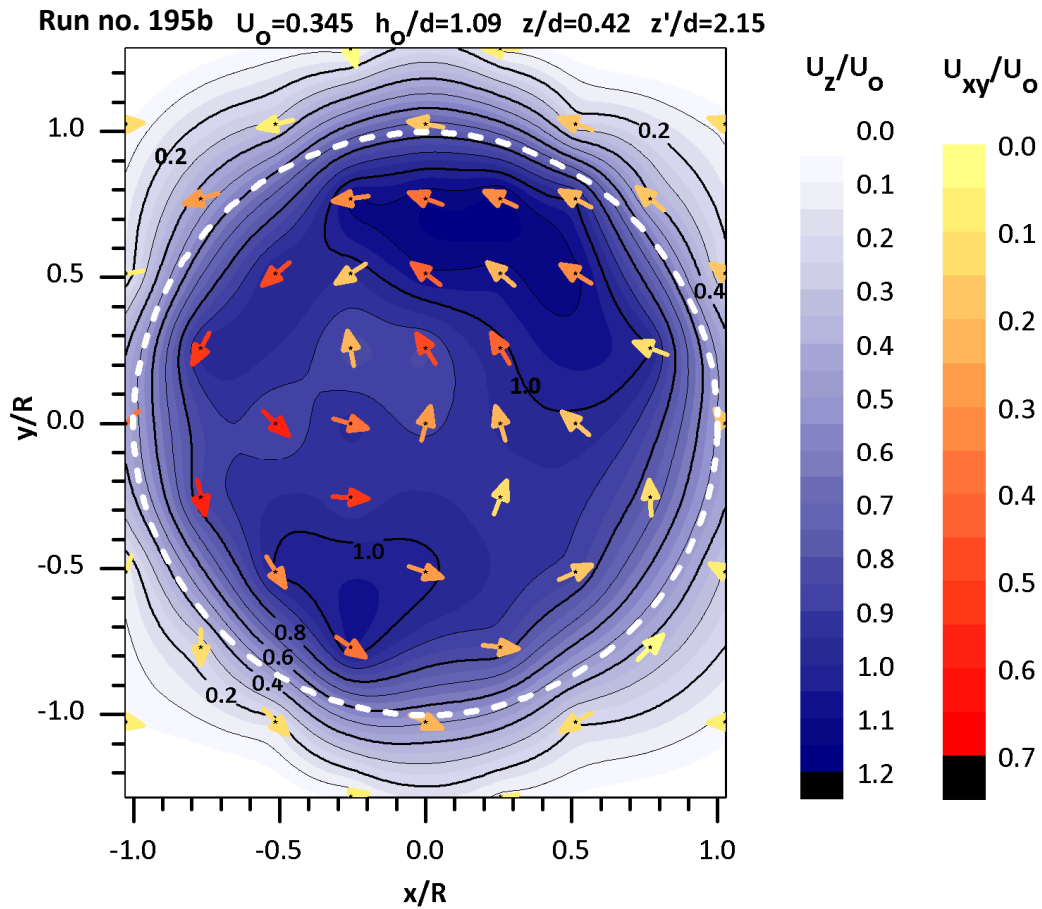


Figure D-33 Dimensionless axial (U_z/U_o) and horizontal (U_{xy}/U_o) velocities in the x - y plane for run number 195b at $z/d = 0.42$. The arrows indicate the location of the ADV measurements. Each arrow shows the magnitude (colour coded) and direction of the dimensionless horizontal velocity vector, U_{xy}/U_o . The magnitude (colour coded) of the dimensionless axial velocities were linearly interpolated / extrapolated for the entire cross-section. The hole boundary is marked by a white circle. The overflow and under-ice flow direction is towards the positive y/R direction.

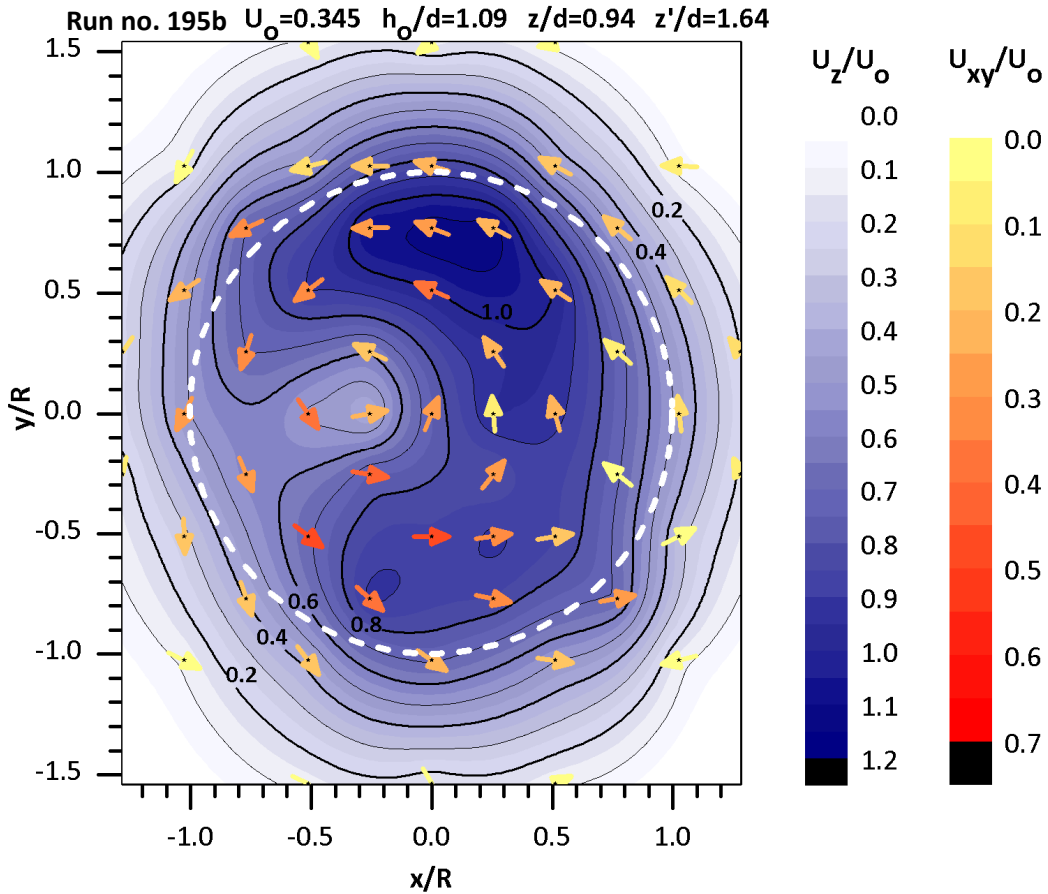


Figure D-34 Dimensionless axial (U_z/U_o) and horizontal (U_{xy}/U_o) velocities in the x - y plane for run number 195b at $z/d = 0.94$. The arrows indicate the location of the ADV measurements. Each arrow shows the magnitude (colour coded) and direction of the dimensionless horizontal velocity vector, U_{xy}/U_o . The magnitude (colour coded) of the dimensionless axial velocities were linearly interpolated / extrapolated for the entire cross-section. The hole boundary is marked by a white circle. The overflow and under-ice flow direction is towards the positive y/R direction.

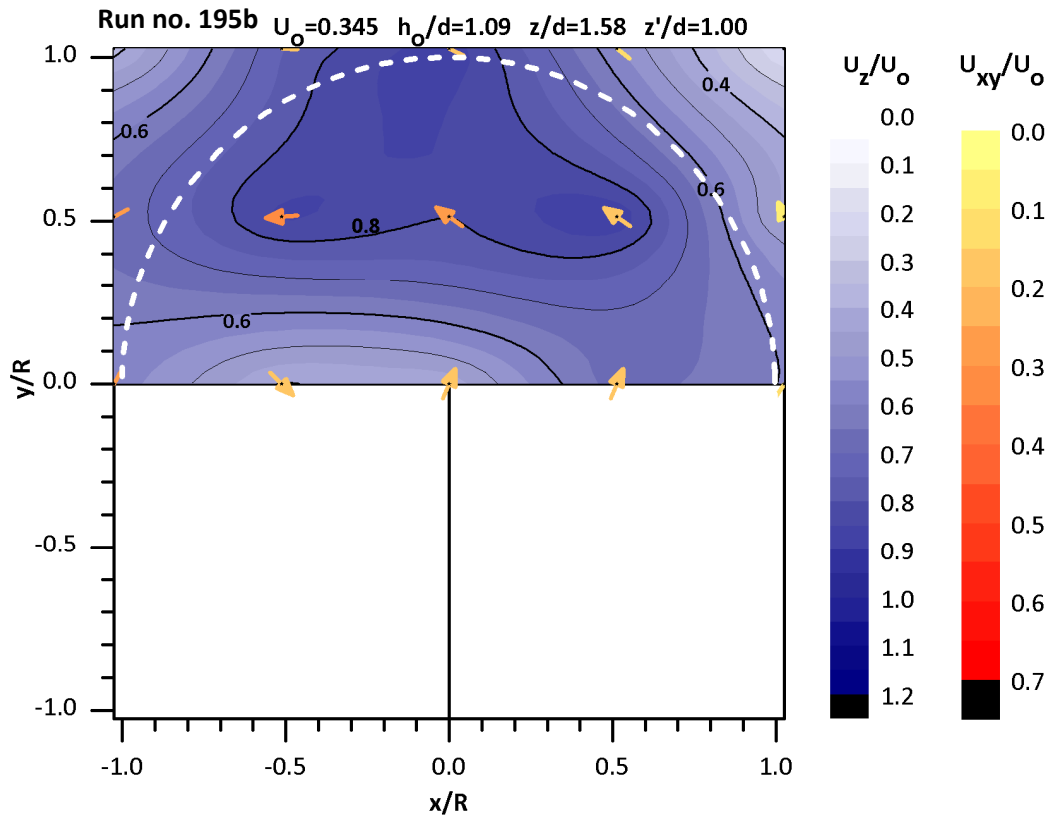


Figure D-35 Dimensionless axial (U_z/U_o) and horizontal (U_{xy}/U_o) velocities in the x - y plane for run number 195b at $z/d = 1.58$. The arrows indicate the location of the ADV measurements. Each arrow shows the magnitude (colour coded) and direction of the dimensionless horizontal velocity vector, U_{xy}/U_o . The magnitude (colour coded) of the dimensionless axial velocities were linearly interpolated / extrapolated for half of the cross-section. The hole boundary is marked by a white circle. The overflow and under-ice flow direction is towards the positive y/R direction.

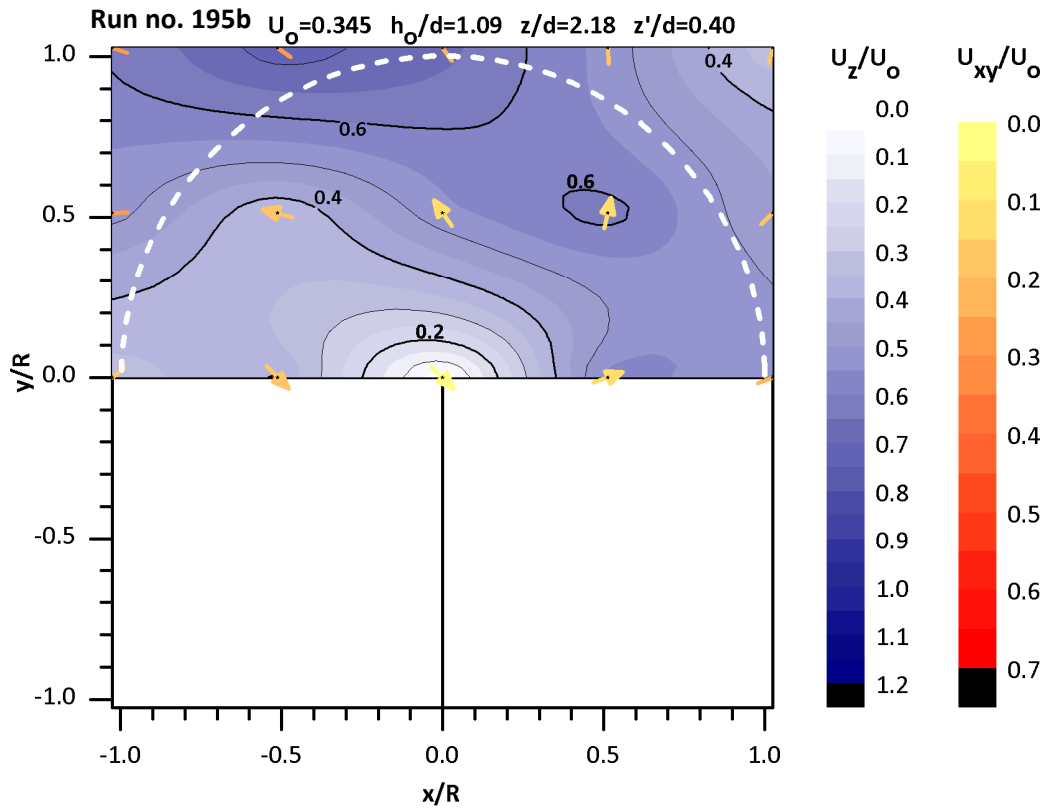


Figure D-36 Dimensionless axial (U_z/U_o) and horizontal (U_{xy}/U_o) velocities in the x-y plane for run number 195b at $z/d = 2.18$. The arrows indicate the location of the ADV measurements. Each arrow shows the magnitude (colour coded) and direction of the dimensionless horizontal velocity vector, U_{xy}/U_o . The magnitude (colour coded) of the dimensionless axial velocities were linearly interpolated / extrapolated for half of the cross-section. The hole boundary is marked by a white circle. The overflow and under-ice flow direction is towards the positive y/R direction.

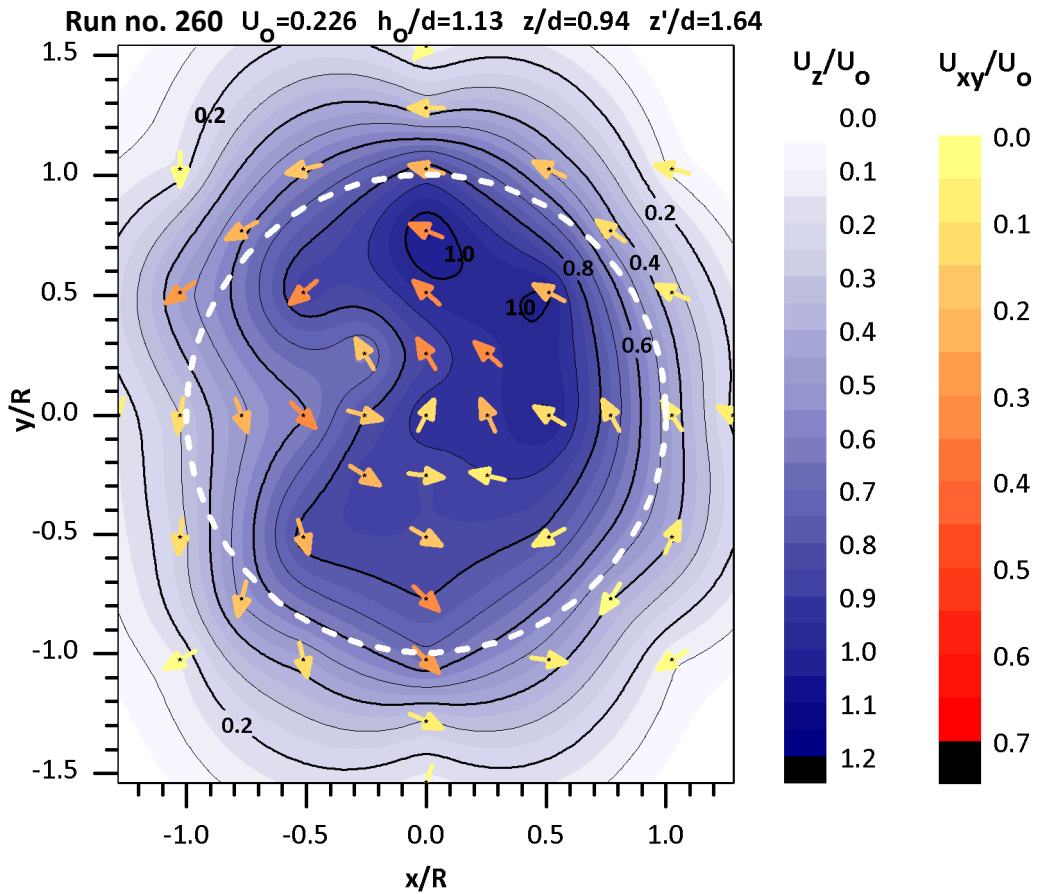


Figure D-37 Dimensionless axial (U_z/U_o) and horizontal (U_{xy}/U_o) velocities in the x - y plane for run number 260 at $z/d = 0.94$. The arrows indicate the location of the ADV measurements. Each arrow shows the magnitude (colour coded) and direction of the dimensionless horizontal velocity vector, U_{xy}/U_o . The magnitude (colour coded) of the dimensionless axial velocities were linearly interpolated / extrapolated for the entire cross-section. The hole boundary is marked by a white circle. The overflow and under-ice flow direction is towards the positive y/R direction.

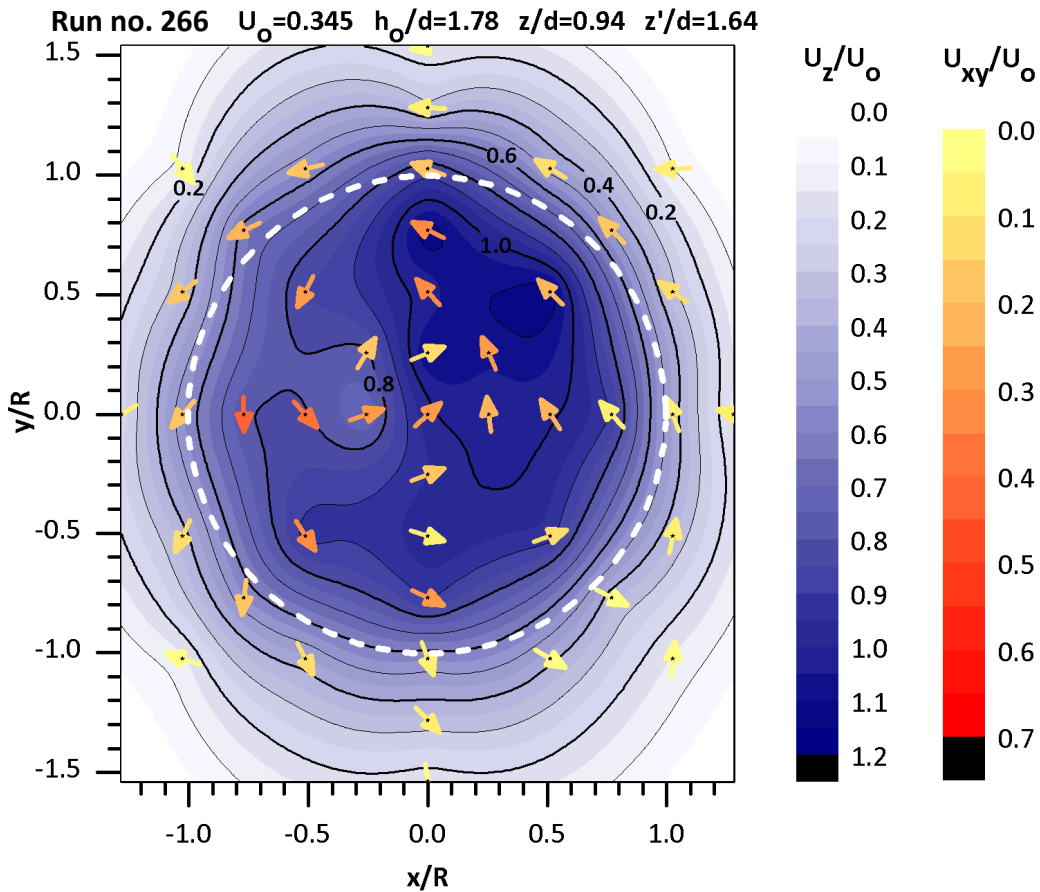


Figure D-38 Dimensionless axial (U_z/U_o) and horizontal (U_{xy}/U_o) velocities in the x - y plane for run number 266 at $z/d = 0.94$. The arrows indicate the location of the ADV measurements. Each arrow shows the magnitude (colour coded) and direction of the dimensionless horizontal velocity vector, U_{xy}/U_o . The magnitude (colour coded) of the dimensionless axial velocities were linearly interpolated / extrapolated for the entire cross-section. The hole boundary is marked by a white circle. The overflow and under-ice flow direction is towards the positive y/R direction.

Appendix E

Poster Abstract, Extended Abstract and Poster

Presented at the CRIPE Conference in 2009

Belanger, M., Hicks, F., Solomon, S., & Loewen, M. (2009). Influence of Mackenzie Delta Breakup on the Timing and Duration of Water Overflow on the Outer Delta Sea Ice Surface. Poster presented at the *CGU HS Committee on River Ice Processes and the Environment (CRIPE) - 15th Workshop on River Ice*, St. John's, Newfoundland and Labrador.



Influence of Mackenzie Delta Breakup on the Timing and Duration of Water Overflow on the Outer Delta Sea Ice Surface

M. Belanger¹, F. Hicks¹, S. Solomon², M. Loewen¹

¹*Dept. of Civil and Env. Eng. University of Alberta, Edmonton, AB, T6G 2W2*

²*Natural Resources Canada - Geological Survey of Canada (Atlantic), Dartmouth, NS*

*belangermaxime@hotmail.com, faye.hicks@ualberta.ca,
steve.solomon@nrcan-rncan.gc.ca, mark.loewen@ualberta.ca*

POSTER ABSTRACT

In winter, the shallow water depth regions of the outer Mackenzie Delta freeze to the bed thus forming bottomfast ice. During breakup, fresh water quickly floods the outer delta ice surface. This overflow is caused by a rapidly increasing water discharge from the upstream rivers, combined with an insufficient under-ice flow capacity in the outer delta. This overflow phenomenon is important in terms of defining boundary conditions in our numerical models of the Mackenzie Delta, during the ice breakup period.

In an attempt to predict the duration and the timing of this overflow to aid in planning field observations, our investigations, accomplished using 2005 to 2008 data, revealed that the overflow duration is highly dependent on the type of breakup that occurs in the upper delta. The floating ice overflow lasts for a much longer period of time when thermal breakup occurs compared to a dynamic breakup. Furthermore, it appears that the timing of the overflow can be predicted from the water level in the Mackenzie River at Arctic Red River (MARR).

The water level at MARR stays under 10m during thermal breakup years and peaks above 12 m during the years where dynamic breakup occurs. A water level of about 10 m at MARR appears to be the breakup transition threshold between an intact ice cover and a dynamic breakup. The nature of the breakup in the upper delta seems to be thermal when the freeze-up ice jam at MARR peaks below a 5.5m water level and the pre-breakup water level is less than 3.2m.

This poster describes our efforts in developing an understanding of what leads the Mackenzie Delta to breakup thermally versus dynamically, and describes a means by which we can predict the timing and duration of this overflow phenomenon.



CGU HS Committee on River Ice Processes and the Environment
15th Workshop on River Ice
St. John's, Newfoundland and Labrador, June 15 - 17, 2009

Influence of Mackenzie Delta Breakup on the Timing and Duration of Water Overflow on the Outer Delta Sea Ice Surface

M. Belanger¹, F. Hicks¹, S. Solomon², M. Loewen¹

¹*Dept. of Civil and Env. Eng. University of Alberta, Edmonton, AB, T6G 2W2*

²*Natural Resources Canada - Geological Survey of Canada (Atlantic), Dartmouth, NS*

*belangermaxime@hotmail.com, faye.hicks@ualberta.ca, Steve.Solomon@NRCan-RNCan.gc.ca,
mark.loewen@ualberta.ca*

EXTENDED ABSTRACT

In winter, the shallow water depth regions of the outer Mackenzie Delta freeze to the bed thus forming bottomfast ice. During breakup, fresh water quickly floods the outer delta ice surface. This overflow is caused by a rapidly increasing water discharge from the upstream rivers, combined with an insufficient under-ice flow capacity in the outer delta. This overflow phenomenon is not only interesting from a sea ice perspective, but is also important in terms of defining boundary conditions in our numerical models of the Mackenzie Delta, during the ice breakup period. In an attempt to predict the duration and the timing of this overflow, to aid in planning field observations, our investigations revealed that the overflow duration is highly dependent on the type of breakup (thermal versus dynamic) that occurs in the upper delta. Furthermore, it appears that the timing of the overflow can be predicted from the water level in the Mackenzie River at Arctic Red River (MARR). This poster describes our efforts in developing an understanding of what leads the Mackenzie Delta to breakup thermally versus dynamically, and describes a means by which we can predict the timing and duration of this overflow phenomenon.

Figure 1 shows a map of the Mackenzie Delta including the key location used in this study. The nature of breakup at MARR was determined by examining both the water level gauge at this site (Water Survey of Canada (WSC), 2009) and high-resolution Landsat satellite images (U.S. Geological Survey, 2009) as illustrated in Figure 2. WSC data from 2002 to 2008 suggests that the water level at MARR, referenced to the Geodetic Survey of Canada datum, stays under 10m during thermal breakup years (2003 and 2007) and peaks above 12 m during the years where dynamic breakup occurs. A water level of about 10 m at MARR appears to be the transition threshold, since an intact ice cover was observed at a water level of 10.4 m in 2008, and a

dynamic breakup was observed at a water level of 9.9 m in 2002. Furthermore, the study showed that a small freeze-up ice jam with a maximum peak water level of 5.5 m and a pre-breakup water level less than 3.2 m at MARR might predict that the subsequent breakup will be thermal.

Figure 1: Map of the Mackenzie Delta, NWT. (Natural Resources Canada, 2009)

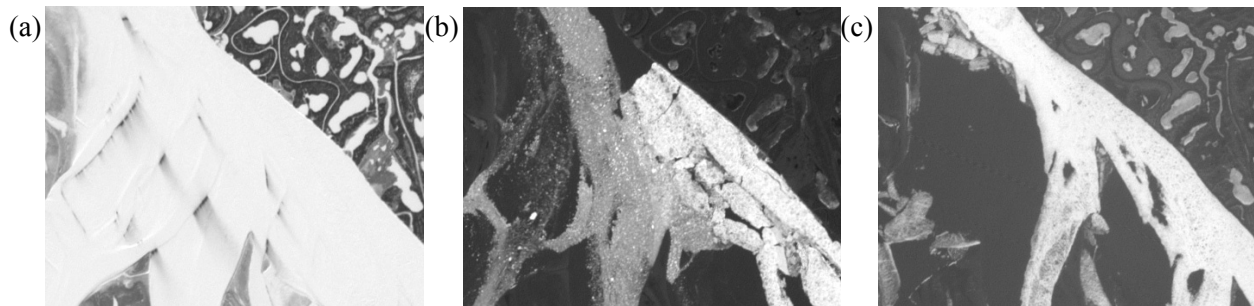
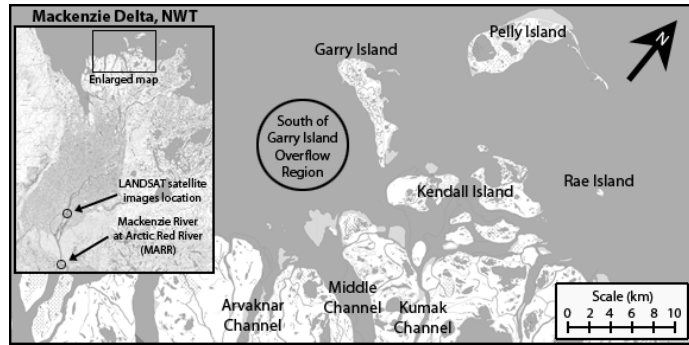


Figure 2: Landsat satellite images of the Mackenzie Delta 58km downstream of MARR showing (a) typical pre-breakup ice condition on April 22, 2002, (b) dynamic breakup on May 24, 2002, and (c) thermal breakup on May 27, 2003.

As verified some years ago, the bottomfast ice of the outer Mackenzie Delta can be identified using a Synthetic Aperture Radar (SAR). Using ENVISAT ASAR images (European Space Agency, 2009) in combination with MODIS satellite images (University of Alaska, 2009), the bottomfast ice was outlined and four stages of water overflow were identified as presented in Figure 3 for the 2008 overflow event. An overflow analysis south of Garry Island from 2005 to 2008 suggests that, on average: the first overflow on bottomfast ice occurs on May 14th; the first overflow on floating ice occurs on May 18th; the floating ice overflow peaks on May 20th; and the floating ice is drained on May 25th.

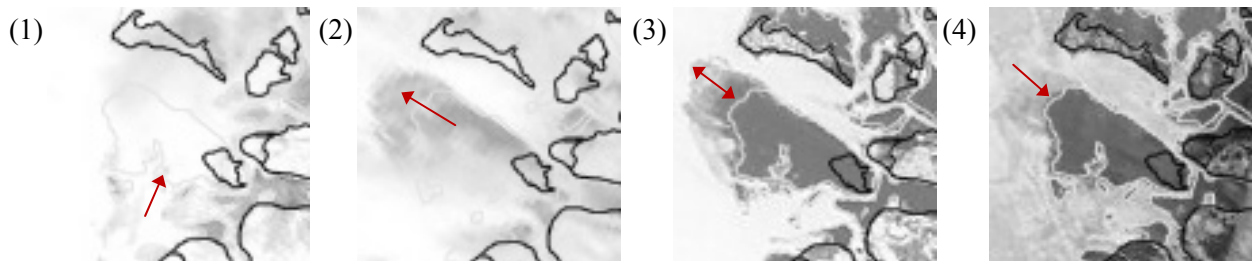


Figure 3: Overflow south of Garry Island in 2008 at (1) first overflow on bottomfast ice: May 16th, (2) first overflow on floating ice: May 20th, (3) maximum overflow on floating ice: May 22nd, and (4) drained floating ice: May 25th. The yellow border outlines the bottomfast ice location.

The overflow stages usually last for a shorter duration in years when breakup at MARR is dynamic, compared to years when it is thermal. For example, south of the Garry Island region, the four stages of overflow were completed in only 6 days in 2006 (dynamic breakup at MARR) whereas they took 18 days to complete during 2007 (thermal breakup at MARR).

The number of days it took for the overflow stages to occur south of Garry Island following a known water level increase at MARR is summarized in Table 1. In this table, the 0.3 m/d water level rise (WL rise) refers to the first date when the water level at MARR increased by 0.3 m in a day. Also, the 2 m difference in water level (Δ WL) refers to the first date when the water level at MARR increased by 2 m with respect to its pre-breakup level. The data correlates very well from year to year thus providing a confident overflow prediction. Water level data at MARR from 2002 to 2008 suggests that, on average, the 0.3 m/d water level rise occurs on May 10th and the 2.0 m cumulative water level increase happens on May 12th.

Table 1: Number of days the different stages of overflow south of Garry Island happened following a given water level event in the Mackenzie River at Arctic Red River (MARR) from 2005 to 2008.

Overflow Stage and Description	Days since WL rise > 0.3m/d	Days since Δ WL > 2m	Days since WL is declining
Stage 1 - First overflow on bottomfast ice	5 to 8	3 to 6	
Stage 2 - First overflow on floating ice	9 to 10	7 to 8	
Stage 3 - Maximum overflow on floating ice	11 to 13	9 to 12	
Stage 4 - Drained floating ice			1 to 4

This investigation showed that the overflow of the outer Mackenzie Delta is predictable and is related to a rapid increase in discharge which can be observed from the water level at MARR. As observed from satellite images, the nature of the breakup in the upper delta, which controls the duration of the outer delta overflow, seems to be thermal when the freeze-up ice jam and the pre-breakup water level are lower than average at MARR. The overflow duration lasts for a much longer period of time when thermal breakup occurs compared to a dynamic breakup. Additional studies concerning the nature of breakup at MARR would provide us with more confident and precise results which would then supply more accurate boundary conditions for the numerical model of the Mackenzie Delta. These studies would also be useful to improve predictions for the timing and the duration of the overflow which are valuable for field observations.

Acknowledgments

This research was funded by the Natural Sciences and Engineering Research Council of Canada (NSERC) through a scholarship to the first author, and the Government of Canada International Polar Year (IPY) program through a grant to the second author. This support is gratefully acknowledged. Special thanks are given to all the mentioned references which provided images and water level data for free and made this study possible.

References

- Environment Canada – Water Survey of Canada. (2009). *Real-Time & Archived Hydrometric Data*. Retrieved April 2, 2009, from <http://scitech.pyr.ec.gc.ca/waterweb/>
- European Space Agency – Earth Observation Link (Java Software). (2009). *ENVISAT ASAR On Line Collection*. Retrieved April 2009, from <http://earth.esa.int/EOLi/EOLi.html>
- Natural Resources Canada – Atlas of Canada. (2009). *Toporama – Topographic Maps*. Retrieved June 2008, from <http://atlas.nrcan.gc.ca/site/english/maps/topo/index.html>
- University of Alaska – Geographic Information Network of Alaska. (2009). *MODIS Images*. Retrieved 2008, from <http://www.gina.alaska.edu/data/gina-modis-images>
- U.S. Geological Survey – USGS Global Visualization Viewer. (2009). *Landsat Archive*. Retrieved March 2009, from <http://glovis.usgs.gov/>



CRIPE 2009 - 15th River Ice Workshop

Influence of Mackenzie Delta Breakup on the Timing and Duration of Water Overflow on the Outer Delta Sea Ice Surface



M. Belanger¹, F. Hicks¹, S. Solomon², M. Loewen¹
¹ Dept. of Civil and Environmental Engineering, University of Alberta
² Natural Resources Canada, Geological Survey of Canada (Atlantic)

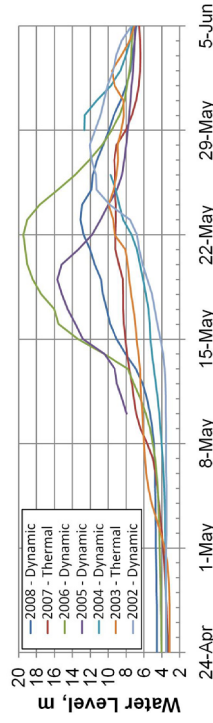
Introduction

In winter, the shallow water depth regions of the outer Mackenzie Delta freeze to the bed thus forming bottomfast ice. During breakup, rapidly increasing water discharge from the upstream rivers reaches the delta and overflows onto the sea ice surface possibly due to insufficient under-ice flow capacity in the outer delta. This overflow phenomenon is important in terms of defining boundary conditions in our numerical models of the Mackenzie Delta, during the ice breakup period.

This poster describes our efforts in developing an understanding of what leads the Mackenzie Delta to breakup thermally versus dynamically and describes a means by which we can predict the timing and duration of this overflow phenomenon.

Nature of Breakup in the Mackenzie River at Arctic Red River (MARR)

Thermal breakup years: water level remains below the 10m level.
Dynamic breakup years: water level peaks above the 12m level.



Daily average water level in the Mackenzie River at Arctic Red River (MARR).

A water level of about 10m is a breakup transition threshold:

- Dynamic breakup was observed at a water level of 9.9m.
- Intact ice cover was observed at a water level of 10.4m.

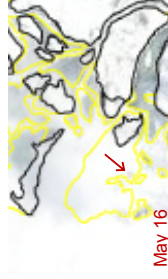
Thermal breakup predictions:

- Freeze-up ice jam water level less than 5.5m.
- Pre-breakup (late April) water level less than 3.2m.

Overflow Stages and Duration

Duration of the outer delta's floating ice overflow is longer during thermal breakup at MARR compared to years when it is dynamic:

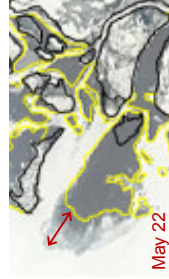
2008: 5 days 2007: 14 days 2006: 4 days 2005: 6 days



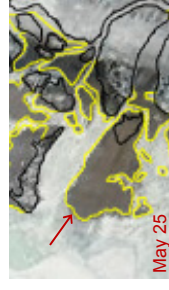
May 16
Stage 1 - First overflow on bottomfast ice



May 20
Stage 2 - First overflow on floating ice



May 22
Stage 3 - Maximum overflow on floating ice



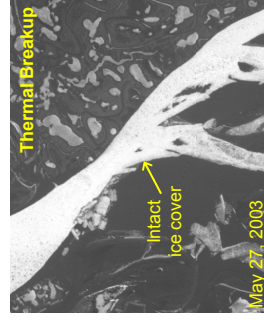
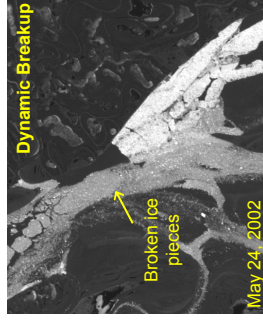
May 25
Stage 4 - Drained floating ice

Four overflow stages south of Garry Island in 2008. The yellow border outlines the bottomfast ice boundary.

Timing of Overflow

Number of days the different stages of overflow south of Garry Island happened following a given water level event in the Mackenzie River at Arctic Red River (MARR) and average date of overflow stage occurrence from 2005 to 2008.

Overflow Stage	Days since		Days since		Average	
	WL rise ≥ 0.3 m/d	Δ WL ≥ 2 m	WL is decreasing	date	date	date
Stage 1 - First overflow on bottomfast ice	5 to 8	3 to 6		May 14		
Stage 2 - First overflow on floating ice	9 to 10	7 to 8		May 18		
Stage 3 - Maximum overflow on floating ice	11 to 13	9 to 12		May 20		
Stage 4 - Drained floating ice			1 to 4		May 25	



Landsat satellite images of the Mackenzie Delta 58km downstream of MARR.